Mathematical modelling of flexural waves in structured elastic plates

Thesis submitted in accordance with the requirements of the
University of Liverpool for the degree of Doctor in Philosophy
by

Stewart Gavin Haslinger

February 2014

Abstract

This thesis discusses properties of flexural waves in thin elastic plates that incorporate a structured system of gratings of defects. The defects may take the form of inclusions or masses, but we focus on circular inclusions, and in particular, holes with a clamped edge. We place the work in the relatively new field of platonics, which is the study of flexural waves in plates governed by the fourth-order biharmonic plate equation. By analogy with photonic and phononic crystals, the two-dimensional structures in thin elastic plates are known as platonic crystals.

We present a novel analysis of trapped modes and transmission resonances in grating stacks, arising from the interaction with plane waves incident on the gratings. We show that the evanescent modes are important in demonstrating interesting and unusual filtering effects. In particular we analyse the previously unstudied effect of elasto-dynamically inhibited transmission (EDIT), where a resonance in transmission is cut in two by a resonant minimum arising from destructive interference. Similar destructive interference-induced phenomena have been observed in other settings, notably classical optical oscillators, metamaterials and plasmonics, but we are the first to do it for flexural plates.

The phenomenon of EDIT is a central theme of this thesis, and is linked to the analysis of even and odd Bloch modes in the grating waveguides. We develop a method that identifies the parameters of the model, the relative separations η and lateral shifts ξ of the gratings, and the spectral parameter β and angle of incidence θ_i of the plane wave, to find EDIT efficiently.

The method is powerful and universal, based on a recurrence procedure for the construction of reflection and transmission matrices. A multipole method is employed for circular scatterers and the limiting case of rigid pins, whereby the solutions are determined analytically. Recent developments have also been made with arbitrarily-shaped holes, and other future research is likely to focus on the association with Dirac-like cones that are linked to the standing modes arising in platonic crystals.

Contents

Abstract **i**

Contents **ii**

List of Figures **v**

Acknowledgements **xv**

List of Publications **xvi**

1 Introduction and background **1**

2 Underlying theory **8**

2.1 Governing equation 8

2.1.1 Structured interaction region 9

2.2 Plane wave representations of scattered waves 11

2.3 Quasi-periodicity conditions 13

2.3.1 Direct lattice and reciprocal lattice 14

2.3.2 Dispersion of Bloch waves and band diagrams 16

2.4 Concepts from classical optics 17

2.4.1 Diffraction grating 17

2.4.2 Efficiency curves and Wood anomalies 20

2.4.3 Stokes-Helmholtz reciprocity principle 22

2.4.4 Fabry-Pérot theory 23

2.4.5 Electromagnetically induced transparency 27

2.5 Spectral problem for biharmonic operator for doubly periodic square array 29

2.5.1 Governing equations 30

2.5.2 Multipoles 31

2.5.3 Boundary conditions and their multipole representations 32

2.5.4 Rayleigh identities and lattice sums 33

2.5.5 Band diagrams and stop-bands 36

2.6 Green's functions 38

2.6.1 Quasi-periodic Green's function for an infinite grating of circular scatterers . . . 39

3 Method of solution for a platonic grating stack 45

3.1 Multipole method . . . 47
3.1.1 Governing equations . . . 48
3.1.2 Multipoles . . . 49
3.1.3 Rayleigh identities . . . 50
3.1.4 Reconstruction equations . . . 54
3.1.5 Conservation of energy . . . 56
3.1.6 Zero-radius limit: rigid pins . . . 62
3.2 Recurrence algorithm for multipole method . . . 65
3.2.1 Propagation matrices . . . 66
3.2.2 Geometric series . . . 68
3.2.3 Enhanced transmission . . . 69
3.3 Waveguide approach . . . 72
3.3.1 Grating Green's function: plane wave form . . . 73
3.3.2 Mode symmetry in a general triplet stack . . . 73
3.4 Analysis of transmission resonances . . . 74

4 Pinned platonic grating stacks 78

4.1 Pairs of rigid-pin platonic gratings . . . 79
4.1.1 Varying angle of incidence . . . 79
4.1.2 Varying relative grating separation and analogy with Fabry-Pérot theory . . . 81
4.2 Triplets of rigid-pin platonic gratings . . . 83
4.2.1 Numerical results for symmetric triplets . . . 85
4.2.2 Odd and even modes . . . 85
4.2.3 Quality factors for the trapped modes . . . 87
4.3 Double resonances and the analogy with EIT . . . 88

5 Nonzero-radius platonic grating stacks 91

5.1 Governing equations: scattering by a single grating . . . 93
5.2 Transmission and reflection properties of a single grating . . . 94
5.3 Transmission resonance for pairs of aligned gratings: normal incidence . . . 96
5.3.1 Examples for various nonzero radii . . . 97
5.3.2 Convergence properties . . . 98
5.4 Transmission resonance for pairs of aligned gratings: oblique incidence . . . 100
5.5 Controlling transmission resonances for triplets of gratings . . . 102
5.5.1 Triplets of identical gratings . . . 103

5.5.2 Non-uniform triplets with rigid pins on the exterior boundary . . 105
5.5.3 Non-uniform triplets with rigid pins in the central grating 106
5.6 Shifted systems of gratings and the EDIT phenomenon 108
5.7 EDIT examples without rigid pins 110

6 Symmetry and resonant modes in platonic grating stacks 113
6.1 Structured waveguide 114
6.1.1 Grating Green's function: plane wave form 114
6.2 Mode symmetry in a general triplet stack 116
6.2.1 Odd and even Bloch modes 117
6.2.2 Analogue of EDIT for waveguide 117
6.2.3 Matrix elements near light lines 120
6.3 Mode symmetry in an unshifted triplet stack 121
6.3.1 Surface plots 123
6.3.2 Projection method for even modes 123
6.4 Optimized method to steer waveguide modes 126

7 Conclusions and future work 132

A Grating sums and accelerated convergence 135
A.1 Grating sums 135
A.2 Accelerated convergence 138

Index 150

List of Figures

1.1 (a) Triplet of aligned rigid-pin gratings with period d and relative grating separation $\eta = 1$. The angle of incidence is θ_i. (b) Flexural displacement plotted as a function of x and y for the transmission resonance associated with a symmetric trapped mode for $\theta_i = 30^\circ$ for the grating stack illustrated in (a). 5

1.2 Normalised transmitted energy T_{tot} versus spectral parameter β for a triplet of rigid pins with $\theta_i = 30^\circ$, $d = 1$, $\eta_1 = \eta_2 = 1$ in both cases and: (a) $\xi = 0$; (b) $\xi = 0.25200$. The parameter ξ represents relative lateral shift of the central grating. 6

2.1 Stack of gratings consisting of an outer pair of finite nonzero inclusions with radius a and period d, and a central grating of rigid pins. The relative grating separation between consecutive gratings is η, and the relative lateral shift of the central grating is ξ. 10

2.2 A plane wave ($\boldsymbol{I}$) incident on a grating of rigid pins from above. We show the generic scattered field consisting of reflected and transmitted waves $\boldsymbol{R}$ and $\boldsymbol{T}$ respectively. The lines γ^+ and γ^- are used to indicate the upper and lower sides of the grating. 12

2.3 A two-dimensional lattice composed of particles of the same mass, placed at equal distances from one another along two lines intersecting at an arbitrary angle θ. 14

2.4 (a) Infinite plate with a doubly periodic array of cylindrical voids. (b) The irreducible Brillouin zone for the doubly periodic square array. . . . 15

2.5 Converged band diagrams for clamped-edge boundary conditions, for radii (a) $a = 0.2$ and (b) $a = 0.35$. Γ, X and M are the vertices of the irreducible part of the Brillouin zone. The inset in (b) shows a magnification of a "collapsed" band. Taken from Poulton *et al.* (2010). . 16

2.6 Converged band diagrams for free-edge boundary conditions, with Poisson ratio $\nu = 0.3$, for radii (a) $a = 0.2$ and (b) $a = 0.35$. The bands lie close to those for the Bloch modes of a homogeneous structure. Taken from Poulton *et al.* (2010). 17

2.7 A plane wave ($\boldsymbol{I}$) incident on a grating of rigid pins from above with angle of incidence θ_i. We show the diffraction order $p = -1$ as well as the zeroth order reflected and transmitted fields. 20
2.8 Normalised transmitted energy T_{tot}, summed over propagating orders (see equation (3.93)), versus β for a pair of gratings, and normalised reflected energy R_{tot} for a single grating (dashed line) of rigid pins with $d = 1$. The incident wave is of Helmholtz type, with angle of incidence $\theta_i = 30°$. Adapted from Movchan *et al.* (2009). 22
2.9 Normalised reflected energy (efficiency) versus angle of incidence θ_i for a single grating of rigid pins for $\beta = 8.0$. Solid curve: $p = 1$, Dashed curve: $p = -1$. The lines of symmetry for the Littrow angle $\pm 23.1225°$ (± 0.403565 radians) are shown by the vertical lines. 23
2.10 Multiple-beam interference for a transparent plate with thickness h and refractive indices n for the ambient medium, and n' for the plate. The angles of incidence and refraction are θ and θ' respectively. 25
2.11 Susceptibility as a function of the frequency ω_p of the applied field relative to the atomic resonance frequency ω_{31}, for a radiatively broadened two-level system with radiative width γ_{31} (dashed line) and an EIT system with resonant coupling field (solid line): top, imaginary part of $\chi^{(1)}$ characterizing absorption; bottom, real part of $\chi^{(1)}$ determining the refractive properties of the medium. Taken from Fleischhauer *et al.* (2005). 28
2.12 Generic system for EIT: lambda-type scheme with probe field of frequency ω_p and coupling field of frequency ω_c. $\Delta_1 = \omega_{31} - \omega_p$ and $\Delta_2 = \omega_{32} - \omega_c$ denote field detunings from atomic resonances and Γ_{ik} radiative decay rates from state $|i\rangle$ to state $|k\rangle$. Taken from Fleischhauer *et al.* (2005). 29
2.13 (a) Infinite plate with a doubly periodic array of circular voids. (b) The central unit cell $\Omega_{0,0}$ containing a circular scatterer. 30
2.14 Radius of convergence for multipole expansion. 32
2.15 (a) First quadrant of the band surface for the lowest band for the square array of clamped cylinders of zero radius, with β on the vertical axis. (b) Contours of constant β for the same surface. The ranges for k_{0x} and k_{0y} are $0 \leq k_{0x} \leq \pi d$ and $0 \leq k_{0y} \leq \pi d$; the numbers shown along the intervals ΓX and ΓY correspond to positions of the points of the grid rather than the values of k_{0x} and k_{0y}. Taken from McPhedran *et al.* (2009). 37
2.16 Two different views showing the "sandwiching" of the first band (blue) between the plane wave surfaces shown in red for orders $(0, 0)$ and $(-1, 0)$ in part(a), and $(0, 0)$ and $(0, -1)$ in part (b). 38

2.17 Triangle illustrating Graf's addition theorem for a platonic grating. . . . 40

3.1 Example of a multiple-grating waveguide. The elementary cell is indicated by the dashed rectangle. 46
3.2 The unit cell Ω containing a circular scatterer. The boundary $\partial\Omega$ is the union of its constituent parts: $\partial\Omega = \Gamma^+ \cup \Gamma^- \cup \Gamma_l \cup \Gamma_r \cup C_0$. We also indicate the unit outward normals $\boldsymbol{n}$ for each part of the boundary. . . . 52
3.3 Normalised reflected energy R_{tot} versus β for normal incidence for a single grating of voids with period $d = 1$ and radius $a = 0.1$ (brown), $a = 0.01$ (black), $a = 1.0 \times 10^{-6}$ (blue) and the limiting case of $a = 0$ (dashed). 65
3.4 Coordinate systems for the top (x_1, y_1) and bottom (x_2, y_2) gratings for a shifted pair of rigid-pin gratings, and the central line of symmetry (x, y) to which we shift the phase origins of the reflection and transmission matrices. Reflection and transmission matrices for the sth and $(s+1)$th gratings are also shown. 66
3.5 (a) Normalised transmitted energy T_{tot}, summed over propagating orders versus β for three pairs of gratings, and normalised reflected energy R_{tot} for a single grating (dot-dashed line) of rigid pins. The incident wave is of Helmholtz type with $\theta_i = 30°$. Data: $d = 1$, $\eta = 1$. (b) Detail in the neighbourhood of the transmission resonance for a shift of $\xi = 0.4$. Dashed lines are used to emphasise the full-power and half-power points. 71
3.6 Enhanced transmission peaks for shifted pairs of gratings with $d = 1$, $\eta = 1$ and $\theta_i = 30°$. Normalised transmitted energy T_{tot} for propagating orders (zeroth order only) is plotted versus β for shifts ξ in steps of 0.1 from left to right. The narrowest peaks occur for $\xi = 0.5$ and $\xi = 0$ and these correspond to the highest Q. 72
3.7 Triplet of rigid-pin gratings. 75
3.8 EDIT effect for a triplet of rigid-pin gratings with the central grating shifted by $\xi = 0.25200$ for $\theta_i = 30°$. Normalised transmitted energy T_{tot} (curve **1**, blue) as a function of β for the triplet. Curve **2** (red) represents the total transmission for the outer pair of gratings. 76
3.9 Normalised transmitted energy T_{tot} versus spectral parameter β for a triplet of rigid pins with $\alpha_0 = 2.1$ in both cases: (a) $\eta d = 1$; (b) optimized resonances for a triplet with $\eta^* d = 1.185266$. The normalised reflected energy R_{tot} is shown by the dashed curve. 77

4.1 (a) Normalised transmitted energy T_{tot} versus β for a pair of unshifted rigid-pin gratings (left spike) and for a shift of half the period (right). For both pairs, $d = 1$, $\eta = 1$ and $\theta_i = 30°$. Also shown are the normalised reflected energy R_{tot} versus β for a single grating (solid green curve close to $T_{\text{tot}} = 1$) and a straight line (dashed) indicating maximum normalised energy of 1. The other two pictures are blow ups of the transmission peaks. These detailed plots illustrate the separation shapes of the Fano resonances. 80

4.2 Normalised transmitted energy T_{tot}, summed over propagating orders versus β for five pairs of gratings, and normalised reflected energy R_{tot} for a single grating (dashed line) of rigid pins. The incident wave is of Helmholtz type with $\theta_i = 27°$, and $d = 1$, $\eta = 1$. The lateral shift values are $\xi = 0, 0.1, 0.2, 0.4$ and 0.5 from left to right. 81

4.3 Normalised transmitted energy T_{tot}, summed over propagating orders versus β for five pairs of gratings, and normalised reflected energy R_{tot} for a single grating (dashed line) of rigid pins, with $d = 1$ and $\eta = 1$. The incident wave is of Helmholtz type with (a) $\theta_i = 30°$ (b) $\theta_i = 29°$ (c) $\theta_i = 31°$. The lateral shift values are $\xi = 0, 0.1, 0.2, 0.4$ and 0.5 from left to right. 82

4.4 Total transmittance T_{tot} (curve **1**, solid blue) for a pair of rigid-pin gratings and total reflectance R_{tot} (curve **2**, dashed olive green) for a single grating of rigid pins as functions of β. Data used: (a) $\eta = 1$, (b) $\eta = 2$. Here $L = 0$. 83

4.5 (a) General incidence for the scattering problem for a symmetric triplet with a shifted middle grating. $\boldsymbol{I}$ represents the incident plane wave with amplitude 1, and R_0 and T_0 denote complex amplitudes for zeroth order in reflection and transmission. (b) Anti-symmetric incidence for a stack of three parallel gratings with a shifted middle grating. The modes are odd functions of y. The amplitudes of the incident waves are 1 above and -1 below the triplet, and R_a and $-R_a$ are the corresponding complex amplitudes for zeroth order reflection. (c) Symmetric incidence for a shifted triplet. The modes are even functions of y. Here R_s is used to denote the complex amplitudes for zeroth order reflection for this symmetric case. 84

4.6 (a) T_{tot} versus β for aligned and shifted triplets for $\theta_i = 30°$ and $d = 1$. The central spike represents a trapped mode for both geometries. The peak on the right (dotted green) occurs for the triplet with the shifted middle grating ($\xi = 0.5$) and the peak on the left (solid blue) occurs for the geometry with three aligned gratings with $\xi = 0$. The grating separation is $\eta = 1$ for all consecutive gratings. Also shown is R_{tot} versus β for a single grating and a straight line (dashed) indicating maximum normalised energy of 1. (b) T_{tot} versus β in the region of $\beta_* = 3.61747$. Three geometries are virtually coincident: pair of unshifted gratings with $\eta = 2$ (dashed black curve), triplet of aligned gratings (solid blue curve) and triplet with shifted middle grating ($\xi = 0.5$) with $\eta = 1$ between each pair (solid green curve). 86

4.7 Transmission resonances for symmetric trapped mode for a triplet with shifted middle grating $\xi = 0.5$ (dotted curve), with $d = 1$ and $\eta = 1$ between each grating, and a pair of shifted gratings ($\xi = 0.5$) with $d = 1$, $\eta = 1$. In both cases, $\theta_i = 30°$. 87

4.8 Resonant β_* representing trapped modes for horizontal shifts ξ in steps of 0.1 across a single unit period for both shifted pairs (green, dashed), and triplets with a shifted middle grating (blue, solid). For both geometries, $\theta_i = 30°$ is considered. We also illustrate the fixed, anti-symmetric resonance with a horizontal straight line. 88

4.9 T_{tot} versus β for triplets for $\theta_i = 30°$, $d = 1$, $\xi = 0$, with various relative grating separation η. The outer gratings are separated by $\eta d = 2$. The brown curve represents the structure where the central grating is positioned at 35 % of the separation, with respect to the bottom grating. The red curve has the middle grating at 40 %, and the blue curve has its middle grating positioned 45 % into the separation with respect to the bottom of the triplet structure. 89

4.10 (a) EDIT effect for a triplet of rigid-pin gratings with the central grating shifted by $\xi = 0.25200$ for $\theta_i = 30°$. Normalised transmitted energy T_{tot} (blue curve **1**) as a function of β for the triplet. Curve **2** (red) is T_{tot} for the outer pair of gratings. (b) Flexural displacement for the outer pair of gratings of rigid pins ($\eta = 2$) as a function of x and y for $\beta_* = 3.61747$. (c) Flexural displacement for the triplet of rigid-pin gratings ($\eta = 1$) as a function of x and y for $\beta_* = 3.61747$. 90

5.1 Examples of periodic arrays in elastic systems incorporating plates (a) aircraft wings (www.instartupland.com) (b) cable-stayed bridge (Femern A/S, http://buildipedia.com). 92

5.2 Stack of gratings consisting of an outer pair of finite nonzero inclusions of radius a and period d and a central grating of rigid pins characterised by the relative lateral shift ξ. The relative grating separation between consecutive gratings is η. 93
5.3 Normalised reflected energy versus spectral parameter β for $\theta_i = 30^\circ$ for a single grating of voids with radius $a = 0$ using (a) quasi-periodic grating Green's function and (b) direct summation of grating sums. . . 95
5.4 Normalised reflected (blue) and transmitted (red) energy versus spectral parameter β for $\theta_i = 30^\circ$ for a single grating of voids with radius $a = 0.01$ using (a) direct summation of grating sums and (b) Twersky accelerated convergence formulae. 96
5.5 Pair of gratings consisting of inclusions of finite radius a, with period d and relative grating separation η. 97
5.6 Normalised transmitted energy T_{tot} (curve **1**, solid blue) for a pair of gratings of inclusions of radius a and normalised reflected energy R_{tot} (curve **2**, dashed green) for a single grating of inclusions as functions of β for separation $\eta d = 1$ and $L = 2$. Data used: (a) $a = 0.1$, (b) $a = 0.01$. 99
5.7 Normalised transmitted energy T_{tot} (curve **1**, solid blue) for a pair of rigid-pin gratings and normalised reflected energy R_{tot} (curve **2**, dashed red) for a single grating of rigid pins as functions of β. Data used: $\eta = 2$, $\theta_i = 30^\circ$, $d = 1$ and $L = 0$. The diagram (b) is a blow-up of the sharp transmission resonance from (a). 101
5.8 Normalised reflected energy R_{tot} as a function of β for a single grating with inclusions of radius $a = 0.1$ (with order of truncation $L = 2$) for the angle of incidence (a) $\theta_i = 0^\circ$ (curve **1**, red), 7.5° (curve **2**, blue), 15° (curve **3**, black) and (b) $\theta_i = 30^\circ$ (curve **1**, green), 25° (curve **2**, blue), $\theta_i = 20^\circ$ (curve **3**, red). 101
5.9 (a) Triplet consisting of three identical gratings of inclusions with nonzero radius a; (b) triplet consisting of a central grating of inclusions of nonzero radius a, surrounded by a pair of rigid-pin gratings; (c) triplet consisting of a pair of gratings with inclusions of nonzero radius a surrounding a grating of rigid pins. 102
5.10 Normalised transmitted energy T_{tot} (curve **1**, solid blue) as a function of β for normal incidence for a triplet of gratings of inclusions with $a = 0.02$, $\eta d = 1$ and $L = 2$. Curve **2** (dashed) represents normalised reflected R_{tot} for a single grating of such scatterers: (a) aligned gratings, $\xi = 0$; (b) shifted central grating with $\xi = 0.2$. 103

5.11 (a) Normalised transmitted energy T_{tot} as a function of β for a triplet of unshifted gratings of rigid inclusions with $a = 0.01$, $\eta d = 1$, for $\theta_i = 30°$. Field plots for transmission resonances: (b) a symmetric mode with $\beta_*^{(1)} = 3.819908$; (c) an anti-symmetric mode with $\beta_*^{(2)} = 3.93678$. . . . 104

5.12 Normalised transmitted energy T_{tot} as a function of β for normal incidence for a symmetric triplet with (a) $a = 0$ (normalised reflected energy R_{tot} for a single grating of zero-radius scatterers is shown by the dashed curve) (b) $a = 0.15$ and (c) $a = 0.20$ for the central grating. Here $\xi = 0$, $\eta d = 1$, and $L = 2$. 105

5.13 Flexural displacement as a function of x and y for (a) an anti-symmetric mode ($\beta_* = 3.9995073$) and (b) a symmetric mode ($\beta_* = 4.041664$). Data used: central grating inclusions with $a = 0.1$, $\theta_i = 18°$ and $\eta d = 1$. 107

5.14 Normalised transmitted energy T_{tot} as a function of β: (a) for a triplet consisting of an outer pair of gratings with $a = 0.1$ and the central grating of rigid pins ($\eta d = 1$); (b) for the outer pair of gratings with $a = 0.1$ and $\eta = d = 2$. Data used: $\theta_i = 15°$, $L = 2$. 107

5.15 Flexural displacement as a function of x and y for a triplet consisting of an outer pair of gratings with inclusions of radius $a = 0.1$ and a central unshifted rigid-pin grating, for an angle of incidence of 15°. (a) Anti-symmetric mode ($\beta_* = 4.011852$); (b) symmetric mode ($\beta_* = 4.0496094$). Data: $\eta d = 1$ and $L = 2$. 108

5.16 Normalised transmitted energy T_{tot} as a function of β for two shifted triplets, $\xi = 0.25$ (solid blue) and $\xi = 0.5$ (solid red), containing a central grating of rigid pins ($\eta d = 1$). (a) Angle of incidence $\theta_i = 15°$, outer scatterer radius $a = 0.1$; (b) $\theta_i = 20°$, $a = 0.085$. 109

5.17 EDIT: normalised transmitted energy T_{tot} (solid black curve) as a function of β for a shifted rigid-pin triplet with $\xi = 0.25200$ for $\theta_i = 30°$. The two peaks represent the transmission resonances for the outer pair (solid blue) and the inner pair (dashed). 109

5.18 Normalised transmitted energy T_{tot} (curve **1**, solid blue) as a function of β for a triplet with a shifted central grating of rigid pins and the outer pair of gratings of inclusions of radius $a = 0.01$. Curve **2** (solid red) represents the total transmittance for the outer pair of gratings. Data used: (a) $\xi = 0.3112$, $\theta_i = 27°$. (b) $\xi = 0.23265$, $\theta_i = 26°$. 110

5.19 (a) Flexural displacement as a function of x and y for a pair of gratings consisting of inclusions of radius $a = 0.01$ with grating separation $\eta d = 2$ for $\beta_* = 3.748779850$. (b) Flexural displacement as a function of x and y for a triplet with a shifted central grating of rigid pins ($\xi = 0.23265$) and the outer pair of gratings consisting of inclusions of radius $a = 0.01$ for $\beta_* = 3.748779784$, $\eta d = 1$. Data: $\theta_i = 26°$. 111
5.20 Normalised transmitted energy $T_{\rm tot}$ as a function of β for a triplet with a shifted central grating of finite radius inclusions with $a = 0.0035$, and an outer pair of gratings of inclusions of radius $a = 0.01$, $\theta_i = 26°$. Data used: (a) $\xi = 0.4$ (red curve), $\xi = 0.42$ (blue curve); (b) $\xi = 0.45556$. . 112

6.1 Example of a triple grating waveguide. The elementary cell is indicated by the dashed rectangle. 115
6.2 Contours for logarithm of modulus of $M_{11}-M_{13}$ (solid), and of $2M_{12}M_{21}-M_{11}(M_{11}+M_{13})$ (dashed) for a shifted three-grating stack of rigid pins ($\xi = 0.25200$, $d = 1$), as a function of α_0 and β. The circle corresponds to $(\alpha_0, \beta) = (1.808735, 3.61747)$. 119
6.3 Surface plot of the logarithm of the modulus of (a) $M_{11}-M_{13}$ (odd mode) (b) $2M_{12}M_{21}-M_{11}(M_{11}+M_{13})$ (even mode) for the shifted three grating stack of rigid pins ($\xi = 0.25200$, $d = 1$), as a function of α_0 and β. . . . 120
6.4 Contours for logarithm of modulus of $M_{11} - M_{13}$ (solid), and of $2M_{12}^2 = M_{11}(M_{11}+M_{13})$ (dashed) for an aligned three grating stack of rigid pins ($d = 1$, $\xi = 0$), as a function of α_0 and β. The circle corresponds to $(\alpha_0, \beta) = (1.66451, 3.596951)$. 122
6.5 Surface plot of the logarithm of modulus of $M_{11} - M_{13}$ for an aligned three grating stack of rigid pins ($d = 1$, $\xi = 0$), as a function of α_0 and β. 122
6.6 Surface plot of the logarithm of modulus of $M_{11} - M_{13}$ for an aligned three grating stack of rigid pins ($d = 1$, $\xi = 0$), as a function of α_0 and β, giving the odd mode trajectory in the vicinity of the light line. 123
6.7 (a) Normalised transmitted energy $T_{\rm tot}$ versus spectral parameter β for a triplet of rigid pins ($d = 1$, $\xi = 0$) with $\alpha_0 = 2.1$ (blue curve / right-hand pair), $\alpha_0 = 2.3$ (black curve / central pair) and $\alpha_0 = 2.5$ (red curve / left-hand pair). The corresponding curves for the reflectance of a single grating of rigid pins are dashed. (b) $\mathrm{Log}|p(\mathbf{v})|$ from equation (6.32) for $\alpha_0 = 2.1$. 124
6.8 (a) $\mathrm{Log}|p(\mathbf{v}_A)|$ with $\alpha_0 = 2.1$ ($d = 1$, $\xi = 0$), $3.4 \le \beta \le 3.6$ and $-2 \le A \le 2$. (b) $\mathrm{Log}|p(\mathbf{v})|$ versus β for $\mathbf{v}^T = 1/\sqrt{6}(1, 2, 1)$. 125

6.9 Dispersion diagram for a waveguide consisting of an unshifted triplet with the horizontal axis representing α_0 in the range $0.5 \leq \alpha_0 \leq 3$, and β on the vertical axis in the range $3 \leq \beta \leq 3.8$. The dashed curve represents the odd modes, and the blue curve, the even modes. 126
6.10 Normalised transmitted energy T_{tot} versus spectral parameter β for an unshifted triplet ($\xi = 0$) of rigid pins with $\alpha_0 = 2.1$ and $d = 1$ and: (a) $\eta = 1$; (b) optimized resonances for a triplet with $\eta^* = 1.185266$. . . . 127
6.11 β versus α_0 for odd (red) and even (blue) modes for optimized grating separation η^* for unshifted triplets (Data from Table 6.1). 129
6.12 The logarithm of the modulus of the determinant of the matrix $\mathbf{M}$ as a function of β for $\theta_i = 60°, d = 1, \eta^* = 2.131958$ (a) $\xi = 0$ (b) $\xi = 0.2476$. 129
6.13 Optimized EDIT with $\theta_i = 60°$, $\eta^* = 2.13196$ and $\xi = 0.2476$ with $d = 1$. In (b), we replace β by $2.94715999 + \Delta\beta$, because the transmission minimum is so narrow. 130
6.14 Normalised transmitted energy T_{tot} versus spectral parameter β for a triplet of rigid pins with $d = 1$, $\eta = 1.00866$ and $\theta_i = 30°$ for various shifts of the central grating: (a) $\xi = 0.22$ (solid curve), $\xi = 0.23$ (dot-dashed curve) and $\xi = 0.24$ (dashed curve) (b) $\xi = 0.2285$ (dot-dashed curve), $\xi = 0.2287$ (solid curve) and $\xi = 0.2288$ (dashed curve). 130
6.15 Normalised transmitted energy T_{tot} versus spectral parameter β for a triplet of rigid pins with $d = 1$ and $\theta_i = 1°$ for the optimized grating separation $\eta = 0.705679367$ and the EDIT shift of the central grating $\xi = 0.165868$. 131

A.1 (a) An example of a typical K-type grating sum which can be evaluated directly because of its exponential convergence. (b) An example of a Hankel-type grating sum which demonstrates why Twersky's alternative representation is valuable. 136
A.2 (a) Real part of Hankel function grating sum evaluated by direct summation of 50 terms for $\beta = 3.6$ for normal incidence. (b) Real part of Hankel function grating sum evaluated using Twersky accelerated convergence formulae for 50 terms for $\beta = 3.6$ for normal incidence. 138
A.3 (a) Imaginary part of Hankel function grating sum evaluated by direct summation of 50 terms for $\beta = 3.6$ for normal incidence. (b) Imaginary part of Hankel function grating sum evaluated using Twersky accelerated convergence formulae for 50 terms for $\beta = 3.6$ for normal incidence. . . . 139

A.4 Normalised reflected energy R_{tot} (blue curve) and transmitted energy T_{tot} (red) versus spectral parameter β for normal incidence for a single grating with $a = 0.1$ in the range $0.1 < \beta < 2\pi$ for propagating orders (zeroth order only in this range). (a) grating sums evaluated by direct summation and (b) Twersky accelerated convergence formulae. 140

Acknowledgements

I would like to thank the Duncan Norman Charitable Trust whose financial support through the Duncan Norman Research Scholarship has enabled me to undertake my PhD in applied mathematics at the University of Liverpool. This made it possible for me to continue my studies under the supervision of Professors Alexander and Natasha Movchan, with whom I worked during my MSc.

It has been both a tremendous privilege and a great pleasure to work with them. Their dedication, encouragement, numerous insights and support have been invaluable over the last few years. I would also like to thank Sasha for encouraging me to return to academia to study for a PhD after a spell away playing chess professionally, and for his and Natasha's understanding and support in allowing me to play several tournaments during the last four years.

I owe a huge amount of gratitude to Ross McPhedran, the co-author of all of our published papers. I feel extremely fortunate to have worked with a great mathematical physicist and a great man over the last few years, and I hope to continue our collaborations in the future. I should also like to mention Daniel Colquitt and Mike Nieves who have always been ready to help me with both advice and more technical matters.

The dedication, approachability and enthusiasm of the Mathematical Sciences Department staff hugely influenced my decision to pursue an academic career so I was very keen to continue my studies here. I would like to give a special mention to Özgür Selsil and Peter Giblin, whose sage advice and support I have regularly sought over the last few years. I would also like to thank Joanna Seed, Shirley Farrell, Ingrid Harper, Lyn Hughes and Rebecca Morton who have provided me with the answer on every occasion that I had a question throughout my studies.

I would like to thank my fellow post-graduate student friends, of whom there are too many to mention all by name. I would also like to mention my Italian friends Giorgio Carta (my office-mate), Luigi Cabras, Michele Brun and Felice Giaccu who have taught me so much about their language, culture, food and most importantly friendship over the last few years. Grazie mille!

And of course I would like to thank my family for their unconditional love and support. My parents Mike and Sandy, and my brothers and sister Gareth, Toby and Mandy, have all shown tremendous understanding and patience during my PhD studies.

List of Publications

1. Haslinger, S. G., Movchan, N. V., Movchan, A. B. & McPhedran, R. C. (2011), Wave localisation in structured elastic plates, *Proc. Int. Conf. on Vibration Problems* (ed. Náprstek et al.), 737-743, Springer Proceedings in Physics 139.

2. Haslinger, S. G., Movchan, N. V., Movchan, A. B. & McPhedran, R. C. (2012) Transmission, trapping and filtering of waves in periodically constrained elastic plates. *Proc. R. Soc. A* **468**, 76-93.

3. Haslinger S. G., McPhedran R. C., Movchan N. V. & Movchan A. B. (2013) Localisation near defects and filtering of flexural waves in structured plates. *Int. J. Fract.* **184**, 25-41.

4. Haslinger S. G., McPhedran R. C., Movchan N. V. & Movchan A. B. (2013) Structured interfaces for flexural waves - trapped modes and transmission resonances. *Journal of Physics: Conference Series* **451** 012024.

5. Haslinger S. G., Movchan A. B., Movchan N. V. & McPhedran R. C. (2014) Symmetry and resonant modes in platonic grating stacks. *Waves in Random and Complex Media* (published online February 2014).
   DOI: 10.1080/17455030.2014.884733

Chapter 1

Introduction and background

In this thesis we consider thin structured plates that contain an interaction region consisting of a finite number of periodic gratings, and our particular interest is in the localisation of flexural waves within the grating structure. Many elastic systems such as aircraft, long bridges and reinforced roads encompass periodic arrangements of inclusions, voids and masses. These structures are frequently subjected to stress concentrations and therefore the study of the resonant action of incident flexural waves within our structured plates has applications in engineering, in addition to its intrinsic interest.

We place this work in the relatively new field of platonics, which concerns the propagation of elastic waves, in the form of flexural bending waves, through thin structured plates. The term platonic crystal was first used by McPhedran *et al.* (2009), and was defined as "any structured system that is governed by the biharmonic plate equation". The key words here are structured and plate, since the first half of the word platonic is derived directly from plate, and the second half alludes to the analogy of the structured periodic system with photonic and phononic crystals.

Since the 1980's, there has been substantial interest in problems concerned with wave properties in doubly periodic structures among mathematicians, engineers and physicists. The majority of the research is concerned with electromagnetism and addresses Maxwell's system and the Helmholtz equation, so it is referred to as the photonic band-gap problem. Photonic crystals are designed to control the propagation of light through periodic media with varying refractive indices. The books on the subject by Joannopoulos *et al.* (2008) and Sakoda (2005) provide excellent coverage of the present state of the field. The extensive body of literature directed to the study of photonics was a primary motivation in considering similar periodic problems for alternative media.

One such smaller body of the literature concerns acoustic and elastodynamic waves, where the properties of solutions of the Lamé system for structured media are investigated. This field is referred to as the phononic band-gap problem. The recent book

by Deymier (2013) provides an up-to-date overview of phononic crystals and acoustic metamaterials. An excellent collection of references to results in both of these fields may be found in the online bibliography (The Photonic and Sonic Band Gap Bibliography, 2008). A combination of the exponential growth of the work, and competition from Google Scholar, influenced the editor Jonathan Dowling to cease updating the website from 2008.

A recent search for photonic and phononic crystal publications indicated that there have been around 40,000 papers dealing with photonic crystals compared with around 400 for phononic papers. In contrast, the topic we discuss here has received very little prior attention, numbering fewer than 20 papers at the time of writing. It concerns the vibrational modes of thin structured elastic plates governed by an equation involving the biharmonic operator. It is distinguished from the electromagnetic and acoustic cases by the important fact that the Green's function for this operator is non-singular at the source point, whereas the Green's function for the two-dimensional Helmholtz operator diverges logarithmically.

One essential tool in understanding the behaviour of waves in photonic crystals and related systems is that of Bloch waves. These provide a basis set of functions suitable for expanding any wave within such structures. Another crucial tool implemented throughout this work is the Rayleigh method for which field quantities are represented by multipole expansions. The underlying principle of such a multipole method is the application of a field identity (Rayleigh identity) that, by the use of lattice sums (see Borwein *et al.* 2013), relates the regular field in the vicinity of any scatterer to the fields radiated by the other scatterers and external sources (Rayleigh 1892).

We are interested in periodic arrays embedded in thin elastic plates. The simplest periodic array is a diffraction grating, which contains an infinite number of equally spaced scatterers positioned along a line. A diffraction grating is used to scatter incident plane waves (Born & Wolf 1959). Two crucial concepts imported from classical optics are directly applicable here; quasi-periodicity and the Fraunhofer diffraction grating equation. The dispersive properties of electromagnetic diffraction gratings (Born & Wolf 1959) have analogous counterparts in platonic diffraction grating arrays used to scatter and disperse flexural waves.

Diffraction grating theory is very relevant for the analysis of wave propagation through two-dimensional periodic structures since any doubly periodic array may be regarded as an infinite stack of gratings. An alternative treatment uses Bloch-Floquet theory to determine the dispersion relation for the platonic crystal. Both methods generate spectral band diagrams and reveal when the propagation of the flexural waves is supported through a two-dimensional array.

There is much scope regarding both the nature and geometry of possible scatterers. We primarily analyse circular scatterers with clamped boundaries, but our method is

equally valid for inclusions or point masses. Similarly any smooth geometrical shapes may be used, but we favour circular boundaries which support an elegant analytic method of solution. The boundary conditions imposed on the edges of the scatterers may range from fully clamped to free edge, which allow for free bending of the plate. A special case where the radius of the clamped holes tends to zero, gives us a periodically pinned plate.

One of the earliest papers on a two-dimensional periodic array, by Movchan *et al.* (2007), addressed the spectral problem for a thin elastic plate containing a square array of circular holes or rigid stationary inclusions. Platonic band diagrams were obtained, and it was shown that in the case of a free boundary, the band diagram tends to that of the unstructured elastic plate as the radius of cylinders tends to zero. However for clamped boundaries it was shown that the zero-radius case corresponds to a complete platonic band gap running from zero frequency up to a finite value that can be evaluated simply. This striking result means that the flexural wave properties of gratings made of fixed pins having zero radius are non-trivial, and such gratings when stacked together can give good filtering action, an effect that can be accurately described using a theory that is both elegant and easily understood.

The work done by Evans & Porter (2007) emphasised the role of trapped modes within these grating systems. This followed on from related research on supported plates (Evans & Meylan 2005 and Evans & Porter 2006) where pinned elastic plates floating on water were investigated. We restrict our attention to biharmonic plates containing periodic arrays, with the emphasis on the importance of evanescent modes.

Konenkov (1960, 1964) considered the case of a single circular inclusion using multipole techniques. The additional complexity of one- and two-dimensional arrays being embedded within the plates was investigated later. Some early references are Kouzov & Lukyanov (1976) where a doubly periodic array of pins and point masses were considered for plates, interacting with ambient sound waves in the context of modelling acoustically-absorbing sandwich structures. Norris and Vemula provided comprehensive coverage of circular inhomogeneities for both Kirchhoff-Love (1995) and Mindlin (1997) theories. The work by Evans & Porter (2007) and Movchan *et al.* (2007) was carried out independently later, and emphasised the elegance and simplicity of the method of solution for pinned plates.

The work was advanced in several papers by Movchan *et al.* (2009, 2011), McPhedran *et al.* (2009) and Poulton *et al.* (2010, 2012). This included the analysis of finite stacks of gratings, wave trapping, nonzero radius of scatterers and a comparison of results for Kirchhoff-Love and Mindlin plates. The filtering effects associated with the trapping of waves within grating systems exhibit optical-type behaviour linked to Fabry-Pérot theory.

Other related work on platonic crystals has been the engineering of structures that

exhibit complex diffraction behaviour. Farhat *et al.* (2009, 2010a,b) theoretically demonstrated negative refraction in thin plates, whereby a point source is refocused around a finite disk. Recent papers by Smith *et al.* (2011-2013) observed negative refraction properties and flexural lensing. A recent example of experimental cloaking was successfully carried out by Stenger *et al.* (2009) who based their approach on the theory of Farhat *et al.* (2009). A cloak in the form of a concentric ring was designed to surround a single clamped circular scatterer, and cloaking was observed for a wide frequency range of 200-400 Hz.

This thesis considers various structured regions that are used to filter flexural (out-of-plane displacement) plane waves. The main body of work incorporates three papers. The first concerns a platonic crystal containing a finite number of gratings stacked above one another. The elegance and simplicity of the analytic solution for a grating of rigid pins arises from the linearity of the biharmonic plate equation. This linearity allows the scattered field to be expressed as a superposition of Helmholtz and modified Helmholtz waves (see Section 2.2). A related expansion involving the Green's function of the plate was used by Evans & Porter (2007).

We develop a recurrence algorithm for constructing the reflection and transmission matrices required to characterise the filtering of plane waves by the structured system with shifted gratings. Similar recurrence procedures have been extensively used in electromagnetism. We refer the reader to the overview by Botten *et al.* (2003), where material on the accompanying lattice sums is instructive, and to the papers by Botten *et al.* (2001) and Platts *et al.* (2002, 2003) amongst others. An early example for a platonic grating system is the paper by Movchan *et al.* (2009). In Chapter 3 we go through the method of solution in detail, both for an incident plane wave scattering problem, and the treatment of the system as a waveguide.

The variation of the grating system parameters demonstrates several interesting filtering properties related to trapped modes and transmission resonances. The effect of resonant transmission is illustrated in Fig. 1.1 where the field plot shows the flexural displacement inside a stack of three gratings of rigid pins, and the plane wave outside the stack. The plane wave appears for this case to be virtually unperturbed for the chosen frequency. However we show that controlled lateral shifts of three gratings can give rise to a transmission peak with a sharp central suppression region, akin to the phenomenon of *electromagnetic induced transparency* (EIT), a quantum-mechanical effect which arises in three-level atomic systems (Fleischhauer *et al.* 2005).

We discuss EIT in Section 2.4.5 but the characteristic curve of absorption versus frequency in Fig. 2.11 bears a striking resemblance to the transmitted energy curve for a three-grating stack shown in Fig. 1.2(b), where symmetric and anti-symmetric modes coincide, discussed in detail in Chapters 4 to 6. Destructive interference results and the total transmitted energy is negligibly small at this minimum and we therefore term

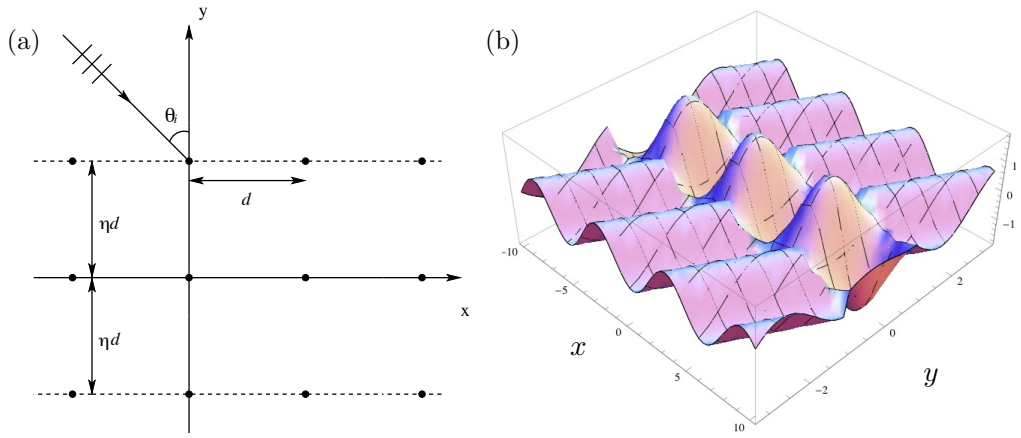

Figure 1.1: (a) Triplet of aligned rigid-pin gratings with period d and relative grating separation $\eta = 1$. The angle of incidence is θ_i. (b) Flexural displacement plotted as a function of x and y for the transmission resonance associated with a symmetric trapped mode for $\theta_i = 30°$ for the grating stack illustrated in (a).

the platonic effect Elasto-Dynamically Inhibited Transmission (EDIT).

EDIT features strongly in our published papers (see Haslinger *et al.* 2012, 2013, 2014) but there are analogies with EIT in other fields. A recent paper by Lin *et al.* (2009) described EIT-like effects linked to optomechanical interference for nano-optomechanical structures (NOMS). The authors refer to induced mechanical transparency (IMT) where two modes, one optically bright and the other optically dark (akin to our symmetric and anti-symmetric modes) coincide. The destructive interference suppresses excitation of the mechanical system.

Recent literature in metamaterials also refer to EIT analogues. These include the papers by Zhang *et al.* (2008), Papasimakis *et al.* (2008) and Tassin *et al.* (2009). Liu *et al.* (2009) consider a planar metamaterial analogue of EIT for plasmonic sensing, which involves a shift control parameter similar to the one we employ for the central grating in a finite grating stack. The structural asymmetry is an important factor in coupling the modes to induce the interference effects that underpin the EIT-like effect.

In our second paper described in Chapter 5, we studied the localisation of flexural waves within shifted grating systems composed of clamped holes or rigid inclusions of finite radius in the structured plate. The effect of the finite value of the radius on the dynamic localisation was analysed for the range of frequencies where only zeroth grating orders propagate. Poulton *et al.* (2010) presented a thorough coverage of nonzero-radius gratings for the doubly periodic square array. The structure of the resonant modes within gratings of inclusions is of special interest, since EDIT is dependent on the coincidence of symmetric and anti-symmetric modes. The increased radius of the voids makes it necessary to carefully take into account higher-order multipole terms characterising the scattered field, and associated higher-order lattice sums. Lattice

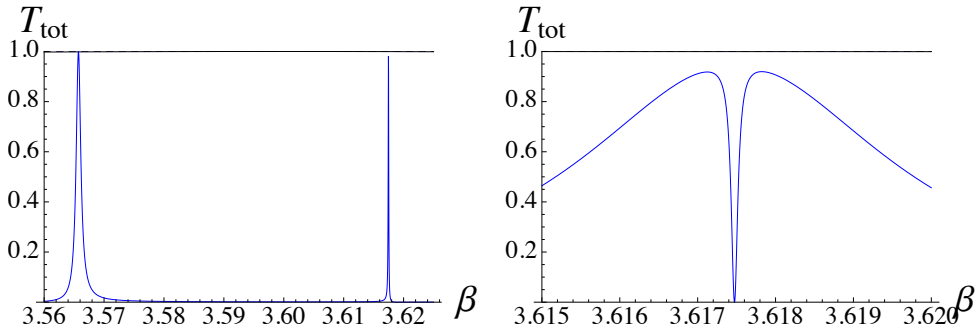

Figure 1.2: Normalised transmitted energy T_{tot} versus spectral parameter β for a triplet of rigid pins with $\theta_i = 30°$, $d = 1$, $\eta_1 = \eta_2 = 1$ in both cases and: (a) $\xi = 0$; (b) $\xi = 0.25200$. The parameter ξ represents relative lateral shift of the central grating.

sums (see Borwein *et al.* 2013) are an essential aspect of multipole methods for periodic systems, and are sums of terms evaluated at each point of the array's structure. Their evaluation is both important and subtle, with complications arising from the definition of conditionally convergent series.

In the culminating third paper described in Chapter 6, the grating stack is considered as a structured waveguide for trapped modes. For a stack of rigid pins, a quasi-periodic Green's function is employed to derive the dispersion equation for Bloch waves in such a waveguide. The dispersion equation solutions are displayed graphically in band diagrams. A connection is established with the transmission problem by identifying parameters of the grating stack and of the incident wave, to generate a transmission resonance linked to a trapped Bloch wave within the structured waveguide. We classify the even and odd classes of modes, and we show how the EDIT interaction may be steered over a wide range of frequencies and angles, using a strategy in which the single-grating reflectance is kept high. In this way, the quality factors of the even and odd resonances may be kept large.

The filtering effects we have discovered have several potential applications in wave filtering. Surface acoustic waves (SAW) are acoustic waves travelling along the surface of an elastic material, with an amplitude that typically decays exponentially with depth into the substrate. In seismology for example, surface acoustic waves travelling along the Earth's surface are often the most destructive type of seismic wave produced by earthquakes. There may be the possibility of fabricating switches linked to the EDIT effect where a peak in transmission is suppressed by finely tuning the lateral shift control. The resonances which provide the EDIT phenomenon are, as we show in Chapters 4 to 6, extremely narrow and may thus find application in flexural wave filters.

Before describing the method of solution, which incorporates several complex techniques including multipoles, Rayleigh method, Graf's addition theorem, grating sums

and a recurrence procedure, we introduce the important underlying concepts. This includes a brief summary of the important ideas that we use from the classical optical theory of gratings. We also outline the derivation of the quasi-periodic Green's function for a single grating of clamped circular voids and introduce the lattice sums used to characterise the interaction of the flexural waves with the periodic structured interface. Lattice sums are needed both for the Helmholtz and modified Helmholtz equations. We conclude with a chapter summarising the overall findings of our work, and discuss potential applications and future continuation of the research.

Chapter 2

Underlying theory

2.1 Governing equation

The underlying equation of this thesis is the biharmonic plate equation. It is derived using the Kirchhoff-Love plate theory, which may be viewed as the two-dimensional analogue of the Euler-Bernoulli beam equation. The basic hypothesis of Euler-Bernoulli beam theory is that plane cross-sections initially perpendicular to the axis of the beam remain plane and perpendicular to the neutral axis during bending. This assumption implies that the longitudinal strains vary linearly across the depth of the beam and, for elastic behaviour, the beam's neutral axis passes through the centroid of the cross-section (Graff 1975). Euler-Bernoulli theory yields a dispersive system unlike the wave equation for strings.

For the two-dimensional plate, the main kinematic assumptions are that

- straight lines normal to the mid-surface remain straight, and normal to the mid-surface after deformation;

- thickness of plate does not change during deformation. Graff (1975) provides a derivation based on moments and forces, and an alternative method using asymptotics is sketched by Movchan & Movchan (1995).

The standard Kirchhoff plate equation of motion is

$$D\Delta^2 w(\mathbf{x};t) \,+\, \rho h \frac{\partial^2 w}{\partial t^2}\,(\mathbf{x};t) \,=\, 0, \tag{2.1}$$

where w is the out-of-plane displacement, $\mathbf{x} = (x, y)$, ρ is the mass density of the plate, h is its thickness and D is the flexural rigidity of the plate, $D = Eh^3/(12(1-\nu^2))$, where the physical parameters of the elastic material are the Young's modulus E and the Poisson ratio ν. We assume time-harmonic vibrations $w(\mathbf{x};t) = W(\mathbf{x})\sin(\omega t)$ where W is the amplitude and ω is the angular frequency. Substituting this into equation (2.1) we obtain an equation satisfied by the amplitude $W(\mathbf{x})$:

$$\Delta^2 W(\mathbf{x}) - \beta^4 W(\mathbf{x}) = 0, \tag{2.2}$$

with $\beta^2 = \omega\sqrt{\rho h/D}$. The spectral parameter β has dimension $1/L$ with units m^{-1} and therefore may be considered as a wavenumber. This equation is widely known as the biharmonic plate equation.

Kirchhoff-Love plate theory is concerned with the analysis of out-of-plane bending waves, and contributes little with respect to the propagation of in-plane elastic waves. The flexural bending waves are fundamentally different in character from compressional acoustic or electromagnetic waves. They account for the lowest frequency waveguide mode for elastic waves, and they are dispersive.

The solution to the Kirchhoff-Love, or biharmonic, plate equation depends on the geometry of the plate and the boundary conditions. For the scattering problems that we consider within this thesis, we assume an infinitely large plate containing circular inclusions. For strong filtering effects, clamped boundary conditions provide the best examples. Therefore these are used throughout the thesis, the details of which are given in Section 2.1.1.

Kirchhoff theory is the classical approach and is usually applicable for the case of thin plates where the thickness h is smaller than the wavelength λ of flexural out-of-plane displacements. Mindlin theory is the alternative, and Movchan *et al.* (2011) conducted a comparative analysis of the two plate models for the dynamic response of platonic structures. In this thesis, we consider classical Kirchhoff theory. For the application of Mindlin theory to elastic plates incorporating cylindrical cavities or inclusions, we refer the reader to the work by Vermula & Norris (1995, 1997) and to Movchan *et al.* (2011), as well as earlier research carried out by Pao & Chao (1964) and Lu (1966).

2.1.1 Structured interaction region

We consider an infinite thin elastic plate with an internal structure which consists of a finite number of parallel gratings. Our model allows for the gratings to consist of cylindrical inclusions whose cross-sections are of arbitrary smooth shape or size. Here we concentrate on circular voids of finite radius with clamped boundaries, and the limiting case of the radius tending to zero, corresponding to a pinned point. We demonstrate that the periodically structured grating stack supports sharp transmission resonances for low-frequency flexural vibrations. The resonances arise from the interaction with the plane wave, characterised by the angle of incidence θ_i and spectral parameter β.

We show one such configuration in Fig. 2.1, where the outer pair of the triplet consists of clamped-edge voids or rigid inclusions with a finite radius a, whilst the central grating contains pinned points. The other parameters are the angle of incidence θ_i, the period of the gratings d and the relative grating separation η. We also indicate the scattered field. An important additional parameter is the relative shift of the central grating denoted by ξ, which is crucial for supporting a filtering effect similar

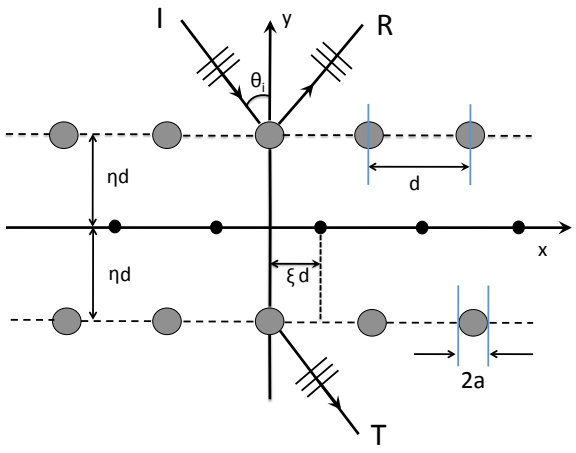

Figure 2.1: Stack of gratings consisting of an outer pair of finite nonzero inclusions with radius a and period d, and a central grating of rigid pins. The relative grating separation between consecutive gratings is η, and the relative lateral shift of the central grating is ξ.

to electromagnetically induced transparency (EIT). We term this Elasto-Dynamically Inhibited Transmission (EDIT). This novel phenomenon for elasticity problems was first observed by Haslinger *et al.* (2012, 2013, 2014). It is characterised by a resonant peak in transmission being cut in two by a resonant dip with an extremely high quality factor. We discuss it in more detail in Section 2.4.5 and Chapters 4 to 6.

The two most natural types of boundary conditions to consider are clamped and free edge on the circular boundary of the scatterers in Fig. 2.1. Clamped boundaries provide the best conditions for strong filtering effects.

Dirichlet clamped edge conditions are

$$W\Big|_{r=a} = 0, \quad \frac{\partial W}{\partial r}\Big|_{r=a} = 0. \tag{2.3}$$

In particular, when the radius a tends to zero we retrieve the case of fixed pins.

Our results arise from modelling the propagation of flexural waves through the structured grating stack. We consider plane waves which propagate freely through the homogeneous material until they reach the stack of gratings whereupon they are reflected and transmitted. We use plane wave representations, where both propagating and evanescent orders are taken into account.

2.2 Plane wave representations of scattered waves

The biharmonic plate equation (2.2) may be written in its factorised form:

$$\Delta^2 W(\mathbf{x}) - \beta^4 W(\mathbf{x}) = (\Delta + \beta^2)(\Delta - \beta^2)W = 0, \tag{2.4}$$

where $\beta^2 = \omega\sqrt{\rho h/D}$ with the physical parameters being defined as in Section 2.1.

Hence W is the superposition of two types of wave, one satisfying the Helmholtz equation and the other satisfying the modified Helmholtz equation:

$$(\Delta + \beta^2)W_H = 0 \quad \text{and} \quad (\Delta - \beta^2)W_M = 0. \tag{2.5}$$

An important aspect of the physics of the problem is that W_H contains both propagating and evanescent waves, while W_M consists entirely of evanescent waves (decay exponentially). The incident field is represented by plane waves of two types:

1. Propagating (or evanescent) solution of the Helmholtz equation

$$W_{i,\,H}(\mathbf{x}) = \frac{1}{\sqrt{|\chi_0|}} \exp\{i(\alpha_0 x - \chi_0 y)\}, \tag{2.6}$$

   where $\alpha_0^2 + \chi_0^2 = \beta^2$. Here χ_0 is real and positive for a propagating solution. For the evanescent solution, χ_0 is pure imaginary, with positive imaginary part.

2. Evanescent solution of the modified Helmholtz equation

$$W_{i,\,M}(\mathbf{x}) = \frac{1}{\sqrt{|\hat{\chi}_0|}} \exp\{i(\alpha_0 x - \hat{\chi}_0 y)\}, \tag{2.7}$$

   where $\alpha_0^2 + \hat{\chi}_0^2 = -\beta^2, \quad \hat{\chi}_0 = i\tau_0, \quad \tau_0 > 0.$

As in Movchan *et al.* (2009), we use plane wave series expansions to describe the reflected and transmitted waves. We consider a single grating lying on the horizontal x-axis. We define two straight lines γ^+ and γ^- parallel to the grating, placed at an arbitrary distance either side of the x-axis (see Fig. 2.2). We use these lines to represent the upper and lower "sides" of the grating. This notation is important for the recurrence algorithm we employ to build a stack of multiple gratings, since we must distinguish between the directions of the waves as they hit the grating. Throughout this thesis, we use the superscript "+" to denote waves from above the grating, and the superscript "−" to label waves arriving at the grating from below.

If we consider an incident field, of Helmholtz or modified Helmholtz type defined using representations (2.6) or (2.7), hitting a grating, we may represent the total field by

$$W(\mathbf{x}) = W_i(\mathbf{x}) + W_{s,\,H}(\mathbf{x}) + W_{s,\,M}(\mathbf{x}), \tag{2.8}$$

where the scattered field $W_s(\mathbf{x})$ has been split into two parts. Each of these parts consists of reflected and transmitted fields, the reflected waves being present on γ^+ and the transmitted waves emanating from γ^-. The plane wave expansions are given below:

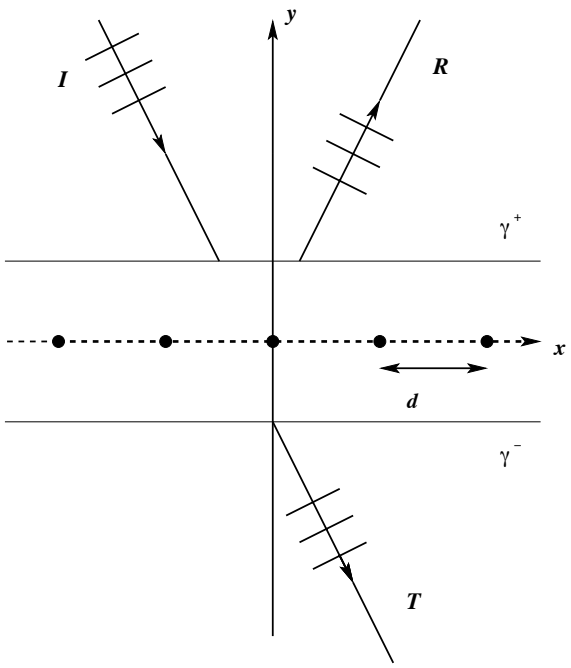

Figure 2.2: A plane wave ($\boldsymbol{I}$) incident on a grating of rigid pins from above. We show the generic scattered field consisting of reflected and transmitted waves $\boldsymbol{R}$ and $\boldsymbol{T}$ respectively. The lines γ^+ and γ^- are used to indicate the upper and lower sides of the grating.

Plane wave expansions for scattered field

1. On γ^+, we have reflected waves of Helmholtz and modified Helmholtz type:

$$W_{s,\,H}(\mathbf{x}) = \sum_p \frac{R_p}{\sqrt{|\chi_p|}} \exp\{i(\alpha_p x + \chi_p y)\}, \quad \alpha_p = \alpha_0 + \frac{2\pi p}{d}, \;\; \alpha_p^2 + \chi_p^2 = \beta^2, \tag{2.9}$$

   where the integer p describing the order of the scattered field, covers an infinite range which can be divided into two sets, one containing propagating waves for which χ_p are real, and the other comprises evanescent waves, for which χ_p are pure imaginary with positive imaginary part. We discuss the concept of diffraction orders in more detail in Section 2.4 when we consider the diffraction grating of classical optics.

   We have a similar expression for the evanescent waves arising from the modified Helmholtz equation:

$$W_{s,\,M}(\mathbf{x}) = \sum_p \frac{\hat{R}_p}{\sqrt{|\hat{\chi}_p|}} \exp\{i(\alpha_p x + \hat{\chi}_p y)\}, \qquad \alpha_p^2 + \hat{\chi}_p^2 = -\beta^2, \;\; \hat{\chi}_p = i\tau_p, \;\; \tau_p > 0. \tag{2.10}$$

2. On γ^-, we have transmitted waves of Helmholtz and modified Helmholtz type:

$$W_{s,\,H}(\mathbf{x}) = \sum_p \frac{T_p}{\sqrt{|\chi_p|}} \exp\{i(\alpha_p x - \chi_p y)\}, \quad \alpha_p^2 + \chi_p^2 = \beta^2, \tag{2.11}$$

and

$$W_{s,\,M}(\mathbf{x}) = \sum_p \frac{\hat{T}_p}{\sqrt{|\hat{\chi}_p|}} \exp\{i(\alpha_p x - \hat{\chi}_p y)\}, \quad \alpha_p^2 + \hat{\chi}_p^2 = -\beta^2,\ \hat{\chi}_p = i\tau_p,\ \tau_p > 0. \tag{2.12}$$

These plane wave representations are valid outside of the strip bounded by the lines γ^+ and γ^- in Fig. 2.2, but we use cylindrical multipole expansions within this strip (see Section 2.5.2).

2.3 Quasi-periodicity conditions

The periodicity of platonic gratings in the horizontal direction imposes a quasi-periodicity condition (Bloch-Floquet condition) on plane waves that interact with the grating. A quasi-periodic function is similar to a periodic function $\phi(x+d) = \phi(x)$, but there is a change in phase across each period d:

$$f(x+d) = e^{i\kappa_x d} f(x),$$

where real κ_x is called the Bloch factor. So for a quasi-periodic function f, the modulus $|f|$ is periodic since $|e^{i\kappa_x d}| = 1$.

Quasi-periodic representations arise in problems involving periodic arrays and are extremely convenient since they allow a reduction of the domain to a single period for a grating, or an elementary cell for a two-dimensional array. In this latter case, the elementary cell containing the origin is called the *primitive* or *Wigner-Seitz* cell. The corresponding quasi-periodicity condition is

$$W(\mathbf{x} + \mathbf{R}_p) = W(\mathbf{x}) e^{i\boldsymbol{\kappa}.\mathbf{R}_p}, \tag{2.13}$$

with $\mathbf{x} = (x, y)$ and $\mathbf{R}_p$ the array vector which locates the position of each individual scatterer within the array. For example, for a square array we have $\mathbf{R}_p = (md, nd)$ where m, n are integers. In equation (2.13), $\boldsymbol{\kappa}$ denotes the Bloch vector, and solutions of (2.13) which satisfy the condition are called Bloch waves, or occasionally Floquet-Bloch waves.

The platonic grating is a particular case whereby the displacement field W satisfies the Bloch quasi-periodicity condition along the horizontal x-axis:

$$W(\mathbf{x} + pd\mathbf{e}^{(1)}) = W(\mathbf{x}) e^{i\alpha_0 pd}. \tag{2.14}$$

Here p is an integer, d is the period, and $\alpha_0 = \beta \sin\theta_i$, where θ_i is the angle of incidence (see Fig. 2.1).

The two-dimensional arrays we primarily consider consist of an integer number N of platonic gratings, so equation (2.14) is fundamental to our treatment. However in

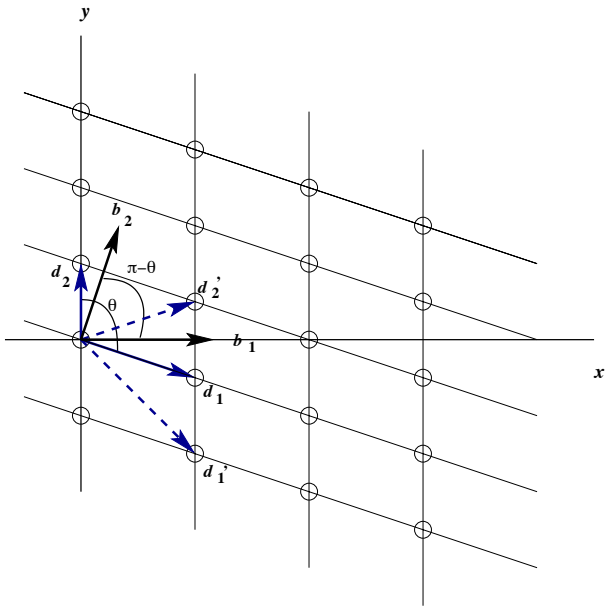

Figure 2.3: A two-dimensional lattice composed of particles of the same mass, placed at equal distances from one another along two lines intersecting at an arbitrary angle θ.

the limit as $N \to \infty$, the structure tends towards the infinite doubly periodic array. Comparison is subsequently made between the two approaches so we introduce the ideas of direct and reciprocal lattice vectors and Brillouin zones for two-dimensional arrays in Section 2.3.1.

Platonic crystals are fundamentally periodic arrays and have many things in common with lattice structures. Therefore several concepts from the fields of crystallography and solid-state physics have been used in the extensive photonic crystal literature, and we introduce some of them here.

2.3.1 Direct lattice and reciprocal lattice

We draw upon the analysis by Brillouin in his classical book *Wave Propagation in Periodic Structures* (1953) by illustrating a general two-dimensional lattice composed of particles of the same mass, placed at equal distances from one another along two lines intersecting at an arbitrary angle θ in Fig. 2.3. The small circles represent the masses, and distances between the particles in directions $\mathbf{d}_1$ and $\mathbf{d}_2$ are not necessarily the same.

The vectors $\mathbf{d}_1$ and $\mathbf{d}_2$ are basis vectors from the particle designated as the origin of the lattice, and then any point in the array is given by

$$\mathbf{r}_{l_1,l_2} = l_1\mathbf{d}_1 + l_2\mathbf{d}_2, \tag{2.15}$$

where l_i are integers. The basis $\{\mathbf{d}_1, \mathbf{d}_2\}$ is not unique; the pair $\{\mathbf{d}_1, \mathbf{d}_2'\}$ would also

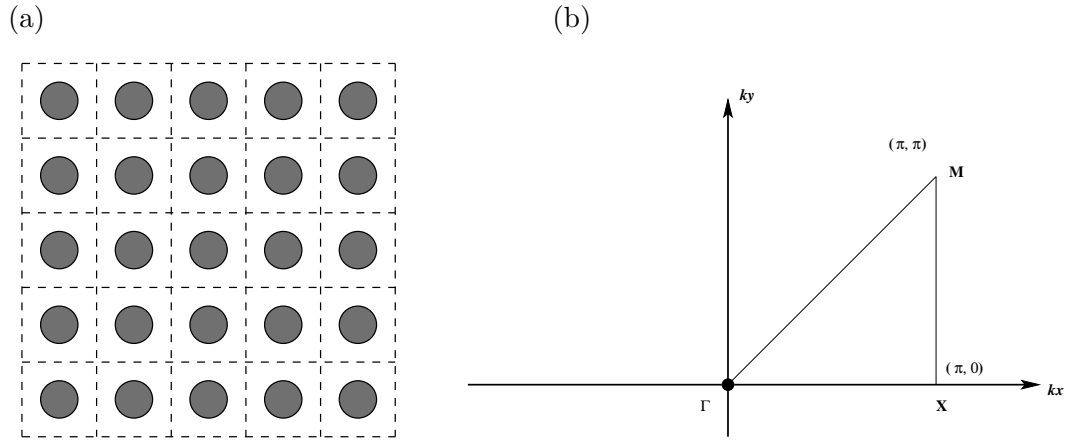

Figure 2.4: (a) Infinite plate with a doubly periodic array of cylindrical voids. (b) The irreducible Brillouin zone for the doubly periodic square array.

suffice and any linearly independent pair $\mathbf{d}_1''$ and $\mathbf{d}_2''$ would form a valid basis with

$$\left.\begin{aligned}\mathbf{d}_1'' &= m_1\mathbf{d}_1 + n_1\mathbf{d}_2\\ \mathbf{d}_2'' &= m_2\mathbf{d}_1 + n_2\mathbf{d}_2\end{aligned}\right\}, \qquad \frac{m_1}{m_2} \neq \frac{n_1}{n_2}, \tag{2.16}$$

where m_i, n_i are integers. The lattice described by a basis $\{\mathbf{d}_1, \mathbf{d}_2\}$ is known as the *direct lattice*.

For any direct lattice, we define a *reciprocal lattice* with basis vectors $\mathbf{b}_1$ and $\mathbf{b}_2$ defined by the equation

$$\mathbf{b}_i \cdot \mathbf{d}_k = \delta_{ik}, \tag{2.17}$$

where δ_{ik} is the Kronecker delta and $i, k = 1, 2$.

Brillouin (1953) demonstrates some simple analysis to explain reasons for the term reciprocal lattice. The area of the elementary cell for the direct lattice S_d is given by

$$S_d = |\mathbf{d}_1 \times \mathbf{d}_2| = |\mathbf{d}_1||\mathbf{d}_2| \sin\theta, \tag{2.18}$$

and similarly for the reciprocal lattice, $S_b = |\mathbf{b}_1||\mathbf{b}_2| \sin\theta$. The product of these areas is shown to be unity and therefore the areas S_d and S_b are reciprocals.

The fundamental cell in the direct lattice has the origin at its centre, and is commonly known as the primitive or Wigner-Seitz cell. In Fig. 2.4(a) we show the array and primitive cell for the particular case of the doubly periodic square array that we discuss in more detail in Section 2.5. The elementary cell is symmetric about the origin and is repeated across the periodic array.

When we move from the direct lattice to the reciprocal lattice, we are effectively considering the Fourier transform. The associated fundamental cell in this reciprocal or Fourier space is called the first Brillouin zone. It is geometrically constructed by drawing the perpendicular bisectors of the reciprocal lattice vectors in the vicinity of the origin. The area enclosed by the intersections of these bisectors is the first Brillouin

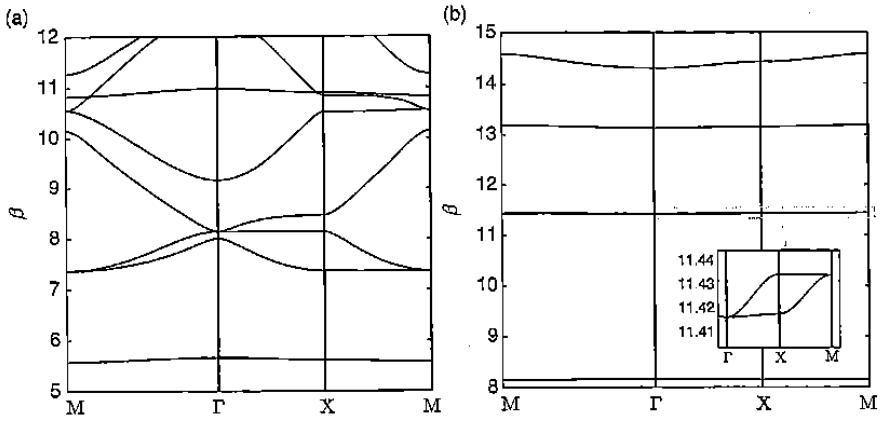

Figure 2.5: Converged band diagrams for clamped-edge boundary conditions, for radii (a) $a = 0.2$ and (b) $a = 0.35$. Γ, X and M are the vertices of the irreducible part of the Brillouin zone. The inset in (b) shows a magnification of a "collapsed" band. Taken from Poulton *et al.* (2010).

zone. Within this zone, we may then use symmetry to derive the irreducible Brillouin zone which is the smallest area required to determine the band surfaces of a platonic crystal over the whole of the first Brillouin zone. For the example of the square array, this is a triangular region shown in Fig. 2.4(b). We now introduce some examples of band diagrams for Bloch-Floquet bending waves in a thin elastic plate containing the doubly periodic square array of cylindrical voids.

2.3.2 Dispersion of Bloch waves and band diagrams

The dispersion equation for Bloch waves within the doubly periodic square array of circular voids has been derived by Movchan *et al.* (2007). We give an outline of this problem in Section 2.5. The dispersion equation solutions are displayed graphically in band diagrams, and Poulton *et al.* (2010) provided several illustrative examples for various boundary conditions applied to the scatterers.

In Fig. 2.5 (Poulton *et al.* 2010), we show the band diagram formulated using the standard convention for photonic crystal literature, in that the modulus of the Bloch vector $\mathbf{k}_0$ is on the horizontal axis, with the spectral parameter β on the vertical axis, and three *principal lines* are selected to represent the variation of the Bloch vector $\mathbf{k}_0 = (k_{0x}, k_{0y})$. These lines are drawn from $\mathbf{k}_0 = (0, 0)$ to $(\pi, 0)$, ΓX; from $\mathbf{k}_0 = (\pi, 0)$ to (π, π), XM; and from $\mathbf{k}_0 = (0, 0)$ to $(-\pi, -\pi)$ with $k_{0x} = k_{0y}$, $M\Gamma$. These three regions of interest for the variation of $\mathbf{k}_0 = (k_{0x}, k_{0y})$ arise from the irreducible Brillouin zone (Fig. 2.4(b)).

The band diagrams indicate several modes, or band orders, and the two most notable features of Fig. 2.5(a) for radius $a = 0.2$ are the total band gaps above and below the fundamental (zero order) mode, and the lack of a band gap between the second and

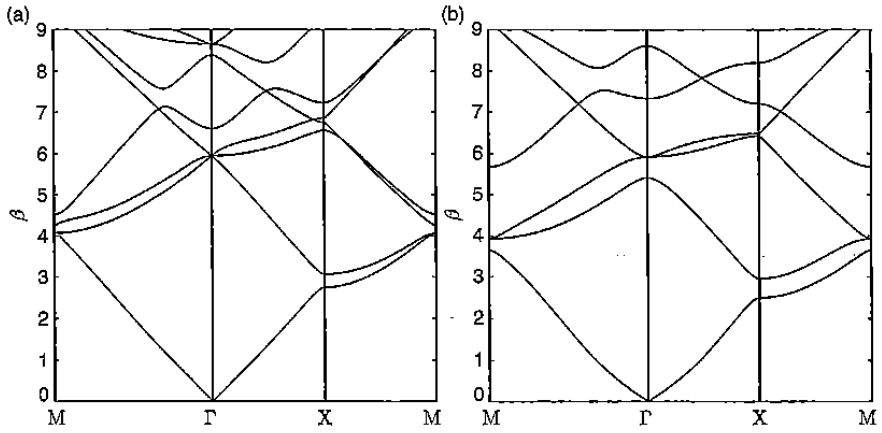

Figure 2.6: Converged band diagrams for free-edge boundary conditions, with Poisson ratio $\nu = 0.3$, for radii (a) $a = 0.2$ and (b) $a = 0.35$. The bands lie close to those for the Bloch modes of a homogeneous structure. Taken from Poulton *et al.* (2010).

third modes. For radius $a = 0.35$ in Fig. 2.5(b), there is a band gap between every band shown, and upon closer inspection, there is the interesting feature that increased radius leads to the second and third bands "collapsing" upon one another, forming a quasi-degenerate pair, shown in the inset.

One further observation made by Poulton *et al.* (2010) is the tendency of the bands to become very flat as the radius of the voids increase. This is clearly illustrated in Fig. 2.5(b) and these flat bands correspond to trapped modes and slow waves, a very important feature of our analysis throughout this thesis. In Fig. 2.6 (taken from Poulton *et al.* 2010), we show dispersion curves for the free-edge boundary condition for the same radii. Comparing the two types of boundary condition, flat bands are more likely to arise from clamped-edge conditions, and dispersion curves closer to freely-propagating waves are more likely to arise from the free-edge conditions.

2.4 Concepts from classical optics

The periodic gratings are composed of circular voids separated by a fixed distance d, and are used as the fundamental building block of the platonic periodic arrays. An incident flexural wave is scattered by the grating, producing a set of reflected and transmitted waves. This behaviour is analogous to that of a diffraction grating in a photonic crystal.

2.4.1 Diffraction grating

In optics, a diffraction grating is a periodic structure that splits and diffracts light into multiple beams propagating in different directions, at different wavelengths. The grating acts as a dispersive element. The directions of the beams depend on the spacing

(period) of the grating, the wavelength (or frequency) and each beam is characterized by its specular order m. The relationship between these factors is determined using the Fraunhofer grating equation, which has an equivalent expression for the platonic grating, with a separate case for each of Helmholtz and modified Helmholtz type waves.

For general practical applications, the photonic gratings have ridges or rulings on their surface, and are either reflective (analogous to a mirror) or transmissive (analogous to a lens). The grating's zero-order mode (i.e. specular order $m = 0$) affords no diffraction and the incident wave behaves according to Snell's laws of reflection and refraction. For an arbitrary angle of incidence θ_i (defined as in Fig. 2.1), the grating equation for a diffraction grating of period d is

$$\sin\theta_m \;=\; \sin\theta_i + \frac{m\lambda}{d}, \tag{2.19}$$

where λ is the wavelength of the beam of light of specular order m. From this equation we obtain the explicit expression for θ_m:

$$\theta_m \;=\; \arcsin\left(\frac{m\lambda}{d} \;+\; \sin\theta_i\right). \tag{2.20}$$

The nonzero integers m may be positive or negative, giving diffracted orders on both sides of the zero order beam.

For the platonic grating, the equivalent Fraunhofer equation describing the relationship between the order of the flexural waves p, the angle of incidence θ_i and the spectral parameter β is

$$\alpha_p \;=\; \alpha_0 + \frac{2\pi p}{d}, \tag{2.21}$$

where

$$\alpha_0 = \beta\sin\theta_i \quad \text{and} \quad \alpha_p = \beta\sin\theta_p = \alpha_0 + \frac{2\pi p}{d}. \tag{2.22}$$

To solve uniquely the Helmholtz and modified Helmholtz equations (2.5), a radiation condition must be imposed to guarantee that only outgoing waves are present at infinity. This is the Sommerfeld radiation condition, named after Arnold Sommerfeld who observed that the energy radiated from the sources must scatter to infinity, and that no energy may be incoming from infinity (Sommerfeld, 1949). The Sommerfeld radiation condition ensures that the complex exponentials in the plane wave expansions in Section 2.2 decay exponentially, rather than grow, and contribute evanescent waves.

We define Ω_H to represent the set of propagating orders of Helmholtz type. The sets Ω_H^e and Ω_M^e contain evanescent waves, of Helmholtz and modified Helmholtz type respectively. The set Ω_M^e comprises all integers p since all modified Helmholtz waves that satisfy the Sommerfeld radiation condition are evanescent. Propagating orders are commonly projected onto the normal Oy axis, whilst evanescent waves decay exponentially and travel in the direction parallel to the Ox axis. For any propagating incident wave, of Helmholtz type, which is characterised by its angle of incidence θ_i,

the zeroth order is certain to be propagating. To determine the wave numbers β for which additional orders are propagating, we use the identity

$$\alpha_p^2 + \chi_p^2 = \beta^2. \tag{2.23}$$

The terms χ_p are defined by

$$\chi_p = \begin{cases} \sqrt{\beta^2 - {\alpha_p}^2} \ , \ {\alpha_p}^2 \leq \beta^2 \\ i\sqrt{{\alpha_p}^2 - \beta^2} \ , \ {\alpha_p}^2 > \beta^2, \end{cases} \tag{2.24}$$

and the propagating orders require χ_p to be real and positive. The diffraction angle for the pth order is denoted by θ_p and is defined by

$$\theta_p = \arcsin\left(\sin\theta_i + \frac{2\pi p}{\beta d}\right). \tag{2.25}$$

Evanescent orders arise for $\theta_p = \pm\pi/2$. We consider both cases, combining equations (2.19) and (2.22). If $\theta_p = -\pi/2$,

$$-\beta = \beta\sin\theta_i + \frac{2\pi p}{d} \Rightarrow \beta(1+\sin\theta_i) = -\frac{2\pi p}{d} \Rightarrow \beta = \frac{-2\pi p}{(1+\sin\theta_i)d},$$

and for $\theta_p = \pi/2$,

$$\beta = \beta\sin\theta_i + \frac{2\pi p}{d} \Rightarrow \beta = \frac{2\pi p}{(1-\sin\theta_i)d}. \tag{2.26}$$

Combining the two cases, we have an expression for both positive and negative diffraction orders:

$$\beta = \begin{cases} \frac{-2\pi p}{(1+\sin\theta_i)d} \ , \ p < 0 \\ \frac{2\pi p}{(1-\sin\theta_i)d} \ , \ p > 0. \end{cases} \tag{2.27}$$

These formulae give us the values of β at which the specular order passes off, i.e. becomes propagating. For values of β lower than this threshold, the waves are evanescent (non-propagating) and decay exponentially away from the grating. For normal incidence, we would observe symmetry regarding the propagating orders, i.e. in the event of p_1 being propagating, so would $-p_1$. However, as the angle changes, this symmetry would no longer be observed, and propagating orders will be skewed to the positive or negative side.

For example for a grating with unit periodicity and $\theta_i = 30^\circ$, the first six propagating orders are 0, -1 ($\beta = 4\pi/3d$), -2 ($\beta = 8\pi/3d$), -3 and 1 simultaneously ($\beta = 4\pi/d$), and -4 ($\beta = 16\pi/3d$). We note that in classical optical theory, it is the wavelength that is used to determine the passing off of diffraction orders, rather than the frequency parameter β that we are employing. This is precisely the reason that the -1^{th} order passes off "before" the 1^{th} order, which is contrary to what one would expect when studying an electromagnetic diffraction grating.

We illustrate this example in Fig. 2.7 where $\beta = 4.5$ is considered for the oblique angle of incidence $\theta_i = 30^\circ$. For these values, the 0^{th} and -1^{th} orders are propagating, whilst the other orders are evanescent.

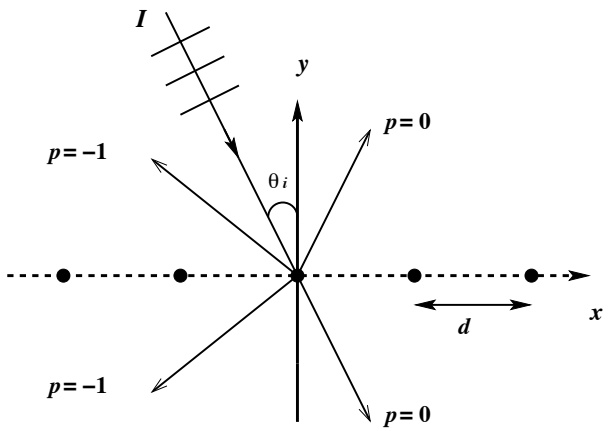

Figure 2.7: A plane wave ($\boldsymbol{I}$) incident on a grating of rigid pins from above with angle of incidence θ_i. We show the diffraction order $p = -1$ as well as the zeroth order reflected and transmitted fields.

2.4.2 Efficiency curves and Wood anomalies

In the field of optics, there are several physical effects arising from diffraction gratings that apply to a platonic diffraction grating. Wood anomalies are one such phenomenon, and were first discovered by R. W. Wood in 1902. Here we introduce the concept of efficiency curves for the reflected and transmitted energies associated with an optical diffraction grating, and discuss a set of these curves showing illustrative examples of Wood anomalies for a platonic analogue.

Efficiency curves

Efficiency and its variation with wavelength and spectral order are important characteristics of a diffraction grating. For a reflection grating, absolute efficiency is defined as the ratio of the intensity of monochromatic light diffracted into the specular order being measured, to the intensity of the incident light (see Diffraction Grating Handbook, Loewen 1970).

In essence, efficiency is the ratio of the flow of energy along the normal to the grating, relative to that for the incident wave. Therefore the efficiency E_n of an order n with plane wave amplitude B_n is

$$E_n = \frac{|B_n|^2 \cos\theta_n}{|B_i|^2 \cos\theta_i},$$

where the subscript i represents the incident wave. Evanescent orders carry energy parallel to Ox, and therefore have nonzero intensity, but zero efficiency.

The control of the magnitude and variation of diffracted energy with wavelength is called blazing. For optical gratings, it involves manipulating the micro-geometry of the grating grooves. For platonic gratings, the alterations are in the grating period and

geometry of the scatterers, in our case the radius of the circular voids. It is useful to plot efficiency versus wavelength for a given diffraction order and these efficiency curves usually show a single maximum. The characteristic wavelength in optics is known as the peak wavelength or blaze wavelength. We observe a similar profile when we plot normalised reflected energy versus the spectral parameter β for a platonic grating, as illustrated by the dashed curve in Fig. 2.8.

Anomalies

In 1902, R. W. Wood observed that the intensity of light diffracted by a grating generally changed slowly as the wavelength was varied. Occasionally, a sharp change in intensity was observed at certain wavelengths (Wood 1902). These abrupt changes in efficiency are now known as Wood anomalies, and appear as sharp peaks and troughs on efficiency curves. Later, they were grouped into two types, Rayleigh anomalies and resonance anomalies (Hessel & Oliner 1965).

Lord Rayleigh predicted spectral locations where certain sets of anomalies would be found. In particular he stated that anomalies occur when light of a specific wavelength λ' and spectral order m' is diffracted at $|\theta_d| = 90°$ from the grating normal (i.e. parallel to the grating itself) and becomes evanescent. For wavelengths $\lambda < \lambda'$, $|\theta_d| < 90°$, propagation is possible for order m' and all lower orders $m < m'$, but for $\lambda > \lambda'$, no propagation is possible for order m' (but is still possible for lower orders). This is sometimes called the passing off of a specular order.

There is a discontinuity in the diffracted power versus wavelength in order m' at wavelength λ', and the power that would diffract into this order for $\lambda > \lambda'$ is redistributed among the other propagating orders. Therefore Rayleigh anomalies arise from the abrupt redistribution of energy when a diffracted order changes from propagating to evanescent, or vice versa. They are also known as threshold anomalies (see Loewen & Popov 1997).

The second group of anomalies are normally more noticeable than Rayleigh anomalies, and are caused by resonance phenomena. Both classes were illustrated by Movchan *et al.* (2009) for a platonic grating (see Fig. 2.8). In Fig. 2.8, normalised reflected energy is plotted versus the spectral parameter β for a single grating (dashed curve), and for a pair of unshifted gratings, normalised transmitted energy is plotted versus β (solid curve). The sharp spike in transmission for a pair coincides with the discontinuity in reflection for a single grating with $d = 1$ at $\beta = 4\pi/3$, and corresponds to a Rayleigh anomaly. The second peak in transmission for the pair at around $\beta = 4.8$ is linked to resonance anomalies.

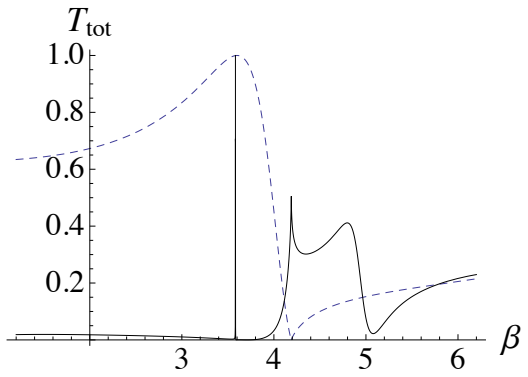

Figure 2.8: Normalised transmitted energy T_{tot}, summed over propagating orders (see equation (3.93)), versus β for a pair of gratings, and normalised reflected energy R_{tot} for a single grating (dashed line) of rigid pins with $d = 1$. The incident wave is of Helmholtz type, with angle of incidence $\theta_i = 30°$. Adapted from Movchan *et al.* (2009).

2.4.3 Stokes-Helmholtz reciprocity principle

The Stokes-Helmholtz reciprocity principle applied to gratings relates two diffraction problems. In the first, an incident plane wave is diffracted by a grating into a particular reflected order (say p), with an efficiency E_p. In the second, the incident wave comes in along the same line as order p went out, and the diffracted order p retraces the path of the first incident wave, its efficiency also being E_p. This follows an application of Green's Theorem using the boundary conditions on the grating surface and the periodicity of the total field. The reciprocity principle holds whether or not the grating is lossy (see Maystre & McPhedran 1974).

Loewen & Popov (1997) state that there are three important consequences of the reciprocity principle:

1. The zeroth-order efficiency, represented by $E_0(\lambda)$ where λ is a given wavelength, is a symmetric function of the angle of incidence θ_i about $\theta_i = 0$.

2. The rotation of the grating through π (whilst keeping θ_i constant) does not affect $E_0(\lambda)$. If only two diffraction orders are propagating (for example $p = 0$, $p = 1$), the efficiency $E_1(\lambda)$ will be unchanged too.

3. The efficiency $E_p(\lambda)$ for a given diffraction order p is a symmetric function of λ versus $\sin\theta_i$ about the Littrow condition $\theta_i = \theta_d$.

The Littrow condition or mounting ensures that for a reflection grating, there is a certain value of order p such that the p^{th} diffracted wave is reflected back along the path of the incident wave, i.e. they are propagating in opposite directions (Petit 1982).

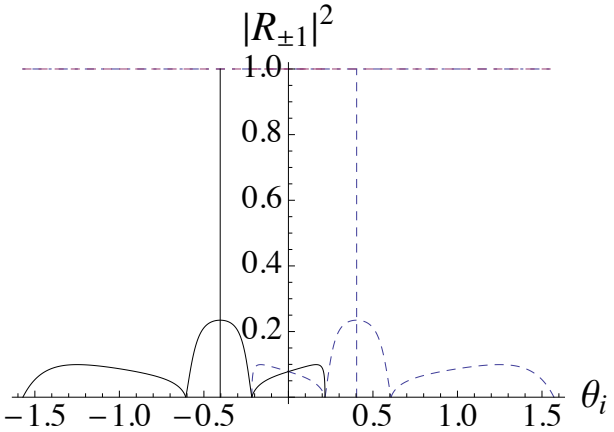

Figure 2.9: Normalised reflected energy (efficiency) versus angle of incidence θ_i for a single grating of rigid pins for $\beta = 8.0$. Solid curve: $p = 1$, Dashed curve: $p = -1$. The lines of symmetry for the Littrow angle $\pm 23.1225^\circ$ (± 0.403565 radians) are shown by the vertical lines.

This may be expressed as $\theta_p = -\theta_i$. Referring to the grating equation (2.22), we have

$$2 \sin \theta_i = -\frac{2\pi p}{\beta d}.$$

For $p = \pm 1$ with $d = 1$, the Littrow condition angle is given by

$$\theta_{\mp 1,L} = \pm \arcsin\left(\frac{\pi}{\beta}\right). \tag{2.28}$$

In Fig. 2.9 we show an example illustrating the third consequence of the reciprocity principle outlined by Loewen & Popov (1997). The normalised reflected energy, or equivalently the efficiency, of the orders $p = \pm 1$ for a single grating of rigid pins is plotted versus angle of incidence θ_i for $\beta = 8.0$. The solid curve represents the propagating waves for $p = 1$ and the dashed curve, those for $p = -1$. The orders $p = \pm 1$ pass off at $\theta_{\pm 1,W} = \mp \arcsin(\pi/4 - 1) = \pm 0.21628$, as can be seen in Fig. 2.9, giving rise to Rayleigh anomalies on either side of the origin.

The symmetry about the Littrow angle $\theta_{\pm 1,L}$ is also apparent. For this case $\theta_{1,L} = -\theta_{-1,L} = -\arcsin(\pi/\beta) = -0.403565$. We use vertical lines to demonstrate the symmetry arising as a consequence of the reciprocity principle. McPhedran & Waterworth (1972, 1973) provide detailed coverage of diffraction grating anomalies, and refer to this concept in their Fig.1 (1973).

2.4.4 Fabry-Pérot theory

The platonic grating structures possess Bloch modes that couple with the incident waves to support transmission through the system for specific combinations of θ_i and the spectral parameter β. For stacks of many gratings, the dominant action is reflection.

However there occur narrow frequency bands in which transmission dominates, due to resonances of Bloch modes within the stacks. This phenomenon is linked directly to the trapping of waves between the gratings. Fundamentally, the high reflectance of a single grating supports the trapping of waves between sets of identical gratings, and the associated localisation is observed in the form of resonances.

A classical device in optics is the Fabry-Pérot interferometer. Its principle of operation is at first sight counterintuitive, and is worth explaining since a similar mechanism operates in the systems investigated throughout this thesis. It typically consists of two or more parallel highly-reflecting mirrors. A related device is the Fabry-Pérot étalon, which is made of a transparent plate with two reflecting surfaces. For most frequencies, light is simply reflected off the first mirror. However for specific frequencies, light can be trapped between the mirrors, bouncing back and forth and increasing in intensity. At the resonant frequency, transmission very close to unity can occur. The higher the mirror reflectance, and the larger the number of mirrors, the narrower the frequency region of significant transmission. Such structures commonly occur in laser cavities, and in many other optical devices.

We now present a brief account of the theory of the Fabry-Pérot interferometer. This is useful since it is a scalar version of arguments we develop in Section 3.2 and subsequent chapters, wherein the scalar amplitudes are replaced by scattering matrices.

Governing equations

When a wave is incident on a surface, it is divided into two plane waves, one reflected and one transmitted. For each member of either of the sets of reflected or transmitted waves, the variable part of the phase of the wave function differs from that of the preceding member by an amount corresponding to a double traversal of the plate. This is illustrated in Fig. 2.10 (see Born & Wolf 1959). This phase difference δ is

$$\delta = \frac{4\pi}{\lambda_0} n' h \cos\theta' = 2k_0 l, \tag{2.29}$$

where λ_0 is the wavelength in a vacuum, h is the plate's thickness, n' is its refractive index and θ' is the angle of refraction. In the second expression, k_0 is the wavenumber and l is the optical path length. Taking $A^{(i)}$ to be the complex wave amplitude of the incident wave, we denote the reflection and transmission coefficients for waves travelling from the surrounding medium into the plate by r and t. Similarly, for the corresponding coefficients for waves travelling from the plate to the surrounding medium, we use r' and t'. We then obtain a series of amplitudes for the reflected waves:

$$rA^{(i)}, tt'r'A^{(i)}e^{i\delta}, tt'r'^3A^{(i)}e^{2i\delta}, ..., tt'r'^{(2p-3)}A^{(i)}e^{i(p-1)\delta}, ...$$

and for the transmitted wave coefficients, we have

$$tt'A^{(i)}, tt'r'^2A^{(i)}e^{i\delta}, tt'r'^4A^{(i)}e^{2i\delta}, ..., tt'r'^{2(p-1)}A^{(i)}e^{i(p-1)\delta}...$$

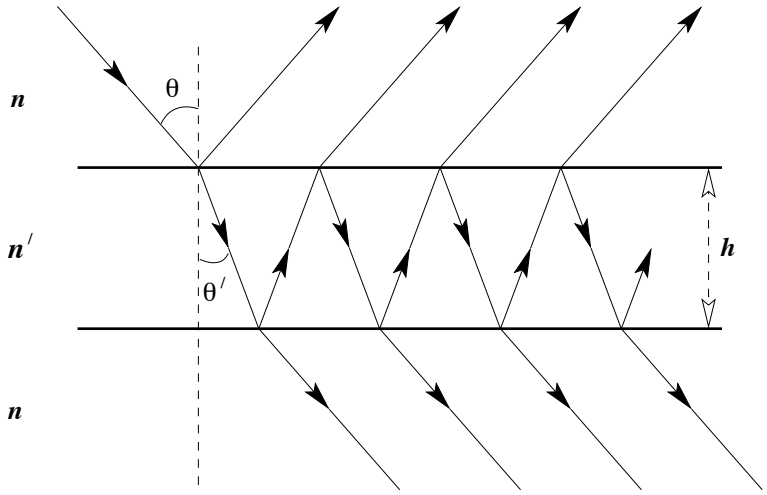

Figure 2.10: Multiple-beam interference for a transparent plate with thickness h and refractive indices n for the ambient medium, and n' for the plate. The angles of incidence and refraction are θ and θ' respectively.

Similar terms are used in the geometric series that we later employ for the platonic gratings in Section 3.2.2.

Born & Wolf (1959) define the reflectivity and transmissivity of the plate surfaces by $\mathcal{R}$ and $\mathcal{T}$ where $r^2 = r'^2 = \mathcal{R}$ and $tt' = \mathcal{T}$. These terms are related by

$$\mathcal{R} + \mathcal{T} = 1.$$

By evaluating the sums $p \to \infty$ for these series, we obtain representations for the reflected and transmitted amplitudes $A^{(r)}$ and $A^{(t)}$:

$$A^{(r)} = \frac{(1 - e^{i\delta})\sqrt{\mathcal{R}}}{1 - \mathcal{R}e^{i\delta}} A^{(i)}, \;\; A^{(t)} = \frac{\mathcal{T}}{1 - \mathcal{R}e^{i\delta}} A^{(i)}.$$

The intensities $I^{(i)}$, $I^{(r)}$ and $I^{(t)}$ are defined as follows

$$I^{(i)} = A^{(i)}A^{(i)*}, \;\; I^{(r)} = A^{(r)}A^{(r)*} = |A^{(r)}|^2, \;\; I^{(t)} = A^{(t)}A^{(t)*} = |A^{(t)}|^2, \tag{2.30}$$

where $*$ denotes complex conjugation. Airy's formulae for the diffracted intensities follow:

$$I^{(r)} = \frac{4\mathcal{R}\sin^2(\delta/2)}{(1 - \mathcal{R})^2 + 4\mathcal{R}\sin^2(\delta/2)} I^{(i)} \tag{2.31}$$

and

$$I^{(t)} = \frac{\mathcal{T}^2}{(1 - \mathcal{R})^2 + 4\mathcal{R}\sin^2(\delta/2)} I^{(i)}. \tag{2.32}$$

The relative efficiency of the transmitted field is

$$\frac{I^{(t)}}{I^{(i)}} = \frac{1}{1 + F\sin^2(\delta/2)}, \tag{2.33}$$

where the parameter F is defined by the equation $F = 4\mathcal{R}/(1 - \mathcal{R})^2$. Jenkins & White (1981) also provide a nice explanation for the derivation of this equation.

Sharpness of the Fabry-Pérot fringes and quality factors

As the reflectance $\mathcal{R}$ of a surface is increased, the fringes due to multiple reflections become much narrower. This is explained by looking at equation (2.33) for the intensities. When $\mathcal{R}$ is small compared with its maximum value of unity, F is also small and we can expand the term on the RHS of (2.33), and retain only the first power of F:

$$\frac{I^{(t)}}{I^{(i)}} = 1 - F\sin^2(\delta/2) = 1 - \frac{F}{2}(1-\cos\delta).$$

If $\mathcal{R}$ is increased, the intensity of the minima for the transmitted pattern falls, whilst its maxima become sharper until as $\mathcal{R} \to 1$ when the transmitted maxima become extremely narrow and sharp but extremely intense. Therefore the pattern becomes an almost completely dark background with narrow, bright fringes corresponding to constructive interference.

The sharpness of the fringes are commonly measured by their half-intensity width or half-width, which is reminiscent of the quality factors we use to quantify the sharpness of transmission resonances for platonic grating structures throughout this thesis. Born & Wolf (1959) define the half-width for transmitted light interference fringes to be the width between points on either side of a maximum where the intensity has fallen to half its maximum value. The finesse $\mathcal{F}$ of the fringes is defined as the ratio of the separation of adjacent fringes to the half-width ϵ.

For a fringe of interference order m, the points at which the intensity is half of its maximum are at

$$\delta = 2m\pi \pm \frac{\epsilon}{2}$$

where from equation (2.33),

$$\frac{1}{1+F\sin^2(\epsilon/4)} = \frac{1}{2},$$

and when F is sufficiently large, ϵ is small enough that we may write $\sin(\epsilon/4) = \epsilon/4$. The half-width is then given by

$$\epsilon = \frac{4}{\sqrt{F}}, \tag{2.34}$$

and the finesse by

$$\mathcal{F} = \frac{2\pi}{\epsilon} = \frac{\pi\sqrt{F}}{2} = \frac{\pi\sqrt{\mathcal{R}}}{1-\mathcal{R}} \tag{2.35}$$

since the separation of adjacent fringes corresponds to a change 2π of the phase change δ. The finesse $\mathcal{F}$ is a classical term for the fineness of a resonance.

We now present the relation between finesse and the quality factors that are commonly used to quantify the sharpness of resonances in wave science. The quality factor or Q-factor is a dimensionless parameter which characterises a resonance's bandwidth relative to the frequency of the maximum energy. We use the standard definition

$$Q = \frac{\beta_*}{\Delta\beta}, \tag{2.36}$$

where β_* characterizes the resonance frequency and $\Delta\beta$ represents the frequency difference between the half-power points. For a given β_*, the narrower or sharper a peak is, the higher the Q. Typically, an equivalent definition is

$$Q = \frac{\beta_*}{\gamma_*}, \tag{2.37}$$

where $\beta_* + i\gamma_*$ represents a complex resonant frequency, and this definition allows us to determine how far we have to go into the complex plane to find a resonance. A third definition of Q expresses it as the ratio of the energy density inside the resonant structure to that outside it.

It follows from equation (2.36) that

$$Q = \frac{\beta_*}{\Delta\beta} = \frac{k_*}{\Delta k}. \tag{2.38}$$

Referring to equations (2.33) and (2.29),

$$\frac{I^{(t)}}{I^{(i)}} = \frac{1}{1 + F\sin^2(\delta/2)} = \frac{1}{1 + F\sin^2(k_0 l)} = \frac{1}{2}$$

when $F\sin^2(k_0 l) = 1$. Therefore in this case,

$$\sin(k_0 l) = \pm\frac{1}{\sqrt{F}} \Rightarrow k_0 l \approx \pm\frac{1}{\sqrt{F}},$$

when F is large. The nth maximum is defined by $k_0 l = n\pi$ and we have $k_0 = n\pi/l$ and $\Delta k_0 \approx 2/l\sqrt{F}$. Therefore

$$Q = \frac{n\pi\sqrt{F}}{2} = n\mathcal{F}, \tag{2.39}$$

using equations (2.38), (2.35). The equations (2.36)-(2.39) will be used in Chapters 4 to 6 to derive the Q-factors for the resonances under investigation.

2.4.5 Electromagnetically induced transparency

The phenomenon of Electromagnetically Induced Transparency (EIT) has been intensively studied in the years since the initial investigations by S. E. Harris and his co-workers in 1989 (Harris 1989). The phenomenon relies on a laser controlling populations in chosen atomic states, causing a quantum interference and transforming an absorption resonance into a band cut in two by a laser-induced region of complete transparency. The result of this process is illustrated in Fig. 2.11 taken from Fleischhauer *et al.* (2005). The phenomenon is important because it gives rise to enhanced non-linear properties of the medium, and an unusual and valuable region of steep dispersion. An alternative descriptor for EIT sometimes used is spectral hole burning.

The way in which EIT works is illustrated in a generic energy level diagram: see Fig. 2.12 taken from Fleischhauer *et al.* (2005). The absorption peak, which is laser-modified, is associated with electrons being moved from state $|2\rangle$ to $|3\rangle$ via absorption

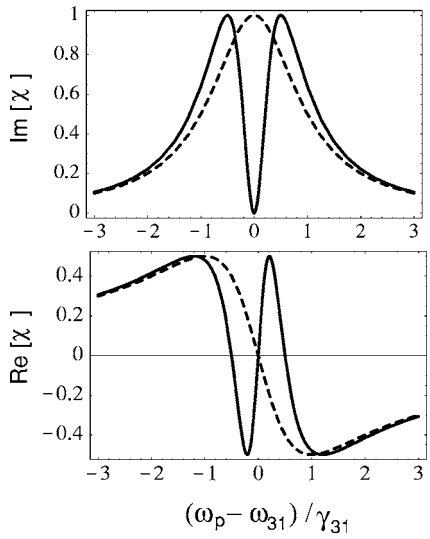

Figure 2.11: Susceptibility as a function of the frequency ω_p of the applied field relative to the atomic resonance frequency ω_{31}, for a radiatively broadened two-level system with radiative width γ_{31} (dashed line) and an EIT system with resonant coupling field (solid line): top, imaginary part of $\chi^{(1)}$ characterizing absorption; bottom, real part of $\chi^{(1)}$ determining the refractive properties of the medium. Taken from Fleischhauer *et al.* (2005).

of photon energy. This process is inhibited by the probe laser promoting electrons from state $|1\rangle$ into state $|3\rangle$, discouraging promotion from $|2\rangle$ to $|3\rangle$ by the Pauli exclusion principle.

The EDIT (elasto-dynamically inhibited transmission) phenomenon we have investigated systematically in this thesis bears a strong similarity in its results to EIT, in that a peak is cut in two by a narrow trough, leading to a steep and interesting dispersion characteristic (see Haslinger *et al.* (2012) and Chapter 4 for the first published results). However the details of the process are quite different. Firstly it is a resonant peak in transmission, of the Fabry-Pérot type, which is cut in two by a region of strong reflection. Thus in the acronym EDIT, the last two letters refer to inhibited transmission rather than induced transparency (see Haslinger *et al.* (2013a) and Chapter 5). Secondly, the exploitation in EIT depends on finding a gas with an appropriate set of energy levels in the desired frequency range. In the case of EDIT, the frequency range is broadly a matter of choosing suitable scale size for the experimental system. EDIT in fact relies on the controlled interaction between a mode of even spatial symmetry and a mode of odd spatial symmetry.

For EDIT, rather than a three-level energy system, we use a stack of three gratings. For the case of rigid pins, the even resonance is sensitive to the lateral position of the central grating while the odd resonance is independent of that position. Thus by shifting the central grating we can align the frequencies of the odd and even resonances inducing

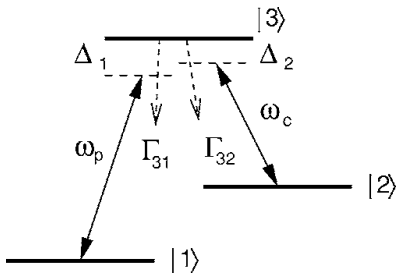

Figure 2.12: Generic system for EIT: lambda-type scheme with probe field of frequency ω_p and coupling field of frequency ω_c. $\Delta_1 = \omega_{31} - \omega_p$ and $\Delta_2 = \omega_{32} - \omega_c$ denote field detunings from atomic resonances and Γ_{ik} radiative decay rates from state $|i\rangle$ to state $|k\rangle$. Taken from Fleischhauer *et al.* (2005).

the "hole burning" via destructive interference, which leads to inhibited transmission.

This novel analogue of EIT-like effects for flexural plates joins examples recently presented in the literature for metamaterials, plasmonics and nano-optomechanical structures (NOMS). The contributions by Liu *et al.* (2009, 2010) refer to the first experimental demonstrations of EIT-like effects in optical metamaterials. The basic idea involves coupling two antennae, one an optically bright dipole in the form of a gold bar, and the other an optically dark quadrupole antenna consisting of a pair of gold wires placed beneath the dipole. Owing to their close proximity, strong coupling can be induced and destructive interference between the two excitation pathways leads to the EIT-like phenomena. As in EDIT, structural asymmetry in the form of a shift control parameter has an important bearing on the destructive interference arising from the coupling of the excitation pathways. Liu *et al.* (2010) report that the strength of coupling increases with increased structural asymmetry, whereas for EDIT, the optimal shift is determined by the other parameter settings in the system.

Further recent contributions for plasmonic metamaterials were made by Wang *et al.* (2013) and Taubert *et al.* (2012, 2013), who extended the work of Liu *et al.* (2009, 2010) in the analysis of the coupling of dipole and quadrupole antennae in plasmonic systems. In particular, Taubert *et al.* (2012, 2013) conducted an investigation of a classical analogue of electromagnetically induced absorption (EIA) where constructive, rather than destructive, interference of the excitation pathways gives rise to an enhancement of absorbance. We discuss the analogous case for flexural plates in Chapter 6, and the link with Fano resonances.

2.5 Spectral problem for biharmonic operator for doubly periodic square array

The propagation of waves in thin homogeneous plates is well described in the classical literature (for example Graff 1975). The research into flexural waves in heterogeneous

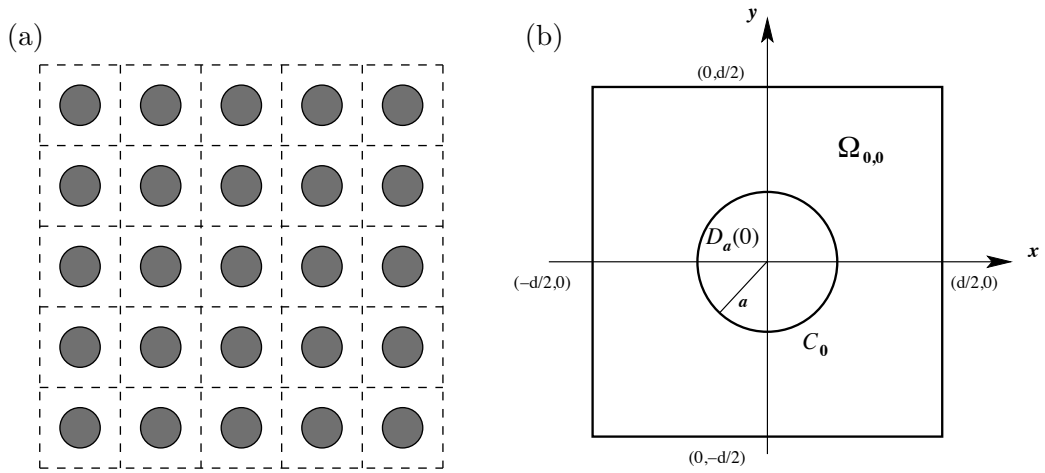

Figure 2.13: (a) Infinite plate with a doubly periodic array of circular voids. (b) The central unit cell $\Omega_{0,0}$ containing a circular scatterer.

platonic structures was initiated relatively recently. A paper by Halkjær *et al.* (2006) concerned the problems of numerical optical design, and maximizing the band gaps for platonic structures. Another early paper by Evans & Porter (2007) analysed flexural waves in thin plates periodically constrained by a square array of points.

Consider a doubly periodic square array of circular voids within a thin infinite elastic plate. A spectral problem for the biharmonic operator is formulated in the elementary cell shown in Fig. 2.13, and its analytical solution is derived using a multipole method. The boundaries of the holes may be clamped or free. This problem was analysed by Movchan *et al.* (2007). The multipole expansions are expressed in terms of Bessel and modified Bessel functions, and are used to represent the eigensolutions. The accompanying dispersion equations may be written in an explicit analytical form.

Important results were outlined by Movchan *et al.* (2007), most notably that the clamped array of circular holes possesses a full band gap at zero frequency, and that this band gap remains even in the limit as the radius of the cylinders tend to zero. This infers that the Dirichlet problem for flexural waves in two dimensions cannot be homogenized, whereas for the platonic structure with holes with free boundaries, the properties of the flexural waves are perturbed only slightly from those for the homogeneous plate. We present the multipole method for the two-dimensional platonic structure, which we later adapt for our specific structured system consisting of a finite number of platonic gratings.

2.5.1 Governing equations

The doubly periodic square array of circular voids within a thin infinite elastic plate is shown from above in Fig. 2.13(a). The elementary cell is illustrated in Fig. 2.13(b),

and is defined by

$$\Omega_{0,0} = \{(-d/2, d/2) \times (-d/2, d/2)\} \setminus \overline{D_a(0)}, \tag{2.40}$$

where $D_a(0) = \{(x, y) : x^2 + y^2 < a^2\}$ is the disc of radius a. The out-of-plane displacement $w(x, y; t)$ satisfies the Kirchhoff equation (2.1). Time harmonic oscillations are considered such that

$$w(x, y; t) = W(r, \theta) \sin(\omega t),$$

where (r, θ) are polar coordinates, ω is the angular frequency and W is the amplitude of the vibrations. The equation of motion then simplifies to the biharmonic plate equation (2.2) which may be written in its factorised form:

$$(\Delta + \beta^2)(\Delta - \beta^2)W = 0, \tag{2.41}$$

where $\beta^2 = \omega\sqrt{\rho h/D}$ with the physical parameters being defined as in Section 2.1.

Hence W is the superposition of two types of wave, one satisfying the Helmholtz equation and the other satisfying the modified Helmholtz equation:

$$(\Delta + \beta^2)W_H = 0 \quad \text{and} \quad (\Delta - \beta^2)W_M = 0. \tag{2.42}$$

2.5.2 Multipoles

Within the elementary cell $\Omega_{0,0}$, shown in Fig. 2.13 (b) and defined by equation (2.40), we use the series representation

$$W(r, \theta) = \sum_{n=-\infty}^{\infty} w_n(r) e^{in\theta}, \tag{2.43}$$

with w_n being the multipole term

$$w_n(r) = A_n J_n(\beta r) + E_n H_n^{(1)}(\beta r) + B_n I_n(\beta r) + F_n K_n(\beta r) \tag{2.44}$$

consisting of a Helmholtz part made up of Bessel functions J_n and Hankel functions $H_n^{(1)}$, and a modified Helmholtz part consisting of the modified Bessel functions I_n and K_n. The amplitudes A_n, E_n, B_n and F_n are the multipole coefficients to be determined. An important representation of the Hankel function $H_n^{(1)}$ is

$$H_n^{(1)}(\beta r) = J_n(\beta r) + iY_n(\beta r),$$

where J_n and Y_n are Bessel functions of the first and second kind. The modified Bessel functions I_n and K_n are related to J_n and $H_n^{(1)}$ by

$$I_n(z) = i^{-n} J_n(iz), \quad K_n(z) = \frac{\pi i}{2} i^n H_n^{(1)}(iz). \tag{2.45}$$

It is important to note that the series expansion (2.43) converges only in the region between the cylinder of interest (the elementary cell's for instance) and the circle

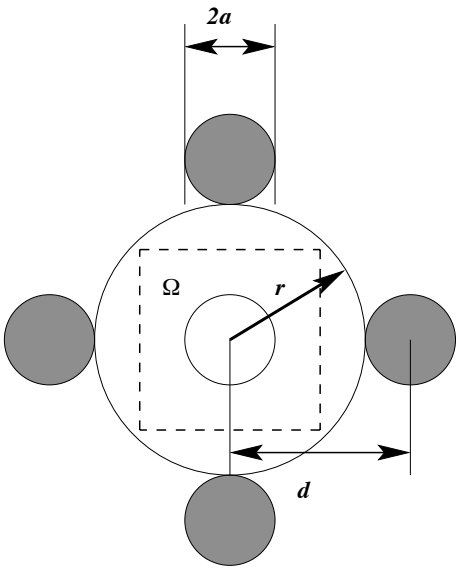

Figure 2.14: Radius of convergence for multipole expansion.

touching its four nearest neighbours, as illustrated in Fig. 2.14. Thus $a \leq r \leq d - a$. The expansion covers the entire elementary cell if $a \leq d(1 - 1/\sqrt{2})$ since the minimum radius of convergence in this case is $d/\sqrt{2}$ as shown in Fig. 2.14.

We use standard Bloch-Floquet quasi-periodicity conditions (see Section 2.3), which are set within the periodic array. They relate the solution within a general cell Ω_{p_1,p_2} to that within the central cell $\Omega_{0,0}$ by

$$W(\mathbf{r} + \mathbf{R}_p) = W(\mathbf{r})e^{i\mathbf{R}_p \cdot \mathbf{k}_0}, \tag{2.46}$$

where

$$\mathbf{R}_p = p_1 d\, \mathbf{e}^{(1)} + p_2 d\, \mathbf{e}^{(2)}, \quad p = \{p_1, p_2\}, \quad p_1, p_2 \in \mathbb{Z};$$

$\mathbf{k}_0$ is the Bloch vector, $\mathbf{e}^{(1)}$ and $\mathbf{e}^{(2)}$ are the axial unit vectors and d is the period of the array. The vector $\mathbf{R}_p$ is often called the lattice vector, as noted in Section 2.3.1. Its polar form is $\mathbf{R}_p = (R_p, \phi_p)$, where $R_p = |\boldsymbol{R}_p|$, $\phi_p = \arg(\mathbf{R}_p)$. This form is required later in equation (2.55) when deriving the Rayleigh identites.

2.5.3 Boundary conditions and their multipole representations

The two most natural types of boundary conditions to consider are clamped and free edge on the circular boundary (C_0 in Fig. 2.13(b)).

(i) Dirichlet clamped edge conditions are

$$W\Big|_{r=a} = 0, \quad \frac{\partial W}{\partial r}\Big|_{r=a} = 0. \tag{2.47}$$

In particular, when the radius a tends to zero we retrieve the case of fixed pins.

(ii) Free boundaries are defined by the moment and transverse force being equal to zero. The details of the relevant moments and forces are given by Movchan *et al.* (2007) but since we are interested in clamped conditions, we omit them here.

For the clamped case, using equations (2.44), (2.47), we have

$$A_n J_n(\beta a) + E_n H_n^{(1)}(\beta a) + B_n I_n(\beta a) + F_n K_n(\beta a) = 0 \tag{2.48}$$

and

$$A_n J_n'(\beta a) + E_n H_n^{(1)'}(\beta a) + B_n I_n'(\beta a) + F_n K_n'(\beta a) = 0. \tag{2.49}$$

We solve the spectral problem by constructing the dispersion relation which links the angular frequency ω with the Bloch vector $\mathbf{k}_0$. To do this we evaluate the multipole coefficients as solutions of the Rayleigh system.

2.5.4 Rayleigh identities and lattice sums

The functions W_H and W_M that satisfy equations (2.41), (2.42) are respectively oscillatory and exponential, and propagate independently in the elastic medium between the circular voids. There are separate consistency relations between the local expansions in the elastic medium surrounding a general void Ω_{p_1,p_2} and the central cell's void $\Omega_{0,0}$, for each of W_H and W_M. These consistency relations are called the Rayleigh identities and are derived in the well established way (see for example Botten *et al.* 2003) using Green's theorem and Graf's addition theorem which we describe in more detail for the case of a platonic grating stack in Section 2.6.1.

Referring to Abramowitz & Stegun (1965), the addition theorem is given for Bessel functions of the type J, Y, $H^{(1)}$ and $H^{(2)}$ which are collectively denoted by the symbol $\mathcal{C}$:

$$\mathcal{C}_\nu(w)e^{i\nu\chi} = \sum_{\kappa=-\infty}^{\infty} \mathcal{C}_{\nu+\kappa}(u)\, J_\kappa(v)e^{i\kappa\alpha}, \tag{2.50}$$

where u, v and w are the magnitudes of the vectors $\mathbf{u}$, $\mathbf{v}$ and $\mathbf{w}$ that form three sides of a triangle, with α the angle between $\mathbf{u}$ and $\mathbf{v}$ and χ the angle between $\mathbf{u}$ and $\mathbf{w}$. An additional constraint is that $v < u$.

For the addition theorem for the modified Bessel functions K and I, we replace u, v and w with iU, iV and iW, and use the relations between $H_l^{(1)}(iz)$ and $K_l(z)$, and $J_l(iz)$ and $I_l(z)$ i.e.

$$H_0^{(1)}(iz) = \frac{2}{i\pi}K_0(z), \quad \frac{\pi}{2}i^{l+1}H_l^{(1)}(iz) = K_l(z), \quad i^{-l}J_l(iz) = I_l(z). \tag{2.51}$$

For the Hankel function for example, equation (2.50) becomes

$$H_0^{(1)}(iW) = \sum_{l=-\infty}^{\infty} H_l^{(1)}(iU)\, J_l(iV)e^{il\alpha}.$$

The substitution of the identities (2.51) yields

$$\frac{2}{\pi i}K_0(W) \;=\; \sum_{l=-\infty}^{\infty} \frac{2}{\pi} i^{-(l+1)} K_l(U)\, I_l(V)\, i^l\, e^{il\alpha},$$

which simplifies to

$$K_0(W) \;=\; \sum_{l=-\infty}^{\infty} K_l(U) I_l(V) e^{il\alpha}, \tag{2.52}$$

an expression with the same structure as the general Bessel function $\mathcal{C}$ expansion (2.50). The general result is

$$K_n(W)e^{in\chi} \;=\; \sum_{k=-\infty}^{\infty} K_{n+k}(U) I_k(V) e^{ik\alpha}, \tag{2.53}$$

with a similar formula for I_n.

The Rayleigh identity for the function W_H which satisfies the Helmholtz equation in (2.42), is given by

$$A_n = \sum_{l=-\infty}^{\infty} (-1)^{l-n} S^H_{l-n}(\beta, \mathbf{k}_0) E_l, \tag{2.54}$$

where $S^H_l(\beta, \mathbf{k}_0)$ is the lattice sum of order l for the Hankel function $H^{(1)}$:

$$S^H_l(\beta, \boldsymbol{k}_0) \;=\; \sum_{p \neq \{0,0\}} H^{(1)}_l\left(\beta R_p\right) e^{il\theta_p}\, e^{i\boldsymbol{k}_0 \cdot \boldsymbol{R}_p}. \tag{2.55}$$

Here, $\boldsymbol{R}_p$ is defined as in (2.46) with $R_p = |\boldsymbol{R}_p|$, $\phi_p = \arg(\mathbf{R}_p)$. These lattice sums are not absolutely convergent so have to be replaced by appropriate expressions for numerical computations. This is discussed in detail for the grating stack model in Sections 3.1.3 and A.1.

The Rayleigh identity for W_M, which satisfies the modified Helmholtz equation (2.42) is given by

$$B_n = \sum_{l=-\infty}^{\infty} (-1)^l S^K_{l-n}(\beta, \mathbf{k}_0) F_l, \tag{2.56}$$

where the lattice sums

$$S^K_l(\beta, \boldsymbol{k}_0) \;=\; \sum_{p \neq \{0,0\}} K_l\left(\beta R_p\right) e^{il\theta_p}\, e^{i\boldsymbol{k}_0 \cdot \boldsymbol{R}_p} \tag{2.57}$$

are exponentially convergent and so can be evaluated by direct summation, provided that βd is not too small. Movchan *et al.* (2007) give accelerated convergence formulae (obtained by repeated integration) for both S^H_l and S^K_l. However the accelerated representations can only be used for $l > 0$. For the case of $l < 0$, relations are required between the positive and negative orders. The following identities were given by Movchan *et al.* (2007):

$$S^Y_l(\beta, -\mathbf{k}_0) = (-1)^l S^Y_l(\beta, \mathbf{k}_0), \qquad S^Y_{-l}(\beta, \mathbf{k}_0) = \left(S^Y_l(\beta, \mathbf{k}_0)\right)^*, \tag{2.58}$$

and

$$S_l^K(\beta, -\mathbf{k}_0) = (-1)^l S_l^K(\beta, \mathbf{k}_0), \qquad S_{-l}^K(\beta, \mathbf{k}_0) = (-1)^l \left(S_l^K(\beta, \mathbf{k}_0)\right)^*, \tag{2.59}$$

where complex conjugation is denoted by the asterisk.

Eigenmodes of flexural vibrations

To solve this problem for the clamped edge condition, we combine the Rayleigh identities (2.54), (2.56) and the boundary conditions (2.48), (2.49). The same is done for the free boundaries (see Movchan *et al.* 2007) but we only consider the clamped condition here. The Rayleigh identities couple multipoles of different orders for the same type of waves, and depend on the geometrical arrangement of the voids in the periodic array. The boundary conditions are used to couple multipoles of the same order, but for two different types of wave. Therefore the boundary conditions carry information about the elastic moduli of the specific problem, the radii of the inclusions or voids and the type of boundary condition, but nothing about the geometry of the array. The necessary coupling between the two types of wave, and the geometry of the system, is brought together by combining the boundary conditions and Rayleigh identities, which yields a soluble algebraic system for the multipole coefficients we seek to evaluate.

For the clamped boundary, we substitute (2.54) and (2.56) into (2.48) and (2.49):

$$\begin{aligned}
&\sum_{l=-\infty}^{\infty} \left[(-1)^{l-n} S_{l-n}^H(\beta, \mathbf{k}_0) J_n(\beta a) + \delta_{ln} H_n^{(1)}(\beta a)\right] E_l \\
&+ \sum_{l=-\infty}^{\infty} \left[(-1)^l S_{l-n}^K(\beta, \mathbf{k}_0) I_n(\beta a) + \delta_{ln} K_n(\beta a)\right] F_l = 0, \qquad (2.60) \\
&\sum_{l=-\infty}^{\infty} \left[(-1)^{l-n} S_{l-n}^H(\beta, \mathbf{k}_0) J_n'(\beta a) + \delta_{ln} (H_n^{(1)})'(\beta a)\right] E_l \\
&+ \sum_{l=-\infty}^{\infty} \left[(-1)^l S_{l-n}^K(\beta, \mathbf{k}_0) I_n'(\beta a) + \delta_{ln} K_n'(\beta a)\right] F_l = 0. \qquad (2.61)
\end{aligned}$$

We assume that the order of truncation L for the Rayleigh system (2.60), (2.61) is chosen according to the radius of the void. Poulton *et al.* (2010) provide tables for selecting the number of multipoles to achieve converged frequencies for a doubly periodic square array consisting of perforations with non-zero radii. These conclusions which link the radius of the hole to the number of necessary multipoles are also applicable to the stacks of gratings in Section 3.1.3. The multipole summation then runs from $-L$ to L ($2L + 1$ terms). The accuracy of the solution to the system depends on the precision with which we evaluate the incorporated lattice sums. In the doubly periodic array, Movchan *et al.* (2007) recommended calculating the lattice sums over orders in the range $-2L$ to $2L$ ($4L + 2$ terms).

For the truncated system, we express the coefficients E_l and F_l as column vectors $\mathbf{E}$ and $\mathbf{F}$, and obtain the matrix equation

$$\begin{pmatrix} R_c^{HH} & R_c^{HM} \\ R_c^{MH} & R_c^{MM} \end{pmatrix} \begin{pmatrix} \mathbf{E} \\ \mathbf{F} \end{pmatrix} = 0, \tag{2.62}$$

where each of the four sub-blocks R_c^{ij}, $\{i,j\} = \{H, M\}$, has dimension $(2L+1)\times(2L+1)$ and H denotes a Helmholtz type wave, and M, the modified Helmholtz type. The suffix c denotes the clamped boundary condition. The matrix of dimension $(4L+2)\times(4L+2)$ in equation (2.62) is complex and depends on β and $\mathbf{k}_0$. We denote it by $\mathcal{M}$ and obtain the dispersion equation

$$\det\left(\mathcal{M}(\beta, \mathbf{k}_0)\right) = 0, \tag{2.63}$$

which we solve numerically for a range of wave vectors $\mathbf{k}_0$. The order of truncation L determines the number of solutions β.

For the case of rigid pins, it is sufficient to use order of truncation $L = 1$ which means that matrix $\mathcal{M}$ has dimension 6×6 in our illustrative examples. For voids of nonzero radius, a greater value of L is required, and this value increases as the radius a increases. One may consult the papers by Platts *et al.* (2002), (2003) and Poulton *et al.* (2010) for further coverage of the dependence of L on a. We also discuss this topic in Chapter 5 and Haslinger *et al.* (2013a) for platonic grating stacks.

2.5.5 Band diagrams and stop-bands

We follow the analysis by Movchan *et al.* (2007) for the clamped square array with unit periodicity. The authors provide a band diagram formulated using the standard convention for photonic crystal literature as outlined in Section 2.3.2. It shows the first three modes, or band orders, and the two most notable features are the total band gaps above and below the fundamental (zero order) mode, and the lack of a band gap between the second and third modes. The band gap at low frequencies is particularly interesting. There is a similar observation from electromagnetism for arrays of perfectly conducting rods (Nicorovici *et al.* 1995a, Pendry *et al.* 1996, Guida *et al.* 1998), where it is an important factor in the construction of metamaterials.

For the monopole approximation $l = n = 0$, equation (2.63) becomes

$$\begin{aligned} &S_0^H(\beta, \mathbf{k}_0) S_0^K(\beta, \mathbf{k}_0)\ (J_0 I_1 + J_1 I_0) + S_0^H(\beta, \mathbf{k}_0)\ (-J_0 K_1 + J_1 K_0) \\ &+ S_0^K(\beta, \mathbf{k}_0)\ (H_0^{(1)} I_1 + H_1^{(1)} I_0) + H_1^{(1)} K_0 - H_0^{(1)} K_1 = 0, \end{aligned} \tag{2.64}$$

where the LHS is the determinant of the 2×2 matrix in (2.62), and we have omitted the argument (βa) for all of the Bessel and modified Bessel functions for convenience. Here we have used the identities (2.45), (2.51) and the derivative formulae:

$$\mathcal{B}_0'(z) = -\mathcal{B}_1(z), \quad I_0'(z) = I_1(z), \quad K_0'(z) = -K_1(z), \tag{2.65}$$

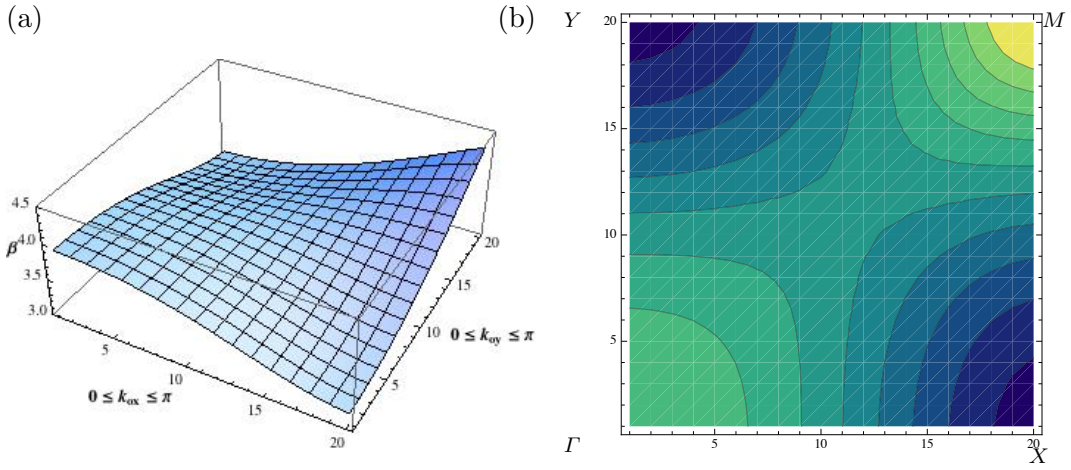

Figure 2.15: (a) First quadrant of the band surface for the lowest band for the square array of clamped cylinders of zero radius, with β on the vertical axis. (b) Contours of constant β for the same surface. The ranges for k_{0x} and k_{0y} are $0 \leq k_{0x} \leq \pi d$ and $0 \leq k_{0y} \leq \pi d$; the numbers shown along the intervals ΓX and ΓY correspond to positions of the points of the grid rather than the values of k_{0x} and k_{0y}. Taken from McPhedran *et al.* (2009).

where $\mathcal{B}$ is a Bessel function of the type J or Y (see Abramowitz & Stegun, 1965). Movchan *et al.* (2007) demonstrated that this monopole approximation is good for cylinders of small radius, using an example with $a = 0.2$, $k_{0x} = \pi/40$ and $k_{0y} = 0$.

A particularly interesting observation arises when we take the limit as the radius a tends to zero in (2.64). The result is the simple equation

$$S_0^Y(\beta, \mathbf{k}_0) = -\frac{2}{\pi} S_0^K(\beta, \mathbf{k}_0), \tag{2.66}$$

which is used to produce the band diagram for a square lattice of clamped voids of zero radius (see Fig.4, Movchan *et al.* 2007). Movchan *et al.* (2007) make a number of important points regarding this band diagram, but the most striking feature is the full band gap below the first mode as already noted in the Introduction. The band surfaces corresponding to equation (2.66) may be constructed using numerical methods. McPhedran *et al.* (2009) did this by taking a grid of values of components of $\mathbf{k}_0$ avoiding symmetry lines, evaluating and placing in ascending order β values corresponding to plane waves, and then searching for zeros of equation (2.66) between those values. We reproduce some of those figures here.

In Fig. 2.15 we show the band surface and the equi-frequency contours for the lowest band surface, giving the data for the first quadrant in which both components of $\mathbf{k}_0$ are non-negative. Using conventional labels for points in the two-dimensional Brillouin zone Fig. 2.4(b), the origin (lower-left corner) is called Γ, the lower right corner is called X, the upper left corner is Y and the top right corner is M. Fig. 2.15(a) shows that the band has minima at X and Y, a maximum at M and a local maximum at Γ.

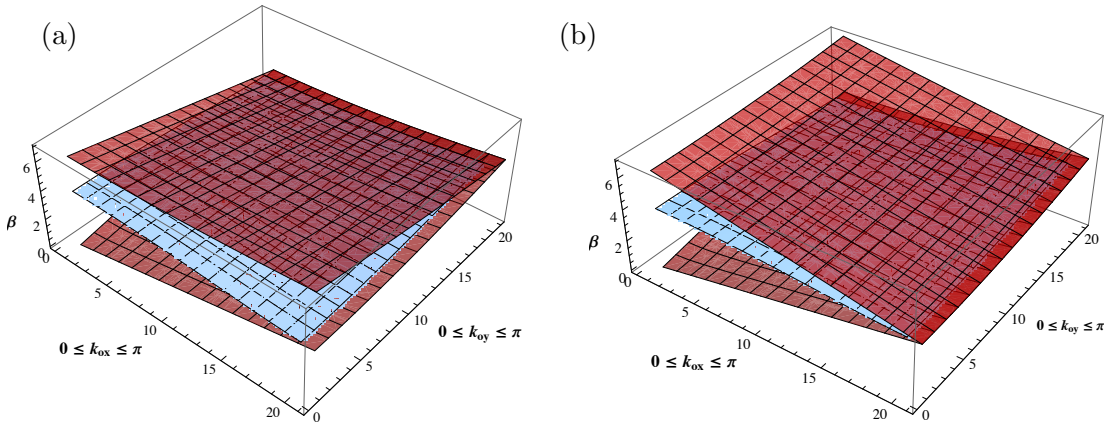

Figure 2.16: Two different views showing the "sandwiching" of the first band (blue) between the plane wave surfaces shown in red for orders $(0,0)$ and $(-1,0)$ in part(a), and $(0,0)$ and $(0,-1)$ in part (b).

In Fig. 2.15(b), we also notice the saddle point not far from where the diagonals ΓM and XY intersect, close to the edge $M\Gamma$ of the irreducible Brillouin zone Fig. 2.4(b).

The first band is confined between dispersion curves for plane waves (first noted by Movchan *et al.* 2007). This is shown explicitly in Fig. 2.16, taken from McPhedran *et al.* (2009). The plane wave surfaces referred to are called "light lines" in the study of photonic crystals, and here they correspond to singularities of the lattice sum S_0^Y. For more detail the reader should consult McPhedran *et al.* (2009) but the dispersion relation (2.66) requires S_0^Y to be equal to a quantity which is always finite because the lattice sums S_0^K have no poles. The only way the band surface can intersect a plane wave surface is for it to intersect two plane wave surfaces simultaneously, as indicated in Fig. 2.16. It approaches the intersection line of the plane wave surfaces in such a way that the singularities of S_0^Y, from these surfaces, balance each other.

2.6 Green's functions

The unit cell for the central void of a platonic grating is illustrated in Fig. 2.13(b). For the limiting case of the radius a tending to zero, we derive the quasi-periodic Green's function for the grating of rigid pins.

We begin with the expression for the Green's function for a biharmonic plate. Referring to the general equation

$$\Delta^2 G(\mathbf{x}) - \beta^4 G(\mathbf{x}) + \delta(\mathbf{r} - \mathbf{r}') = 0, \tag{2.67}$$

we employ the free-space Green's function quoted by McPhedran *et al.* (2009):

$$G(|\mathbf{r} - \mathbf{r}'|) = -\frac{1}{8\beta^2}\left(iH_0^{(1)}(\beta\rho) - \frac{2}{\pi}K_0(\beta\rho)\right), \tag{2.68}$$

where $\boldsymbol{\rho} = \mathbf{r} - \mathbf{r}'$ and $\rho = |\boldsymbol{\rho}|$. Here $H_0^{(1)}$ is the Hankel function of the first kind, of order 0 and K_0 is the modified Bessel function related by the equation $\pi i^{l+1} H_l^{(1)}(iz) = 2K_l(z)$. This Green's function is bounded at $\mathbf{r} = \mathbf{r}'$, rather than diverging logarithmically there as is the case for the two-dimensional Green's functions of the Helmholtz and modified Helmholtz equations. We may derive G by by taking the difference of the individual Green's functions for the Helmholtz and modified Helmholtz equations, whereupon the singularities cancel. We use a similar method for the quasi-periodic Green's function for a periodic grating within the biharmonic plate.

2.6.1 Quasi-periodic Green's function for an infinite grating of circular scatterers

The papers by Nicorovici and McPhedran (1994a,b) give the expression for a one-dimensional periodic array of sources that obeys the inhomogeneous Helmholtz equation:

$$(\Delta + \beta^2) G^H(x, y; \alpha_0) \;=\; \delta(y) \sum_{n=-\infty}^{\infty} \delta(x - nd) \exp\{i\alpha_0\, nd\}, \tag{2.69}$$

where β is the wave number of the medium, and d is the period of the grating. The quasi-periodicity factor is $\exp i\alpha_0 nd$. We summarise their analysis here, including a brief description of the application of Graf's addition theorem, before turning our attention to the modified Helmholtz operator. However we adopt a governing equation of the same form as (2.67):

$$(\Delta + \beta^2) G^H(x, y; \alpha_0) + \delta(y) \sum_{n=-\infty}^{\infty} \delta(x - nd) \exp\{i\alpha_0\, nd\} = 0. \tag{2.70}$$

The Green's function (spatial form) that solves equation (2.70) is

$$G^H(x, y; \alpha_0, \beta) \;=\; \frac{i}{4} \sum_{n=-\infty}^{\infty} H_0^{(1)}(\beta\sqrt{(x - nd)^2 + y^2}) \exp\{i\alpha_0\, nd\}, \tag{2.71}$$

where $H_0^{(1)}$ is the zeroth-order Hankel function of the first kind. The alternative expression is the spectral domain Green's function:

$$G^H(x, y; \alpha_0, \beta) \;=\; \frac{i}{2d} \sum_{n=-\infty}^{\infty} \frac{1}{\chi_n} e^{i(\alpha_n x + \chi_n |y|)}, \tag{2.72}$$

where

$$\alpha_n = \alpha_0 \,+\, nK \,=\, \alpha_0 + \frac{2\pi n}{d}, \tag{2.73}$$

$$\chi_n = \begin{cases} \sqrt{\beta^2 \,-\, {\alpha_n}^2} \;, & {\alpha_n}^2 \le \beta^2 \\ i\sqrt{{\alpha_n}^2 \,-\, \beta^2} \;, & {\alpha_n}^2 > \beta^2. \end{cases} \tag{2.74}$$

Equating (2.71) and (2.72) gives

$$\sum_{n=-\infty}^{\infty} H_0^{(1)}\left(\beta\sqrt{(x - nd)^2 + y^2}\right) e^{i\alpha_0\, nd} \;=\; \frac{2}{d} \sum_{n=-\infty}^{\infty} \frac{1}{\chi_n} e^{(\alpha_n x + \chi_n |y|)}. \tag{2.75}$$

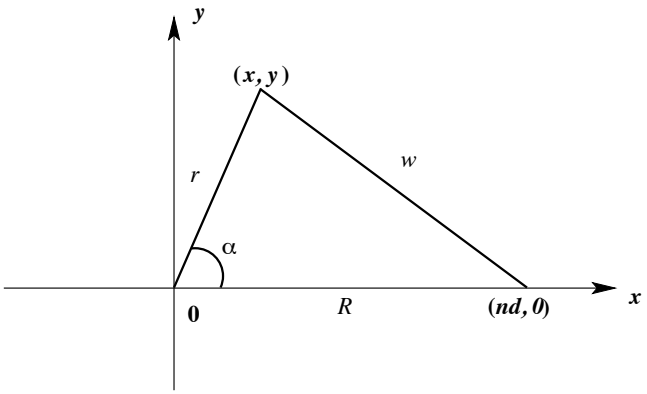

Figure 2.17: Triangle illustrating Graf's addition theorem for a platonic grating.

We apply Graf's addition theorem to expand the Hankel function in the vicinity of the origin. Referring to Section 2.5.4 and Abramowitz & Stegun (1965),

$$H_0^{(1)}(w) \;=\; \sum_{\kappa=-\infty}^{\infty} H_\kappa^{(1)}(u)\, J_\kappa(v) e^{i\kappa\alpha}, \tag{2.76}$$

where u, v and w are the magnitudes of the vectors $\mathbf{u}$, $\mathbf{v}$ and $\mathbf{w}$ that form three sides of a triangle, with α the angle between $\mathbf{u}$ and $\mathbf{v}$. An additional constraint is that $v < u$. Our triangle is illustrated in Fig. 2.17 and two of its vertices are the positions of rigid pins at the origin and $(nd, 0)$. The third vertex is (x, y) whose position vector we denote by $\mathbf{r}$ (equivalent to $\mathbf{v}$ in formula (2.76)). The pin $(nd, 0)$ has position vector $\mathbf{R}$ which corresponds to $\mathbf{u}$ in (2.76). Then $\mathbf{w} = \mathbf{R} - \mathbf{r}$ and $|\mathbf{w}| = w = \sqrt{(x - nd)^2 + y^2}$. Graf's addition theorem gives

$$H_0^{(1)}(\beta\sqrt{(x - nd)^2 + y^2}) \;=\; \sum_{\kappa=-\infty}^{\infty} H_\kappa^{(1)}(\beta\, nd)\, J_\kappa(\beta r) e^{i\kappa\, arg(\mathbf{r})}, \tag{2.77}$$

for $n > 0$. Denoting $\theta = arg(\mathbf{r})$, we replace $e^{i\kappa\theta}$ with $e^{i\kappa\theta}\,(-1)^\kappa$ for $n < 0$. Considering the case $n = 0$ separately, we replace the left hand side of the identity (2.75) with

$$H_0^{(1)}(\beta r) \;+ \sum_{n\neq 0} \sum_{\kappa=-\infty}^{\infty} H_\kappa^{(1)}(\beta\,|n|d)\, J_\kappa(\beta r) e^{i\kappa\, arg(n)}\, e^{i\kappa\theta}\, e^{i\alpha_0\, nd}, \tag{2.78}$$

where we have combined the cases of $n > 0$ and $n < 0$ using a Heaviside function:

$$e^{i\kappa\, arg(n)} = 1 \quad \text{or} \quad -1^\kappa$$

respectively. At the origin, all of the Bessel J functions vanish with the exception of J_0 which tends to 1. The lattice sums $S_\kappa(\alpha_0, \beta, d)$ for the Helmholtz operator have the definition:

$$S_\kappa^H(\alpha_0, \beta, d) \;=\; \sum_{n\neq 0} H_\kappa^{(1)}(\beta\,|n|d)\, e^{i\alpha_0\, nd}\, e^{i\kappa\, arg(n)}, \tag{2.79}$$

where the superscript H denotes Hankel type lattice sums.

For $n < 0$, we have $e^{i\kappa\pi} = (-1)^\kappa$, and for $n > 1$, we have $e^{i\kappa 0} = 1$. The lattice sums can be written in the form

$$S_\kappa^H = \sum_{n=1}^{\infty} H_\kappa^{(1)}(\beta\, nd)\, e^{i\alpha_0\, nd} + \sum_{n=-\infty}^{-1} H_\kappa^{(1)}(\beta\, |n|d)\, e^{i\alpha_0\, nd}\,(-1)^\kappa \tag{2.80}$$

$$= \sum_{n=1}^{\infty} H_\kappa^{(1)}(\beta\, nd)\, e^{i\alpha_0\, nd} + \sum_{n=1}^{\infty} H_\kappa^{(1)}(\beta\, nd)\, e^{-i\alpha_0\, nd}\,(-1)^\kappa \tag{2.81}$$

$$= \sum_{n=1}^{\infty} H_\kappa^{(1)}(\beta\, nd)\{[1+(-1)^\kappa]\cos(\alpha_0 nd) + i[1-(-1)^\kappa]\sin(\alpha_0 nd)\}. \tag{2.82}$$

We can then split the sums into even and odd parts.

$$S_{2\kappa}^H(\alpha_0,\beta,d) = 2\sum_{n=1}^{\infty} H_{2\kappa}^{(1)}(\beta\, nd)\cos(\alpha_0 nd), \tag{2.83}$$

$$S_{2\kappa+1}^H(\alpha_0,\beta,d) = 2i\sum_{n=1}^{\infty} H_{2\kappa+1}^{(1)}(\beta\, nd)\sin(\alpha_0 nd). \tag{2.84}$$

Nicorovici & McPhedran (1994b) proceed to derive recurrence relations for the lattice sums S^J and S^Y using equation (2.75) and the Poisson addition formula. We discuss grating sums in more detail in Sections 3.1.3 and A.1, but we may express the quasi-periodic Green's function for the Helmholtz operator, using (2.78), in the following form:

$$G^H(x,y;\alpha_0,\beta) = \frac{i}{4}\left(H_0^{(1)}(\beta r) + \sum_{\kappa=-\infty}^{\infty} S_\kappa^H(\alpha_0,\beta,d) J_\kappa(\beta r) e^{i\kappa\theta}\right). \tag{2.85}$$

We now consider the lattice sums involving Bessel K functions that arise from the modified Helmholtz operator:

$$(\Delta - \beta^2)G^M(x,y;\alpha_0,\beta) + \delta(y)\sum_{n=-\infty}^{\infty}\delta(x-nd)\exp\{i\alpha_0\, nd\} = 0. \tag{2.86}$$

Recalling equation (2.76) for the Hankel function, we would like to expand the term $K_0(\beta\sqrt{(x-nd)^2+y^2})$ in a similar way. We replace u, v and w with iU, iV and iW, and use the relations between $H_l^{(1)}(iz)$ and $K_l(z)$, and $J_l(iz)$ and $I_l(z)$ i.e.

$$\begin{aligned} H_0^{(1)}(iz) &= \frac{2}{i\pi}K_0(z), \\ \frac{\pi}{2}i^{l+1}H_l^{(1)}(iz) &= K_l(z), \\ i^{-l}J_l(iz) &= I_l(z). \end{aligned} \tag{2.87}$$

Equation (2.76) becomes

$$H_0^{(1)}(iW) = \sum_{l=-\infty}^{\infty} H_l^{(1)}(iU)\, J_l(iV) e^{il\alpha}.$$

The substitution of the identities (2.87) yields

$$\frac{2}{\pi i}K_0(W) \;=\; \sum_{l=-\infty}^{\infty} \frac{2}{\pi} i^{-(l+1)} K_l(U)\, I_l(V)\, i^l\, e^{il\alpha},$$

which simplifies to

$$K_0(W) \;=\; \sum_{l=-\infty}^{\infty} K_l(U) I_l(V) e^{il\alpha}, \tag{2.88}$$

an expression with the same structure as the Hankel function expansion (2.76).

The application of Graf's addition theorem for the Bessel function K_0 produces results consistent with those obtained for the Hankel function. Thus we have

$$K_0(\beta\sqrt{(x-nd)^2+y^2}) \;=\; \sum_{l=-\infty}^{\infty} K_l^{(1)}(\beta\,|n|d)\, I_l(\beta r) e^{il\,arg(n)}\, e^{il\theta}, \tag{2.89}$$

from which we can define the lattice sums for the Bessel K functions as follows

$$S_{2l}^K(\alpha_0,\beta,d) \;=\; 2\sum_{n=1}^{\infty} K_{2l}(\beta\, nd)\cos(\alpha_0 nd), \tag{2.90}$$

$$S_{2l+1}^K(\alpha_0,\beta,d) \;=\; 2i\sum_{n=1}^{\infty} K_{2l+1}(\beta\, nd)\sin(\alpha_0 nd). \tag{2.91}$$

We may then express the quasi-periodic Green's function for the modified Helmholtz equation (2.86) in the following way:

$$G^M(x,y;\alpha_0,\beta) \;=\; \frac{1}{2\pi}\left(K_0(\beta r) \;+\; \sum_{l=-\infty}^{\infty} S_l^K(\alpha_0,\beta,d) I_l(\beta r) e^{il\theta}\right). \tag{2.92}$$

The quasi-periodic Green's function for a grating of periodically spaced rigid pins is of the form

$$G(x,y;\alpha_0) = \sum_{n=-\infty}^{\infty} g(\mathbf{r}-\mathbf{r'},y)\, e^{i\alpha_0 nd}, \tag{2.93}$$

where $\mathbf{r} = (x,y)$ and $\mathbf{r'} = (nd,0)$. It solves the equation

$$(\Delta^2 - \beta^4)G(x,y;\alpha_0,\beta) \;+\; \delta(y)\sum_{n=-\infty}^{\infty}\delta(x-nd)\exp\{i\alpha_0\, nd\} = 0. \tag{2.94}$$

We may express G as the difference of the Green's function for the Helmholtz part G^H (2.85) and the Green's function for the modified Helmholtz part G^M (2.92), $G = C(G^H - G^M)$, where C is a constant.

Using $H_0^{(1)}(z) \;=\; J_0(z) + iY_0(z)$, we may write

$$G_H(r;\alpha_0,\beta) \;=\; \frac{i}{4}J_0(\beta r) - \frac{1}{4}Y_0(\beta r) + \frac{i}{4}\sum_l J_l(\beta r) e^{il\theta}\, S_l^H(\beta,\alpha_0),$$

and for the limiting case of the radius r tending to zero i.e. rigid pins, only the neighbourhood of $r = 0$ is important. We have

$$G_H(r;\alpha_0,\beta) \simeq \frac{i}{4} - \frac{\gamma}{2\pi} - \frac{1}{2\pi}\log\left(\frac{\beta r}{2}\right) + \frac{i}{4}S_0^H.$$

For the modified Helmholtz equation, we have

$$G_M(r;\alpha_0,\beta) \simeq -\frac{\gamma}{2\pi} - \frac{1}{2\pi}\log\left(\frac{\beta r}{2}\right) + \frac{1}{2\pi}S_0^K.$$

Combining these representations, we obtain

$$G(r;\alpha_0,\beta) = -\frac{1}{2\beta^2}\left(\frac{i}{4} + \frac{i}{4}S_0^H - \frac{1}{2\pi}S_0^K\right). \tag{2.95}$$

The constant $C = -1/2\beta^2$ is determined by using more terms in the expansions because the log terms cancel in equation (2.95). Writing G_H, G_M in the forms

$$G_H(r;\alpha_0,\beta) = \frac{i}{4}J_0(\beta r) - \frac{1}{4}Y_0(\beta r) + \frac{i}{4}S_0^H J_0(\beta r) + O(\beta r) + \dots,$$

$$G_M(r;\alpha_0,\beta) = \frac{1}{2\pi}K_0(\beta r) + \frac{1}{2\pi}I_0(\beta r)S_0^K + O(\beta r) + \dots, \tag{2.96}$$

we obtain the expansion for $G_H - G_M$ by implementing the formulae from Abramowitz & Stegun (1965) for the expansions of the Bessel functions J_0, Y_0 and modified Bessel functions I_0, K_0:

$$\begin{aligned}
J_0(\beta r) &= 1 - \frac{(\beta r)^2}{4} + O((\beta r)^4), \quad I_0(\beta r) = 1 + \frac{(\beta r)^2}{4} + O((\beta r)^4),\\
Y_0(\beta r) &= \frac{2}{\pi}\left(\log\left(\frac{\beta r}{2}\right) + \gamma\right)\left(1 - \left(\frac{\beta r}{2}\right)^2\right) + \frac{2}{\pi}\left(\frac{\beta r}{2}\right)^2 + O((\beta r)^4),\\
K_0(\beta r) &= -\left(\log\left(\frac{\beta r}{2}\right) + \gamma\right)\left(1 + \left(\frac{\beta r}{2}\right)^2\right) + \left(\frac{\beta r}{2}\right)^2 + O((\beta r)^4).
\end{aligned} \tag{2.97}$$

After some simplification, we obtain

$$\frac{i}{4} - \frac{i(\beta r)^2}{16} + \frac{1}{4\pi}\left(\log\left(\frac{\beta r}{2}\right) + \gamma\right)(\beta r)^2 - \frac{(\beta r)^2}{4\pi}, \tag{2.98}$$

which may be expressed in the form

$$\frac{i}{4} - \frac{1}{4\pi}(\log 2 - \log(\beta r) - \gamma + i/4 + 1)(\beta r)^2. \tag{2.99}$$

The only non-trivial term after the application of the Laplacian operator twice will be that arising from $\log(\beta r)$. Therefore the crucial term is

$$\frac{C\beta^2}{4\pi}r^2\log(\beta r),$$

where C is the constant to be determined, such that

$$\Delta^2\left[\frac{C\beta^2}{4\pi}r^2\log(\beta r)\right] \to -\delta(\mathbf{r}). \tag{2.100}$$

Here the Laplacian operator Δ is defined by

$$\Delta = \frac{\partial^2}{\partial r^2} + \frac{1}{r}\frac{\partial}{\partial r}.$$

Using the fact that the fundamental Green's function for this Laplacian operator is $-\log r/2\pi$, and the observation that

$$\Delta\left[\frac{r^2\log(\beta r)}{8\pi}\right] = \frac{\log r}{2\pi} + \frac{\beta + \log\beta}{2\pi}, \tag{2.101}$$

we determine C from the equation

$$-\frac{C\beta^2}{4\pi} = \frac{1}{8\pi}. \tag{2.102}$$

i.e. $C = -1/2\beta^2$, and we obtain equation (2.95).

The spectral form of the Green's function is

$$G(x,y;\alpha_0,\beta) = \frac{1}{2\beta^2}\left(\frac{1}{2id}\sum_{n=-\infty}^{\infty}\frac{1}{\chi_n}e^{i(\alpha_n x + \chi_n|y|)} + \frac{1}{2d}\sum_{n=-\infty}^{\infty}\frac{1}{\tau_n}e^{i\alpha_n x}\,e^{-\tau_n|y|}\right), \tag{2.103}$$

where

$$\alpha_n = \alpha_0 + \frac{2\pi n}{d}, \tag{2.104}$$

$$\chi_n = \begin{cases} \sqrt{\beta^2 - {\alpha_n}^2}\ , & {\alpha_n}^2 \le \beta^2, \\ i\sqrt{{\alpha_n}^2 - \beta^2}\ , & {\alpha_n}^2 > \beta^2, \end{cases} \tag{2.105}$$

$$\tau_n = \sqrt{\beta^2 + \alpha_n^2}. \tag{2.106}$$

The spatial form (2.95) is used in the Rayleigh method that we adopt to solve the scattering of a plane wave by a platonic grating stack, whilst the spectral version (2.103) is implemented when we use a waveguide approach. The spatial form incorporates cylindrical Bessel functions and grating sums, and the spectral form involves plane wave representations.

Chapter 3

Method of solution for a platonic grating stack

The basic building block of the work described in this chapter is a method for the solution of the problem for the scattering of plane waves by a grating of circular voids. This is extended using a recurrence procedure to give the solution for any finite number of platonic gratings. The results of the recurrence algorithm are reflection and transmission matrices that characterise the filtering of plane waves by the structured system. The general method involves deriving multipole expansions and the corresponding Rayleigh identities. We discussed these techniques for the homogeneous problem for a doubly periodic square array in Sections 2.5.2 - 2.5.4. There are differences that arise because of the introduction of a plane wave incident field, and between the singly and doubly periodic arrays. We also refer to the book by Movchan *et al.* (2002), where the dynamic generalised Rayleigh method for doubly periodic structures is described in great detail, and we use some of the techniques outlined.

The scattered field solution relies on the fact that we may express the flexural wave function (i.e. the out-of-plane displacement) in terms of both plane wave expansions (equations (2.6)-(2.12) in Section 2.2) and multipole expansions composed of cylindrical harmonics (equations (2.43), (2.44) in Section 2.5.2). The expressions and calculations are greatly simplified for the special case of rigid pins, which is of particular importance in the rest of this thesis. We use Rayleigh identities to align the consistency of the multipole expansions about individual cylinders with the Bloch quasi-periodicity condition (Section 2.3) used to describe an individual grating. Reconstruction equations are then derived to convert the multipole coefficients back to plane wave coefficients consistent with our initial plane wave expansion.

We subsequently developed an alternative approach, where we consider a single grating of rigid pins as a line of point forces with constant separation d. We use a quasi-periodic Green's function $G(x, y; \alpha_0, \beta)$ for the biharmonic operator (2.95),(2.103) satisfying the equation (2.94). Our general structure consists of a pair of layered stacks (LS) sandwiching a symmetry-breaking layer (SBL), shown in Fig. 3.1. The identical

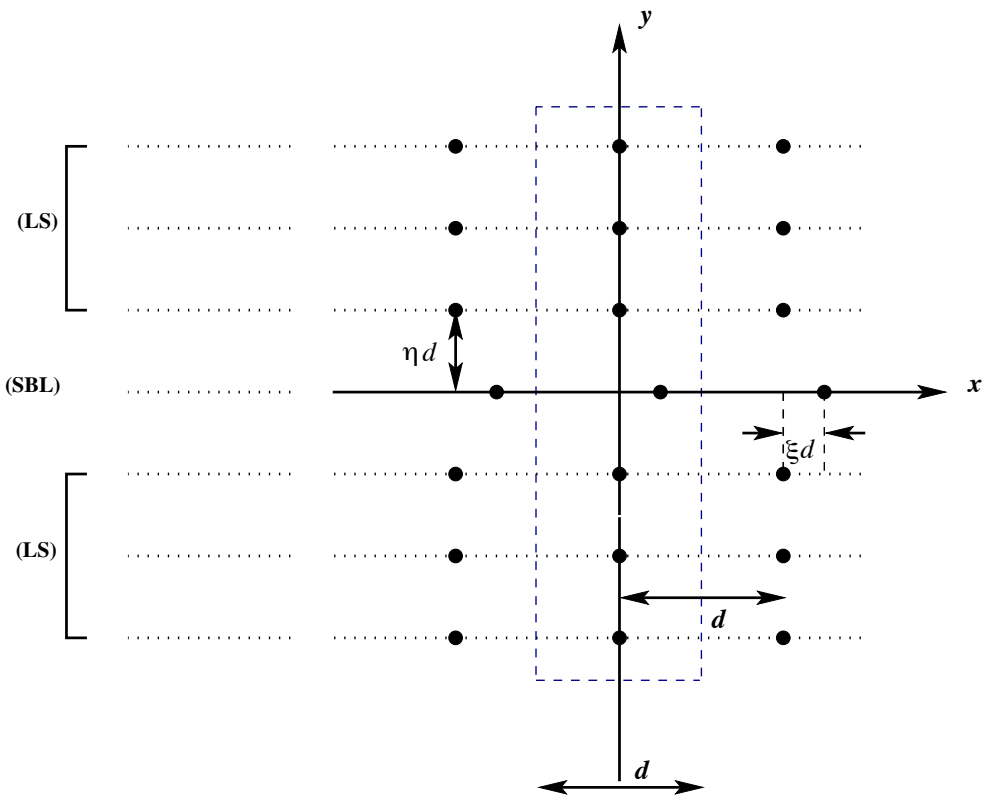

Figure 3.1: Example of a multiple-grating waveguide. The elementary cell is indicated by the dashed rectangle.

layered stacks contain a finite number of periodic gratings N and act as symmetric mirrors. Note that with the mirror systems chosen to preserve up-down symmetry, there is always an odd number of layers. Of course the simplest example is when $N = 1$, producing a triplet, which is discussed in detail in Chapter 6, and is briefly outlined below in Section 3.3.

We study the flexural wave modes existing in these finite stacks of gratings containing zero-radius pins. By solving the associated eigenvalue problem, we group the modes into even and odd classes, and derive dispersion equations for each. The dispersion curves for modes are trajectories along which the eigenvalues are zero, and these Bloch modes correspond to the transmission resonances that we observe for the analogous scattering problem. By combining the two methods, we define an efficient algorithm to design structures for which the EDIT interaction (mentioned in the Introduction and discussed in Section 2.4.5) may be steered over a wide range of frequencies and angles.

3.1 Multipole method

The cornerstone of a multipole method is an ingenious field identity, named after Lord Rayleigh who first employed it in 1892 in a problem involving the Laplace equation, and lattices of either cylinders or spheres. The Rayleigh identity (discussed in Section 2.5.4 for the doubly periodic square array) relates the regular field in the vicinity of an individual scatterer to fields radiated by the array's other scatterers and any external sources. A key element is the implementation of lattice sums for periodic systems, whereby the sums account for each point of the array. Here we employ grating sums rather than the lattice sums used for the two-dimensional array of Section 2.5. Difficulties arise through the occurrence of conditionally convergent series over the direct lattice.

Multipole techniques have been used extensively since the 1970's in particular for dynamic problems in electromagnetism and solid mechanics for periodic systems. We reviewed the problem for a doubly periodic square array of cylindrical voids within a thin infinite elastic plate in Section 2.5. The spectral problem for the biharmonic operator was solved in the form of a dispersion equation. Here we adapt those multipole methods to a scattering problem for the interaction of a plane incident wave with a finite number of platonic gratings embedded in a thin biharmonic plate.

The basic governing equations are the same as (2.2), (2.41), (2.42) but we repeat them here for the convenience of the reader. However the presence of an incident wave leads to important differences in the method of solution, most notably the use of reconstruction equations to convert multipole representations to plane wave expansions. General plane wave expansions for both the incident field and the scattered field were given in Section 2.2, taking into account the distinction between Helmholtz and modified Helmholtz type waves. We use Bessel and modified Bessel functions to determine multipole expansions, one for Helmholtz and one for modified Helmholtz type, in the vicinity of the central cylinder. We substitute the boundary conditions into these expansions, obtaining identities for the multipole coefficients.

We derive Rayleigh identities to account for the rest of the array, meshing the multipoles with the periodicity of the grating, via the quasi-periodicity condition (2.14). This involves using Green's theorem and Graf's addition formula (see Sections 2.5.4 and 2.6.1). The Rayleigh identities are uncoupled for Helmholtz and modified Helmholtz type waves, but the necessary coupling is provided using the boundary conditions. The result is an inhomogeneous algebraic system which is truncated and solved to find the unknown multipole coefficients. Once these have been established, we derive reconstruction equations in Section 3.1.4 to transform these coefficients back to plane wave coefficients which are used to derive the scattering matrices we seek.

3.1.1 Governing equations

The governing equations and accompanying explanations were presented by Movchan *et al.* (2009) and Haslinger *et al.* (2012). We repeat them here for the convenience of the reader. The flexural displacement $w(\mathbf{x};t) = W(\mathbf{x})\exp(i\omega t)$ is considered to be time-harmonic of radian frequency ω, and its amplitude W satisfies the following equation

$$\Delta^2 W(\mathbf{x}) - \beta^4 W(\mathbf{x}) = 0, \tag{3.1}$$

with $\beta^2 = \omega\sqrt{\rho h/D}$. We also note that the flexural rigidity of the plate is denoted by $D = Eh^3/(12(1-\nu^2))$, where h stands for the thickness of the plate, ρ is the mass density, E is the Young modulus and ν is the Poisson ratio.

The solution of equation (3.1) can be divided into two parts W_H and W_M (see equation (2.41)), which satisfy the Helmholtz equation and its counterpart form the modified Helmholtz equation:

$$(\Delta + \beta^2)W_H = 0 \quad \text{and} \quad (\Delta - \beta^2)W_M = 0. \tag{3.2}$$

Hence

$$W(\mathbf{x}) = W_H(\mathbf{x}) + W_M(\mathbf{x}), \tag{3.3}$$

with W_H containing both propagating and evanescent waves, and W_M consisting entirely of evanescent waves. For each rigid inclusion, the boundary conditions are

$$W\Big|_{r=a} = 0, \quad \frac{\partial W}{\partial r}\Big|_{r=a} = 0, \tag{3.4}$$

where r represents the distance from the centre of the inclusion. Physically the above boundary conditions represent clamping on the rigid boundary. In particular, when the radius a tends to zero we retrieve the case of fixed pins discussed by Evans & Porter (2007), Movchan *et al.* (2009) and Haslinger *et al.* (2012).

A plane incident wave is propagating towards the grating in the upper half-plane. We need to consider two cases, the first dealing with an incident wave of the Helmholtz type, with amplitude $\mathcal{A}_H$:

$$W_{i,H}(\mathbf{x}) = \frac{\mathcal{A}_H}{\sqrt{|\chi_0|}}\exp\{\mathrm{i}(\alpha_0 x - \chi_0 y)\}, \tag{3.5}$$

where $\alpha_0^2 + \chi_0^2 = \beta^2$ and α_0 is the Bloch parameter, $\alpha_0 = \beta\sin\theta_i$, with θ_i being the angle of incidence (see Fig. 2.1). The second case treats an incident wave of modified Helmholtz type, with amplitude $\mathcal{A}_M$:

$$W_{i,M}(\mathbf{x}) = \frac{\mathcal{A}_M}{\sqrt{|\hat{\chi}_0|}}\exp\{\mathrm{i}(\alpha_0 x - \hat{\chi}_0 y)\}, \tag{3.6}$$

where this wave is always evanescent so that $\alpha_0^2 + \hat{\chi}_0^2 = -\beta^2$, $\hat{\chi}_0 = i\tau_0$, $\tau_0 > 0$.

The periodicity of the structure in the horizontal direction and the parameters of the incident wave are represented by the quasi-periodicity condition for W along the horizontal axis (see Section 2.3):

$$W(\mathbf{x} + pd\mathbf{e}^{(1)}) = W(\mathbf{x})e^{i\alpha_0 pd}, \tag{3.7}$$

where p is an integer and d is the period.

3.1.2 Multipoles

We now sketch the method used to treat the scattering of the plane incident waves, either of the Helmholtz type (3.5) or of the modified Helmholtz type (3.6), by a grating of inclusions of radius a. The flexural displacement W can be expanded for $y > a$ and $y < -a$ in terms of sums of plane waves (W_H) and modified plane waves (W_M). Above the grating the expansion has a down-going incident wave term and up-going reflected waves with amplitudes R_p and $\hat{R}_p$, for the respective wave types. Below the grating the amplitudes of the down-going transmitted waves are denoted by T_p and $\hat{T}_p$ (see Fig. 2.2). The plane wave expansions are given by (2.9)-(2.12) in Section 2.2.

In order to connect the two types of expansions we introduce multipole expressions for W in the region $-a \leq y \leq a$. The multipole expansion for W_H involves cylindrical waves $J_n(\beta r)e^{\mathrm{i}n\theta}$ and $H_n^{(1)}(\beta r)e^{\mathrm{i}n\theta}$ with respective amplitudes A_n and E_n:

$$W_H(\mathbf{x}) = \sum_{n=-\infty}^{\infty} \{A_n J_n(\beta r) + E_n H_n^{(1)}(\beta r)\}e^{in\theta}. \tag{3.8}$$

The multipole expansion for W_M involves modified Bessel function terms $I_n(\beta r)e^{\mathrm{i}n\theta}$ and $K_n(\beta r)e^{\mathrm{i}n\theta}$ with respective amplitudes B_n and F_n:

$$W_M(\mathbf{x}) = \sum_{n=-\infty}^{\infty} \{B_n I_n(\beta r) + F_n K_n(\beta r)\}e^{in\theta}. \tag{3.9}$$

The amplitudes A_n, B_n, E_n, F_n are the multipole coefficients to be determined, and they are related by the boundary conditions (3.4):

$$A_n J_n(\beta a) + E_n H_n^{(1)}(\beta a) + B_n I_n(\beta a) + F_n K_n(\beta a) = 0, \tag{3.10}$$

$$A_n J_n'(\beta a) + E_n H_n^{(1)\prime}(\beta a) + B_n I_n'(\beta a) + F_n K_n'(\beta a) = 0. \tag{3.11}$$

The Bessel function expansions from Abramowitz & Stegun (1965) will be needed for the incident fields of both the Helmholtz type:

$$W_{i,H}(r\cos\theta, r\sin\theta) = \frac{\mathcal{A}_H}{\sqrt{|\chi_0|}} \sum_{l=-\infty}^{\infty} J_l(\beta r)e^{il\theta} i^l \Big(\frac{\alpha_0 + i\chi_0}{\beta}\Big)^l, \tag{3.12}$$

with χ_0 real and positive for a propagating wave, and χ_0 pure imaginary with positive imaginary part for an evanescent wave, and the modified Helmholtz type:

$$W_{i,M}(r\cos\theta, r\sin\theta) = \frac{\mathcal{A}_M}{\sqrt{|\hat{\chi}_0|}} \sum_{l=-\infty}^{\infty} I_l(\beta r)e^{il\theta} i^l \Big(\frac{\alpha_0 + i\hat{\chi}_0}{\beta}\Big)^l, \tag{3.13}$$

with $\hat{\chi}_0$ being imaginary with positive imaginary part. Here we have used formula 9.1.41 from Abramowitz & Stegun (1965):

$$e^{\frac{1}{2}\beta r(t-1/t)} = \sum_{l=-\infty}^{\infty} J_l(\beta r)t^l, \quad t \neq 0. \tag{3.14}$$

For the incident field (3.5), we set

$$i(\alpha_0 x - \chi_0 y) = \frac{1}{2}\beta r(t - 1/t) \iff \frac{2i}{\beta}(\alpha_0 \cos\theta - \chi_0 \sin\theta) = \frac{t^2-1}{t},$$

where we have used $x = r\cos\theta$ and $y = r\sin\theta$. Thus,

$$t^2 - \frac{2i}{\beta}(\alpha_0 \cos\theta - \chi_0 \sin\theta)t - 1 = 0,$$

and using equation (2.23) for $p = 0$, we obtain

$$t_{\mp} = \frac{1}{\beta}[i\alpha_0(\cos\theta \pm i\sin\theta) - \chi_0(\pm\cos\theta + i\sin\theta)]. \tag{3.15}$$

It follows that

$$t_- = \frac{1}{\beta}[e^{i\theta}(i\alpha_0 - \chi_0)] \iff t_- = e^{i\theta} i\left(\frac{\alpha_0 + i\chi_0}{\beta}\right), \tag{3.16}$$

which explains how we obtain (3.12) from (3.14). The expression (3.13) is obtained similarly.

As in Section 2.5.2, the above series expansions for W (3.8), (3.9) converge only in the region between the central cylinder (i.e. when $x = 0$) and the circle touching its two nearest neighbours (see Fig. 2.14 although the periodicity in our problem is in the horizontal direction only). Therefore the annulus of convergence may be described using the inequality

$$a \leq r \leq (d - a).$$

Provided that $a \leq d(1 - 1/\sqrt{2})$, the expansion covers the entire unit cell shown in Fig. 3.2. We also mention here that the derivation of the Rayleigh identity requires only that there exists a circle between the boundaries of the cylinder and the unit cell i.e. $r < d/2$ (Movchan *et al.* 2007). Of course as r increases towards $d/2$, the number of multipole terms required in the series (3.8) and (3.9), for an accurate solution, increases.

3.1.3 Rayleigh identities

The next step is to write down the Rayleigh identity, which expresses the part of the expansion for W which is regular near the origin (i.e. the terms involving the Bessel functions J_n and I_n) as sums over the part which is irregular near the origin (i.e. the terms involving $H_n^{(1)}$ and K_n), together with a term representing the expansion of the incident wave in multipoles. While we refer to Section 2.5.4 and Movchan *et al.* (2007),

here the Rayleigh equations are written with the use of the appropriate grating lattice sums in place of the doubly periodic array lattice sums. For a single periodic grating, the wave satisfies the Bloch-Floquet condition (3.7) along the grating, and the effect of interaction between the inclusions within the grating is represented via the grating sums.

The grating sums used in this thesis are denoted by $S_{l-n}^{(K,G)}$ and $S_{l-n}^{(H,G)}$, and consist of K-type modified Bessel functions and Hankel functions. The superscript G is used to denote that these are grating sums rather than those for the two-dimensional case. We defined them in Section 2.6.1, equations (2.83), (2.84) and equations (2.90), (2.91), and Movchan *et al.* (2009) expressed them in the same form. For convenience, we repeat them here. The sums over even and odd integers are expressed separately;

$$S_{2l}^{(K,G)}(\beta,\alpha_0) \;=\; 2\sum_{p=1}^{\infty} K_{2l}(\beta p)\cos(\alpha_0 p), \tag{3.17}$$

$$S_{2l+1}^{(K,G)}(\beta,\alpha_0) \;=\; 2i\sum_{p=1}^{\infty} K_{2l+1}(\beta p)\sin(\alpha_0 p), \tag{3.18}$$

are the K-type sums. These are evaluated by direct summation, since they are exponentially convergent. Note that l can be positive or negative which is consistent with the structure of the gratings sums featured in the Rayleigh system below (3.26) and (3.27). The grating sums over Hankel functions are of the form:

$$S_{2l}^{(H,G)}(\beta,\alpha_0) \;=\; 2\sum_{p=1}^{\infty} H_{2l}^{(1)}(\beta p)\cos(\alpha_0 p), \tag{3.19}$$

$$S_{2l+1}^{(H,G)}(\beta,\alpha_0) \;=\; 2i\sum_{p=1}^{\infty} H_{2l+1}^{(1)}(\beta p)\sin(\alpha_0 p). \tag{3.20}$$

As Movchan *et al.* (2009) mentioned, these sums are not exponentially convergent but are oscillatory, and would require an excessive number of terms to observe convergence.

We use accelerated convergence formulae based on those derived by Twersky (1961) for the Schlömich series:

$$\mathcal{H}_n \;=\; \sum_{p=1}^{\infty} H_n(p\beta)\,[\exp\{ip\,\beta\sin\theta_i\}(-1)^n \;+\; \exp\{-ip\,\beta\sin\theta_i\}], \tag{3.21}$$

where $\beta\sin\theta_i = \alpha_0$ in our formulation. In Appendix A.1, we outline the convergence formulae and explain, with the aid of illustrative examples, the necessity for their use.

The Bessel function expansions for the central cylinder $x = 0$ are related to similar expansions in the vicinity of any other cylinder $x = pd$ in the periodic grating, by the Bloch factor, where d is the period of the grating. We derive two types of consistency relations between the local expansions in the vicinity of a general inclusion, and the inclusion in the central cell with boundary C_0 in Fig. 3.2. One describes Helmholtz

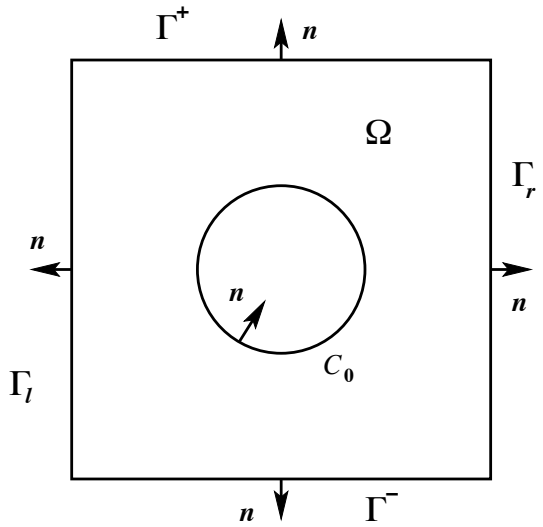

Figure 3.2: The unit cell Ω containing a circular scatterer. The boundary $\partial\Omega$ is the union of its constituent parts: $\partial\Omega = \Gamma^+ \cup \Gamma^- \cup \Gamma_l \cup \Gamma_r \cup C_0$. We also indicate the unit outward normals $\boldsymbol{n}$ for each part of the boundary.

type waves, and the other accounts for modified Helmholtz type waves. These Rayleigh identities are derived in the standard way using Green's theorem and Graf's addition formula (see Movchan *et al.* (2002), Botten *et al.* (2003), Movchan *et al.* (2007), Movchan *et al.* (2009) and Haslinger *et al.* (2012)).

The Green's function G that we outlined in Section 2.6.1 (see equations (2.95)-(2.103)) obeys the same quasi-periodicity condition as the displacement fields W_H and W_M, so it automatically satisfies (3.7), and a conjugate condition on its second variable:

$$G(\mathbf{r} + pd\mathbf{e}^{(1)};\, \mathbf{r}') \;=\; G(\mathbf{r};\, \mathbf{r}')\, e^{i\alpha_0 pd},$$

$$G(\mathbf{r};\, \mathbf{r}' + pd\mathbf{e}^{(1)}) \;=\; G(\mathbf{r};\, \mathbf{r}')\, e^{-i\alpha_0 pd}. \tag{3.22}$$

This quasi-periodic Green's function is a sum of an infinite set of outgoing waves which emanate from each point of the grating. To derive the Rayleigh identities, we apply Green's theorem within the unit cell (see Fig. 3.2), in the region Ω, to the two Bessel function expansions W and G, where W is either W_H or W_M:

$$\int_\Omega (W\Delta^2 G - G\Delta^2 W)d\mathbf{x} = \int_{\partial\Omega} \left(\Delta W \frac{\partial G}{\partial n} - G\frac{\partial}{\partial n}(\Delta W) + W\frac{\partial}{\partial n}(\Delta G) - \Delta G \frac{\partial W}{\partial n} \right) ds. \tag{3.23}$$

For the two vertical parts of the boundary Γ_l and Γ_r, the Bloch quasi-periodicity condition leads to cancellation, since the outward normals have opposite directions. For the top and bottom sides of the boundary Γ^+ and Γ^- respectively, we use the plane wave expansions for the incident waves, and on the interior boundary C_0, we substitute the Bessel function expansion for W, and expand the Green's function in coordinates

centred on the origin. Once these integrals have been determined, we can evaluate expressions for the coefficients linking the representations for the displacement field W.

The connection between the two sets of coefficients A_n, B_n and E_n, F_n is given by the equations:

$$B_n = \sum_{l=-\infty}^{\infty} (-1)^l S_{l-n}^{(K,\,G)}(\beta, \alpha_0) F_l + \frac{\mathcal{A}_M}{\sqrt{|\hat{\chi}_0|}}\, i^n \left(\frac{\alpha_0 + i\hat{\chi}_0}{\beta}\right)^n, \tag{3.24}$$

$$A_n = \sum_{l=-\infty}^{\infty} (-1)^{l-n} S_{l-n}^{(H,\,G)}(\beta, \alpha_0) E_l + \frac{\mathcal{A}_H}{\sqrt{|\chi_0|}}\, i^n \left(\frac{\alpha_0 + i\chi_0}{\beta}\right)^n, \tag{3.25}$$

where the grating sums $S_{l-n}^{(K,\,G)}$ and $S_{l-n}^{(H,\,G)}$ are defined by equations (3.17) to (3.20). The sums are run over all cylinders in the grating apart from that at the origin, taking into account the phase differences between the multipole coefficients in different cylinders (see the quasi-periodicity condition (3.7)) and are re-expressed using the Graf addition theorem for Bessel functions (see Section 2.6.1 and Fig. 2.17). Various methods exist for evaluating them accurately (see Section A.1 where we discuss grating sums in greater detail, explaining how increased radius leads to more complexity in evaluating the higher-order sums).

The Rayleigh identities (3.24), (3.25) correspond respectively to the modified Helmholtz and Helmholtz equations. They are coupled by the boundary conditions (3.10), (3.11). The result is an inhomogeneous system of algebraic equations in the multipole coefficients E_l, F_l:

$$\begin{aligned}
&\sum_{l=-\infty}^{\infty} \Big[(-1)^{l-n} S_{l-n}^{(H,G)}(\beta, \alpha_0) J_n(\beta a) + \delta_{ln} H_n^{(1)}(\beta a)\Big] E_l \\
&+ \sum_{l=-\infty}^{\infty} \Big[(-1)^{l} S_{l-n}^{(K,G)}(\beta, \alpha_0) I_n(\beta a) + \delta_{ln} K_n(\beta a)\Big] F_l \\
&= -\Big[\frac{i^n \mathcal{A}_M}{\sqrt{|\hat{\chi}_0|}}\Big(\frac{\alpha_0 + i\hat{\chi}_0}{\beta}\Big)^n\Big] I_n(\beta a) - \Big[\frac{i^n \mathcal{A}_H}{\sqrt{|\chi_0|}}\Big(\frac{\alpha_0 + i\chi_0}{\beta}\Big)^n\Big] J_n(\beta a),
\end{aligned} \tag{3.26}$$

$$\begin{aligned}
&\sum_{l=-\infty}^{\infty} \Big[(-1)^{l-n} S_{l-n}^{(H,G)}(\beta, \alpha_0) J_n'(\beta a) + \delta_{ln} (H_n^{(1)})'(\beta a)\Big] E_l \\
&+ \sum_{l=-\infty}^{\infty} \Big[(-1)^{l} S_{l-n}^{(K,G)}(\beta, \alpha_0) I_n'(\beta a) + \delta_{ln} K_n'(\beta a)\Big] F_l \\
&= -\Big[\frac{i^n \mathcal{A}_M}{\sqrt{|\hat{\chi}_0|}}\Big(\frac{\alpha_0 + i\hat{\chi}_0}{\beta}\Big)^n\Big] I_n'(\beta a) - \Big[\frac{i^n \mathcal{A}_H}{\sqrt{|\chi_0|}}\Big(\frac{\alpha_0 + i\chi_0}{\beta}\Big)^n\Big] J_n'(\beta a).
\end{aligned} \tag{3.27}$$

This is known as the Rayleigh system for the problem, and is truncated and solved to evaluate a set of multipole coefficients.

We assume that the order of truncation L for the Rayleigh system (3.26), (3.27) is chosen according to the radius of the void. As mentioned in Section 2.5.4, Poulton *et al.* (2010) provide tables for selecting the number of multipoles to achieve converged

frequencies for a doubly periodic square array consisting of perforations with non-zero radii. These tables, which link the radius of the hole to the number of necessary multipoles, are applicable to the stacks of gratings studied here. We provide a convergence table for a platonic triplet in Chapter 5. The multipole summation runs from $-L$ to L ($2L+1$ terms). The accuracy of the solution to the system depends on the precision with which we evaluate the incorporated grating sums. In the doubly periodic array, Movchan *et al.* (2007) recommended calculating the lattice sums over orders in the range $-2L$ to $2L$ ($4L+2$ terms), and we adopt the same strategy here.

3.1.4 Reconstruction equations

The multipole coefficients are used to evaluate plane wave amplitude coefficients for the fields above and below the grating, using reconstruction equations, originally derived by Movchan *et al.* (2009). The reconstruction equations are derived using the Rayleigh identities and Green's formula on the elementary cell in Fig. 3.2. Green's theorem (3.23) is applied to a test function $V_{m,H}$ or $V_{m,M}$ and the part of the total field corresponding to either the Helmholtz W_H or modified Helmholtz equation W_M. We begin with the Helmholtz part of the field, defining the test function as

$$V_{m,H} = \frac{1}{\sqrt{|\mu_m|}} \exp\{-i(\alpha_m x - \mu_m y)\}, \tag{3.28}$$

where m is an integer, and $\alpha_m^2 + \mu_m^2 = \beta^2$ as in equation (2.23). This is defined to have the opposite quasi-periodicity property (3.7) in the horizontal direction to the Helmholtz part of the total field (3.3). Thus, when we apply Green's theorem (3.23) to a rectangular cell with width d equal to the grating's period, and an arbitrary finite vertical length in the y-direction (Fig. 3.2), the rectangle's vertical sides Γ_l and Γ_r do not contribute to the Helmholtz part of the line integral:

$$\int_{\partial\Omega} \left\{ V_{m,H} \frac{\partial W_H}{\partial n} - W_H \frac{\partial V_{m,H}}{\partial n} \right\} dS = 0.$$

For the integrals I_+, I_- on Γ_+ and Γ_- respectively, we obtain

$$I_+ = \frac{-i\mathcal{A}_H d(\chi_0 + \mu_0)\delta_{m0}}{\sqrt{|\chi_0|}\sqrt{|\mu_0|}} e^{i(\mu_0 - \chi_0)y} + \frac{iR_m(\chi_m - \mu_m)d}{\sqrt{|\chi_m|}\sqrt{|\mu_m|}} e^{i(\mu_m + \chi_m)y}, \tag{3.29}$$

and

$$I_- = \frac{iT_m(\chi_m + \mu_m)d}{\sqrt{|\chi_m|}\sqrt{|\mu_m|}} e^{i(\mu_m - \chi_m)y}. \tag{3.30}$$

For the integral on C_0 we need to obtain the Bessel function expansions for the test function (3.28) using equation (3.14). Since this test function's exponent is of opposite sign to that of (3.5), it follows that

$$t_\mp^V = \frac{1}{\beta}[-i\alpha_m(\cos\theta \mp i\sin\theta) + \mu_m(i\sin\theta \mp \cos\theta)]. \tag{3.31}$$

Then

$$t_-^V = e^{-i\theta} i \left(\frac{-\alpha_m + i\mu_m}{\beta} \right), \tag{3.32}$$

and the Bessel function expansion of the test function $V_{m,H}$ is

$$V_{m,H}(\mathbf{x}) = \frac{1}{\sqrt{|\mu_m|}} \sum_{l=-\infty}^{\infty} J_l(\beta r) e^{-il\theta} \left(\frac{-\mu_m - i\alpha_m}{\beta} \right)^l. \tag{3.33}$$

For the integral on C_0, we require the derivatives

$$\frac{\partial V_{m,H}}{\partial r} = \frac{1}{\sqrt{|\mu_m|}} \sum_{l=-\infty}^{\infty} \beta J_l'(\beta r) e^{-il\theta} \left(\frac{-\mu_m - i\alpha_m}{\beta} \right)^l, \tag{3.34}$$

and, from (3.8),

$$\frac{\partial W_H}{\partial r} = \sum_{n=-\infty}^{\infty} [\beta A_n J_n'(\beta r) + \beta E_n (H_n^{(1)})'(\beta r)] e^{in\theta}. \tag{3.35}$$

We substitute these into

$$\int_{C_0} \left\{ -V_{m,H} \frac{\partial W_H}{\partial r} + W_H \frac{\partial V_{m,H}}{\partial n} \right\} r d\theta \, \Big|_{r=a} = I_{C_0}, \tag{3.36}$$

obtaining

$$\int_{\theta=0}^{2\pi} \left\{ \sum_{l=-\infty}^{\infty} \sum_{n=-\infty}^{\infty} \frac{\beta a}{\sqrt{|\mu_m|}} \left[-E_n J_l(\beta a)(H_n^{(1)})'(\beta a) + E_n J_l'(\beta a) H_n^{(1)}(\beta a) \right] \times \right.$$

$$\left. \times \left(\frac{-\mu_m - i\alpha_m}{\beta} \right)^l e^{-il\theta} e^{in\theta} \right\} d\theta, \tag{3.37}$$

where the A_n terms have cancelled. Using the fact that

$$\int_{\theta=0}^{2\pi} e^{-il\theta} e^{in\theta} d\theta = 2\pi \delta_{ln},$$

we obtain

$$I_{C_0} = \sum_{l=-\infty}^{\infty} \frac{\beta a}{\sqrt{|\mu_m|}} \left[-E_l J_l(\beta a)(H_l^{(1)})'(\beta a) + E_l J_l'(\beta a) H_l^{(1)}(\beta a) \right] \left(\frac{-\mu_m - i\alpha_m}{\beta} \right)^l 2\pi. \tag{3.38}$$

Using the Wronskian formula 9.1.16 from Abramowitz & Stegun (1965)

$$J_l(\beta a)(H_l^{(1)})'(\beta a) - H_l^{(1)}(\beta a) J_l'(\beta a) = \frac{2i}{\beta \pi a}, \tag{3.39}$$

(3.38) simplifies to

$$I_{C_0} = \sum_{l=-\infty}^{\infty} -\frac{4i E_l}{\sqrt{|\mu_m|}} \left(\frac{-\mu_m - i\alpha_m}{\beta} \right)^l = -\frac{4i}{\sqrt{|\mu_m|}} \sum_{l=-\infty}^{\infty} E_l (-1)^l \left(\frac{\mu_m + i\alpha_m}{\beta} \right)^l.$$

Combining these integrals on Γ_+, Γ_- and C_0,

$$\frac{-i\mathcal{A}_H d(\chi_0+\mu_0)\delta_{m0}}{\sqrt{|\chi_0|}\sqrt{|\mu_0|}}e^{i(\mu_0-\chi_0)y}+\frac{iR_m(\chi_m-\mu_m)d}{\sqrt{|\chi_m|}\sqrt{|\mu_m|}}e^{i(\mu_m+\chi_m)y}$$

$$+\frac{iT_m(\chi_m+\mu_m)d}{\sqrt{|\chi_m|}\sqrt{|\mu_m|}}e^{i(\mu_m-\chi_m)y}-\frac{4i}{\sqrt{|\mu_m|}}\sum_{l=-\infty}^{\infty}E_l(-1)^l\left(\frac{\mu_m+i\alpha_m}{\beta}\right)^l=0. \tag{3.40}$$

For $\mu_m=-\chi_m$, this simplifies to

$$0+\frac{2iR_m\chi_m d}{\sqrt{|\chi_m|}\sqrt{|\chi_m|}}+0-\frac{4i}{\sqrt{|\chi_m|}}\sum_{l=-\infty}^{\infty}E_l(-1)^l\left(\frac{-\chi_m+i\alpha_m}{\beta}\right)^l=0,$$

$$\iff R_m=\frac{2\sqrt{|\chi_m|}}{\chi_m d}\sum_{l=-\infty}^{\infty}E_l(-1)^l\left(\frac{-\chi_m+i\alpha_m}{\beta}\right)^l. \tag{3.41}$$

For $\mu_m=\chi_m$, we have

$$-\frac{2i\mathcal{A}_H d\chi_0\delta_{m0}}{\sqrt{|\chi_0|}\sqrt{|\chi_0|}}+0+\frac{2iT_m\chi_m d}{\sqrt{|\chi_m|}\sqrt{|\chi_m|}}-\frac{4i}{\sqrt{|\chi_m|}}\sum_{l=-\infty}^{\infty}E_l(-1)^l\left(\frac{\chi_m+i\alpha_m}{\beta}\right)^l=0,$$

$$\iff T_m=\frac{2\sqrt{|\chi_m|}}{\chi_m d}\sum_{l=-\infty}^{\infty}E_l(-1)^l\Big(\frac{\chi_m+i\alpha_m}{\beta}\Big)^l+\mathcal{A}_H\delta_{m0}. \tag{3.42}$$

The reconstruction equations for the reflection and transmission coefficients $\hat{R}_p$ and $\hat{T}_p$ of the modified Helmholtz equation are derived in a similar fashion by applying Green's theorem to $V_{p,M}$ and W_M, and take the form

$$\hat{R}_p=\frac{\pi}{d\sqrt{|\hat{\chi}_p|}}\sum_{l=-\infty}^{\infty}F_l(-1)^l\frac{(-\hat{\chi}_p+i\alpha_p)^l}{\beta^l}, \tag{3.43}$$

$$\hat{T}_p=\frac{\pi}{d\sqrt{|\hat{\chi}_p|}}\sum_{l=-\infty}^{\infty}F_l(-1)^l\frac{(\hat{\chi}_p+i\alpha_p)^l}{\beta^l}+\mathcal{A}_M\delta_{p0}. \tag{3.44}$$

The amplitudes of the reflected and transmitted waves are determined for the set of incident fields corresponding to a range of grating orders, both propagating and evanescent. These are assembled into scattering matrices for reflection and transmission that completely characterise the grating's scattering action.

3.1.5 Conservation of energy

We consider the conservation of energy for the scattering of flexural waves by a single grating. The relations we derive in this section are applicable to scatterers of any smooth shape, and encompass both propagating and evanescent incident waves, as well as both types of reflected and transmitted waves. The conservation of energy is dependent on structure rather than convergence, and is therefore independent of the number of terms in the expansions.

We use the following integral identity:

$$\int_{\Omega}(u\Delta^2 v - v\Delta^2 u)d\mathbf{x} = \int_{\partial\Omega}\left(\Delta u\frac{\partial v}{\partial n} - v\frac{\partial}{\partial n}(\Delta u) + u\frac{\partial}{\partial n}(\Delta v) - \Delta v\frac{\partial u}{\partial n}\right)ds, \quad (3.45)$$

where u and v are two solutions of a problem of time-harmonic flexural vibrations of a thin elastic plate.

This Green's formula is applied to the fundamental cell of a single grating of scatterers shown in Fig. 3.2. As for the derivation of the reconstruction equations in Section 3.1.4, we assume that u and v are chosen in such a way that they have opposite quasi-periodicity factors. Therefore the contributions from Γ_l and Γ_r cancel out. Recalling the boundary conditions (3.4), we also assume that u and v satisfy them, and therefore the boundary integral along C_0 is zero. These assumptions reduce (3.45) to the simpler form:

$$\sum\int_{\Gamma^+,\ \Gamma^-}\left(v_H\frac{\partial u_H}{\partial n} - u_H\frac{\partial v_H}{\partial n} + u_M\frac{\partial v_M}{\partial n} - v_M\frac{\partial u_M}{\partial n}\right)ds = 0, \quad (3.46)$$

where Helmholtz and modified Helmholtz terms are denoted by the subscripts H and M respectively. We apply this equation to our total field (3.3) $u = W_H + W_M$, and its complex conjugate $v = \overline{W}_H + \overline{W}_M$, such that on Γ^+:

$$u_H = W_{i,H} + W^R_{s,H}, \quad u_M = W_{i,M} + W^R_{s,M}, \quad (3.47)$$

and

$$v_H = \overline{W}_{i,H} + \overline{W}^R_{s,H}, \quad v_M = \overline{W}_{i,M} + \overline{W}^R_{s,M}. \quad (3.48)$$

On Γ^-, we have similar expressions which consist only of transmitted waves, rather than incident and reflected fields:

$$u_H = W^T_{s,H}, \quad u_M = W^T_{s,M}, \quad (3.49)$$

and

$$v_H = \overline{W}^T_{s,H}, \quad v_M = \overline{W}^T_{s,M}. \quad (3.50)$$

Upper boundary Γ^+

We concentrate on the upper segment Γ^+ first. Using our plane wave expansions from Section 2.2, we have the following representations:

$$u_H = \sum_p \frac{\delta_p}{\sqrt{|\chi_p|}}\exp\{i(\alpha_p x - \chi_p y)\} + \sum_p \frac{R_p}{\sqrt{|\chi_p|}}\exp\{i(\alpha_p x + \chi_p y)\},$$

$$u_M = \sum_p \frac{\hat{\delta}_p}{\sqrt{|\hat{\chi}_p|}}\exp\{i(\alpha_p x - \hat{\chi}_p y)\} + \sum_p \frac{\hat{R}_p}{\sqrt{|\hat{\chi}_p|}}\exp\{i(\alpha_p x + \hat{\chi}_p y)\},$$

$$v_H = \sum_p \frac{\delta_p}{\sqrt{|\chi_p|}} \exp\{-i(\alpha_p x - \overline{\chi}_p y)\} + \sum_p \frac{\overline{R}_p}{\sqrt{|\chi_p|}} \exp\{-i(\alpha_p x + \overline{\chi}_p y)\},$$

$$v_M = \sum_p \frac{\hat{\delta}_p}{\sqrt{|\hat{\chi}_p|}} \exp\{-i(\alpha_p x - \overline{\hat{\chi}}_p y)\} + \sum_p \frac{\overline{\hat{R}}_p}{\sqrt{|\hat{\chi}_p|}} \exp\{-i(\alpha_p x + \overline{\hat{\chi}}_p y)\}, \tag{3.51}$$

where δ_p and $\hat{\delta_p}$ are incident wave amplitudes of propagating and evanescent type respectively, and R_p and $\hat{R_p}$ are the coefficients for Helmholtz and modified Helmholtz type reflected waves. Since δ_p and $\hat{\delta_p}$ are real, their complex conjugates do not change. For Γ^+ (see Fig. 3.2), we differentiate with respect to the unit outward normal i.e. $\partial/\partial n = \partial/\partial y$. Hence we require the following partial derivatives:

$$\frac{\partial u_H}{\partial n} = \sum_p \frac{\delta_p}{\sqrt{|\chi_p|}}(-i\chi_p) \exp\{i(\alpha_p x - \chi_p y)\} + \sum_p \frac{R_p}{\sqrt{|\chi_p|}}(i\chi_p) \exp\{i(\alpha_p x + \chi_p y)\},$$

$$\frac{\partial v_H}{\partial n} = \sum_p \frac{\delta_p}{\sqrt{|\chi_p|}}(i\overline{\chi}_p) \exp\{-i(\alpha_p x - \overline{\chi}_p y)\} + \sum_p \frac{\overline{R}_p}{\sqrt{|\chi_p|}}(-i\overline{\chi}_p) \exp\{-i(\alpha_p x + \overline{\chi}_p y)\},$$

$$\frac{\partial u_M}{\partial n} = \sum_p \frac{\hat{\delta}_p}{\sqrt{|\hat{\chi}_p|}}(-i\hat{\chi}_p) \exp\{i(\alpha_p x - \hat{\chi}_p y)\} + \sum_p \frac{\hat{R}_p}{\sqrt{|\hat{\chi}_p|}}(i\hat{\chi}_p) \exp\{i(\alpha_p x + \hat{\chi}_p y)\},$$

$$\frac{\partial v_M}{\partial n} = \sum_p \frac{\hat{\delta}_p}{\sqrt{|\hat{\chi}_p|}}(i\overline{\hat{\chi}}_p) \exp\{-i(\alpha_p x - \overline{\hat{\chi}}_p y)\} + \sum_p \frac{\overline{\hat{R}}_p}{\sqrt{|\hat{\chi}_p|}}(-i\overline{\hat{\chi}}_p) \exp\{-i(\alpha_p x + \overline{\hat{\chi}}_p y)\}. \tag{3.52}$$

On Γ^+, $y = \eta d/2$ and $x \in [0, d]$. We substitute these values into (3.46), along with the derivatives (3.52), beginning with the first half of the integral. Thus,

$$\int_0^d \left(v_H \frac{\partial u_H}{\partial n} - u_H \frac{\partial v_H}{\partial n} \right) dx \;=\; d \sum_p \left\{ \frac{|R_p|^2}{|\chi_p|} i(\chi_p + \overline{\chi}_p) \exp\{\frac{i\eta d}{2}(\chi_p - \overline{\chi}_p)\} \right.$$

$$+ \frac{\overline{R}_p \delta_p}{|\chi_p|}(-i)(\chi_p - \overline{\chi}_p) \exp\{-\frac{i\eta d}{2}(\chi_p + \overline{\chi}_p)\} + \frac{R_p \delta_p}{|\chi_p|} i(\chi_p - \overline{\chi}_p) \exp\{\frac{i\eta d}{2}(\chi_p + \overline{\chi}_p)\}$$

$$\left. + \frac{\delta_p^2}{|\chi_p|}(-i)(\chi_p + \overline{\chi}_p) \exp\{-\frac{i\eta d}{2}(\chi_p - \overline{\chi}_p)\} \right\}, \tag{3.53}$$

where we have used the identity

$$\int_0^d \exp\{i(\alpha_p - \alpha_q)x\} dx = d\delta_{pq}, \tag{3.54}$$

where δ_{pq} is the Kronecker delta. We now apply some conjugacy rules for the the sets of propagating and evanescent orders of Helmholtz type, Ω_H and Ω_H^e. For

$$\begin{aligned} &p \in \Omega_H \ , \ \chi_p = \overline{\chi}_p > 0; \\ &p \in \Omega_H^e \ , \ \overline{\chi}_p = -\chi_p = -i|\chi_p|. \end{aligned} \tag{3.55}$$

These relations allow us to affect some cancellations and simplification in (3.53) which leads to:

$$d \sum_{p\in\Omega_H} \left\{ 2i|R_p|^2 - 2i\delta_p^2 \right\} + d \sum_{p\in\Omega_H^e} \left\{ \frac{\overline{R}_p\delta_p}{|\chi_p|}(-i)(i|\chi_p| + i|\chi_p|) + \frac{R_p\delta_p}{|\chi_p|} i(i|\chi_p| + i|\chi_p|) \right\}. \tag{3.56}$$

Thus,

$$\int_{\Gamma^+} \left(v_H \frac{\partial u_H}{\partial n} - u_H \frac{\partial v_H}{\partial n} \right) dx = 2d \left\{ i \sum_{p\in\Omega_H} \left(|R_p|^2 - \delta_p^2 \right) + \sum_{p\in\Omega_H^e} \left(\overline{R}_p\delta_p - R_p\delta_p \right) \right\}. \tag{3.57}$$

For the other half of (3.46) to be evaluated on Γ^+ with $y = \eta d/2$ and $x \in [0, d]$, we have

$$u_M \frac{\partial v_M}{\partial n} - v_M \frac{\partial u_M}{\partial n} \tag{3.58}$$

where $\partial/\partial n = \partial/\partial y$. Thus,

$$\begin{aligned} &\left(\sum_p \frac{\hat{\delta}_p}{\sqrt{|\hat{\chi}_p|}} \exp\{i(\alpha_p x - \hat{\chi}_p \eta d/2)\} + \sum_p \frac{\hat{R}_p}{\sqrt{|\hat{\chi}_p|}} \exp\{i(\alpha_p x + \hat{\chi}_p \eta d/2)\} \right) \times \\ &\times \left(\sum_q \frac{\hat{\delta}_q}{\sqrt{|\hat{\chi}_q|}} (i\overline{\hat{\chi}}_q) \exp\{-i(\alpha_q x - \overline{\hat{\chi}}_q \eta d/2)\} + \sum_q \frac{\overline{\hat{R}}_q}{\sqrt{|\hat{\chi}_q|}} (-i\overline{\hat{\chi}}_q) \exp\{-i(\alpha_q x + \overline{\hat{\chi}}_q \eta d/2)\} \right) \\ &- \left(\sum_p \frac{\hat{\delta}_p}{\sqrt{|\hat{\chi}_p|}} \exp\{-i(\alpha_p x - \overline{\hat{\chi}}_p \eta d/2)\} + \sum_p \frac{\overline{\hat{R}}_p}{\sqrt{|\hat{\chi}_p|}} \exp\{-i(\alpha_p x + \overline{\hat{\chi}}_p \eta d/2)\} \right) \times \\ &\times \left(\sum_q \frac{\hat{\delta}_q}{\sqrt{|\hat{\chi}_q|}} (-i\hat{\chi}_q) \exp\{i(\alpha_q x - \hat{\chi}_q \eta d/2)\} + \sum_q \frac{\hat{R}_q}{\sqrt{|\hat{\chi}_q|}} (i\hat{\chi}_q) \exp\{i(\alpha_q x + \hat{\chi}_q \eta d/2)\} \right). \end{aligned}$$

We apply (3.54) and obtain

$$\begin{aligned} \int_0^d \left(u_M \frac{\partial v_M}{\partial n} - v_M \frac{\partial u_M}{\partial n} \right) dx = d \sum_p \Bigg\{ &\frac{|\hat{R}_p|^2}{|\hat{\chi}_p|}(-i)(\hat{\chi}_p + \overline{\hat{\chi}}_p) \exp\{\frac{i\eta d}{2}(\hat{\chi}_p - \overline{\hat{\chi}}_p)\} + \\ &+ \frac{\hat{R}_p\hat{\delta}_p}{|\hat{\chi}_p|}(i)(\overline{\hat{\chi}}_p - \hat{\chi}_p) \exp\{\frac{i\eta d}{2}(\hat{\chi}_p + \overline{\hat{\chi}}_p)\} + \frac{(\hat{\delta}_p)^2}{|\hat{\chi}_p|}(i)(\overline{\hat{\chi}}_p + \hat{\chi}_p) \exp\{-\frac{i\eta d}{2}(\hat{\chi}_p - \overline{\hat{\chi}}_p)\} \\ &+ \frac{\overline{\hat{R}}_p\hat{\delta}_p}{|\hat{\chi}_p|}(-i)(\overline{\hat{\chi}}_p - \hat{\chi}_p) \exp\{-\frac{i\eta d}{2}(\hat{\chi}_p + \overline{\hat{\chi}}_p)\} \Bigg\}. \end{aligned} \tag{3.59}$$

Recalling our definition for evanescent waves of modified Helmholtz type (3.6), we note that $\hat{\chi}_p = i|\hat{\chi}_p|$. By taking the complex conjugate of both sides, we obtain

$$\overline{\hat{\chi}}_p = -i|\hat{\chi}_p| = -\hat{\chi}_p, \tag{3.60}$$

which can be used to simplify our expression (3.59). The first and third terms cancel, whilst in the second and fourth terms, the exponents vanish and the difference in $\overline{\hat{\chi}}_p$ and $\hat{\chi}_p$ is equivalent to $-2i|\hat{\chi}_p|$. Thus,

$$\int_0^d \left(u_M \frac{\partial v_M}{\partial n} - v_M \frac{\partial u_M}{\partial n} \right) dx = 2d \sum_p \hat{\delta}_p (\hat{R}_p - \overline{\hat{R}}_p). \tag{3.61}$$

Combining our two halves of the integral (3.46) for Γ^+, we obtain:

$$\sum \int_{\Gamma^+} \left(v_H \frac{\partial u_H}{\partial n} - u_H \frac{\partial v_H}{\partial n} + u_M \frac{\partial v_M}{\partial n} - v_M \frac{\partial u_M}{\partial n} \right) dx$$

$$= 2d \Bigg\{ i \sum_{p \in \Omega_H} \left(|R_p|^2 - \delta_p^2 \right) + \sum_{p \in \Omega_H^e} \left(\overline{R}_p \delta_p - R_p \delta_p \right) - \sum_{p \in \Omega_M} \left(\overline{\hat{R}}_p \hat{\delta}_p - \hat{R}_p \hat{\delta}_p \right) \Bigg\}, \tag{3.62}$$

where we use δ_p to denote the amplitude of the Helmholtz type incident wave, and $\hat{\delta}_p$ to represent the amplitude of the incident wave of modified Helmholtz type. Note that the Γ^+ segment accounts for incident and reflected waves only.

Lower boundary Γ^-

We now evaluate (3.46) on Γ^- to determine the energy associated with the transmitted waves (3.50):

$$u_H = W_{s,H}^T = \sum_p \frac{T_p}{\sqrt{|\chi_p|}} \exp\{i(\alpha_p x - \chi_p y)\},$$

$$u_M = W_{s,M}^T = \sum_p \frac{\hat{T}_p}{\sqrt{|\hat{\chi}_p|}} \exp\{i(\alpha_p x - \hat{\chi}_p y)\},$$

$$v_H = \overline{W}_{s,H}^T = \sum_p \frac{\overline{T}_p}{\sqrt{|\chi_p|}} \exp\{-i(\alpha_p x - \overline{\chi}_p y)\},$$

$$v_M = \overline{W}_{s,M}^T = \sum_p \frac{\overline{\hat{T}}_p}{\sqrt{|\hat{\chi}_p|}} \exp\{-i(\alpha_p x - \overline{\hat{\chi}}_p y)\}. \tag{3.63}$$

Referring to Fig. 3.2, we differentiate with respect to the direction of the unit outward normal to Γ^-. Therefore the partial derivatives we require are:

$$\frac{\partial u_H}{\partial n} = -\sum_p \frac{T_p}{\sqrt{|\chi_p|}} (-i\chi_p) \exp\{i(\alpha_p x - \chi_p y)\},$$

$$\frac{\partial v_H}{\partial n} = -\sum_p \frac{\overline{T}_p}{\sqrt{|\chi_p|}} (i\overline{\chi}_p) \exp\{-i(\alpha_p x - \overline{\chi}_p y)\},$$

$$\frac{\partial u_M}{\partial n} = -\sum_p \frac{\hat{T}_p}{\sqrt{|\hat{\chi}_p|}}(-i\hat{\chi}_p)\exp\{i(\alpha_p x - \hat{\chi}_p y)\},$$

$$\frac{\partial v_M}{\partial n} = -\sum_p \frac{\overline{\hat{T}}_p}{\sqrt{|\hat{\chi}_p|}}(i\overline{\hat{\chi}}_p)\exp\{-i(\alpha_p x - \overline{\hat{\chi}}_p y)\}. \tag{3.64}$$

For clarity, we again split the integral for Γ^- into two parts, beginning with

$$\int_0^d \left(v_H \frac{\partial u_H}{\partial n} - u_H \frac{\partial v_H}{\partial n}\right)dx = \int_0^d \left(u_H \frac{\partial v_H}{\partial y} - v_H \frac{\partial u_H}{\partial y}\right)dx,$$

owing to the the sign of the derivatives in (3.64). Thus, remembering that $y = -\eta d/2$ on Γ^-,

$$\int_0^d \Bigg\{\Bigg(\sum_p \frac{T_p}{\sqrt{|\chi_p|}}\exp\{i(\alpha_p x + \chi_p \eta d/2)\}\Bigg)\Bigg(\sum_q \frac{\overline{T}_q}{\sqrt{|\chi_q|}}(i\overline{\chi}_q)\exp\{-i(\alpha_q x + \overline{\chi}_q \eta d/2)\}\Bigg)$$

$$-\Bigg(\sum_p \frac{\overline{T}_p}{\sqrt{|\chi_p|}}\exp\{-i(\alpha_p x + \overline{\chi}_p \eta d/2)\}\Bigg)\Bigg(\sum_q \frac{T_q}{\sqrt{|\chi_q|}}(-i\chi_q)\exp\{i(\alpha_q x + \chi_p \eta d/2)\}\Bigg)\Bigg\}dx$$

$$= d\sum_p \left\{\frac{T_p\overline{T}_p}{|\chi_p|}(i\overline{\chi}_p)\exp\{\frac{i\eta d}{2}(\chi_p - \overline{\chi}_p)\} + \frac{\overline{T}_p T_p}{|\chi_p|}(i\chi_p)\exp\{\frac{i\eta d}{2}(\chi_p - \overline{\chi}_p)\}\right\}, \tag{3.65}$$

once again using the identity (3.54). This expression can be simplified further:

$$\int_0^d \left(v_H \frac{\partial u_H}{\partial n} - u_H \frac{\partial v_H}{\partial n}\right)dx = d\sum_p \frac{|T_p|^2}{|\chi_p|} i(\chi_p + \overline{\chi}_p)\exp\{\frac{i\eta d}{2}(\chi_p - \overline{\chi}_p)\}.$$

By considering the relationship between χ_p and $\overline{\chi}_p$, we can reduce this expression to cover sets of propagating and evanescent Helmholtz type waves. For $p \in \Omega_H$, $\chi_p = \overline{\chi}_p > 0$. Therefore the exponent vanishes for propagating Helmholtz waves, and the remaining χ_p terms cancel. For $p \in \Omega_H^e$, $\overline{\chi}_p = -\chi_p$. Thus, in this evanescent case, the term $(\chi_p + \overline{\chi}_p)$ vanishes and there are no transmission energy terms in the set Ω_H^e. We therefore deduce

$$\int_0^d \left(v_H \frac{\partial u_H}{\partial n} - u_H \frac{\partial v_H}{\partial n}\right)dx = 2di \sum_{p\in\Omega_H} |T_p|^2 \tag{3.66}$$

on Γ^-. For the other part of the integral on Γ^-, we evaluate

$$\int_0^d \left(u_M \frac{\partial v_M}{\partial n} - v_M \frac{\partial u_M}{\partial n}\right)dx = \int_0^d \left(v_M \frac{\partial u_M}{\partial y} - u_M \frac{\partial v_M}{\partial y}\right)dx.$$

We employ the identity (3.54) as in the previous calculations, obtaining the result

$$d\sum_p \left\{\frac{\hat{T}_p\overline{\hat{T}}_p}{|\hat{\chi}_p|}(-i\hat{\chi}_p)\exp\{\frac{i\eta d}{2}(\hat{\chi}_p - \overline{\hat{\chi}}_p)\} - \frac{\hat{T}_p\overline{\hat{T}}_p}{|\hat{\chi}_p|}(i\overline{\hat{\chi}}_p)\exp\{\frac{i\eta d}{2}(\hat{\chi}_p - \overline{\hat{\chi}}_p)\}\right\}. \tag{3.67}$$

Factorising this expression produces a sum comprising terms of products where one of the factors is $(\hat{\chi}_p - \overline{\hat{\chi}}_p)$. Recalling (3.60), we note that this factor vanishes and therefore the sum in (3.67) also vanishes. There are no modified Helmholtz type transmitted waves which contribute to our energy calculations. The total contribution for Γ^- to the integral (3.46) is

$$\sum \int_{\Gamma^-} \left(v_H \frac{\partial u_H}{\partial n} - u_H \frac{\partial v_H}{\partial n} + u_M \frac{\partial v_M}{\partial n} - v_M \frac{\partial u_M}{\partial n} \right) dx = 2di \sum_{p \in \Omega_H} |T_p|^2. \tag{3.68}$$

Conservation of energy

Having completed our calculations for both $\Gamma^+$and Γ^-, we combine the results:

$$\sum \int_{\Gamma^+,\ \Gamma^-} \left(v_H \frac{\partial u_H}{\partial n} - u_H \frac{\partial v_H}{\partial n} + u_M \frac{\partial v_M}{\partial n} - v_M \frac{\partial u_M}{\partial n} \right) ds = 2di \sum_{p \in \Omega_H} |T_p|^2$$

$$+2d \Bigg\{ i \sum_{p \in \Omega_H} \left(|R_p|^2 - \delta_p^2 \right) + \sum_{p \in \Omega_H^e} \left(\overline{R}_p \delta_p - R_p \delta_p \right) - \sum_{p \in \Omega_M} \left(\overline{\hat{R}}_p \hat{\delta}_p - \hat{R}_p \hat{\delta}_p \right) \Bigg\}.$$

Recalling that the simplified integral identity (3.46) we started with vanishes, we are able to deduce an expression which describes the conservation of energy for a single grating. Setting the above equation equal to zero, we rearrange the terms to produce a convenient form for the energy relations. This involves cancelling the constant d (the period of the grating), and some manipulation of i:

$$\sum_{p \in \Omega_H} \left(|R_p|^2 + |T_p|^2 \right) = \sum_{p \in \Omega_H} \delta_p^2 + i \sum_{p \in \Omega_H^e} \left(\overline{R}_p \delta_p - R_p \overline{\delta}_p \right) - i \sum_{p \in \Omega_M^e} \left(\overline{\hat{R}}_p \hat{\delta}_p - \hat{R}_p \overline{\hat{\delta}}_p \right). \tag{3.69}$$

We define Ω_H to represent the set of propagating orders of Helmholtz type. The sets Ω_H^e and Ω_M^e contain evanescent waves, of Helmholtz and modified Helmholtz type respectively. The set Ω_M^e comprises all integers p since all modified Helmholtz waves that satisfy the Sommerfeld radiation condition are evanescent (see Section 2.4.1).

3.1.6 Zero-radius limit: rigid pins

In the limiting case of the radii of the circular voids tending to zero, it may be shown that the multipole coefficients in the algebraic system (3.26), (3.27) are all equal to zero, with the exception of the case $n = 0$. This monopole case is valid to leading order approximation for small a, and the leading multipole coefficients E_0 and F_0 satisfy two equations:

$$\left[S_0^{(H,G)}(\beta, \alpha_0)\, J_0(\beta a) \,+\, H_0^{(1)}(\beta a) \right] E_0 \,+\, \left[S_0^{(K,G)}(\beta, \alpha_0)\, I_0(\beta a) \,+\, K_0(\beta a) \right] F_0$$

$$= \, -\frac{\mathcal{A}_M}{\sqrt{|\hat{\chi}_0|}}\, I_0(\beta a) \,-\, \frac{\mathcal{A}_H}{\sqrt{|\chi_0|}}\, J_0(\beta a) \tag{3.70}$$

and

$$\left[S_0^{(H,G)}(\beta,\alpha_0)\,J_0'(\beta a)\,+\,H_0^{(1)'}(\beta a)\right]E_0\,+\,\left[S_0^{(K,G)}(\beta,\alpha_0)\,I_0'(\beta a)\,+\,K_0'(\beta a)\right]F_0$$
$$=\,-\frac{\mathcal{A}_M}{\sqrt{|\hat{\chi}_0|}}\,I_0'(\beta a)\,-\,\frac{\mathcal{A}_H}{\sqrt{|\chi_0|}}\,J_0'(\beta a). \tag{3.71}$$

For the higher order coefficients the accompanying terms vanish, cancel or are of sufficiently small order to be discounted for the monopole solution that fully satisfies the boundary conditions and Rayleigh system.

Referring to Abramowitz & Stegun (1965), we are able to simplify equations (3.70), (3.71) for $\beta a \to 0$. The Bessel function J_0 is bounded near the origin, with $J_0(0) = 1$. Similarly, the modified Bessel function I_0 approaches 1 close to the origin. Using the formulae

$$J_0'(z)\,=\,-J_1(z),\quad I_0'(z)\,=\,I_1(z),$$

we then use the fact that both J_1 and I_1 are equal to zero at the origin to reduce further the number of terms in (3.71). Hence,

$$H_0^{(1)'}(\beta a)\,E_0\,+\,K_0'(\beta a)\,F_0\,=\,0. \tag{3.72}$$

For small βa, the leading order term is of order $1/\beta a$. By examination of the series expansions at the origin, equation (3.72) can be approximated to leading order by

$$\frac{2i}{\pi}\,E_0\,=\,F_0. \tag{3.73}$$

Substituting (3.73) into (3.70), we obtain

$$E_0\left(S_0^{(H,G)}\,+\,\frac{2i}{\pi}S_0^{(K,G)}\,+\,\left[H_0^{(1)}(\beta a)\,+\,K_0(\beta a)\,\frac{2i}{\pi}\right]\right)\,=\,-\frac{\mathcal{A}_M}{\sqrt{|\hat{\chi}_0|}}\,-\,\frac{\mathcal{A}_H}{\sqrt{|\chi_0|}}, \tag{3.74}$$

where the factors $I_0(\beta a)$ and $J_0(\beta a)$ tend to 1 for $\beta a \to 0$. We observe that the series expansions for $H_0^{(1)}(\beta a)$ and $K_0(\beta a)$ allow for some cancellation when considering their sum. For the first three terms of the series expansion of $H_0^{(1)}(\beta a)$ about the origin, for small βa, we have

$$\frac{1}{\pi}\left(2i\gamma+\pi+\,2i\log\left(\frac{\beta a}{2}\right)\right)+\frac{1}{\pi}\left(2i-2i\gamma-\pi-2i\log\left(\frac{\beta a}{2}\right)\right)\left(\frac{\beta a}{2}\right)^2+O\left(\frac{\beta a}{2}\right)^4,$$

and for $\frac{2i}{\pi}K_0(\beta a)$ we have

$$-\frac{2i}{\pi}\left(\gamma+\log\left(\frac{\beta a}{2}\right)\right)+\frac{2i}{\pi}\left(1-\gamma-\log\left(\frac{\beta a}{2}\right)\right)\left(\frac{\beta a}{2}\right)^2+O\left(\frac{\beta a}{2}\right)^4,$$

where γ is Euler's constant with numerical value 0.577216. The sum of the first terms of each series simplifies to 1 so the term in the square brackets in (3.74) is of the order $1+O(\beta^2\,a^2)$, and therefore we obtain the result

$$E_0\,=\,-\left(S_0^{(H,G)}\,+\,\frac{2i}{\pi}S_0^{(K,G)}\,+\,1\right)^{-1}\left(\frac{\mathcal{A}_M}{\sqrt{|\hat{\chi}_0|}}\,+\,\frac{\mathcal{A}_H}{\sqrt{|\chi_0|}}\right). \tag{3.75}$$

Referring to the reconstruction equations (3.41)-(3.44), we can now provide explicit formulae for the reflection and transmission plane wave coefficients for a grating of rigid pins (see also Movchan *et al.* (2009), Haslinger *et al.* (2012)). For those of Helmholtz type, we have

$$R_m = \frac{2\sqrt{|\chi_m|}}{\chi_m d} E_0 \quad \text{and} \quad T_m = R_m + \mathcal{A}_H \delta_{m0}. \tag{3.76}$$

For the modified Helmholtz type waves, we have

$$\hat{R}_m = \frac{2i}{d\sqrt{|\hat{\chi}_m|}} E_0 \quad \text{and} \quad \hat{T}_m = \hat{R}_m + \mathcal{A}_M \delta_{m0}. \tag{3.77}$$

We establish reflection and transmission characteristics, in the form of reflection and transmission matrices, for finite grating stacks. Owing to the nature of the propagation of plane waves through a stack, we must take into account the scattering of a wave incident from below as well as from above. A discussion of this was provided by Movchan *et al.* (2009), and we apply the same arguments here.

For a wave coming from above with some value of α_0, the values of the coefficients E_0 and F_0 are the same as for the problem with the wave coming from below with the same value of α_0. This can be shown using the Rayleigh identities (3.70) and (3.71). For the case when the incident wave is in the region $y < 0$ rather than $y > 0$, we adapt the arguments used in the derivation of the reconstruction equations. We then obtain the following results for reflection and transmission coefficients, denoting incidence from below with the superscript $(-)$

$$\begin{aligned} R_m^- &= R_m \quad \text{and} \quad T_m^- = T_m, \\ \hat{R}_m^- &= \hat{R}_m \quad \text{and} \quad \hat{T}_m^- = \hat{T}_m. \end{aligned} \tag{3.78}$$

Energy considerations for small radius of scatterers

Consider a single grating of circular inclusions with period $d = 1$. In Fig. 3.3, we illustrate the evolution of the normalised reflected energy curve for normal incidence as the radius of the scatterers is reduced from $a = 0.1$ to $a = 0.01$ and $a = 1.0 \times 10^{-6}$. The limiting case of $a = 0$ is shown by the dashed curve.

We observe that in the limit as $a \to 0$, the normalised reflected energy curves tend towards the dashed curve for rigid pins, in the range of β that we are interested in i.e. those values in the vicinity of the maximum reflectance required for Fabry-Pérot wave-trapping effects (see Section 2.4.4). This is also consistent with the dispersion diagrams for doubly periodic arrays of rigid pins and finite-radius inclusions (see Movchan *et al.* (2007), McPhedran *et al.* (2009) and Poulton *et al.* (2010)).

We also observe a boundary layer effect when $0 < \beta << 1$. This is an effect of noncommuting limits, similar to the one previously analysed for electromagnetic cases

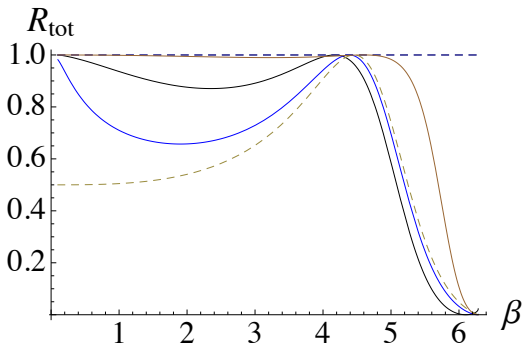

Figure 3.3: Normalised reflected energy R_{tot} versus β for normal incidence for a single grating of voids with period $d = 1$ and radius $a = 0.1$ (brown), $a = 0.01$ (black), $a = 1.0 \times 10^{-6}$ (blue) and the limiting case of $a = 0$ (dashed).

by Poulton *et al.* (2001). This effect is not relevant to the dispersion diagrams for the doubly periodic array, because there is a low-frequency band-gap so the case $0 < \beta << 1$ is excluded. However we observe it here for the transmission problem. This problem for a boundary layer can be solved using a singular perturbation method as in the paper by Poulton *et al.* (2001), but small β is not in the range considered in this thesis, since we analyse cases for which wave trapping and localisation arise.

3.2 Recurrence algorithm for multipole method

As in the papers by Movchan *et al.* (2009) and Haslinger *et al.* (2012), for a single grating, we define reflection and transmission matrices $\mathbf{R}^{\pm}$ and $\mathbf{T}^{\pm}$ to characterise the scattering of an incident wave when it arrives at the grating from above (+) or below (-):

$$\mathbf{R}^{\pm} = \begin{pmatrix} \mathbf{R}^{\pm}_{HH} & \mathbf{R}^{\pm}_{HM} \\ \mathbf{R}^{\pm}_{MH} & \mathbf{R}^{\pm}_{MM} \end{pmatrix}, \ \mathbf{T}^{\pm} = \begin{pmatrix} \mathbf{T}^{\pm}_{HH} & \mathbf{T}^{\pm}_{HM} \\ \mathbf{T}^{\pm}_{MH} & \mathbf{T}^{\pm}_{MM} \end{pmatrix}. \tag{3.79}$$

The subscripts H and M refer to the Helmholtz and modified Helmholtz type waves respectively. The $\mathbf{R}^{+}$ matrix consists of four block matrices of order $(2N+1)\times(2N+1)$, where N denotes the order of truncation for the multipole expressions, and the (p,q)th element of the block $\mathbf{R}^{+}_{HH}$ gives the reflection coefficient R_p when the incident wave comes from above the grating, and its only non-zero amplitude is $\mathcal{A}_H = 1$ for channel q. The (p,q)th element of $\mathbf{R}^{+}_{MH}$ is the reflection coefficient $\hat{R}_p$ for the same incident wave. The (p,q)th entries of $\mathbf{R}^{+}_{HM}$ and $\mathbf{R}^{+}_{MM}$ are the reflection coefficients R_p and $\hat{R}_p$ for the incident wave from above the grating with its only non-zero amplitude being $\mathcal{A}_M = 1$ for channel q. The matrices $\mathbf{R}^{-}$ and $\mathbf{T}^{\pm}$ are filled similarly.

We build up the stack by placing additional gratings on top of the preceding layers. The gratings are identical with a constant periodicity d, but the parameters of relative vertical separation η and relative lateral shift ξ are used to characterise the stack under

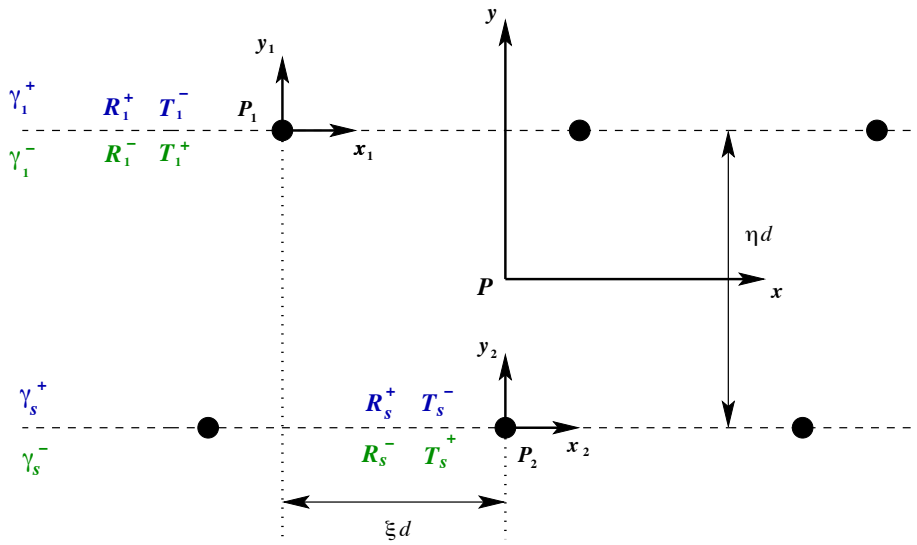

Figure 3.4: Coordinate systems for the top (x_1, y_1) and bottom (x_2, y_2) gratings for a shifted pair of rigid-pin gratings, and the central line of symmetry (x, y) to which we shift the phase origins of the reflection and transmission matrices. Reflection and transmission matrices for the sth and $(s+1)$th gratings are also shown.

consideration. We account for these parameters by defining propagation matrices $\boldsymbol{\mathcal{P}}$ for η and $\boldsymbol{\mathcal{Q}}$ for ξ, which are used in the recurrence procedure. The shift propagation matrix $\boldsymbol{\mathcal{Q}}$ was not used by Movchan *et al.* (2009), who only considered unshifted structures where all of the gratings are aligned. In our treatment (see Haslinger *et al.* 2012), we shift the upper of two gratings to the left of the lower grating (see Fig. 3.4).

3.2.1 Propagation matrices

For a pair of gratings, it is convenient for the system of coordinates to have its origin on the central symmetry line. In this case, we use propagation matrices to shift the phase origin of each of the single grating's reflection and transmission matrices by $\pm\eta d/2$ in the vertical direction, and ξd in the horizontal direction. This is illustrated in Fig. 3.4. P is the origin of the coordinate system (x, y) that we use to evaluate the scattering matrices for the pair. The centre of the system for the top grating is P_1 with coordinates $(x_1, y_1) = (x + \xi d, y - \eta d/2)$, and for the lower grating P_2 with $(x_2, y_2) = (x, y + \eta d/2)$.

The matrices $\boldsymbol{\mathcal{P}}$ and $\boldsymbol{\mathcal{Q}}$ are block matrices of the same order as $\mathbf{R}^{\pm}$ and $\mathbf{T}^{\pm}$. They consist of two $(2N+1) \times (2N+1)$ diagonal matrices on the main diagonal, and two $(2N+1) \times (2N+1)$ null block matrices. We define these $(4N+2) \times (4N+2)$ matrices as follows:

$$\boldsymbol{\mathcal{P}} = \left(\delta_{pq} e^{i\tilde{\chi}_p \eta d/2} \right), \tag{3.80}$$

with $\tilde{\chi}_p = \chi_p$ if p corresponds to a Helmholtz type wave and $\tilde{\chi}_p = \hat{\chi}_p$ if p corresponds

to a plane wave of modified Helmholtz type, and

$$\boldsymbol{\mathcal{Q}} = \left(\delta_{pq} e^{-i\alpha_p \xi d}\right), \tag{3.81}$$

where

$$\alpha_p = \alpha_0 + \frac{2\pi p}{d} \tag{3.82}$$

varies with the diffraction order p of the wave. The Kronecker delta δ_{pq} is used in these expressions with p and q denoting the order of the scattered field, and the channel of the incident field respectively. Therefore propagation matrix entries are nonzero when the type of incident and scattered fields is the same, and their orders match. The diagonal nature of the matrices ensures commutativity of multiplication, allowing convenient notation for the evaluation of the scattering matrices on the central line between successive gratings.

We consider a stack of $s+1$ gratings, and we want to evaluate the reflection and transmission matrices on the central line between the $(s+1)$th and sth gratings. The stack of s gratings is characterized by four matrices $\mathbf{R}_s^+$, $\mathbf{T}_s^-$ on γ_s^+, and $\mathbf{R}_s^-$, $\mathbf{T}_s^+$ on γ_s^-, all relative to the system of coordinates (x_2, y_2) with centre P_2 (see Fig. 3.4). Similarly the additional $(s+1)$th grating is characterized by the matrices $\mathbf{R}_1^+$, $\mathbf{T}_1^-$ on γ_1^+, and $\mathbf{R}_1^-$, $\mathbf{T}_1^+$ on γ_1^-, with origin P_1 and system (x_1, y_1). We use the propagation matrices to represent these matrices on the central line, with respect to the system (x, y). For example, consider waves reflected by the top grating:

$$\sum_p R_p^{(1,+)} e^{i(\alpha_p x_1 + \chi_p y_1)} = \sum_p R_p^{(1,+)} e^{i(\alpha_p \xi d - \chi_p \eta d/2)} e^{i(\alpha_p x + \chi_p y)}.$$

For the coefficients $\mathcal{R}_p^{(1,+)}$ on the central line,

$$\sum_p R_p^{(1,+)} e^{i(\alpha_p \xi d - \chi_p \eta d/2)} = \sum_p \mathcal{R}_p^{(1,+)},$$

and in terms of matrices

$$\boldsymbol{\mathcal{R}}^{(1,+)} = \boldsymbol{\mathcal{Q}}^{-1} \boldsymbol{\mathcal{P}}^{-1} \mathbf{R}^{(1,+)}. \tag{3.83}$$

Similarly, for transmitted wave coefficients $\sum_p T_p^{(1,+)}$,

$$\sum_p T_p^{(1,+)} e^{i(\alpha_p x_1 - \chi_p y_1)} = \sum_p T_p^{(1,+)} e^{i(\alpha_p \xi d + \chi_p \eta d/2)} e^{i(\alpha_p x - \chi_p y)},$$

which gives us

$$\sum_p T_p^{(1,+)} e^{i(\alpha_p \xi d + \chi_p \eta d/2)} = \sum_p \mathcal{T}_p^{(1,+)},$$

and

$$\boldsymbol{\mathcal{T}}^{(1,+)} = \boldsymbol{\mathcal{Q}}^{-1} \boldsymbol{\mathcal{P}} \mathbf{T}^{(1,+)}. \tag{3.84}$$

We have similar plane wave representations for the fields associated with the system (x_2, y_2) with origin P_2:

$$\sum_p R_p^{(s,+)} e^{i(\alpha_p x_2 + \chi_p y_2)} = \sum_p R_p^{(s,+)} e^{i(\alpha_p 0 + \chi_p \eta d/2)} e^{i(\alpha_p x + \chi_p y)},$$

and

$$\boldsymbol{\mathcal{R}}^{(s,+)} = \boldsymbol{\mathcal{P}} \mathbf{R}^{(s,+)}. \tag{3.85}$$

The incident field is also considered. It arrives at P_1 with amplitude $\delta_p^{(1)}$:

$$\sum_p \delta_p^{(1)} e^{i(\alpha_p x_1 - \chi_p y_1)} = \sum_p \delta_p^{(1)} e^{i(\alpha_p \xi d + \chi_p \eta d/2)} e^{i(\alpha_p x - \chi_p y)},$$

$$\sum_p \delta_p^{(1)} e^{i(\alpha_p \xi d + \chi_p \eta d/2)} = \sum_p \delta_p,$$

and

$$(\delta_p^{(1)}) = \boldsymbol{\mathcal{Q}} \boldsymbol{\mathcal{P}}^{-1} (\delta_p). \tag{3.86}$$

We therefore obtain the following representations used for the recurrence algorithm as the wave propagates between the two gratings:

$$\begin{aligned}
\boldsymbol{\mathcal{R}}_1^+ &= \boldsymbol{\mathcal{Q}}^{-1} \boldsymbol{\mathcal{P}}^{-1} \mathbf{R}_1^+ \boldsymbol{\mathcal{P}}^{-1} \boldsymbol{\mathcal{Q}} \qquad \text{and} \qquad \boldsymbol{\mathcal{T}}_1^+ = \boldsymbol{\mathcal{Q}}^{-1} \boldsymbol{\mathcal{P}} \mathbf{T}_1^+ \boldsymbol{\mathcal{P}}^{-1} \boldsymbol{\mathcal{Q}}, \\
\boldsymbol{\mathcal{T}}_1^- &= \boldsymbol{\mathcal{Q}}^{-1} \boldsymbol{\mathcal{P}}^{-1} \mathbf{T}_1^- \boldsymbol{\mathcal{P}} \boldsymbol{\mathcal{Q}} \qquad \text{and} \qquad \boldsymbol{\mathcal{R}}_1^- = \boldsymbol{\mathcal{Q}}^{-1} \boldsymbol{\mathcal{P}} \mathbf{R}_1^- \boldsymbol{\mathcal{P}} \boldsymbol{\mathcal{Q}}, \\
\boldsymbol{\mathcal{R}}_s^+ &= \boldsymbol{\mathcal{P}} \mathbf{R}_s^+ \boldsymbol{\mathcal{P}} \qquad \text{and} \qquad \boldsymbol{\mathcal{T}}_s^+ = \boldsymbol{\mathcal{P}}^{-1} \mathbf{T}_s^+ \boldsymbol{\mathcal{P}}.
\end{aligned} \tag{3.87}$$

3.2.2 Geometric series

An incident wave with amplitude δ arrives at the stack of $s+1$ gratings from above. This wave is either reflected or transmitted. The transmitted wave then passes through to the stack of s gratings. Upon reaching the sth layer, some of the energy is reflected and some is transmitted. For refection off γ_s^+, we use the notation $\mathbf{R}_s^+$, and for the transmission from γ_s^- to the rest of the stack, we use $\mathbf{T}_s^+$. We assume that the stack of s gratings has already been fully evaluated and characterised by the reflection and transmission coefficients denoted by the subscript s. The reflected part of the field defined by $\mathbf{R}_s^+$ returns to the top $(s+1)$th grating whereupon it is reflected or transmitted. The resulting geometric series for the interaction of waves with the pair are:

$$\begin{aligned}
\rho &= \left[\boldsymbol{\mathcal{R}}_1^+ + \boldsymbol{\mathcal{T}}_1^- \boldsymbol{\mathcal{R}}_s^+ \boldsymbol{\mathcal{T}}_1^+ + \boldsymbol{\mathcal{T}}_1^- \boldsymbol{\mathcal{R}}_s^+ \boldsymbol{\mathcal{R}}_1^- \boldsymbol{\mathcal{R}}_s^+ \boldsymbol{\mathcal{T}}_1^+ + \boldsymbol{\mathcal{T}}_1^- \boldsymbol{\mathcal{R}}_s^+ \boldsymbol{\mathcal{R}}_1^- \boldsymbol{\mathcal{R}}_s^+ \boldsymbol{\mathcal{R}}_1^- \boldsymbol{\mathcal{R}}_s^+ \boldsymbol{\mathcal{T}}_1^+ + \ \ldots \right] \delta \\
&= \left[\boldsymbol{\mathcal{R}}_1^+ + \boldsymbol{\mathcal{T}}_1^- \boldsymbol{\mathcal{R}}_s^+ \left(\sum_{k=0}^{\infty} (\boldsymbol{\mathcal{R}}_1^- \boldsymbol{\mathcal{R}}_s^+)^k \right) \boldsymbol{\mathcal{T}}_1^+ \right] \delta
\end{aligned} \tag{3.88}$$

for the reflected field and

$$\tau = \left[\boldsymbol{\mathcal{T}}_s^+ \boldsymbol{\mathcal{T}}_1^+ + \boldsymbol{\mathcal{T}}_s^+ \boldsymbol{\mathcal{R}}_1^- \boldsymbol{\mathcal{R}}_s^+ \boldsymbol{\mathcal{T}}_1^+ + \boldsymbol{\mathcal{T}}_s^+ \boldsymbol{\mathcal{R}}_1^- \boldsymbol{\mathcal{R}}_s^+ \boldsymbol{\mathcal{R}}_1^- \boldsymbol{\mathcal{R}}_s^+ \boldsymbol{\mathcal{T}}_1^+ + \ \ldots \right] \delta,$$

which can be rewritten in the form

$$\tau \;=\; \left[\; \boldsymbol{\mathcal{T}}_s^+ \left(\sum_{k=0}^{\infty} (\boldsymbol{\mathcal{R}}_1^- \boldsymbol{\mathcal{R}}_s^+)^{\,k} \right) \boldsymbol{\mathcal{T}}_1^+ \right] \delta$$

for the transmitted field. We recall Section 2.4.4, and Fig. 2.10 in particular, where we discussed similar geometric series for the traversal of light between two mirrors in a Fabry-Pérot interferometer. By determining the sums to infinity, we obtain

$$\boldsymbol{\mathcal{R}}_{s+1}^+ \;=\; \left[\boldsymbol{\mathcal{R}}_1^+ \;+\; \boldsymbol{\mathcal{T}}_1^- \boldsymbol{\mathcal{R}}_s^+ \left(\mathbf{I} - \boldsymbol{\mathcal{R}}_1^- \boldsymbol{\mathcal{R}}_s^+ \right)^{-1} \boldsymbol{\mathcal{T}}_1^+ \right], \tag{3.89}$$

and

$$\boldsymbol{\mathcal{T}}_{s+1}^+ \;=\; \left[\; \boldsymbol{\mathcal{T}}_s^+ \left(\mathbf{I} - \boldsymbol{\mathcal{R}}_1^- \boldsymbol{\mathcal{R}}_s^+ \right)^{-1} \boldsymbol{\mathcal{T}}_1^+ \right]. \tag{3.90}$$

Using these formulae, we may evaluate the reflection and transmission matrices on the central line of symmetry between the two gratings. We can also rephase these matrices since it makes sense to represent the reflected field with respect to the system (x_1, y_1) at P_1, by multiplying on the left by $\boldsymbol{\mathcal{P}}\boldsymbol{\mathcal{Q}}$. The incident part is also rephased to the top grating by multiplying on the right by $\boldsymbol{\mathcal{Q}}^{-1}\boldsymbol{\mathcal{P}}$. We can then rephase the transmitted field to the system too, or back to the system (x_2, y_2) at P_2, by multiplying on the left by $\boldsymbol{\mathcal{P}}$ and on the right, by $\boldsymbol{\mathcal{Q}}^{-1}\boldsymbol{\mathcal{P}}$. For whichever choice of rephasing, the energy is conserved and for the plots of reflected/transmitted energy versus spectral parameter β, the same results are observed.

3.2.3 Enhanced transmission

In the paper by Movchan *et al.* (2009), attention was drawn to the existence of trapped modes between a pair of gratings, characterised by very sharp transmission resonances at specific frequencies. This analysis was carried out for a pair of gratings where the rigid pins were aligned directly above one another, and the angle of incidence of 30° was highlighted for its particularly striking example of enhanced transmission. We have conducted a thorough investigation of localisation and trapped modes within these platonic systems, the results of which have been published in three journal papers.

For the case of a single grating, it is possible to determine a range of frequencies for which virtually 100 per cent reflection is observed. Therefore intuitively, it is not unreasonable to assume that this shielding effect would be enhanced further upon the introduction of an additional obstacle in the form of a second grating, when observing plane waves over the same frequency range. However we demonstrate that with a specific implementation of the second grating, we observe enhanced *transmission* rather than reflection for plane waves of a given frequency.

This phenomenon is linked directly to the Fabry-Pérot-like trapping of waves between the gratings (see Section 2.4.4). Fundamentally, the high reflectance of a single grating supports the trapping of waves between sets of identical gratings and the associated localisation is observed in the form of resonances.

Enhanced transmission peaks for pairs of shifted gratings

We consider identical gratings of rigid pins with periodicity d, but the upper grating is placed so that the pins are not aligned directly above one another (see Fig. 3.4). The relative grating separation is determined by η where ηd is the vertical distance between the gratings. We denote the relative horizontal shift by ξ. We proceed with the recurrence procedure outlined in the previous section and derive expressions for the reflection and transmission coefficients characterising this pair of gratings:

$$\boldsymbol{\mathcal{R}}_2^+ = \boldsymbol{\mathcal{R}}_U^+ + \boldsymbol{\mathcal{T}}_U^- \boldsymbol{\mathcal{R}}_L^+ (\mathbf{I} - \boldsymbol{\mathcal{R}}_U^- \boldsymbol{\mathcal{R}}_L^+)^{-1} \boldsymbol{\mathcal{T}}_U^+, \tag{3.91}$$

$$\boldsymbol{\mathcal{T}}_2^+ = \boldsymbol{\mathcal{T}}_L^+ (\mathbf{I} - \boldsymbol{\mathcal{R}}_U^- \boldsymbol{\mathcal{R}}_L^+)^{-1} \boldsymbol{\mathcal{T}}_U^+, \tag{3.92}$$

where $\boldsymbol{\mathcal{R}}$, $\boldsymbol{\mathcal{T}}$, $\boldsymbol{\mathcal{P}}$, $\boldsymbol{\mathcal{Q}}$ are defined as in equations (3.80), (3.81) and (3.87), and the subscripts U and L represent the upper and lower grating respectively.

Re-phasing is carried out to obtain $\mathbf{R}_2^+$ and $\mathbf{T}_2^+$ using the appropriate inverse propagation matrices. It is important to remember that as a shifted layer is added onto the existing stack, alternative propagation matrices are required and therefore re-phasing with the corresponding inverse propagation matrices must be carried out at each stage of the recurrence algorithm. This is obviously more relevant as the size of the stack increases from a single pair.

To determine the frequencies for which enhanced transmission occurs for a specific shift ξ, we only require the propagating orders (see Section 2.4.1). In Fig. 3.5(a), Haslinger *et al.* (2012), we show the normalised transmitted energy $\sum |T_p|^2$ as a function of β for a pair of gratings of rigid pins with unit periodicity ($d = 1$) and unit grating separation ($\eta d = 1$), for various relative horizontal shifts ξ of the gratings. This data is calculated for propagating orders for an angle of incidence $\theta_i = 30°$, which is chosen with reference to the work done by Movchan *et al.* (2009). For convenience, we denote the normalised transmitted energy by

$$T_{\text{tot}} = \sum |T_p|^2, \quad p \in \Omega_H. \tag{3.93}$$

The unshifted case (dotted red line) has the lowest value of the spectral parameter β for its transmission resonance. As the relative shift ξ increases from 0.2 (solid green line) to 0.4 (thick solid blue line), the resonance β value increases. In Fig. 3.5(b), we show the detail in the neighbourhood of the transmission resonance for a relative shift of $\xi = 0.4$. Maximum transmission is observed, and the slight separation shape of the resonant peak is reminiscent of Fano resonances (Fano (1961)).

For each specific shift, we note two major observations regarding the transmitted energy. Irrespective of the value of the shift ξ, a sharp peak in transmission occurs near $\beta = 4.2$, where the reflectance for a single grating (dotted-dashed line) is zero. This is a Rayleigh anomaly, where the order -1 passes off (i.e. $\alpha_{-1} = -\beta$), and occurs for $\beta = 4\pi/3$ (see equation (2.27) and Section 2.4.2).

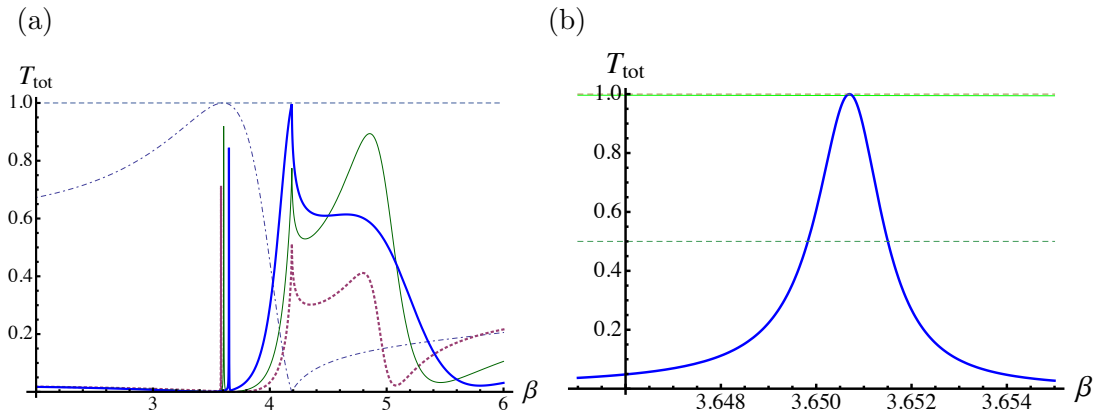

Figure 3.5: (a) Normalised transmitted energy T_{tot}, summed over propagating orders versus β for three pairs of gratings, and normalised reflected energy R_{tot} for a single grating (dot-dashed line) of rigid pins. The incident wave is of Helmholtz type with $\theta_i = 30°$. Data: $d = 1$, $\eta = 1$. (b) Detail in the neighbourhood of the transmission resonance for a shift of $\xi = 0.4$. Dashed lines are used to emphasise the full-power and half-power points.

The other feature is the sharp spike in transmittance which occurs near $\beta = 3.6$ regardless of the shift. This observation is consistent with a discussion by Popov *et al.* (1986) about the consequences of the symmetry of structures incorporating lossless diffraction gratings, in the range of frequency for which only zeroth orders in reflection and transmission are propagating. The passing off of the order -1 at $\beta = 4\pi/3$ confirms that the range $2 < \beta < 4.2$ featured in Fig. 3.5 comprises propagating waves of zero order only.

Popov *et al.* (1986) concluded that if the grating structure has a centre of symmetry then a 100 per cent transmission is achievable. If it has symmetry about a vertical axis then a 100 per cent reflection is achievable. If both these properties exist, or alternatively if it has symmetry with respect to a horizontal axis then a resonant region combining a 100 per cent reflection together with a 100 per cent transmission is achievable. The full transmission we observe around $\beta = 3.6$ is in keeping with these conclusions, since the double grating structure has a centre of symmetry irrespective of the shift value.

The extremely high transmission for a pair of gratings corresponds to nearly 100 per cent reflection for a single grating (dotted-dashed curve), indicating the possibility of a trapped mode. The value of β for which the trapped mode occurs, β_* say, increases with increasing shift up to half of the period, where it attains its maximum. Its minimum corresponds to the case of zero shift. This sharp peak in transmission at β_*, with zero transmission for frequencies either side of the given value, and a correspondence with very high reflectance for a single grating, is the phenomenon of enhanced transmission we are especially interested in. We investigate its dependence on the shift parameter ξ

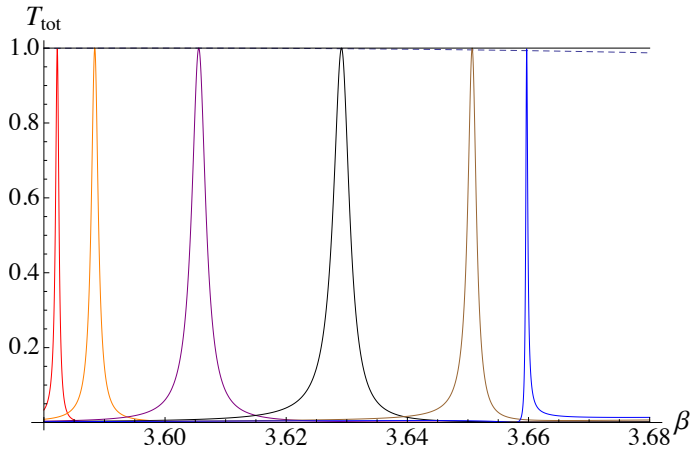

Figure 3.6: Enhanced transmission peaks for shifted pairs of gratings with $d = 1$, $\eta = 1$ and $\theta_i = 30°$. Normalised transmitted energy T_{tot} for propagating orders (zeroth order only) is plotted versus β for shifts ξ in steps of 0.1 from left to right. The narrowest peaks occur for $\xi = 0.5$ and $\xi = 0$ and these correspond to the highest Q.

and how the quality factor (see equations (2.36)-(2.39) in Section 2.4.4) of the resonance relates to the shift and angle of incidence parameters.

In Fig. 3.6 we show a close-up of the enhanced transmission peaks around $\beta = 3.6$ which characterise the trapped modes for $\theta_i = 30°$. We illustrate shifts ξ in steps of 0.1, and these pictures indicate the quality factors of the corresponding transmission resonances. The narrowest peaks, and therefore highest Q-factors, occur for zero shift and a shift of half the period.

3.3 Waveguide approach

We design a waveguide consisting of gratings of rigid pins. We consider triplets for comparison with the scattering problem of Sections 3.1 - 3.2. The spectral parameter β is linked to the angle of incidence θ_i of the plane wave via the relation $\alpha_0 = \beta \sin \theta_i$. For the pinned waveguide, a quasi-periodic Green's function is used to derive the dispersion equation for Bloch modes within the system. These modes take the form of complex resonances close to the real axis which are of even and odd symmetry. Crucially, we establish a connection between the trapped Bloch waves within the structured waveguide and the transmission resonances for a scattered plane wave. This link between the two models enables us to detect and analyse the EDIT effect more efficiently and over a much wider range of parameters, since the waveguide's modes are numerically determined more easily than for the modes of the scattered wave.

3.3.1 Grating Green's function: plane wave form

We consider a single grating of rigid pins as a line of point forces with constant separation d. Therefore we use a quasi-periodic Green's function $G(x, y; \alpha_0, \beta)$ for the biharmonic operator, satisfying equation (2.94), which we repeat here for the convenience of the reader:

$$(\Delta^2 - \beta^4)G(x, y; \alpha_0, \beta) \, + \, \delta(y) \sum_{n=-\infty}^{\infty} \delta(x - nd) \exp\{i\alpha_0 \, nd\} \, = \, 0, \tag{3.94}$$

where α_0 is the Bloch parameter and β is the spectral parameter associated with the frequency ω by $\beta^2 = \omega\sqrt{\rho h/D}$. For the pinned waveguide, it is sufficient to use the plane wave form, rather than the spatial form which incorporates Bessel functions and grating sums. The spectral form of the Green's function (2.103) is also repeated here for the convenience of the reader:

$$G(x, y; \alpha_0, \beta) = \frac{1}{2\beta^2}\left(\frac{1}{2id} \sum_{n=-\infty}^{\infty} \frac{1}{\chi_n} e^{i(\alpha_n x + \chi_n |y|)} + \frac{1}{2d} \sum_{n=-\infty}^{\infty} \frac{1}{\tau_n} e^{i\alpha_n x} \, e^{-\tau_n |y|}\right), \tag{3.95}$$

where

$$\alpha_n \, = \, \alpha_0 + \frac{2\pi n}{d}, \tag{3.96}$$

$$\chi_n \, = \, \begin{cases} \sqrt{\beta^2 \, - \, {\alpha_n}^2} \ , \ {\alpha_n}^2 \leq \beta^2, \\ i\sqrt{{\alpha_n}^2 \, - \, \beta^2} \ , \ {\alpha_n}^2 > \beta^2, \end{cases} \tag{3.97}$$

$$\tau_n \, = \, \sqrt{\beta^2 + \alpha_n^2}. \tag{3.98}$$

3.3.2 Mode symmetry in a general triplet stack

We present detailed coverage of the waveguide method and the association with determining EDIT effects for a scattered wave in Chapter 6, in our culminating journal paper (Haslinger *et al.* 2014). Here we give a brief outline of the derivation of the dispersion equation for the system's Bloch modes. The elementary cell for the general triplet is illustrated in Fig. 6.1. The period of each grating is d and the relative vertical separation between gratings is η. The relative lateral shift of the central grating (or SBL) is denoted by ξ.

We denote the amplitude of the flexural displacement by u to distinguish it from the notation W used for the amplitude in the scattering problem of Sections 3.1 - 3.2. We express u as the sum of three quasi-periodic Green's functions:

$$u \, = \, \sum_{j=-1}^{1} A_j \, G^{(j)} \, (x, \, y; \, \alpha_0, \, \beta), \tag{3.99}$$

where A_j are coefficients to be determined for each Green's function $G^{(j)}$. In terms of the Green's function $G(x, y)$ evaluated for the points $(nd, 0)$ on the horizontal axis, we

have

$$\begin{aligned} G^{(1)}(x,y;\alpha_0,\beta) &= G(x,y-\eta d;\alpha_0,\beta), \\ G^{(0)}(x,y;\alpha_0,\beta) &= G(x-\xi d,y;\alpha_0,\beta), \\ G^{(-1)}(x,y;\alpha_0,\beta) &= G(x,y+\eta d;\alpha_0,\beta). \end{aligned} \tag{3.100}$$

At each pin, it is required that $u = 0$. We therefore take the elementary column cell incorporating the central pin of each of the constituent gratings such that

$$u\Big|_{\mathbf{x}=\boldsymbol{a}^{(m)}} = \sum_{j=-1}^{1} A_j G^{(j)}\left(\boldsymbol{a}^{(m)};\,\alpha_0,\,\beta\right) = 0, \quad \text{where } m=-1,0,1. \tag{3.101}$$

Here $\boldsymbol{a}^{(0)} = (\xi d, 0)$ and $\boldsymbol{a}^{(\pm 1)} = (0, \pm\eta d)$. This is equivalent to the matrix equation

$$\mathbf{M}\,\mathbf{A} = \mathbf{0}, \tag{3.102}$$

where $\mathbf{A}$ is the column vector of the coefficients A_j and

$$\mathbf{M} = \begin{pmatrix} G(0,0) & G(-\xi d,\eta d) & G(0,2\eta d) \\ G(\xi d,-\eta d) & G(0,0) & G(\xi d,\eta d) \\ G(0,-2\eta d) & G(-\xi d,-\eta d) & G(0,0) \end{pmatrix} = \begin{pmatrix} M_{11} & M_{12} & M_{13} \\ M_{21} & M_{11} & M_{21} \\ M_{13} & M_{12} & M_{11} \end{pmatrix}. \tag{3.103}$$

Here we have used the identity $G(x,-y) = G(x,y)$; the arguments α_0 and β in the representation of the matrix elements M_{ij} are left implicit.

Note that the elements M_{12} and M_{21} generally differ if the central layer is shifted with respect to the outer pair. An exception to this arises for normal incidence when $\alpha_0 = 0$. From equations (3.96)-(3.98) we see that when $\alpha_0 = 0$ then $\alpha_{-n} = -\alpha_n$, $\chi_{-n} = \chi_n$, and $\tau_{-n} = \tau_n$. It then follows that

$$M_{12} = G(-\xi d,\eta d) = M_{21} = G(\xi d,-\eta d) \quad \text{for } \alpha_0 = 0.$$

If the gratings are all aligned ($\xi = 0$) or $\alpha_0 = 0$, the matrix $\mathbf{M}$ has a symmetric Töplitz structure. This would be the case regardless of the number of gratings chosen for the mirror layers provided they are placed symmetrically above and below the SBL. In the analysis conducted in Chapter 6 we concentrate on the three-gratings stack, and determine the conditions for odd and even modes. The coincidence of these even and odd Bloch modes gives rise to the EDIT effect in the scattering problem, and we demonstrate the link between the two approaches for a wide range of frequencies and angles.

3.4 Analysis of transmission resonances

The primary motivation for our analysis of trapped modes and transmission resonances in platonic grating structures was the existing literature (Evans & Porter 2007, Movchan

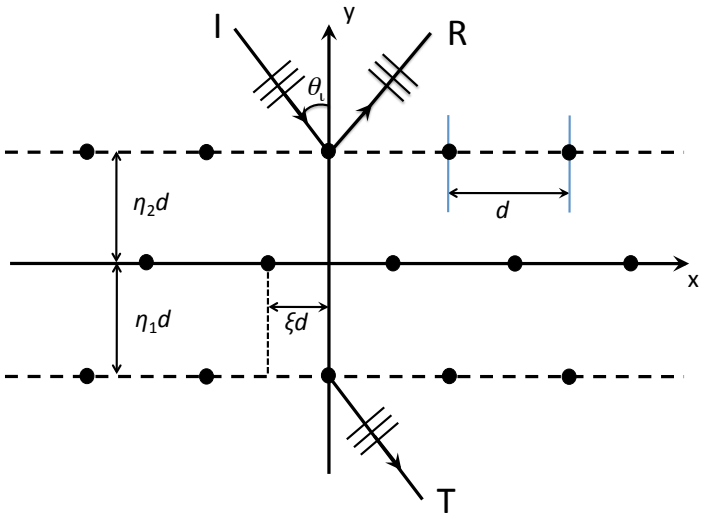

Figure 3.7: Triplet of rigid-pin gratings.

et al. 2009), in which systems composed of two gratings of rigid pins in a Kirchhoff plate were shown to be able to provide Q-factors (see equations (2.36)-(2.39) in Section 2.4.4) of around 6000. This striking result is comparable with some of the best previous designs (Mohammadi *et al.* 2009).

Our initial efforts involved more complicated rigid-pin grating geometries incorporating relative lateral shifts, and in particular, sets of three gratings. The addition of an extra grating means there are two vertical separations $\eta_1 d$, $\eta_2 d$, as illustrated in Fig. 3.7. It is natural to maintain the symmetry of the grating system by setting $\eta_1 = \eta_2 = 1$, and so $\eta_1 d = 1$ i.e. we consider structures where the grating separation in the y-direction matches the period in the x-direction. The lateral shift parameter ξ in grating stacks provides a powerful control over the transmission resonances (see Section 3.2.3), and can give rise to a variety of interesting physical effects, one of these being the EDIT effect (Section 2.4.5). The 3-grating systems support two transmission resonances, characterised by symmetric and anti-symmetric vibration modes, so that the flexural wave within the triplet is an even or odd function of y, respectively.

For the rigid-pin triplet with $\theta_i = 30°$, $d = 1$, and $\eta d = 1$, we observe that the odd mode's spectral parameter value β is invariant with shift ξ, but we can tune the even mode using the shift parameter. For this geometry, it is possible to design a system for which the odd and even modes coincide, and this gives rise to the novel filtering effect that we call elasto-dynamically inhibited transmission (EDIT) where a resonant peak in transmission is cut in two by a resonant dip with an extraordinarily high Q-factor (see Section 2.4.5). In Section 4.3, we discuss this phenomenon (shown in Fig. 3.8) in

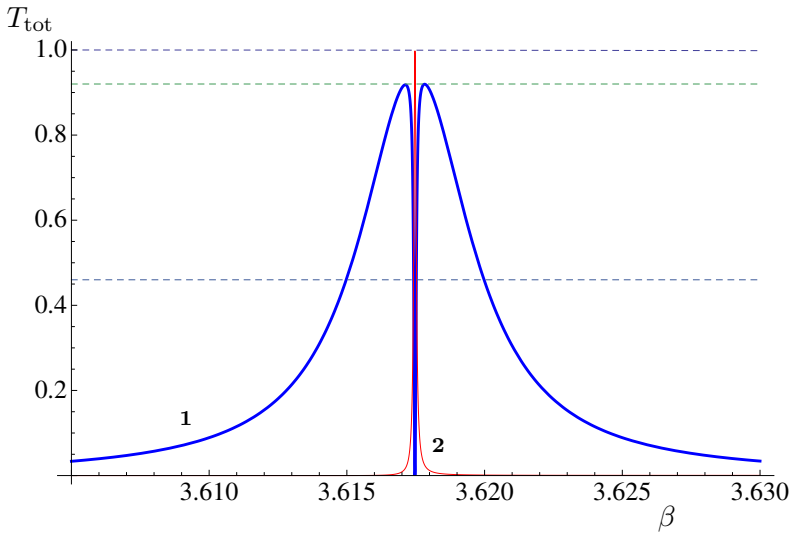

Figure 3.8: EDIT effect for a triplet of rigid-pin gratings with the central grating shifted by $\xi = 0.25200$ for $\theta_i = 30°$. Normalised transmitted energy T_{tot} (curve **1**, blue) as a function of β for the triplet. Curve **2** (red) represents the total transmission for the outer pair of gratings.

detail, and proceed to investigate its viability when we introduce some variation of the parameter θ_i and when we break the symmetry of the structure (i.e. $\eta_1 \neq \eta_2$). The majority of these investigations were published in the paper by Haslinger *et al.* (2012) which forms the bulk of Chapter 4.

Chapter 5 is based on the paper by Haslinger *et al.* (2013a) and considers gratings consisting of voids with nonzero radius $a > 0$. The nonzero radius ensures that higher-order multipole terms, characterising the scattered field, must be taken into account. The change in the geometry from zero-radius pins has important effects on the EDIT phenomenon. In particular, it was noted by Haslinger *et al.* (2013a) that the anti-symmetric resonance mode is no longer unaltered for the case of a horizontal shift of the middle grating. It follows that more care is required to identify the parameter values for EDIT for structures incorporating finite-sized voids.

It is natural to broaden the application of the model by varying more of the parameters. The alternative approach, where the platonic grating interface is treated as a waveguide characterized by quasi-periodic Green's functions (Section 3.3), is discussed in our third paper which makes up Chapter 6. The more efficient determination of resonance values enables us to introduce added complexity regarding the parameters, and in particular the relative vertical separation η_i. In Chapter 6, we show how the EDIT phenomenon can be steered over a wide range of the parameters β and θ_i by optimizing η according to maximum single grating reflectance.

An example of this variation in η is shown in Fig. 3.9. This shows in Fig. 3.9(a) the transmission energy spectrum in the vicinity of two transmission resonances, the lower

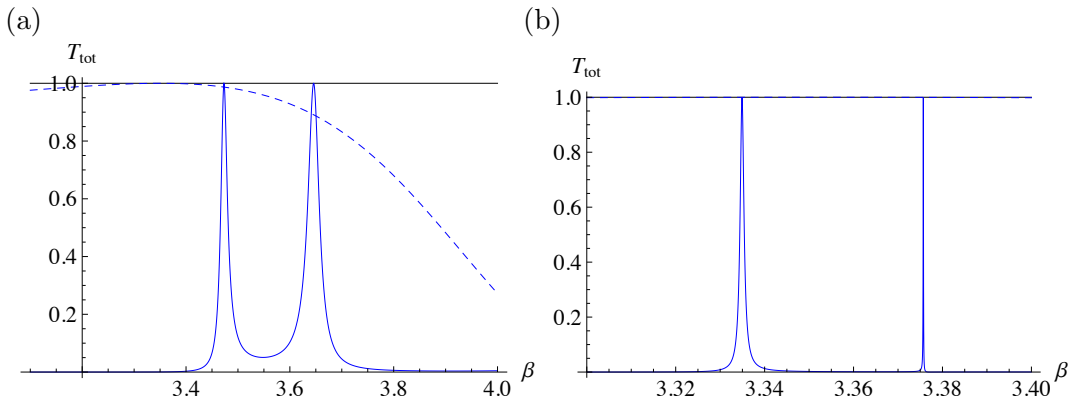

Figure 3.9: Normalised transmitted energy T_{tot} versus spectral parameter β for a triplet of rigid pins with $\alpha_0 = 2.1$ in both cases: (a) $\eta d = 1$; (b) optimized resonances for a triplet with $\eta^* d = 1.185266$. The normalised reflected energy R_{tot} is shown by the dashed curve.

β one being of even symmetry and the upper of odd symmetry. With the initial vertical separation of the gratings being $\eta d = 1$, the resonances have low Q-factors, since the single grating reflectance is significantly below unity. In Fig. 3.9(b), the transmittance spectrum for an optimized value of η shows the resonances after they have been moved into the high reflectance region for the single grating: both have much higher quality factors.

Chapter 4

Pinned platonic grating stacks

This chapter is based on the paper by Haslinger *et al.* (2012), and it studies transmission resonances in rigid-pin platonic grating stacks. The theoretical details of the multipole method employed, and some introductory analysis of enhanced transmission linked to the trapping and localisation of flexural wave energy, has already been discussed in Chapter 3. Here we present numerical examples for systems of two and three gratings. We show geometries containing three gratings for which transmission resonances have very high quality factors of around 3.5×10^4, and expand on the phenomenon of EDIT. The narrow-band transmission resonances and EDIT have potential filtering applications, mirroring the use of resonant systems in physics for filtering. An emerging area in this field concerns the design of systems to achieve narrow band resonances for mechanical (Mohammadi *et al.* 2009) and optomechanical applications (Eichenfeld *et al.* 2009). The ability of a system to give resonant wave effects is often quantified by its quality factor Q, defined in Section 2.4.4, equations (2.36)-(2.39). We discuss the properties and underlying theory of simple geometric structures which give high Q-factor resonances in transmission and reflection for elastic flexural waves.

The structure of the present chapter is as follows. In Section 4.1 we consider pairs of rigid-pin gratings for various angles of incidence θ_i and lateral shifts ξ, and describe the link with Fabry-Pérot theory for the trapping of waves mentioned in Section 2.4.4. In Section 4.2 we present the more complicated systems of three gratings which produce richer resonant spectra. The triplets' characteristic even and odd resonance modes mean that for certain parameter settings, destructive interference results in the EDIT effect, which is reminiscent of optical systems exhibiting electromagnetically induced transparency (see Section 2.4.5). EDIT is illustrated and discussed in the concluding Section 4.3 of this chapter, with reference to our first publication on the subject by Haslinger *et al.* (2012).

4.1 Pairs of rigid-pin platonic gratings

In Section 3.2.3 we presented examples for enhanced transmission for shifted pairs of platonic rigid-pin gratings that were published in the paper by Haslinger *et al.* (2012). These initial examples used angle of incidence $\theta_i = 30°$, period $d = 1$ and relative grating separation $\eta = 1$ (see Fig. 3.5). We now consider the two specific examples $\xi = 0$ and $\xi = 0.5$ in Fig. 4.1, first published by Haslinger *et al.* (2012).

Recall from Section 2.4.4, equations (2.36)-(2.39), that the quality factor (Q-factor) is a dimensionless parameter which characterises a resonance's bandwidth relative to the frequency of the maximum energy. The resonance wavenumbers for the pairs of unshifted and shifted pairs are $\beta = 3.58221$ and 3.65970 respectively. The quality factor for the unshifted pair is around $5,400$ (Movchan *et al.* 2009) and we also find an extraordinarily large quality factor of around $9,400$ for the grating pair with a relative shift of half the period $\xi = 0.5$. Even sharper transmittance spikes are observed when we double the grating separation to $\eta d = 2$. We observe a quality factor of around $35,000$ for the unshifted pair, and $19,000$ for a shifted pair with $\xi = 0.5 = \eta/4$. This increase in Q is consistent with the reduction in the effect of evanescent modes owing to the increased separation of the gratings, relative to their periodicity.

In Fig. 4.1, we show the resonance transmittance spikes for the unshifted and shifted pairs for $\eta d = 1$. Both exhibit the extreme sharpness of the resonance, which arises at these specific frequencies because of the reflectance characteristics of the single grating. We also note the separation shape of the resonant peaks, which is characteristic of Fano resonances (Fano 1961). These arise when there is a slow background variation of transmittance, in the presence of a rapid foreground variation. In our case, the slow variation is that of the transmittance of a single grating, while the rapid variation is caused by the change of phase between the gratings as β varies (see the terms $\boldsymbol{\mathcal{P}}$ and $\boldsymbol{\mathcal{Q}}$ in (3.80) and (3.81)).

4.1.1 Varying angle of incidence

The angle at which the plane waves are incident on the system is an important parameter of the model, and some comparison of the trapped modes arising for 30° and 27° was made by Movchan *et al.* (2009), but only for an unshifted pair. In Figure 4.2, we plot normalised transmitted energy versus β for various shifts ξ for $\theta_i = 27°$. A series of transmission peaks characterised by the lateral shift parameter ξ are obtained, but unlike for 30° (see Fig. 3.6), there isn't a resonance with an explicitly higher Q. This suggests that $\theta_i = 27°$ is not the optimal angle of incidence for zero-radius gratings with respect to the sharpness of the transmission resonances. This is linked to the Fabry-Pérot theory associated with the single grating's reflectance (Section 2.4.4).

In Fig. 4.3 we compare the transmission peaks for $\theta_i = 29°, 30°$ and 31°, with $a = 0$,

(a)

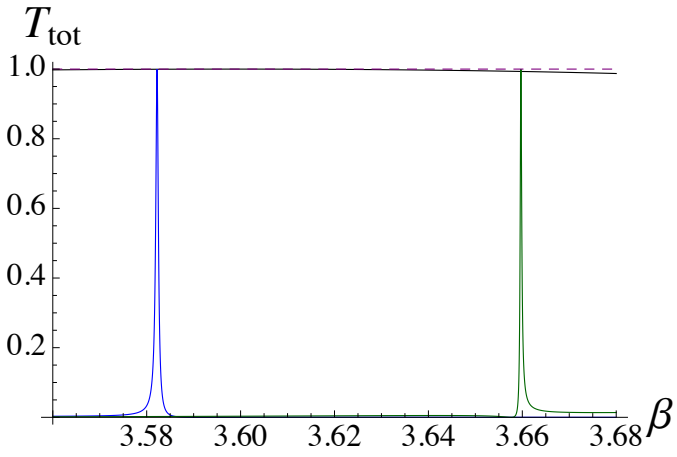

(b)

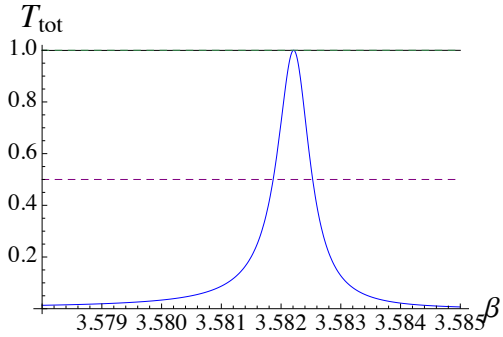

(c)

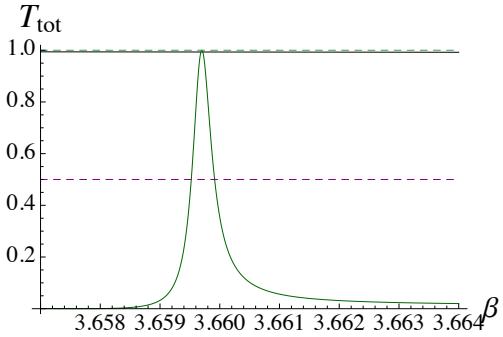

Figure 4.1: (a) Normalised transmitted energy T_{tot} versus β for a pair of unshifted rigid-pin gratings (left spike) and for a shift of half the period (right). For both pairs, $d = 1$, $\eta = 1$ and $\theta_i = 30°$. Also shown are the normalised reflected energy R_{tot} versus β for a single grating (solid green curve close to $T_{\text{tot}} = 1$) and a straight line (dashed) indicating maximum normalised energy of 1. The other two pictures are blow ups of the transmission peaks. These detailed plots illustrate the separation shapes of the Fano resonances.

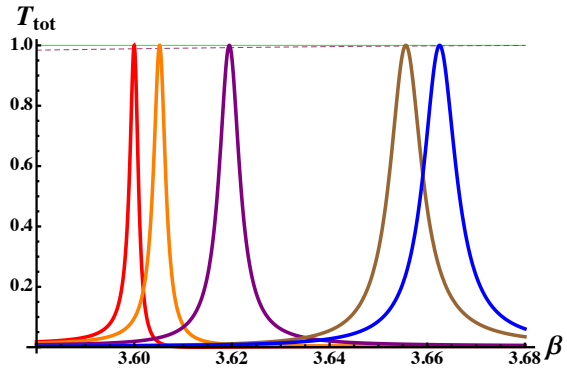

Figure 4.2: Normalised transmitted energy T_{tot}, summed over propagating orders versus β for five pairs of gratings, and normalised reflected energy R_{tot} for a single grating (dashed line) of rigid pins. The incident wave is of Helmholtz type with $\theta_i = 27°$, and $d = 1$, $\eta = 1$. The lateral shift values are $\xi = 0, 0.1, 0.2, 0.4$ and 0.5 from left to right.

$d = 1$ and $\eta = 1$. It is interesting that the case of $\theta_i = 30°$ yields a sharp resonance for the two extreme values of shift $\xi = 0$ and $\xi = 0.5$, whilst $\theta_i = 29°$ supports two sharp resonances for low values of shift, and $\theta_i = 31°$ gives the narrowest peaks for the higher end of the range of shift ξ.

The results suggest that the value of ξ is an important factor in determining the quality factors of the transmission resonances for angles $29° - 31°$ for rigid-pin platonic gratings. Consider the case with zero shift at $\beta \approx 3.59$ for $\theta_i = 29°$ in Fig. 4.3(b). As θ_i increases to 31°, β decreases to around $\beta \approx 3.575$ and the Q factor decreases in Figs. 4.3(a) and (c). A similar pattern applies for the mode at $\beta \approx 3.66$ for $\theta_i = 31°$ and $\xi = 0.5$ in Fig. 4.3(c), which has a very high Q-factor. As θ_i is reduced to 29°, the value of β increases and the Q factor decreases.

4.1.2 Varying relative grating separation and analogy with Fabry-Pérot theory

For all of the examples in which the relative grating separation $\eta = 1$, one enhanced transmission peak is observed, regardless of the value of the lateral shift parameter ξ. For the case of $\eta d = 2$, the very high Q resonance indicative of enhanced transmission is accompanied by additional resonances. This was illustrated by Haslinger *et al.* (2013a) for normal incidence in Fig. 4.4, which also provides a good illustration of the Fabry-Pérot theory in a platonic setting.

For an unshifted pair of gratings of rigid pins with $d = 1$ and $\eta = 1$, the normalised resonant frequency is $\beta_* = 3.62810$ for the transmission peak with a low Q-factor of 20, as illustrated by curve **1** in Fig. 4.4(a). Curve **2** shows the reflected energy for the single grating, and the two peaks are not aligned meaning that the Fabry-Pérot effects are negligible.

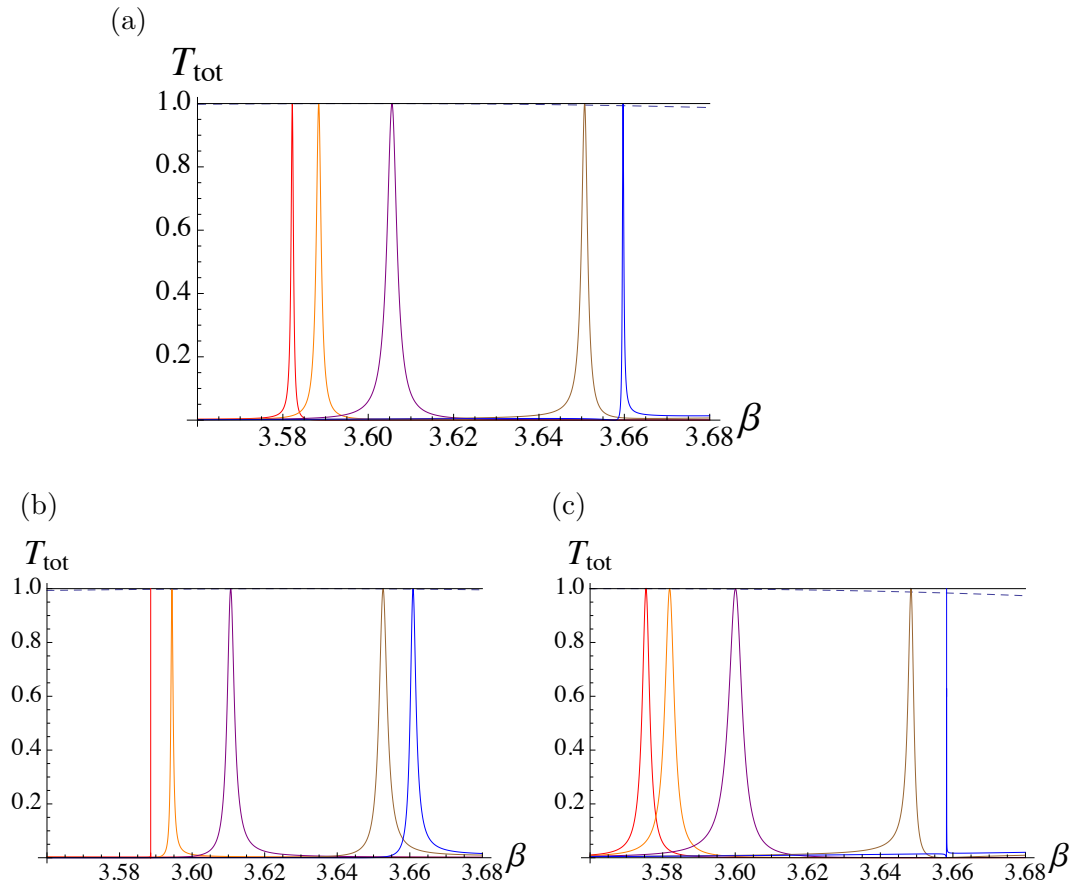

Figure 4.3: Normalised transmitted energy T_{tot}, summed over propagating orders versus β for five pairs of gratings, and normalised reflected energy R_{tot} for a single grating (dashed line) of rigid pins, with $d = 1$ and $\eta = 1$. The incident wave is of Helmholtz type with (a) $\theta_i = 30°$ (b) $\theta_i = 29°$ (c) $\theta_i = 31°$. The lateral shift values are $\xi = 0, 0.1, 0.2, 0.4$ and 0.5 from left to right.

The additional resonances arising from the increased grating separation to $\eta d = 2$ are illustrated in Fig.4.4(b). We observe the peak at $\beta_* = 3.41020$ (rather than at $\beta_* = 3.62810$ as for the vertical separation $\eta d = 1$) and two additional peaks, one at a much lower frequency of $\beta_* = 1.95200$, and the other at a higher frequency ($\beta_* = 4.633083$) and with a significantly higher Q-factor of 539. The reason for the very sharp peak at $\beta_* = 4.633083$ is its proximity in frequency to very high reflectance for a single grating of rigid pins for $\theta_i = 0°$. It is precisely this alignment that enhances the Fabry-Pérot effects (see Section 2.4.4).

Fig.4.4(b) illustrates two requirements for delivering high Q-factor transmission peaks: the first is that the reflectance of a single grating has to be close to unity, and the second is that the separation of the gratings has to be chosen to align the interference peak with the point of high reflectance. We note that the physics here for flexural waves is in keeping with that for optical waves (see Section 2.4.4 on Fabry-Pérot

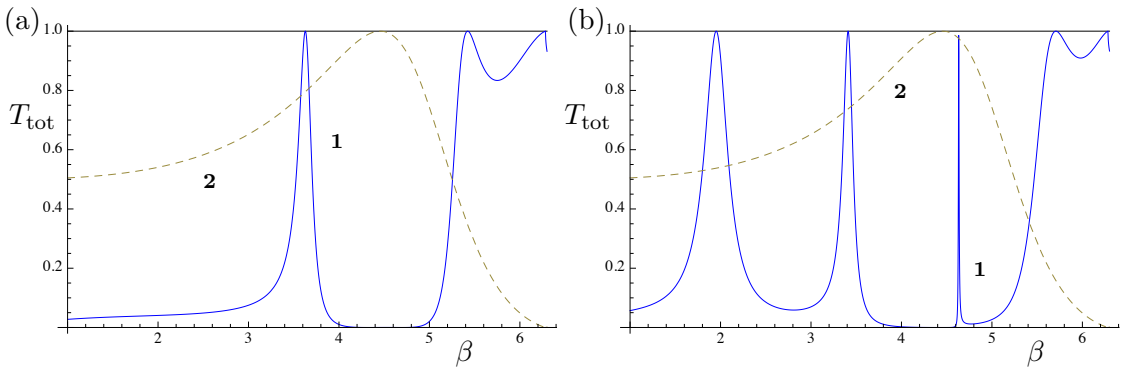

Figure 4.4: Total transmittance $T_{\rm tot}$ (curve **1**, solid blue) for a pair of rigid-pin gratings and total reflectance $R_{\rm tot}$ (curve **2**, dashed olive green) for a single grating of rigid pins as functions of β. Data used: (a) $\eta = 1$, (b) $\eta = 2$. Here $L = 0$.

theory and Born & Wolf 1959, Section 7.6).

4.2 Triplets of rigid-pin platonic gratings

We extend the stack to triplets of gratings as illustrated in Fig. 3.7. We analyse the effect of relative shifts on the spectral parameter β and the quality factor of the resonance. We compare the nature of the trapped modes arising from both doublets and triplets. We begin with a triplet that is constructed wherein the separation between each grating is unity and an overall symmetric geometry is obtained i.e. period $d = 1$ and relative grating separation $\eta = 1$. Two initial geometries are analysed for $\theta_i = 30°$. The first contains three parallel, aligned gratings ($\xi = 0$), and therefore may be considered to consist of two pairs of aligned gratings. Since the separation of the outer gratings is 2, comparison is also made with the pair for $\eta = 2$. The other triplet contains three identical gratings, but with the middle layer incorporating a relative shift of $\xi = 0.5$. This configuration comprises two shifted pairs, and once again the outer gratings are effectively aligned gratings with $\eta = 2$.

Referring to Fig. 3.7, we observe that the horizontal axis $y = 0$ acts as a line of symmetry for the grating stack. In treating diffracting systems with up-down symmetry, it is of value to break the diffraction problem up into symmetric and anti-symmetric parts (see Fig. 4.5), where two types of trapped modes are characterised by their symmetry and anti-symmetry about $y = 0$ (McPhedran & Maystre 1977, Botten *et al.* 1985, Popov *et al.* 1986). The general incidence, illustrated in Fig. 4.5(a), is the superposition of the anti-symmetric and symmetric incidences shown in Figs. 4.5(b) and (c), subject to a constant multiple, i.e. (a) $= \frac{1}{2}$ [(b) + (c)]. For the frequency region where only zeroth orders in reflection and transmission propagate and where complex amplitudes are evaluated with respect to an origin at the centre of symmetry, the consequences of symmetry were discussed in McPhedran & Maystre (1977). We note that in our

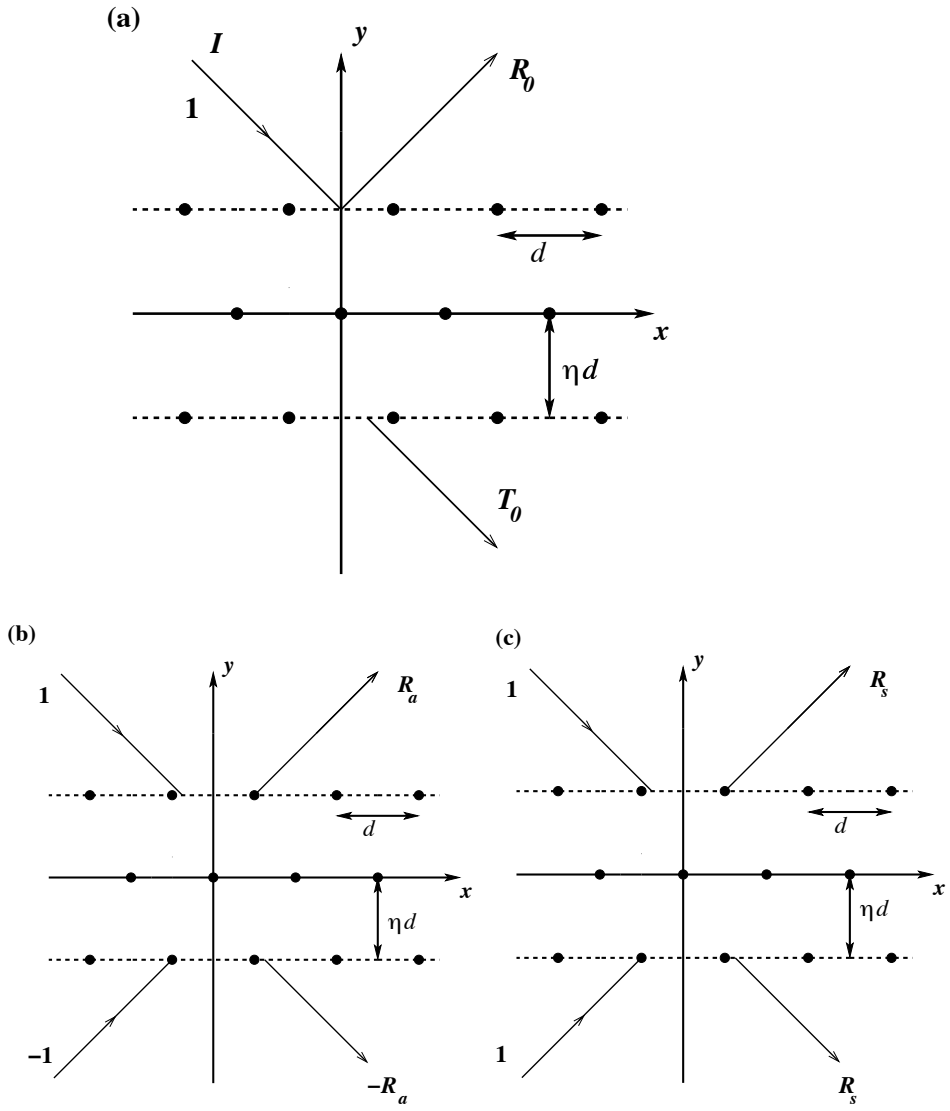

Figure 4.5: (a) General incidence for the scattering problem for a symmetric triplet with a shifted middle grating. $\boldsymbol{I}$ represents the incident plane wave with amplitude 1, and R_0 and T_0 denote complex amplitudes for zeroth order in reflection and transmission. (b) Anti-symmetric incidence for a stack of three parallel gratings with a shifted middle grating. The modes are odd functions of y. The amplitudes of the incident waves are 1 above and -1 below the triplet, and R_a and $-R_a$ are the corresponding complex amplitudes for zeroth order reflection. (c) Symmetric incidence for a shifted triplet. The modes are even functions of y. Here R_s is used to denote the complex amplitudes for zeroth order reflection for this symmetric case.

problem, the reflected and transmitted zero-order amplitudes differ in phase by $\pm\pi/2$, as in McPhedran & Maystre (1977).

4.2.1 Numerical results for symmetric triplets

In Fig. 4.6, we show the transmission resonance peaks for geometries which possess the full symmetry (Popov *et al.* 1986) that permits resonances in which the transmittance varies from zero to unity. We consider more general shifts later. In Fig. 4.6(a), we plot $T_{\rm tot}$ (see equation (3.93)) versus β for $\xi = 0$ (blue curve) and $\xi = 0.5$ (green dashed curve). Each triplet supports two localised resonances for β in the range $1.2 - 4.2$, with one fixed resonance always at $\beta_* = 3.61747$, and the other varying in frequency with the shift. The shared transmission mode has a much higher Q (see Fig. 4.6 (a)).

We also observe a transmission resonance for the frequency $\beta_* = 3.61747$ for the *pair* of unshifted gratings with $\eta = 2$. This is to be expected since the triplet is made up of an outer pair of parallel gratings and a shifted middle grating whose effect is cancelled out by the anti-symmetry, as in Fig. 4.5(b). In effect, the middle grating is not "seen". All three enhanced transmission resonances are shown in detail in Fig. 4.6(b).

The other two resonant frequencies for the triplets occur at $\beta_* = 3.56573$ and 3.68599, the first for the unshifted triplet and the latter for the triplet with the shifted middle grating (see Fig. 4.6(a)). These frequencies are similar to the resonance frequencies for the corresponding pairs of unshifted and shifted gratings (3.58221 and 3.65970 respectively) shown in Fig. 4.1.

This correspondence is explained by the symmetric geometry of the triplet. It is effectively made up of two pairs of shifted pairs. Both of these pairs allow for "trapped" modes at the same resonance wavenumber β_* and thereby support the enhanced transmission across the 3-grating system. The numerical difference (less than 1%) arises in the transmission problem due to the inclusion of evanescent modes in our model, which allows for some field coupling between the gratings. In Fig. 4.7, we show these transmission resonances for a shift of half the period. The proximity of the peaks is evident, as is the Fano nature of the resonances, which is more pronounced for the resonance arising from the pair of shifted gratings (solid line). This spike displays the higher Q (over 9,000).

4.2.2 Odd and even modes

Three-grating systems support two transmission resonances, characterised by symmetric and anti-symmetric vibration modes, so that the flexural wave within the triplet is an even or odd function of y, respectively. For the general shift, we observe both the odd mode's resonance at $\beta_* = 3.61747$ (straight line in Fig. 4.8), and the same correlation for the even mode's transmission peak and the corresponding shifted pair. This is shown in Fig. 4.8, where we plot β_* versus ξ for shifted pairs (green dashed

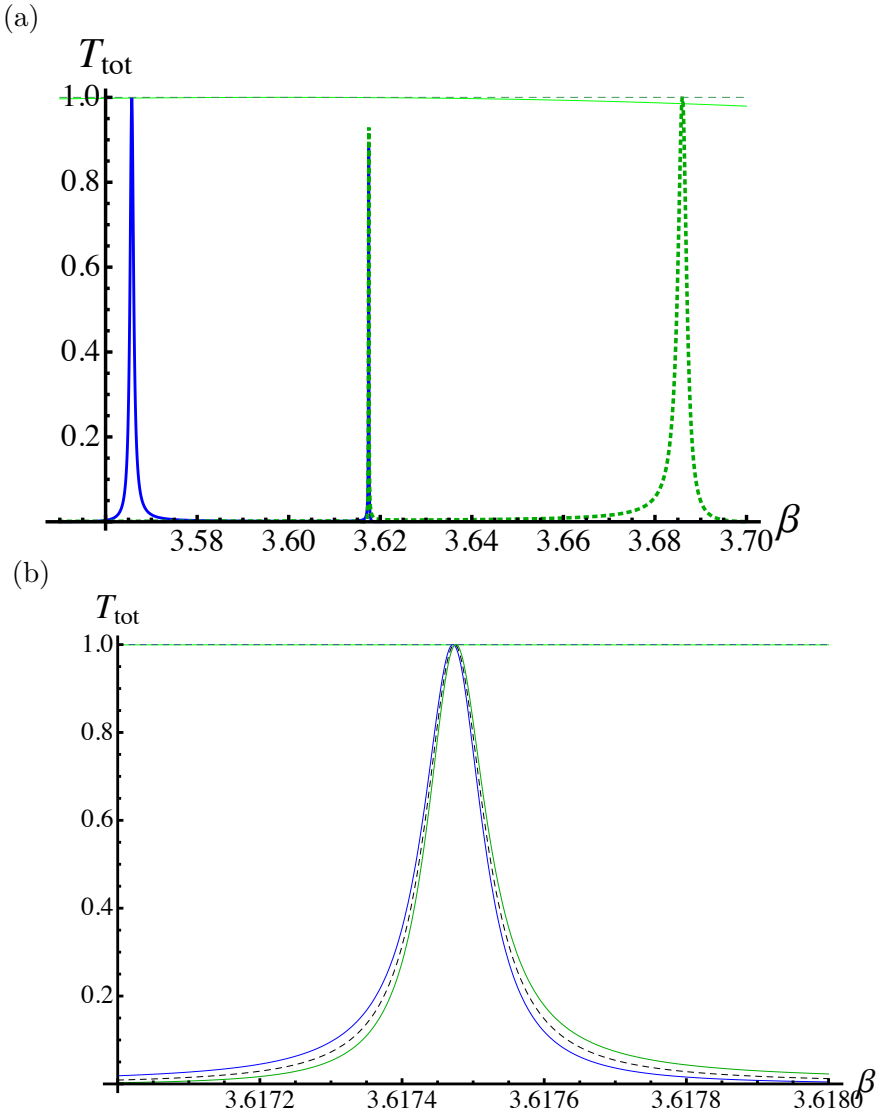

Figure 4.6: (a) T_{tot} versus β for aligned and shifted triplets for $\theta_i = 30°$ and $d = 1$. The central spike represents a trapped mode for both geometries. The peak on the right (dotted green) occurs for the triplet with the shifted middle grating ($\xi = 0.5$) and the peak on the left (solid blue) occurs for the geometry with three aligned gratings with $\xi = 0$. The grating separation is $\eta = 1$ for all consecutive gratings. Also shown is R_{tot} versus β for a single grating and a straight line (dashed) indicating maximum normalised energy of 1. (b) T_{tot} versus β in the region of $\beta_* = 3.61747$. Three geometries are virtually coincident: pair of unshifted gratings with $\eta = 2$ (dashed black curve), triplet of aligned gratings (solid blue curve) and triplet with shifted middle grating ($\xi = 0.5$) with $\eta = 1$ between each pair (solid green curve).

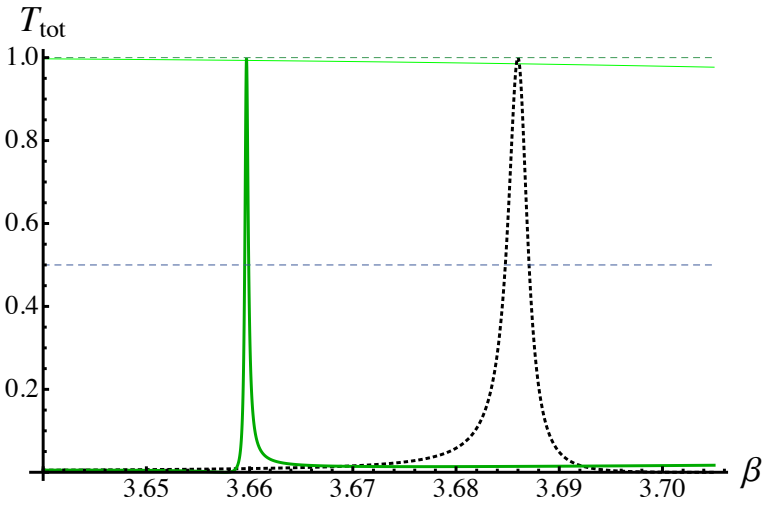

Figure 4.7: Transmission resonances for symmetric trapped mode for a triplet with shifted middle grating $\xi = 0.5$ (dotted curve), with $d = 1$ and $\eta = 1$ between each grating, and a pair of shifted gratings ($\xi = 0.5$) with $d = 1$, $\eta = 1$. In both cases, $\theta_i = 30°$.

curve) and the symmetric trapped modes for the triplets with a shifted middle grating (blue solid curve).

For a triplet with outer gratings separated by $\eta d = 2$, but with the middle grating placed away from $y = 0$, we break the symmetry that was discussed in Sections 3.2.3 and 4.2.1 (Popov *et al.* 1986, McPhedran & Maystre 1977). This removal of the centre of symmetry results in the reduction of the system's ability to facilitate enhanced transmission (see Fig. 4.9). The numerical computations do not produce enhanced transmission peaks with high Q for only small deviations from the symmetrical geometries we have discussed.

4.2.3 Quality factors for the trapped modes

We have noted the correspondence between trapped modes arising at the same value of β for pairs and triplets. It is interesting to determine which geometry produces the sharper transmission resonance. In Section 4.1, we noted the extraordinarily high quality factors arising from pairs of gratings. For the triplets, we still observe sharp resonances but they are not as pronounced as for the equivalent geometry with two gratings.

For the unshifted triplet, we record a quality factor of around $3,800$ for the symmetric trapped mode, which is below that of the equivalent localised mode for a pair of aligned gratings (around $5,400$). For the shifted triplet with $\xi = 0.5$, the symmetric mode's resonance quality factor is also down on the analogous pair, being around $1,600$ compared with $9,400$. This difference arises because of the increased coupling effect of evanescent modes since the triplets consist of two of the pairs we are comparing them

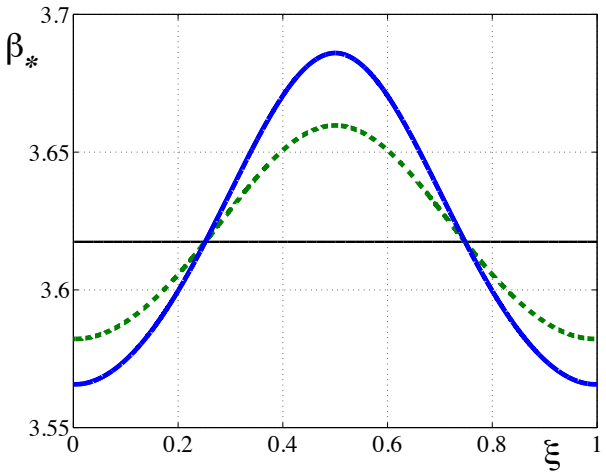

Figure 4.8: Resonant β_* representing trapped modes for horizontal shifts ξ in steps of 0.1 across a single unit period for both shifted pairs (green, dashed), and triplets with a shifted middle grating (blue, solid). For both geometries, $\theta_i = 30^\circ$ is considered. We also illustrate the fixed, anti-symmetric resonance with a horizontal straight line.

with. However, the anti-symmetric modes arising for both triplets, which are a more precise fit with the equivalent localisation for two aligned gratings since $\eta = 2$ for the outer pair in both cases, have extremely large and almost identical quality factors to the pair, being around $35,000$. The aligned triplet results in the marginally higher Q, being closer to $36,000$.

4.3 Double resonances and the analogy with EIT

As illustrated in Fig. 4.6, enhanced transmission occurs at frequencies corresponding to resonances of symmetric and anti-symmetric modes within the triplet of gratings. The frequency of the anti-symmetric mode is independent of the shift of the middle grating, whereas that of the symmetric mode changes with the shift ξ, as shown in Fig. 4.8. For an angle of incidence $\theta_i = 30^\circ$, the frequencies of symmetric and anti-symmetric modes coincide for the specific value of $\xi = 0.25200$, and have the common value $\beta_* = 3.61747$. We now discuss the double resonance effect associated with this particular geometry.

In Fig. 4.10(a) we show the transmittance for the three grating stack with the optimized shift ξ, and that for the outer pair of gratings (field plot shown in Fig. 4.10(b)). It will be noted that the pair of gratings has a transmission resonance reaching unity, while for the triplet the peak is suppressed, and replaced by a sharp minimum reaching down to zero. The presence of this minimum shows that the phases of the symmetric and anti-symmetric parts of the solution referred to in Section 4.2 differ by either 0 or

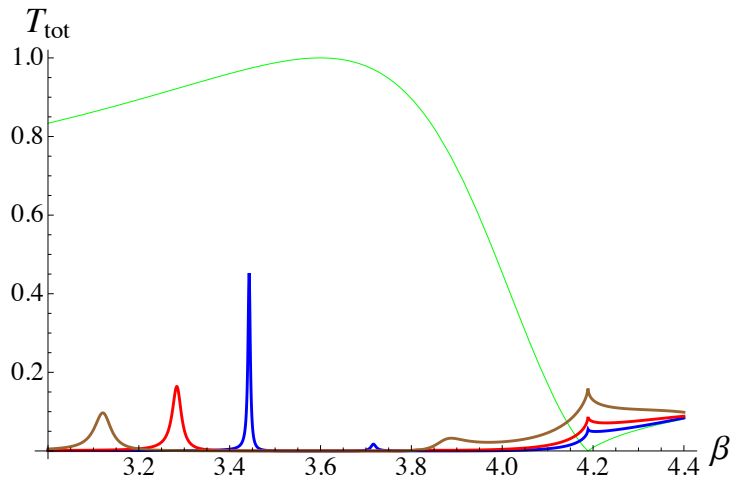

Figure 4.9: T_{tot} versus β for triplets for $\theta_i = 30°$, $d = 1$, $\xi = 0$, with various relative grating separation η. The outer gratings are separated by $\eta d = 2$. The brown curve represents the structure where the central grating is positioned at 35 % of the separation, with respect to the bottom grating. The red curve has the middle grating at 40 %, and the blue curve has its middle grating positioned 45 % into the separation with respect to the bottom of the triplet structure.

π. In the first case, the symmetric and anti-symmetric parts will add in the upper half of the triplet, but cancel in the lower half, preventing energy flow into the transmitted field region. The result is that the flux of energy into the region below the triplet is zero and the field above the triplet takes the form of a standing wave as illustrated in Fig. 4.10(c). In the second case, they will cancel in the upper half of the structure, leading to total reflectance off its upper surface.

We note that the normalised transmission energy is less than one (approximately 0.92) for the two identical peaks shown on Fig. 4.10. This is because of the extreme dip to zero transmission observed at $\beta_* = 3.61747$, and this notch has an extraordinarily high Q-factor of over $36,000$. The dashed lines, indicating the half-power and full-power points, clearly illustrate the extreme sharpness of this dip.

The phenomenon of electromagnetically induced transparency (EIT) is a quantum-mechanical effect which arises in three-level atomic systems (see Section 2.4.5). It involves a peak in absorption of a probe beam, which is suppressed by the addition of a coupling beam which creates a "window of transparency" for the probe beam. The curve of absorption versus frequency for EIT bears a striking resemblance to the transmittance curve of Fig. 4.10. Corresponding factors between EIT and our double resonance phenomenon are the three levels (read three gratings), the creation of destructive interference (in EIT due to the choice of atomic system and the coupling beam, in our double resonance, the accurate control of the shift parameter) and the very high Q-factors attainable. Differing factors are that our double resonant system does not absorb, and that it does not need separate probe and control beams. Never-

theless, this analogy between EIT and the double resonant grating stack illustrates the intrinsic wave nature of quantum mechanics.

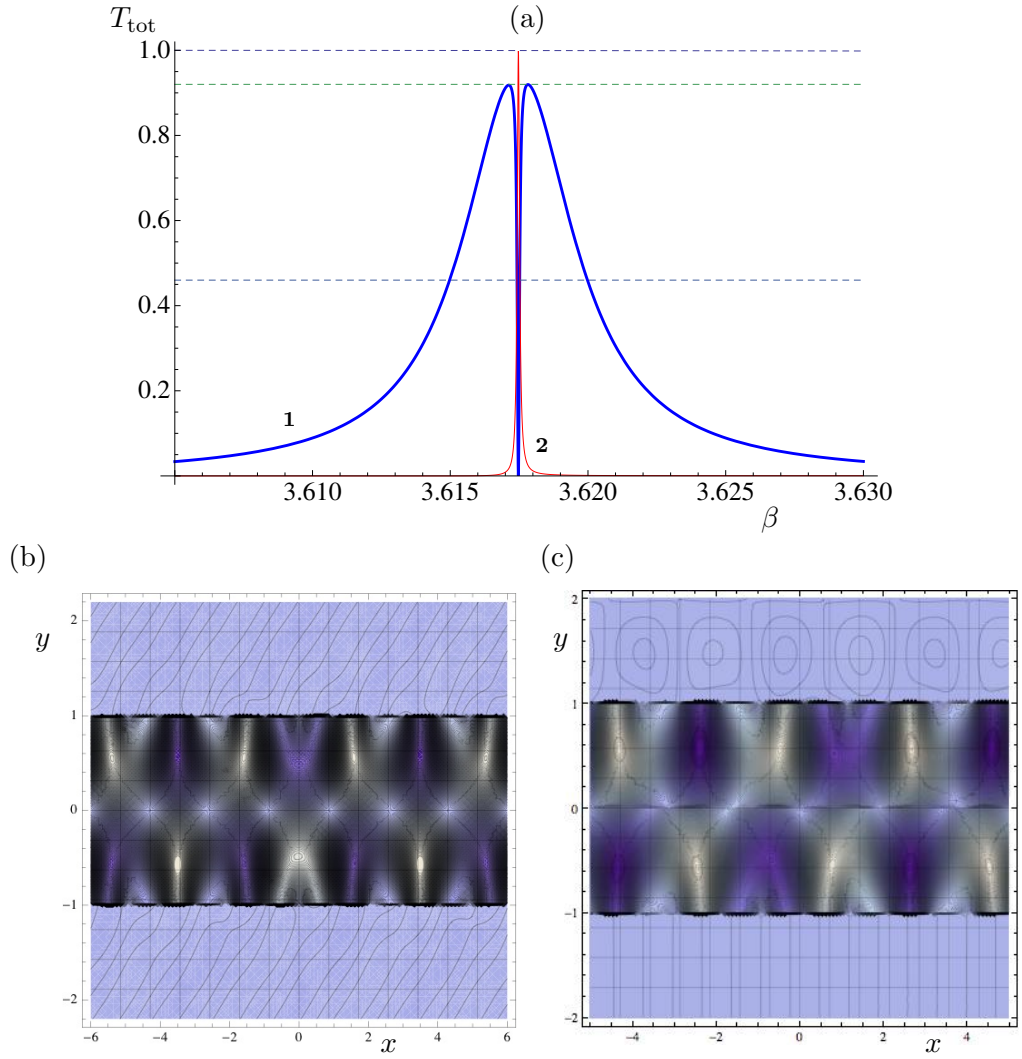

Figure 4.10: (a) EDIT effect for a triplet of rigid-pin gratings with the central grating shifted by $\xi = 0.25200$ for $\theta_i = 30°$. Normalised transmitted energy T_{tot} (blue curve **1**) as a function of β for the triplet. Curve **2** (red) is T_{tot} for the outer pair of gratings. (b) Flexural displacement for the outer pair of gratings of rigid pins ($\eta = 2$) as a function of x and y for $\beta_* = 3.61747$. (c) Flexural displacement for the triplet of rigid-pin gratings ($\eta = 1$) as a function of x and y for $\beta_* = 3.61747$.

Additional remarks

Fig. 4.10(a) was the first published illustration of EDIT's characteristic central minimum bracketed by two transmission peaks. The destructive interference suppresses the total transmitted energy to be negligibly small at this minimum, explaining the label elasto-dynamically inhibited transmission adopted by Haslinger *et al.* (2013a). Chapter 5 extends analysis of transmission resonances and EDIT to nonzero-radius systems, and is based on the paper by Haslinger *et al.* (2013a).

Chapter 5

Nonzero-radius platonic grating stacks

The main emphasis of this chapter is how the radius of the gratings' voids or inclusions affects the multipole method of solution for the transmission problem. This case of finite radius rather than the limiting case of zero-radius fixed pins has two important implications. There is a greater relevance of the model to real-life applications, and there are significant differences in the implementation of the method of solution, and in the results of the illustrative examples. Much of the material here is based on our paper by Haslinger *et al.* (2013a), published in the *International Journal of Fracture*. The localisation of flexural waves within the grating system and the associated transmission resonance regimes are possible sources of fracture or structural failure.

The vibration of plates is relevant for studying the response of elastic systems to earthquakes and other dynamic loads, and many of these systems incorporate periodic arrangements of inclusions, voids or masses as part of their structural design. Examples include aircraft whose wings comprise panels riveted together in a periodic manner, as shown in Fig. 5.1. Other structures incorporating periodic arrays are bridges, railways and reinforced roads, although in the latter case this is primarily a doubly periodic example.

All of these cases concern structures that accommodate vibrational plane waves that propagate in the plane of the plate, with their amplitudes perpendicular to the plane. It is important to be aware of the possibility of transmission resonances generated by the trapping of waves within the grating system, and to take appropriate measures during the design phase.

The chapter deals with localisation of flexural waves within gratings composed of both pinned points and rigid inclusions of finite radius in a structured plate. The effect of the finite size of inclusions on the dynamic localisation is analysed for the range of frequencies where only zeroth grating orders propagate. The structure of the resonant modes within gratings of inclusions is of special interest, and are illustrated using field plots. In particular, we consider the circumstances under which such gratings can

(a)  (b) 

Figure 5.1: Examples of periodic arrays in elastic systems incorporating plates (a) aircraft wings (www.instartupland.com) (b) cable-stayed bridge (Femern A/S, http://buildipedia.com).

deliver the EDIT effect.

We also mention that there have been related investigations involving transmission properties of electromagnetic waves through doubly periodic grids (Botten *et al.* (1985), Ulrich & Tacke (1973), Pelton & Munk (1979)). In these papers, square symmetric grids illuminated by normally-incident plane waves exhibited a resonant transmission maximum, whereas for slightly off-normal incidence, the transmission maximum was bisected by a zero of transmission. It was shown that this was due to the presence of a mode with the opposite symmetry (odd) to that of the resonant mode for normal incidence (even), the former not being able to couple to the incident wave. However, for off-axis angles, its coupling coefficient became nonzero, and the null of reflectance was then caused by the resonances of the even and odd modes coinciding and cancelling each other. The paper of Botten *et al.* (1985) gives information on the phase as well as amplitude of reflection and transmission coefficients, and also remarks that the resonance of the even mode can involve the carriage of more than 100% of the incident energy in the downward direction (i.e. parallel to the incident wave), since the odd mode resonance involves energy being carried upwards (i.e. anti-parallel to the incident wave).

The symmetry of the localised field is affected by the scattering from the inclusions of nonzero radius. As noted in Section 4.2 an anti-symmetric resonance mode, where displacements are equal to zero along the neutral line within the triple of rigid pins, is unaltered for the case of a horizontal shift of the middle grating; this is no longer the case for the situation when the middle grating consists of rigid inclusions of finite radius.

In Section 5.1 we give a brief overview of the governing equations and the method of solution for the scattering of a flexural wave by a finite set of gratings of nonzero rigid inclusions. The studies that follow Section 5.1 address interaction of scatterers of finite radius. We show that the EDIT phenomenon can still be obtained for the

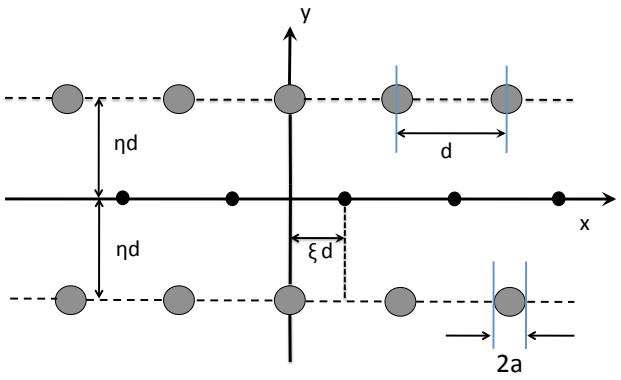

Figure 5.2: Stack of gratings consisting of an outer pair of finite nonzero inclusions of radius a and period d and a central grating of rigid pins characterised by the relative lateral shift ξ. The relative grating separation between consecutive gratings is η.

configuration in which the central grating has rigid pins and the outer gratings have finite radius scatterers. Parameters of the system which enable the quality factors of transmission and reflection resonances to be controlled are identified, and flexural wave patterns within the grating stack are exhibited.

5.1 Governing equations: scattering by a single grating

For the case of stacks of gratings containing voids with clamped boundaries or rigid inclusions of finite radius a, rather than fixed pins, most of the governing equations are the same as outlined in Sections 2.1, 2.2 and 3.1 to 3.2. However the analysis of Section 3.1.6 is no longer sufficient, and it is necessary to take into account higher-order multipole terms characterising the scattered field, and higher-order grating sums related to the periodicity of the gratings when considering the equations (3.26), (3.27) and (3.41)-(3.44). The account of the theory given below is kept to the bare minimum and further details can be found in the aforementioned sections.

We repeat the governing biharmonic plate equation (2.2) and its factorized form for the convenience of the reader:

$$\Delta^2 W(\mathbf{x}) - \beta^4 W(\mathbf{x}) = (\Delta + \beta^2)(\Delta - \beta^2)W = 0, \tag{5.1}$$

where W is the amplitude, and $\beta^2 = \omega\sqrt{\rho h/D}$. Figure 5.2 shows a sample configuration of nonzero-radius and rigid-pin scatterers, which serves to highlight important parameters characterising the grating structure and emphasise the role of the radius a. The stack of gratings comprises two or three elements, each assumed to be periodic, of period d, in the horizontal direction, and typically the gratings are separated by

the common distance ηd in the vertical direction where η denotes the relative grating separation. The successive gratings again have a relative horizontal shift, denoted by ξ in Fig. 5.2.

As in equations (2.47), the boundary conditions for each rigid inclusion are

$$W\Big|_{r=a} = 0, \quad \frac{\partial W}{\partial r}\Big|_{r=a} = 0, \tag{5.2}$$

where r represents the distance from the centre of the inclusion. Physically the above boundary conditions represent clamping on the rigid boundary. In particular, when the radius a tends to zero we retrieve the case of fixed pins discussed extensively in Chapters 3 and 4.

A plane incident wave is propagating towards the grating in the upper half-plane. The equations for the plane wave representations of the incident and scattered fields are given by equations (2.6) to (2.12). The periodicity of the structure in the horizontal direction and the parameters of the incident wave are represented by the familiar quasi-periodicity condition (see Section 2.3) for W along the horizontal axis:

$$W(\mathbf{x} + md\mathbf{e}^{(1)}) = W(\mathbf{x})e^{i\alpha_0 md}, \tag{5.3}$$

where m is an integer and d is the period.

We now apply the multipole method used to treat the scattering of the plane incident waves, either of the Helmholtz type (3.5) or of the modified Helmholtz type (3.6), by a grating of inclusions of radius a. As in Section 3.1, the flexural displacement W is expanded for $y > a$ and $y < -a$ in terms of sums of plane waves (W_H) and modified plane waves (W_M). In order to connect these two expansions, multipole expressions for W are introduced in the region $-a \leq y \leq a$. The multipole expansion for W_H involves cylindrical Bessel functions and the multipole expansion for W_M involves modified Bessel function terms (see equations (3.8) and (3.9)).

The Rayleigh system (3.26), (3.27) is derived as in Section 3.1.3, and the summation is run from $-L$ to L, with L being the order of truncation. The number of terms used in the grating sums is $4L + 2$, as mentioned in Section 3.1.3. An important aspect of the grating sums is the necessity for convergence formulae for those terms that are not exponentially convergent. As outlined in Section A.1, we use formulae based on those of Twersky (1961), and their implementation becomes more complicated for larger values of radius a. We discuss this in more detail below, but first review the case of rigid pins.

5.2 Transmission and reflection properties of a single grating

For a single grating of rigid pins, a monopole expansion is sufficient to determine the reflected and transmitted energies of an incident plane wave to great accuracy. This

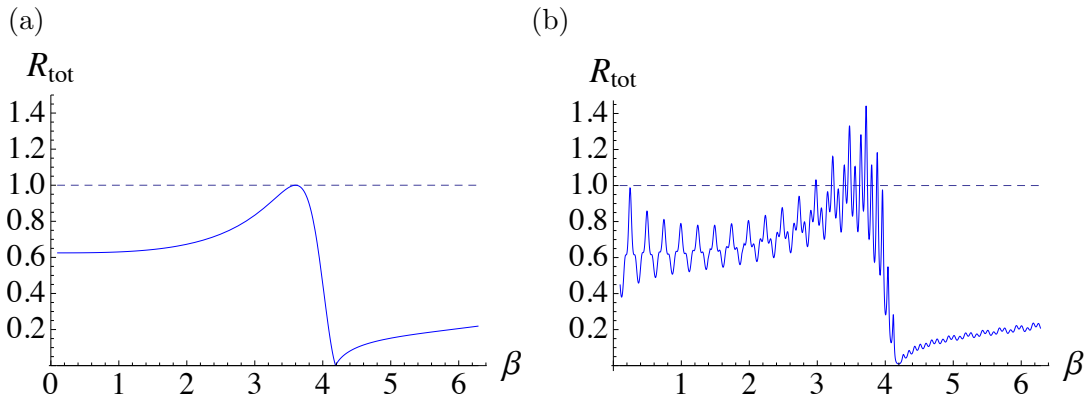

Figure 5.3: Normalised reflected energy versus spectral parameter β for $\theta_i = 30°$ for a single grating of voids with radius $a = 0$ using (a) quasi-periodic grating Green's function and (b) direct summation of grating sums.

was explained in Sections 2.6.1, 3.1.3, 3.1.6 and A.1, where the quasi-periodic Green's function (2.95), (2.103) for a single grating of rigid pins is used to evaluate the expansion for the monopole case. It is sufficient to use only a few terms in the grating sum as illustrated in Fig. 5.3 where the reflected energies for a grating obtained using both the Green's function sum and the direct sum are compared. The Green's function for the biharmonic operator is finite at the origin, not singular as is the case for the two-dimensional Helmholtz operator. Consequently we obtain the smooth curve for the reflected energy in Fig. 5.3(a) rather than the oscillatory behaviour observed for the direct summation in Fig. 5.3(b).

For the case of nonzero radius, more multipole terms are required in the expansions. This in turn means that more terms are needed in the grating sums. We also use an accelerated convergence for these grating sums, based on Twersky's formulae (see Section A.1 and Twersky 1961). The larger the radius a, the greater the number of terms required.

We consider some examples of single gratings whose voids or inclusions have a nonzero radius $a > 0$. For $a = 0.01$ shown in Fig. 5.4(a),(b) we show the results for the normalised reflected and transmitted energies for both the direct sums and the Twersky accelerated convergence formulae. The difference between the direct summation and the accelerated sum is more pronounced than in the case of fixed pins (Fig. 5.3), but it is particularly striking that the direct summation graph is obtained using 200 terms whilst the Twersky formulae produce the converged result of Fig. 5.4(b) with only two terms. Indeed for additional terms, the same result is observed.

The other important observation from Fig. 5.4 is that the reflected energies for the range $0 < \beta < \beta^{\max}$ (where $\beta^{\max}$ denotes the maximum single grating reflectance) are higher than for the corresponding case with rigid pins shown in Fig. 5.3. This is a feature common to nonzero-radius cases, as shown by Fig. 3.3 in Section 3.1.3, and as

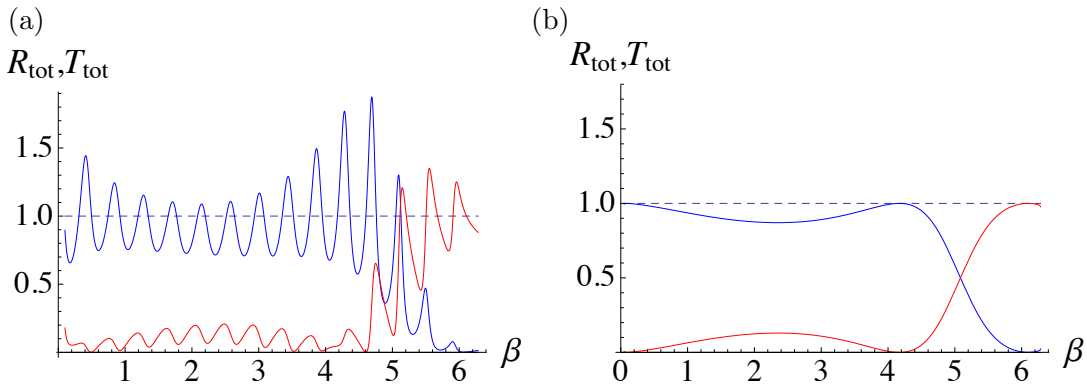

Figure 5.4: Normalised reflected (blue) and transmitted (red) energy versus spectral parameter β for $\theta_i = 30°$ for a single grating of voids with radius $a = 0.01$ using (a) direct summation of grating sums and (b) Twersky accelerated convergence formulae.

radius a increases, the reflected energies become greater.

5.3 Transmission resonance for pairs of aligned gratings: normal incidence

Here we consider the filtering action in the transmission of flexural waves by systems of two gratings of inclusions, with both of the gratings aligned. We concentrate on the effects of inclusion radius a and relative vertical separation η between gratings on the filtering action, characterised by the Q-factor[1] of the transmittance peak.

The increase of the radius of inclusions within the gratings affects the scattered fields; this consequently leads to the change in the frequency of the resonance mode as well as its Q-factor. The analytical representation of the physical fields between the gratings incorporates multipole representations (3.8) and (3.9) outlined in Section 3.1.2.

The formulae for transmission and reflection matrices were already obtained for a single grating, together with the formulae for the transmission and reflection matrices for a pair of identical gratings (see equations (3.91), (3.92) here).

$$\boldsymbol{\mathcal{T}}_2 = \boldsymbol{\mathcal{T}}_1[\mathbf{I} - (\boldsymbol{\mathcal{R}}_1)^2]^{-1}\boldsymbol{\mathcal{T}}_1,$$

$$\boldsymbol{\mathcal{R}}_2 = \boldsymbol{\mathcal{R}}_1 + \boldsymbol{\mathcal{T}}_1\boldsymbol{\mathcal{R}}_1[\mathbf{I} - (\boldsymbol{\mathcal{R}}_1)^2]^{-1}\boldsymbol{\mathcal{T}}_1. \tag{5.4}$$

The matrices $\boldsymbol{\mathcal{T}}_i$, $\boldsymbol{\mathcal{R}}_i$ comprise the matrices $\mathbf{T}_i$ and $\mathbf{R}_i$ respectively, where $i = 1, 2$, which are formed using the coefficients for the plane wave representations (3.41)-(3.44), together with a diagonal propagation matrix $\boldsymbol{\mathcal{P}}$:

$$\boldsymbol{\mathcal{R}}_i = \boldsymbol{\mathcal{P}}\mathbf{R}_i\boldsymbol{\mathcal{P}}, \ \boldsymbol{\mathcal{T}}_i = \boldsymbol{\mathcal{P}}\mathbf{T}_i\boldsymbol{\mathcal{P}}. \tag{5.5}$$

[1]For a resonant peak of transmittance T occurring at $\beta = \beta_*$ with $T = T_{\max}$ there, if $T = T_{\max}/2$ for $\beta = \beta_+$ and β_-, then $Q = \beta_*/|\beta_+ - \beta_-|$.

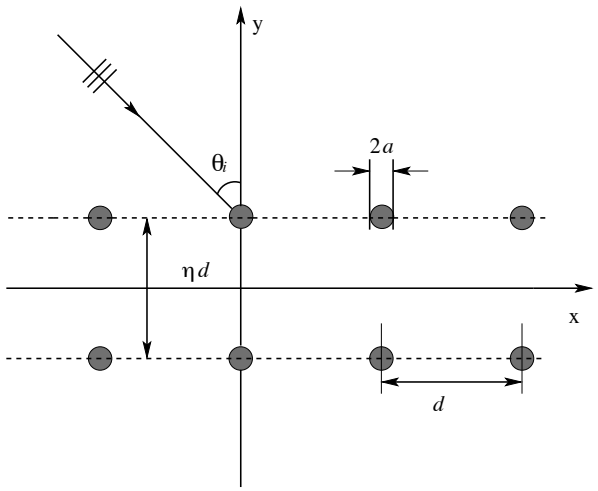

Figure 5.5: Pair of gratings consisting of inclusions of finite radius a, with period d and relative grating separation η.

For the unshifted pair, this propagation matrix $\boldsymbol{\mathcal{P}}$ changes with the change of the relative vertical separation η between the gratings,

$$\boldsymbol{\mathcal{P}} = \begin{pmatrix} P & 0 \\ 0 & P \end{pmatrix}, \qquad \text{where} \qquad P = [\delta_{tp} e^{i\tilde{\chi}_p \eta d/2}], \tag{5.6}$$

with $\tilde{\chi}_p = \chi_p$ if p corresponds to a Helmholtz type plane wave and $\tilde{\chi}_p = \hat{\chi}_p$ if p corresponds to a plane wave of modified Helmholtz type. In contrast, the scattering matrices $\mathbf{T}_i$ and $\mathbf{R}_i$ change with β.

5.3.1 Examples for various nonzero radii

For the purpose of illustration, we consider several configurations. A symmetric pair of gratings of inclusions of finite radius is shown in Fig. 5.5. The geometrical dimensions are normalised so that the distance d between the centres of inclusions is unity. Table 5.1 gives a summary of the resonance frequencies for different configurations for the case of normal incidence.

The resonant wavenumber corresponding to the peak in transmission is denoted by β_*. For very high Q resonances, additional decimal places are required to evaluate the spectral parameter β_* because the sampling, needed to identify the characteristic values of the spectral parameter, must be much finer. The first line in Table 5.1 corresponds to the pair of gratings of rigid pins featured in Chapter 4.

Throughout this thesis we consider the range of β values for which only the zeroth order plane waves in reflection and transmission propagate i.e. $p = 0$. For zero-radius pins, it is sufficient for the corresponding order of truncation L to be zero. Accordingly, the total energy transmitted T_{tot} is defined by $|T_0|^2$, with $|T_0|$ being the amplitude of the zeroth order transmission coefficient (see equation (3.93)). Similarly, the total

Table 5.1: Resonant frequencies β_* and the corresponding Q-factors for various pairs of unshifted gratings for normal incidence. In this table, $d = 1$.

a	η	Resonant wavenumber	Q
0	1	$\beta_* = 3.62810$	20.0
0	2	$\beta_*^{(1)} = 1.95200$	6.19
		$\beta_*^{(2)} = 3.41020$	25.2
		$\beta_*^{(3)} = 4.63308$	539
0.01	1	$\beta_* = 3.82890$	208
0.01	2	$\beta_*^{(1)} = 2.13669$	33.4
		$\beta_*^{(2)} = 3.53658$	138
		$\beta_*^{(3)} = 4.72190$	76.6
0.02	1	$\beta_* = 3.90296$	477
0.02	2	$\beta_*^{(1)} = 2.17529$	50.8
		$\beta_*^{(2)} = 3.57980$	219
		$\beta_*^{(3)} = 4.76865$	68.2
0.1	1	$\beta_* = 4.5572187$	6.51×10^4
0.1	2	$\beta_*^{(1)} = 2.40631$	617
		$\beta_*^{(2)} = 3.925255$	1.19×10^3
		$\beta_*^{(3)} = 5.23749$	202

reflectance R_{tot} is equal to $|R_0|^2$. However as the radius of the inclusion is increased, more terms are required in the grating sums thereby increasing L.

For a grating of inclusions of radius $a = 0.1$, Figure 5.6(a) shows that the transmission resonance for a pair of gratings lies in the region of β values where the reflectance of a single grating is very close to unity. This results in a high Q-factor (6.51×10^4) for the pair of such gratings. By comparison, for a pair of gratings with inclusions of radius $a = 0.01$ (Fig. 5.6(b)), the Q-factor is 208, with the peak in transmitted energy for a pair being significantly separated from the reflectance peak for a single grating.

5.3.2 Convergence properties

As mentioned in Section 3.1.5, energy is conserved regardless of the number of terms used in the grating sums. Convergence affects the value of β for the transmission resonances of the grating systems. As we have already stated, the greater the value of a, the more terms are required in the grating sums. We include a convergence table 5.2 for the case of $a = 0.2$ for normal incidence for a pair of gratings with $\eta = 1$ and $\xi = 0$. The order of truncation L determines the number of multipoles $2L+1$ and the number of terms in the grating sums is denoted by N.

As discussed in Sections 2.5.4 and 3.1.3, the minimum number of terms required for convergence is $N = 4L+2$. Table 5.2 includes values of $N > 4L+2$ and shows how

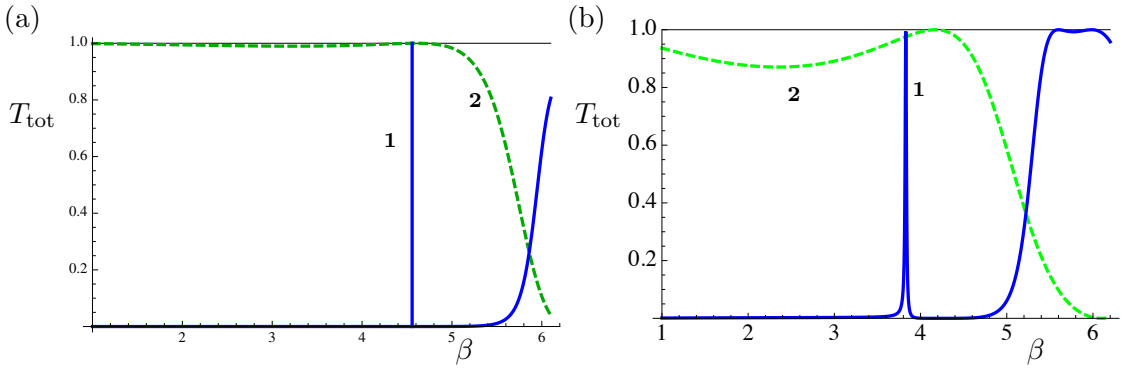

Figure 5.6: Normalised transmitted energy $T_{\rm tot}$ (curve **1**, solid blue) for a pair of gratings of inclusions of radius a and normalised reflected energy $R_{\rm tot}$ (curve **2**, dashed green) for a single grating of inclusions as functions of β for separation $\eta d = 1$ and $L = 2$. Data used: (a) $a = 0.1$, (b) $a = 0.01$.

Table 5.2: Resonant frequencies β_* and the corresponding Q-factors for normal incidence for a pair of unshifted gratings with $a = 0.2$ and $\eta = 1$. In this table $d = 1$, L is the order of truncation and N is the number of terms used in the grating sums.

N	L	Resonant wavenumber	Q
14	2	$\beta_* = 5.588509$	2.23×10^3
	3	$\beta_* = 5.628505$	1.68×10^4
	4	$\beta_* = 5.6344885$	1.065×10^4
	5	$\beta_* = 5.6346574$	1.076×10^4
	6	$\beta_* = 5.6346574$	1.076×10^4
	7	$\beta_* = 5.6346574$	1.076×10^4
20	2	$\beta_* = 5.588637$	2.245×10^3
	3	$\beta_* = 5.6286498$	1.716×10^4
30	2	$\beta_* = 5.588709$	2.253×10^3
	3	$\beta_* = 5.628729$	1.736×10^4
	4	$\beta_* = 5.6347141$	1.09×10^4
	5	$\beta_* = 5.6348829$	1.103×10^4
	6	$\beta_* = 5.6348829$	1.103×10^4
	7	$\beta_* = 5.6348829$	1.103×10^4
40	2	$\beta_* = 5.588733$	2.255×10^3
	3	$\beta_* = 5.6287572$	1.7425×10^4

Table 5.3: Resonant frequencies β_* and the corresponding Q-factors for various pairs of unshifted gratings for examples of oblique incidence. In this table $d = 1$.

θ_i	a	η	Resonant wavenumber	Q
30°	0	1	$\beta_* = 3.58221$	5.42×10^3
30°	0	2	$\beta_*^{(1)} = 3.6174737$	3.55×10^4
			$\beta_*^{(2)} = 2.15950$	10.4
30°	0.01	1	$\beta_* = 3.86164$	238
30°	0.05	1	$\beta_* = 4.18486$	253
20°	0.01	1	$\beta_* = 3.8507342$	2.23×10^4
20°	0.05	1	$\beta_* = 4.1606161$	2.57×10^3
15°	0.1	2	$\beta_*^{(1)} = 4.011852$	1.75×10^3
			$\beta_*^{(2)} = 2.45092$	639
10°	0.1	2	$\beta_*^{(1)} = 3.963273$	1.40×10^3
			$\beta_*^{(2)} = 2.42564$	626

the convergence of the resonance value β_* depends on L and N.

5.4 Transmission resonance for pairs of aligned gratings: oblique incidence

With the introduction of nonzero angle of incidence, additional physical effects become apparent. Firstly, from equations (3.80) and (3.82) it follows that, if η is fixed and the angle of incidence θ_i increases, then χ_0 decreases and thus the resonant value β_* must increase to preserve the resonance transmission condition. Secondly, the range of β values in which only the zeroth order of diffraction propagate changes according to the equation

$$\beta_{-1} = \frac{2\pi}{d(1 + \sin\theta_i)}, \tag{5.7}$$

with β required to be smaller than β_{-1} (see equations (2.23)-(2.27) in Section 2.4.1). Thirdly, the angle of incidence θ_i may be used to bring the resonant frequency β_* for a pair of gratings into proximity with the value for peak reflectance of a single grating. Table 5.3 presents the results of computations of the resonance frequencies in transmission and of the quality factors for pairs of aligned gratings (of zero shift).

In Fig. 5.7 we give the transmittance curves for a pair of rigid-pin gratings with the separation being $\eta d = 2$ and with the angle of incidence $\theta_i = 30°$, with corresponding curves for $\eta d = 1$ being given by Fig. 3.5 in this thesis. With the doubling of the grating separation, the Q-factor goes up from 5.42×10^3 to 3.55×10^4. Note the very strong contrast in the quality factors of the two transmission resonances in Fig. 5.7(a), caused by the difference in the reflectance values of the single grating.

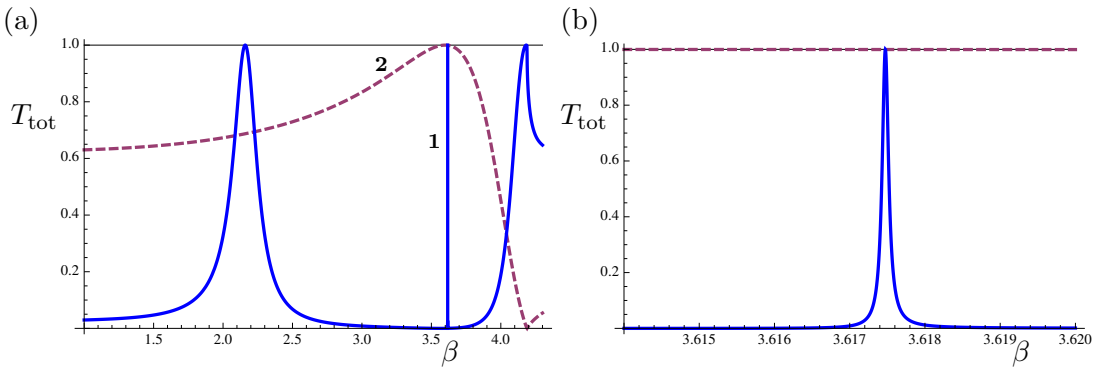

Figure 5.7: Normalised transmitted energy $T_{\rm tot}$ (curve **1**, solid blue) for a pair of rigid-pin gratings and normalised reflected energy $R_{\rm tot}$ (curve **2**, dashed red) for a single grating of rigid pins as functions of β. Data used: $\eta = 2$, $\theta_i = 30°$, $d = 1$ and $L = 0$. The diagram (b) is a blow-up of the sharp transmission resonance from (a).

For the particular inclusion radius $a = 0.1$ we show in Fig. 5.8 reflectance curves for a single grating for angles of incidence ranging from 0° to 30°. The possible frequency range, for which the interference peak may be aligned with the almost total reflectance, is $4.4 < \beta < 4.7$ for $0° \leq \theta_i \leq 15°$. Note that as the angle of incidence increases the reflectance peak moves closer and closer to the position of the Wood anomaly whose frequency is given by equation (5.7). Since this Wood anomaly marks the boundary of the region where two orders propagate in both reflection and transmission, it then becomes more and more difficult to choose parameters giving a sharp transmission resonance for a pair of gratings.

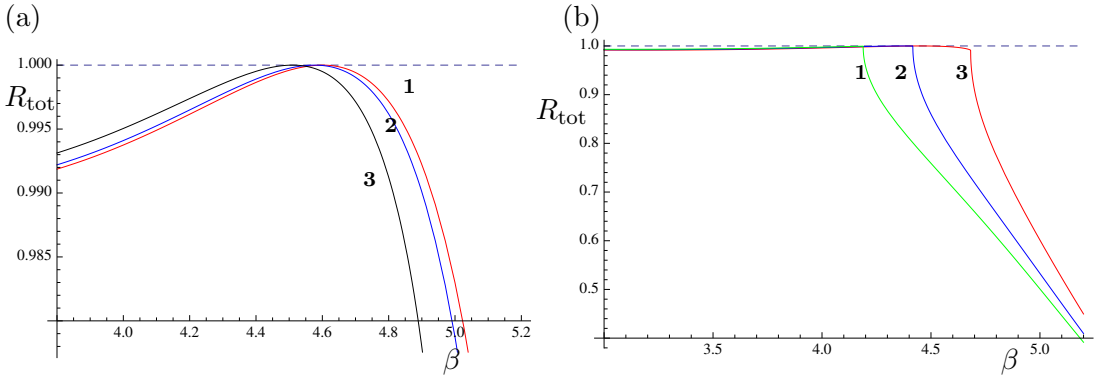

Figure 5.8: Normalised reflected energy $R_{\rm tot}$ as a function of β for a single grating with inclusions of radius $a = 0.1$ (with order of truncation $L = 2$) for the angle of incidence (a) $\theta_i = 0°$ (curve **1**, red), 7.5° (curve **2**, blue), 15° (curve **3**, black) and (b) $\theta_i = 30°$ (curve **1**, green), 25° (curve **2**, blue), $\theta_i = 20°$ (curve **3**, red).

5.5 Controlling transmission resonances for triplets of gratings

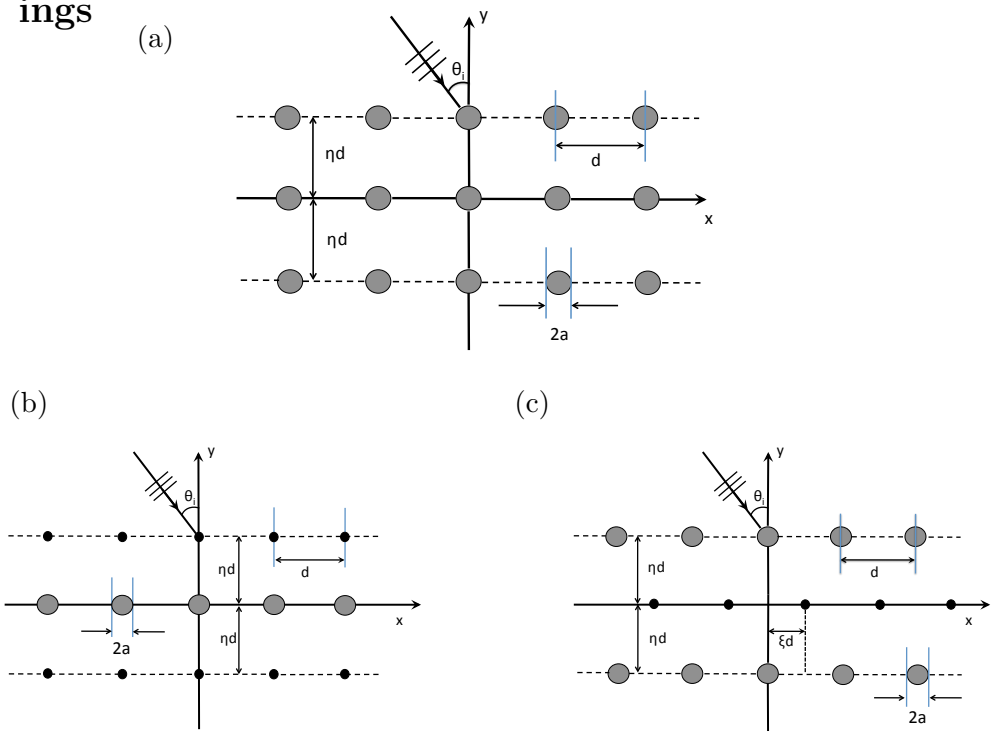

Figure 5.9: (a) Triplet consisting of three identical gratings of inclusions with nonzero radius a; (b) triplet consisting of a central grating of inclusions of nonzero radius a, surrounded by a pair of rigid-pin gratings; (c) triplet consisting of a pair of gratings with inclusions of nonzero radius a surrounding a grating of rigid pins.

In previous sections we have considered stacks in which all gratings were aligned. In this section we generalise the discussion to non-aligned stacks, recalling the recurrence procedure of Section 3.2 where the additional propagation matrix $\boldsymbol{\mathcal{Q}}$ is used to account for the lateral shift of the central grating. In the paper by Haslinger *et al.* (2012) the propagation matrices shift the phase origin of the reflection and transmission matrices by $\pm\eta d/2$ in the vertical direction and $\xi d/2$ in the horizontal direction. Smith *et al.* (2014) also place the phase origin halfway between the gratings whereas in this thesis, we adopt the formulae (3.87) associated with the choice of phase origin in Fig. 3.4. Either treatment is possible provided that the subsequent re-phasing is consistent with the original choice.

Three types of triplets are considered here:

- triplets of identical gratings consisting of inclusions with the same nonzero radius;

- triplets consisting of an outer pair of gratings of rigid pins with a central grating of inclusions with a nonzero radius;

- triplets with the central grating consisting of rigid pins surrounded by a pair of gratings with inclusions of nonzero radius.

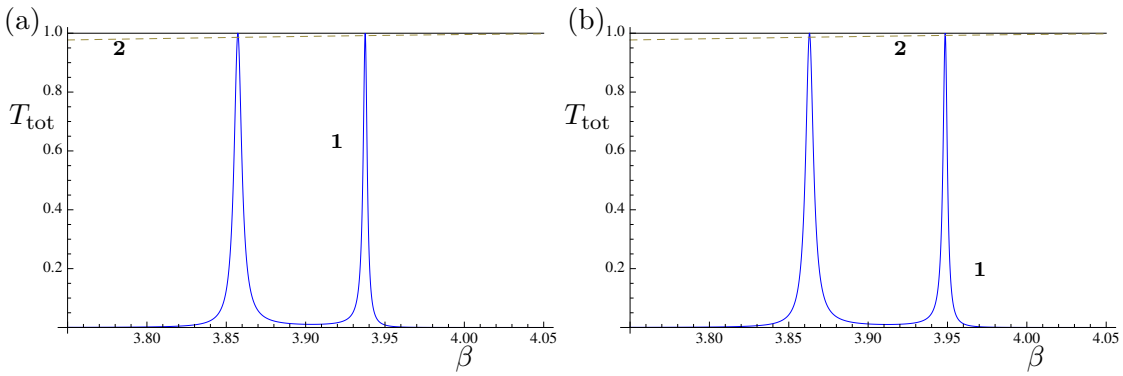

Figure 5.10: Normalised transmitted energy $T_{\rm tot}$ (curve **1**, solid blue) as a function of β for normal incidence for a triplet of gratings of inclusions with $a = 0.02$, $\eta d = 1$ and $L = 2$. Curve **2** (dashed) represents normalised reflected $R_{\rm tot}$ for a single grating of such scatterers: (a) aligned gratings, $\xi = 0$; (b) shifted central grating with $\xi = 0.2$.

The corresponding geometries are illustrated in Fig. 5.9.

5.5.1 Triplets of identical gratings

The results of computations of the transmitted energy, in normal incidence, for the triplet of gratings of small inclusions of radius $a = 0.02$, are shown in Figure 5.10. We observe a double peak, characterised by symmetric and anti-symmetric vibration modes, so that the flexural wave within the triplet is an even or odd function of y, respectively. A shift of the central grating results in a perturbative effect on the frequency for which enhanced transmission is observed. This shift in the double peak's frequency is illustrated in Fig. 5.10(b) where the central grating is shifted by $\xi = 0.2$ relative to the outer pair. Although the change in the resonance frequencies in the diagrams (a) and (b) appears to be small, we note that the anti-symmetric mode depends on the longitudinal shift for the case of inclusions of nonzero radius.

As a consequence of the symmetry of the grating stack, we deduce that the resonant flexural vibration modes are either symmetric or anti-symmetric. The flexural displacement for frequencies $\beta_*^{(2)} = 3.93753$ and $\beta_*^{(2)} = 3.948562$ for the right hand peaks in Fig. 5.10 correspond to anti-symmetric flexural modes, whereas the other two frequencies $\beta_*^{(1)} = 3.857309$ and $\beta_*^{(1)} = 3.863065$ correspond to symmetric flexural modes.

The results given here for inclusions of nonzero radius differ from those shown in Chapter 4 and by Haslinger *et al.* (2012) for triplets of rigid pins. One of the main differences is related to anti-symmetric flexural modes, which vanish on the central line of the grating stack. The frequency of the transmission resonance for anti-symmetric vibrations within the triplet of gratings of rigid pins is invariant with respect to a horizontal shift of the middle grating. This feature disappears when the radius of

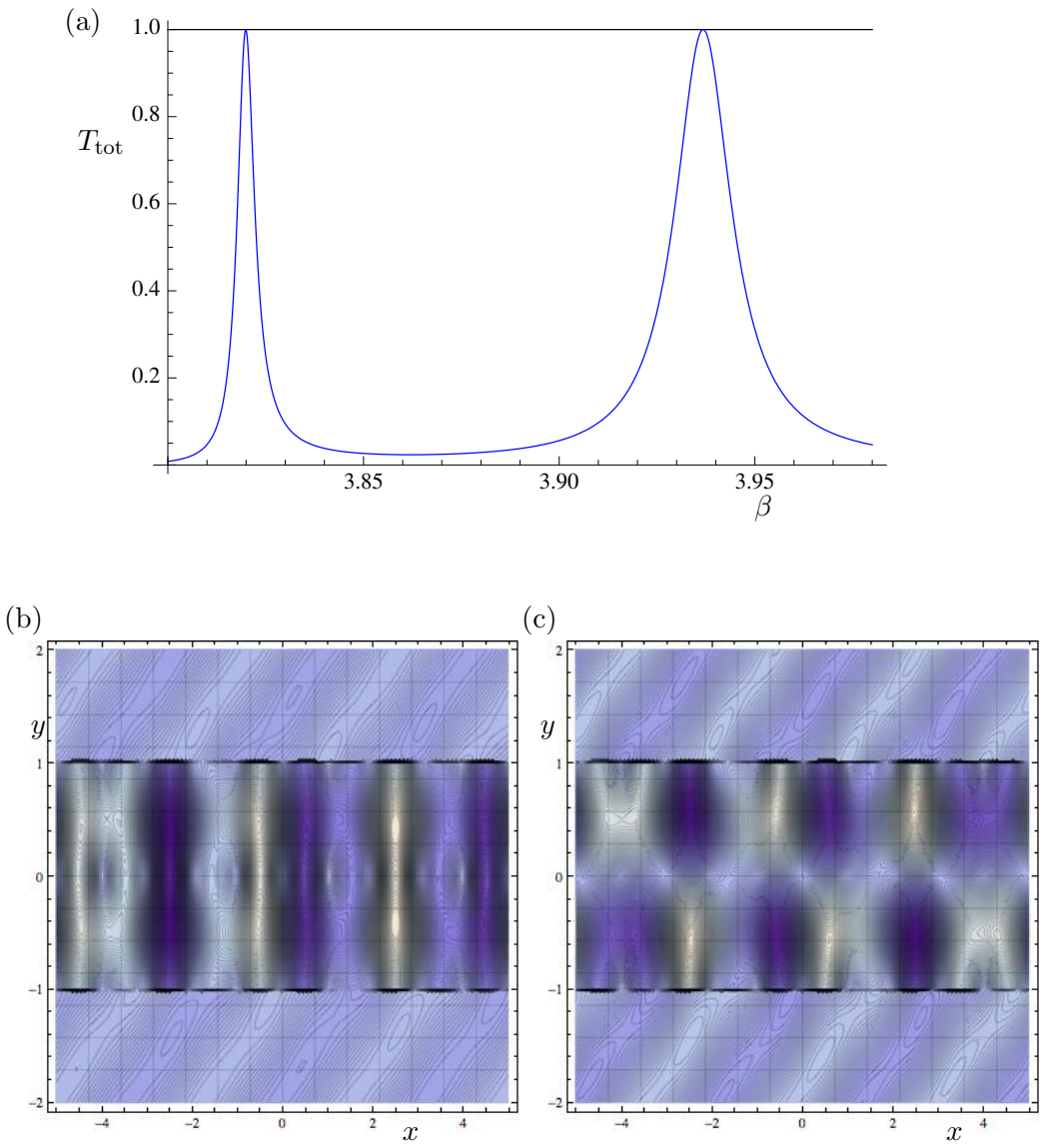

Figure 5.11: (a) Normalised transmitted energy $T_{\rm tot}$ as a function of β for a triplet of unshifted gratings of rigid inclusions with $a = 0.01$, $\eta d = 1$, for $\theta_i = 30°$. Field plots for transmission resonances: (b) a symmetric mode with $\beta_*^{(1)} = 3.819908$; (c) an anti-symmetric mode with $\beta_*^{(2)} = 3.93678$.

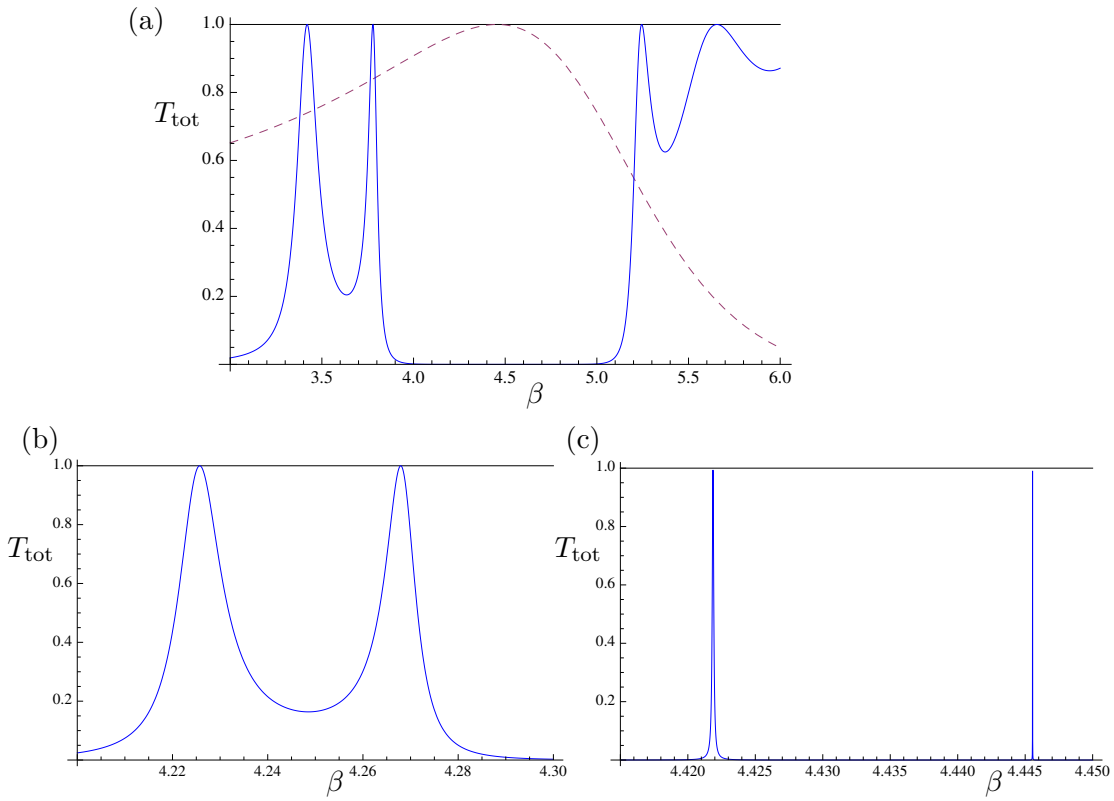

Figure 5.12: Normalised transmitted energy $T_{\rm tot}$ as a function of β for normal incidence for a symmetric triplet with (a) $a = 0$ (normalised reflected energy $R_{\rm tot}$ for a single grating of zero-radius scatterers is shown by the dashed curve) (b) $a = 0.15$ and (c) $a = 0.20$ for the central grating. Here $\xi = 0$, $\eta d = 1$, and $L = 2$.

inclusions is nonzero.

These comments are exemplified in the field plots of Fig. 5.11, where for a triplet of unshifted gratings of radius $a = 0.01$, we identify two resonance transmission peaks for $\theta_i = 30°$. It is noted that the symmetric mode corresponds to a lower value of $\beta_*^{(1)} = 3.819908$ than the anti-symmetric mode, which occurs at $\beta_*^{(2)} = 3.93678$. While plane waves outside the grating stack have the orientation of the incident wave, inside the stack the nodes and anti-nodes of the flexural displacement lie broadly parallel to the y-axis.

5.5.2 Non-uniform triplets with rigid pins on the exterior boundary

We consider the triplet configuration shown in Fig. 5.9(b), where all three gratings are aligned with each other (i.e. $\xi = 0$). The triplet has rigid-pin gratings on the outer boundaries, and a grating of finite-size inclusions in the middle.

In order for this configuration to deliver sharp transmission resonances in normal incidence it is necessary for the radius of inclusions in the middle grating to be around 0.20 or larger. This is evident from Fig. 5.12 where transmittance curves are compared

Table 5.4: Resonant frequencies β_* and the corresponding quality factors for triplets of gratings with a middle grating consisting of finite radius inclusions, and an outer pair comprising rigid pins. The relative lateral shift of the central grating is ξ and the relative vertical separation between successive gratings is η.

θ_i	a	η	ξ	Resonant wavenumber	Q
0°	0.2	1	0	$\beta_*^{(1)} = 4.42186394$	3.42×10^4
				$\beta_*^{(2)} = 4.445547468$	7.68×10^5
0°	0.15	1	0	$\beta_*^{(1)} = 4.22572$	377
				$\beta_*^{(2)} = 4.26794$	521
18°	0.1	1	0	$\beta_*^{(1)} = 3.9995073$	7.89×10^4
				$\beta_*^{(2)} = 4.0416640$	4.48×10^3
18°	0.1	1	0.5	$\beta_*^{(1)} = 4.06325990$	4.79×10^4
				$\beta_*^{(2)} = 4.10531818$	1.99×10^4
25°	0.01	1	0	$\beta_*^{(1)} = 3.72273076$	6.03×10^5
				$\beta_*^{(2)} = 3.7251407$	1.24×10^4

for radii $a = 0$, $a = 0.15$ and $a = 0.20$. The transmission peaks for the rigid-pin triplet in part (a) are far from being aligned with the maximal reflectance for the single grating in normal incidence. To align the peaks, and thereby increase the quality factors of the resonances, the radius of the inclusions is increased to $a = 0.15$ in part (b), and $a = 0.20$ in part (c). The data for resonant frequencies and Q-factors for these and other radii, together with data for different angles of incidence, are given in Table 5.4. Of the two sharp peaks in Fig. 5.12(c) that at $\beta_*^{(1)} = 4.42186394$ has a Q-factor of 3.42×10^4 and corresponds to an anti-symmetric flexural mode. The other peak at $\beta_*^{(2)} = 4.445547468$ has the very high Q-factor of 7.68×10^5 and corresponds to a symmetric flexural mode.

High quality factor transmission resonances may be achieved either by specifying the angle of incidence and then tuning the radius or by varying the angle of incidence for a fixed radius. Examples of this can be seen in Table 5.4. In Fig. 5.13 we show field plots of the flexural displacement for the third case of Table 5.4. The anti-symmetric mode $\beta_*^{(1)} = 3.9995073$ in this case has a higher Q-factor (7.89×10^4) than the symmetric mode ($\beta_*^{(2)} = 4.0416640$, $Q = 4.48 \times 10^3$).

5.5.3 Non-uniform triplets with rigid pins in the central grating

Triplets with a central grating of rigid pins have the important property that the frequency of the transmission resonance associated with the anti-symmetric mode is invariant with respect to the horizontal shift of the central grating. As the resonant frequency of the symmetric mode is affected by such horizontal shifts, they offer a means of controlling the frequency gap between these modes. We illustrate this property by

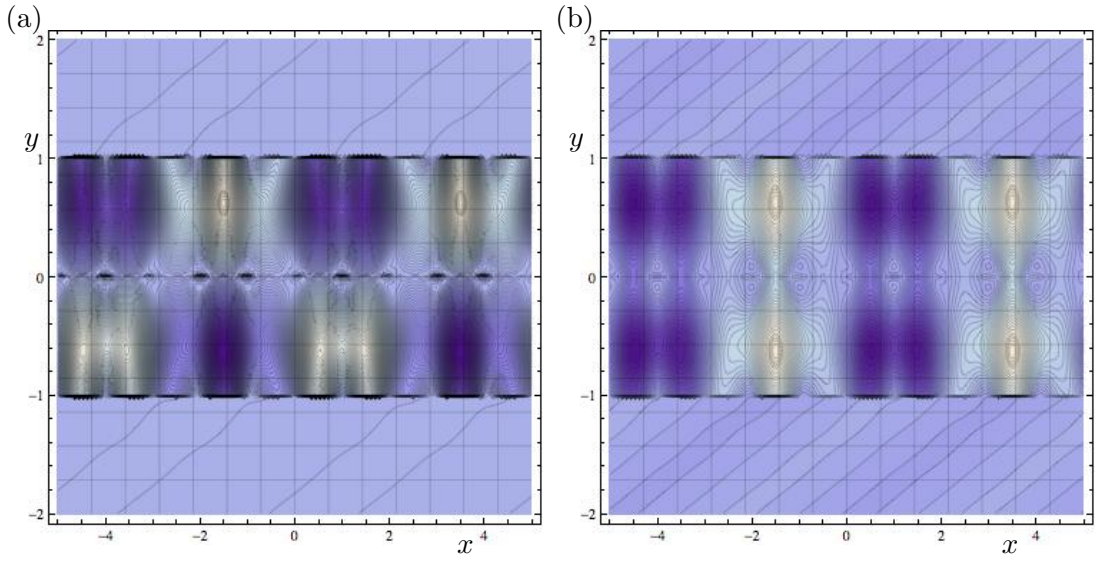

Figure 5.13: Flexural displacement as a function of x and y for (a) an anti-symmetric mode ($\beta_* = 3.9995073$) and (b) a symmetric mode ($\beta_* = 4.041664$). Data used: central grating inclusions with $a = 0.1$, $\theta_i = 18°$ and $\eta d = 1$.

studying the relationship between the transmission resonances of grating triplets and those for the outer pair of gratings.

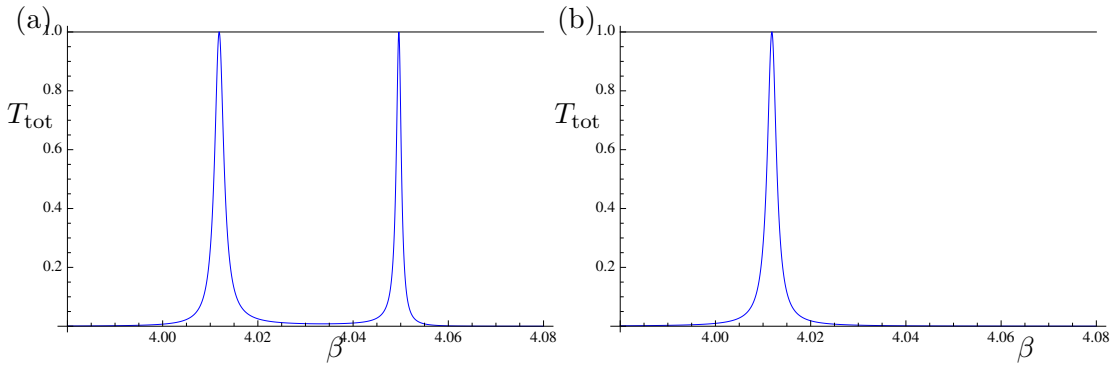

Figure 5.14: Normalised transmitted energy T_{tot} as a function of β: (a) for a triplet consisting of an outer pair of gratings with $a = 0.1$ and the central grating of rigid pins ($\eta d = 1$); (b) for the outer pair of gratings with $a = 0.1$ and $\eta = d = 2$. Data used: $\theta_i = 15°$, $L = 2$.

In Fig. 5.14 we show total transmittance curves for an aligned triplet with the outer gratings having $a = 0.1$ (part (a)) and for the structure with the central grating of rigid pins removed (part (b)). The transmission resonance shown in part (b) occurs at $\beta_* = 4.011852$ and it coincides with the leftmost peak in part (a). The flexural displacement plotted in Fig. 5.15(a) for this mode confirms its anti-symmetric nature and shows also its nodal line, coinciding with the central grating. The second transmission peak in Fig.5.14(a), of course, corresponds to a symmetric mode, as confirmed in Fig.5.15(b).

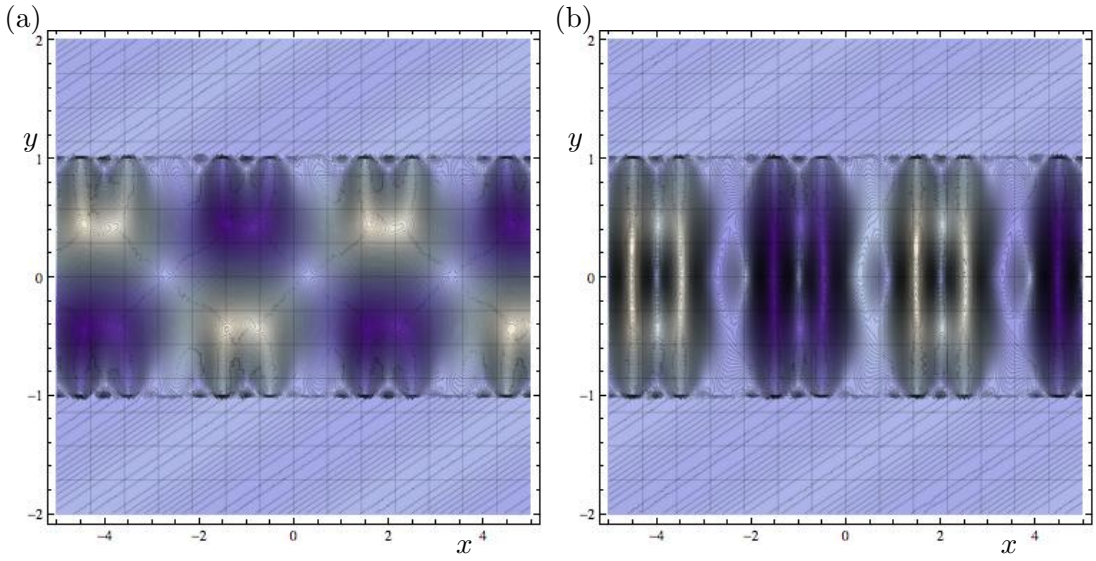

Figure 5.15: Flexural displacement as a function of x and y for a triplet consisting of an outer pair of gratings with inclusions of radius $a = 0.1$ and a central unshifted rigid-pin grating, for an angle of incidence of 15°. (a) Anti-symmetric mode ($\beta_* = 4.011852$); (b) symmetric mode ($\beta_* = 4.0496094$). Data: $\eta d = 1$ and $L = 2$.

Figure 5.16 illustrates two different circumstances which can arise when the central grating of pins is shifted with respect to the outer gratings of inclusions with nonzero radius. In case (a) the angle of incidence is $\theta_i = 15°$ and the radius of inclusions is $a = 0.1$. The anti-symmetric transmission resonance (peak **1**) occurs at $\beta_* = 4.011852$ for all values of $\xi \in [-0.5, 0.5]$. The symmetric mode resonance value is an even function of ξ which moves to higher values of β as ξ increases from 0 to 0.5 (Peaks **2** and **3** correspond respectively to $\xi = 0.25$ and $\xi = 0.5$). Our calculations show that, for this system, the positions of the anti-symmetric and symmetric resonance peaks do not coincide for any values of ξ in this range. However, for the angle of incidence of $\theta_i = 20°$ and the inclusion radius of $a = 0.085$, Fig. 5.16(b) shows that the symmetric transmission resonance peaks for $\xi = 0.25$ (peak **2**) and $\xi = 0.5$ (peak **3**) bracket the position of the anti-symmetric resonance (peak **1**). Therefore, the symmetric and anti-symmetric resonances can be brought into a coincidence for a value of ξ in the interval between 0.25 and 0.5.

5.6 Shifted systems of gratings and the EDIT phenomenon

By adjusting the shift parameter ξ, the resonant frequencies of the two modes can be aligned. For the case of rigid-pin triplets, three types of resonance coincide: the symmetric and anti-symmetric resonances occurring in the entire triplet, and the anti-symmetric resonance for the outer pair of gratings. It should also be noted that for examples of EDIT where the transmission resonances are well aligned with the single

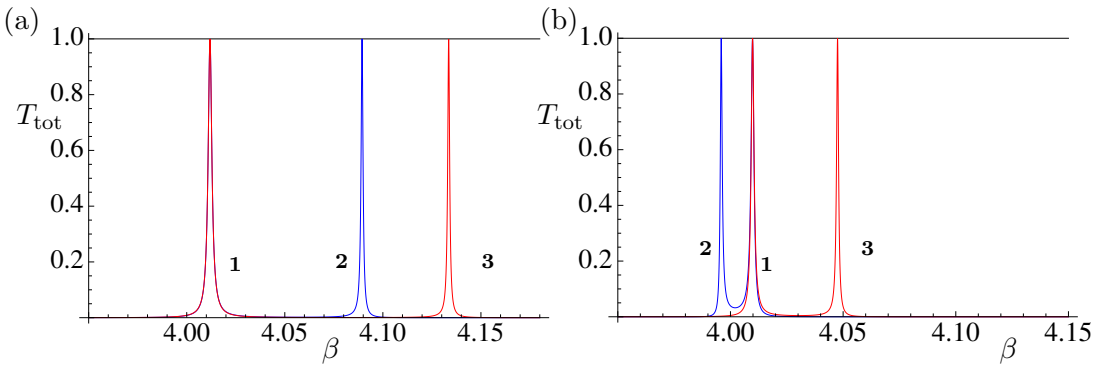

Figure 5.16: Normalised transmitted energy T_{tot} as a function of β for two shifted triplets, $\xi = 0.25$ (solid blue) and $\xi = 0.5$ (solid red), containing a central grating of rigid pins ($\eta d = 1$). (a) Angle of incidence $\theta_i = 15°$, outer scatterer radius $a = 0.1$; (b) $\theta_i = 20°$, $a = 0.085$.

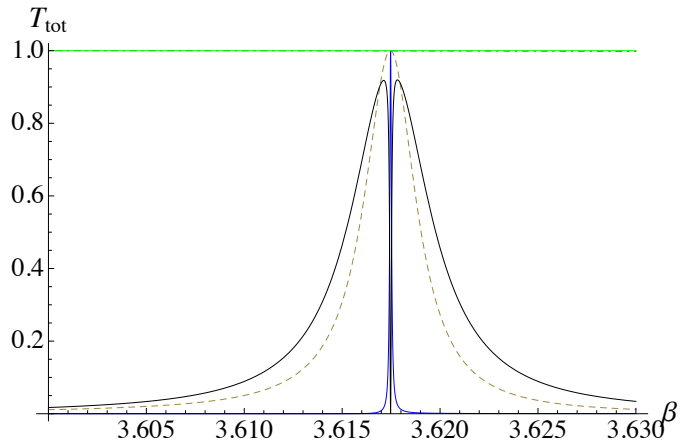

Figure 5.17: EDIT: normalised transmitted energy T_{tot} (solid black curve) as a function of β for a shifted rigid-pin triplet with $\xi = 0.25200$ for $\theta_i = 30°$. The two peaks represent the transmission resonances for the outer pair (solid blue) and the inner pair (dashed).

grating reflectance peak, in accordance with Fabry-Pérot theory, the resonance for the pair of shifted gratings making up one half of the triplet also coincides with the other resonances. This latter resonance is linked to the triplet's even mode, as observed in Section 4.2.1 and shown in Figs. 4.7 and 4.8. However its coincidence with the other resonances is not observed for weaker forms of EDIT for which the peaks have lower Q-factors.

Figure 4.10 illustrates the EDIT effect for a rigid-pin triplet, with the coincidence of the three types of resonance resulting in the normalised transmitted energy being negligibly small at the characteristic minimum. We show the additional broader transmission resonance peak associated with the half-triplet's symmetric mode here in Fig. 5.17. The triplet's modes are shown by the solid black curve; they interfere de-

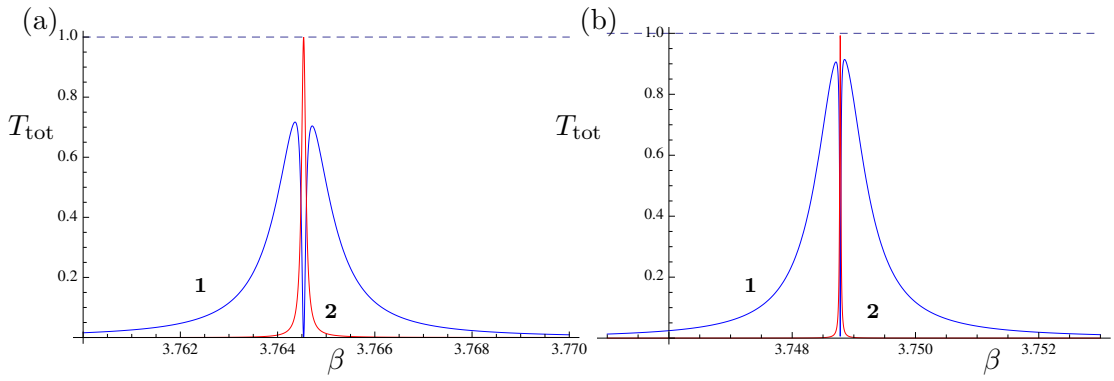

Figure 5.18: Normalised transmitted energy $T_{\rm tot}$ (curve **1**, solid blue) as a function of β for a triplet with a shifted central grating of rigid pins and the outer pair of gratings of inclusions of radius $a = 0.01$. Curve **2** (solid red) represents the total transmittance for the outer pair of gratings. Data used: (a) $\xi = 0.3112$, $\theta_i = 27°$. (b) $\xi = 0.23265$, $\theta_i = 26°$.

structively resulting in EDIT's characteristic high Q dip. The outer pair's odd mode is represented by the blue curve and the inner pair's broader resonance peak is illustrated by the dashed curve.

We now show that it is possible to obtain a strong EDIT effect for grating triplets containing inclusions of finite radius. To construct examples of this, it is preferable to use triplets with the outer gratings having inclusions of small but nonzero radius, with the central grating consisting of rigid pins. Note that, if the inclusions in the outer gratings are not sufficiently small, the resonances of the anti-symmetric and symmetric modes can be made to coincide, but the transmittance peaks on either side of the zero transmittance point are quite weak.

We have been able to achieve striking examples of the EDIT phenomenon for triplets using inclusions with radius $a = 0.01$ for the outer pair of gratings. The results for an initial design with an angle of incidence of 27° are given in Fig. 5.18(a) while the results for an optimised system are shown in Fig. 5.18(b) for the angle of incidence of 26°. The transmittance notch in the latter case has an extremely high quality factor (around 1.80×10^5), five times the Q-factor for the rigid-pin triplet of Fig. 4.10. We give the field plots in Fig. 5.19. The plot in part (a) shows the anti-symmetric mode for the outer pair of gratings, which is a plane propagating wave above and below the pair. The corresponding plot (part (b)) for the triplet shows a standing wave above the triplet and an evanescent field below it.

5.7 EDIT examples without rigid pins

Shortly after the journal paper Haslinger *et al.* (2013a) was accepted for publication, we were able to determine examples of EDIT for grating systems with nonzero-radius

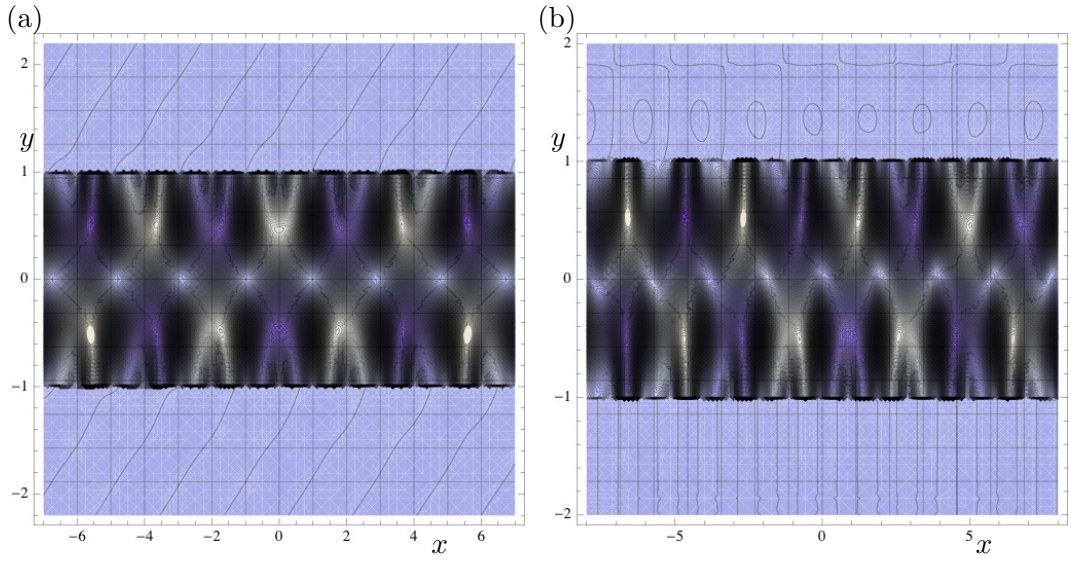

Figure 5.19: (a) Flexural displacement as a function of x and y for a pair of gratings consisting of inclusions of radius $a = 0.01$ with grating separation $\eta d = 2$ for $\beta_* = 3.748779850$. (b) Flexural displacement as a function of x and y for a triplet with a shifted central grating of rigid pins ($\xi = 0.23265$) and the outer pair of gratings consisting of inclusions of radius $a = 0.01$ for $\beta_* = 3.748779784$, $\eta d = 1$. Data: $\theta_i = 26°$.

inclusions, rather than those containing a central grating of rigid pins. The process is more difficult because altering the control parameter ξ shifts both the symmetric and anti-symmetric resonance modes, but importantly, the anti-symmetric mode is affected less than the symmetric one.

In Fig. 5.20(a), we consider a triplet with an outer pair consisting of inclusions of radius $a = 0.01$, and a central grating with $a = 0.0035$. Two shifts of the central grating are illustrated, $\xi = 0.4$ shown by the red curve, and $\xi = 0.42$ in blue. It is clear that there is no invariant mode, but the odd mode has a higher value of β and is being perturbed more slowly than the even mode, which is brought closer to its partner by an increase in ξ. By tuning this value of ξ carefully, we show the characteristic dip to zero transmittance of the EDIT phenomenon for the alignment of the two modes at $\xi = 0.45556$ in Fig. 5.20(b).

We note that although this is one of the best examples we have demonstrated for a 3-grating stack of nonzero-radius scatterers, the characteristic peak in transmission is suppressed (around 80%) in comparison with the systems involving rigid pins (see Figs. 4.10 and 5.18(b) both with around 90% for example). In addition, the symmetry of the two peaks is harder to refine, and it is time-consuming to locate EDIT phenomena for systems of gratings with nonzero-radius scatterers because of the sensitivity of both resonances to the shift parameter.

However it is a significant step forward in demonstrating the EDIT phenomenon

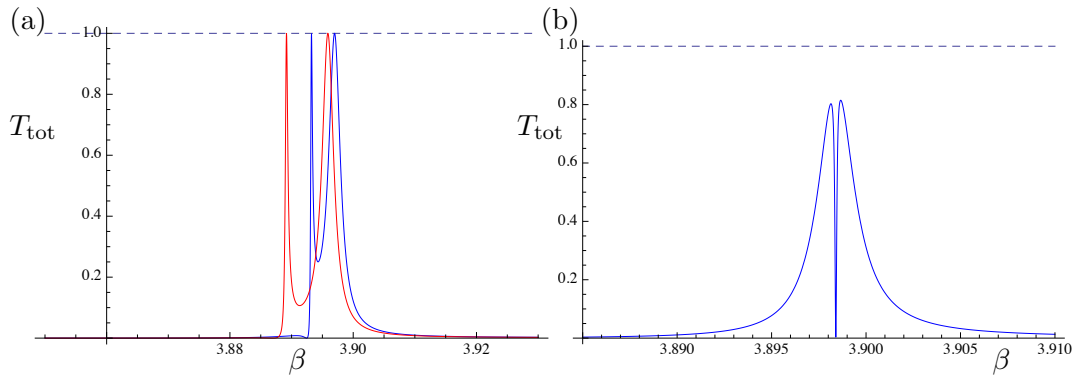

Figure 5.20: Normalised transmitted energy T_{tot} as a function of β for a triplet with a shifted central grating of finite radius inclusions with $a = 0.0035$, and an outer pair of gratings of inclusions of radius $a = 0.01$, $\theta_i = 26°$. Data used: (a) $\xi = 0.4$ (red curve), $\xi = 0.42$ (blue curve); (b) $\xi = 0.45556$.

for systems that may be manufactured, and in the next chapter, we take several strides forward. We discuss how the EDIT phenomenon for rigid-pin systems is determined using an extremely efficient method with quasi-periodic Green's functions. This suggests that a similar approach may be adopted for the nonzero-radius structures we ultimately seek to fabricate.

Chapter 6

Symmetry and resonant modes in platonic grating stacks

In this chapter, we study the flexural wave modes existing in finite stacks of gratings containing rigid zero-radius pins. We treat the stack of gratings as a structured waveguide. For a stack of rigid pins, a quasi-periodic Green's function is employed to derive the dispersion equation for Bloch waves within the system. We group the modes into even and odd classes, and derive dispersion equations for each. The solutions of the eigenvalue problem correspond to complex resonances close to the real axis. A connection is established with the transmission problem by identifying parameters of the grating stack and of the incident wave, to generate a transmission resonance linked to the trapped Bloch wave within the structured waveguide. We discuss how the combination of the two methods ensures that the EDIT interaction may be steered over a wider range of frequencies and angles, and located more efficiently.

A limitation of the investigations conducted in Chapters 4 and 5 is that the EDIT phenomenon is limited to a narrow range of frequency and angle of incidence values. We show how to remove these restrictions, and demonstrate that the EDIT phenomenon can be steered over a wide range of these two parameters. This combined propagation / scattering approach unifies the material of this thesis such that the EDIT phenomenon is now observable via a prescribed method, rather than being a filtering effect dependent on specific parameter settings.

The structure of the present chapter is as follows. In Section 6.1, we consider the concept of a structured waveguide (introduced in Section 3.3) and give the plane wave expansion of the Green's function for the biharmonic equation. This will be employed in later sections, replacing the cylindrical function expansion used by Movchan *et al.* (2009), Haslinger *et al.* (2012), (2013a,b). In Section 6.2, we consider stacks of three gratings of rigid pins, with the central grating not necessarily aligned with the outer pair of gratings. We construct the dispersion equations for modes in the triplet, considering both modes which are even and odd as functions of the coordinate y (see Fig. 5.2) orthogonal to the gratings. These modes correspond to complex resonances close to

the real axis. We investigate the conditions for odd and even modes to coincide since their coincidence yields EDIT in the scattering problem. In Section 6.3, we concentrate on triplets in which all three gratings are aligned. In Section 6.4, we describe the procedure we have developed which enables us to steer modes in general and the EDIT phenomenon in particular over a wide range of angles and frequencies.

The method involves choosing (say) the angle of incidence, then finding the frequency parameter which delivers a single-grating reflectance as close as desired to unity. The grating separation in the triplet stack is then chosen to make the frequency parameter correspond to a resonance of the odd mode in the triplet. The final step is to shift the central layer to move the frequency of the even mode to the desired value. We demonstrate the effectiveness of this strategy for angles of incidence ranging from 1° to 60°, for which the biharmonic spectral parameter β varies from 4.454 down to 2.947. A preliminary account of some of the results presented here were given in the conference paper by Haslinger *et al.* (2013b).

6.1 Structured waveguide

Recall Section 3.3 where we consider a waveguide consisting of gratings of rigid pins. A finite number of platonic gratings, which may be shifted relative to one another, are considered and we are primarily interested in a triplet (Fig. 6.1) because there are similarities with the scattering problem for which we identify extremely narrow frequency bands that support transmission resonances. The combination of the specific angle of incidence θ_i and its corresponding spectral parameter β means that each transmission peak is defined by a specific value of the Bloch parameter $\alpha_0 = \beta \sin\theta_i$.

The quasi-periodic Green's function (3.94)-(3.98) is used to derive the dispersion equation for Bloch modes within the rigid-pin system. The modes take the form of complex resonances close to the real axis, and we classify them as even and odd modes. We repeat the plane wave form of the quasi-periodic Green's function below, for the convenience of the reader.

6.1.1 Grating Green's function: plane wave form

We consider a single grating of rigid pins as a line of point forces with constant separation d, as discussed in Section 3.3.1. Therefore we use a quasi-periodic Green's function $G(x, y; \alpha_0, \beta)$ for the biharmonic operator, satisfying the equation

$$(\Delta^2 - \beta^4)G(x, y; \alpha_0, \beta) \,+\, \delta(y) \sum_{n=-\infty}^{\infty} \delta(x - nd) \exp\{i\alpha_0\, nd\} \,=\, 0, \qquad (6.1)$$

where α_0 is the Bloch parameter and β is the spectral parameter associated with the frequency ω by $\beta^2 = \omega\sqrt{\rho h/D}$. For the waveguide approach, it is sufficient to use the

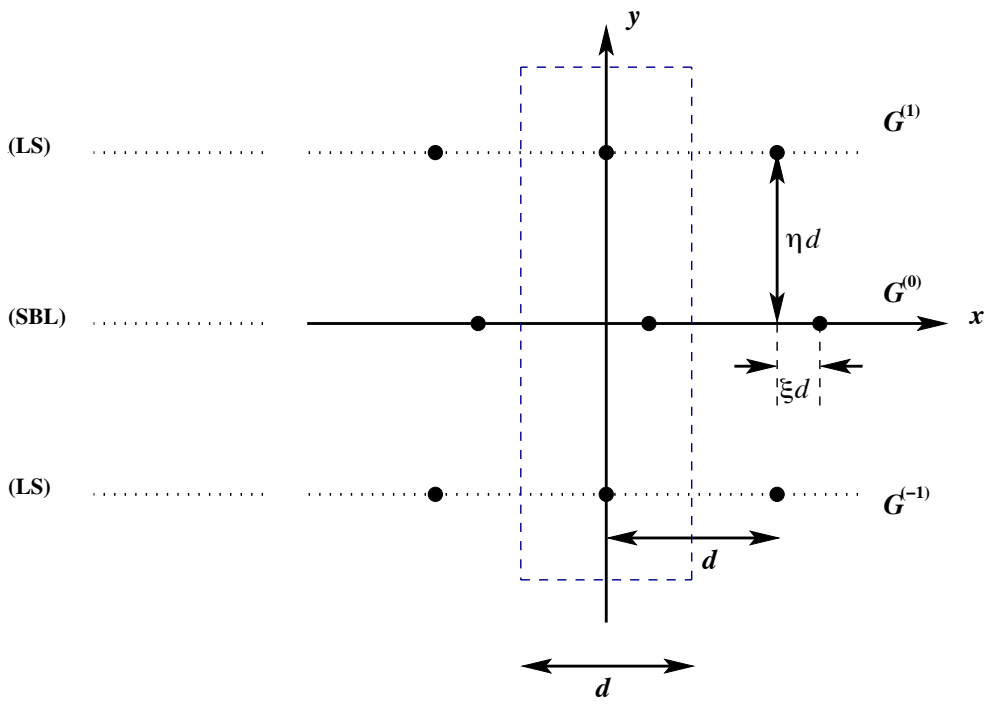

Figure 6.1: Example of a triple grating waveguide. The elementary cell is indicated by the dashed rectangle.

plane wave form, rather than the spatial form which incorporates Bessel functions and grating sums. The spectral form of the Green's function is

$$G(x,y;\alpha_0,\beta) = \frac{1}{2\beta^2}\left(\frac{1}{2id}\sum_{n=-\infty}^{\infty}\frac{1}{\chi_n}e^{i(\alpha_n x+\chi_n|y|)} + \frac{1}{2d}\sum_{n=-\infty}^{\infty}\frac{1}{\tau_n}e^{i\alpha_n x}\,e^{-\tau_n|y|}\right), \quad (6.2)$$

where

$$\alpha_n = \alpha_0 + \frac{2\pi n}{d}, \quad (6.3)$$

$$\chi_n = \begin{cases} \sqrt{\beta^2 - {\alpha_n}^2} \ , & {\alpha_n}^2 \le \beta^2, \\ i\sqrt{{\alpha_n}^2 - \beta^2} \ , & {\alpha_n}^2 > \beta^2, \end{cases} \quad (6.4)$$

$$\tau_n = \sqrt{\beta^2 + \alpha_n^2}. \quad (6.5)$$

As mentioned by Evans & Porter (2007), the Green's function for the biharmonic operator is cubically convergent, given that the two sums are considered together, even though the sums for the Helmholtz and modified Helmholtz parts are not absolutely convergent unless combined. We also note that it is necessary to use a far greater number of terms for evaluations of the Green's function for the central grating than for other gratings within a stack (typically 1000 and 20 respectively).

Our general structure consists of two layer stacks (LS) and a symmetry breaking layer (SBL) as shown by Fig. 3.1. The identical layer stacks contain a finite number of periodic gratings N and act as symmetric mirrors. Note that with the mirror systems

chosen to preserve up-down symmetry, there is always an odd number of layers. Of course the simplest example is when $N = 1$, producing a triplet, shown in Fig. 6.1.

6.2 Mode symmetry in a general triplet stack

The elementary cell for the general triplet is illustrated in Fig. 6.1. The period of each grating is d and the relative vertical separation between gratings is η. The relative lateral shift of the central grating (or SBL) is denoted by ξ. We denote the amplitude of the flexural displacement by u to distinguish it from the scattering model in Chapters 2 to 5 where we use W, but we remind the reader that in both cases the factor $e^{-i\omega t}$ has already been accounted for. We express u as the sum of three quasi-periodic Green's functions:

$$u \,=\, \sum_{j=-1}^{1} A_j \, G^{(j)} \, (x,\, y;\, \alpha_0,\, \beta), \tag{6.6}$$

where A_j are coefficients to be determined for each Green's function $G^{(j)}$. In terms of the canonical Green's function $G(x, y)$ evaluated for the points $(nd, 0)$ on the horizontal axis, we have

$$\begin{aligned} G^{(1)}(x, y; \alpha_0, \beta) \;&= G(x, y - \eta d; \alpha_0, \beta), \\ G^{(0)}(x, y; \alpha_0, \beta) \;&= G(x - \xi d, y; \alpha_0, \beta), \\ G^{(-1)}(x, y; \alpha_0, \beta) \;&= G(x, y + \eta d; \alpha_0, \beta). \end{aligned} \tag{6.7}$$

At each pin, it is required that $u = 0$. We therefore take the elementary column cell incorporating the central pin of each of the constituent gratings such that

$$u\Big|_{\mathbf{x}=\boldsymbol{a}^{(m)}} = \sum_{j=-1}^{1} A_j G^{(j)} \, (\boldsymbol{a}^{(m)};\, \alpha_0,\, \beta) \,=\, 0, \quad \text{where} \;\; m = -1, 0, 1. \tag{6.8}$$

Here $\boldsymbol{a}^{(0)} = (\xi d, 0)$ and $\boldsymbol{a}^{(\pm 1)} = (0, \pm\eta d)$. This is equivalent to the matrix equation

$$\mathbf{M}\,\mathbf{A} \,= \mathbf{0}, \tag{6.9}$$

where $\mathbf{A}$ is the column vector of coefficients A_j and

$$\mathbf{M} = \begin{pmatrix} G(0,0) & G(-\xi d, \eta d) & G(0, 2\eta d) \\ G(\xi d, -\eta d) & G(0,0) & G(\xi d, \eta d) \\ G(0, -2\eta d) & G(-\xi d, -\eta d) & G(0,0) \end{pmatrix} \,=\, \begin{pmatrix} M_{11} & M_{12} & M_{13} \\ M_{21} & M_{11} & M_{21} \\ M_{13} & M_{12} & M_{11} \end{pmatrix}. \tag{6.10}$$

Here we have used the identity $G(x, -y) = G(x, y)$; the arguments α_0 and β in the representation of the matrix elements M_{ij} are left implicit.

Note that the elements M_{12} and M_{21} generally differ if the central layer is shifted with respect to the upper and lower layers. An exception to this arises for normal

incidence when $\alpha_0 = 0$. From equations (6.3)-(6.5) we see that when $\alpha_0 = 0$ then $\alpha_{-n} = -\alpha_n$, $\chi_{-n} = \chi_n$, and $\tau_{-n} = \tau_n$. It then follows that

$$M_{12} = G(-\xi d, \eta d) = M_{21}.$$

If the gratings are all aligned ($\xi = 0$), or we deal with the case $\alpha_0 = 0$, the matrix $\mathbf{M}$ has a symmetric Töplitz structure. This would be the case regardless of the number of gratings chosen for the mirror layers which are placed symmetrically above and below the SBL. In the analysis below we focus on the three-gratings stack.

6.2.1 Odd and even Bloch modes

The matrix $\mathbf{M}$ has three eigenvalues:

$$\lambda_1 = M_{11} - M_{13}, \quad \lambda_\pm = \frac{1}{2}(2M_{11} + M_{13} \pm \sqrt{8M_{12}M_{21} + M_{13}^2}). \tag{6.11}$$

The eigenvector corresponding to λ_1 is

$$v_{odd} = \begin{bmatrix} -1 \\ 0 \\ 1 \end{bmatrix}, \tag{6.12}$$

and has odd symmetry. The other two vectors have even symmetry:

$$v_{even}^- = \begin{bmatrix} 1 \\ \left(-M_{13} - \sqrt{8M_{12}M_{21} + M_{13}^2}\right)/(2M_{12}) \\ 1 \end{bmatrix}, \tag{6.13}$$

and

$$v_{even}^+ = \begin{bmatrix} 1 \\ \left(-M_{13} + \sqrt{8M_{12}M_{21} + M_{13}^2}\right)/(2M_{12}) \\ 1 \end{bmatrix}. \tag{6.14}$$

The dispersion curves for Bloch modes correspond to the condition that the eigenvalues of $\mathbf{M}$ are zero. Thus for the odd mode, the dispersion curve corresponds to the condition:

$$M_{11} - M_{13} = 0. \tag{6.15}$$

For the even modes, the dispersion curves correspond to

$$2M_{11} + M_{13} \pm \sqrt{8M_{12}M_{21} + M_{13}^2} = 0. \tag{6.16}$$

The even eigenvectors for the shifted waveguide are not orthogonal, whereas they are for the unshifted case when $M_{12} = M_{21}$.

6.2.2 Analogue of EDIT for waveguide

In accordance with the conditions required for the EDIT effect within the scattering problem, it is natural to consider the coincidence of the even and odd symmetries of the Bloch modes. We initially summarize the results for the coincidence of two even modes, since the general result (6.12)-(6.14) indicates that the triplet supports one odd Bloch mode, and two even modes.

Condition for even modes to coincide

The condition for the two even modes to coincide is

$$2M_{11} + M_{13} - \sqrt{8M_{12}M_{21} + M_{13}^2} = 2M_{11} + M_{13} + \sqrt{8M_{12}M_{21} + M_{13}^2} = 0.$$

This gives us the conditions

$$M_{13} = -2M_{11} \text{ and } M_{21} = -\frac{M_{11}^2}{2M_{12}}, \tag{6.17}$$

from which we obtain the matrix

$$\mathbf{M} = \begin{pmatrix} M_{11} & M_{12} & -2M_{11} \\ -\frac{M_{11}^2}{2M_{12}} & M_{11} & -\frac{M_{11}^2}{2M_{12}} \\ -2M_{11} & M_{12} & M_{11} \end{pmatrix}, \tag{6.18}$$

which has a double zero eigenvalue and a nonzero eigenvalue $3M_{11}$. The matrix is defective and has only two eigenvectors:

$$\begin{bmatrix} 1 \\ \frac{M_{11}}{M_{12}} \\ 1 \end{bmatrix}, \quad \begin{bmatrix} -1 \\ 0 \\ 1 \end{bmatrix}. \tag{6.19}$$

This shows that it is impossible for the two even modes of the triplet to have an avoided crossing, since for this to occur the null space of the matrix $\mathbf{M}$ at the crossing would have to have dimension two.

Condition for even and odd modes to coincide

For the odd mode dispersion curve, we have the condition $M_{11} - M_{13} = 0$ and the matrix

$$\mathbf{M} = \begin{pmatrix} M_{11} & M_{12} & M_{11} \\ M_{21} & M_{11} & M_{21} \\ M_{11} & M_{12} & M_{11} \end{pmatrix}. \tag{6.20}$$

For an even mode's dispersion curve, we have $M_{12} = M_{11}(M_{11} + M_{13})/2M_{21}$ so for the coincidence of an odd and an even mode, $M_{12} = M_{11}^2/M_{21}$ and

$$\mathbf{M} = \begin{pmatrix} M_{11} & M_{12} & M_{11} \\ \frac{M_{11}^2}{M_{12}} & M_{11} & \frac{M_{11}^2}{M_{12}} \\ M_{11} & M_{12} & M_{11} \end{pmatrix}, \tag{6.21}$$

which has eigenvalues 0, 0 and $3M_{11}$, with corresponding eigenvectors

$$\begin{bmatrix} -1 \\ 0 \\ 1 \end{bmatrix}, \begin{bmatrix} -\frac{M_{12}}{M_{11}} \\ 1 \\ 0 \end{bmatrix}, \quad \begin{bmatrix} 1 \\ \frac{M_{11}}{M_{12}} \\ 1 \end{bmatrix}. \tag{6.22}$$

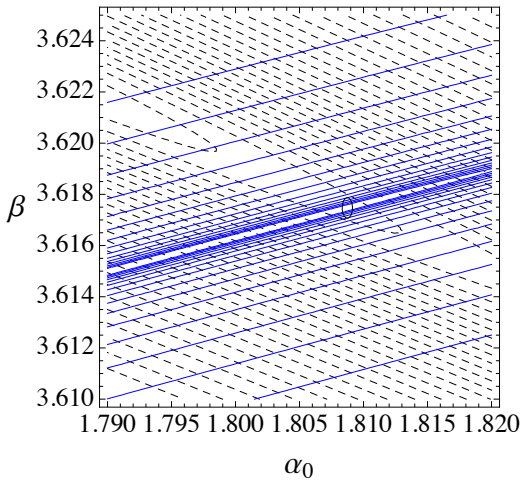

Figure 6.2: Contours for logarithm of modulus of $M_{11} - M_{13}$ (solid), and of $2M_{12}M_{21} - M_{11}(M_{11} + M_{13})$ (dashed) for a shifted three-grating stack of rigid pins ($\xi = 0.25200$, $d = 1$), as a function of α_0 and β. The circle corresponds to $(\alpha_0, \beta) = (1.808735, 3.61747)$.

The coincidence of the other even mode and the odd mode occurs with eigenvalues 0, 0 and $-3M_{11}$ with the corresponding eigenvectors

$$\begin{bmatrix} -1 \\ 0 \\ 1 \end{bmatrix}, \begin{bmatrix} \frac{M_{12}}{M_{11}} \\ 1 \\ 0 \end{bmatrix}, \begin{bmatrix} 1 \\ -\frac{M_{11}}{M_{12}} \\ 1 \end{bmatrix}. \tag{6.23}$$

EDIT example

An illustrative example is shown in Fig. 6.2. The dispersion curves for the odd modes are defined by equation (6.15) where the matrix $\mathbf{M}$ is determined over a range of β and α_0 values. The matrix elements are complex, and their moduli are close to zero, being of the order $\leq 10^{-3}$. Therefore we plot the logarithm of the modulus of condition (6.15) as contours, taking the most negative value to be the best approximation to the zero that we seek. We do the same for the even dispersion curves (6.16), and identify where the two critical level curves intersect.

In Fig. 6.2, the odd modes are represented by the solid contours, and the even dispersion curves are represented by the dashed contours. It is clear that the odd modes' contours concentrate around, and bracket a bare region, whereas the even modes' contours are more evenly spaced, but also bracket a bare region containing the closest approximation to the zero. The surfaces shown in Fig. 6.3 highlight this difference between the odd and even modes. The odd modes' characteristic dispersion curve (the valley) is more pronounced than the even modes'.

The trapezoid region bounded by the odd mode contours (log of the modulus of condition (6.15), -12.88) and the even mode contours (log of the modulus of condi-

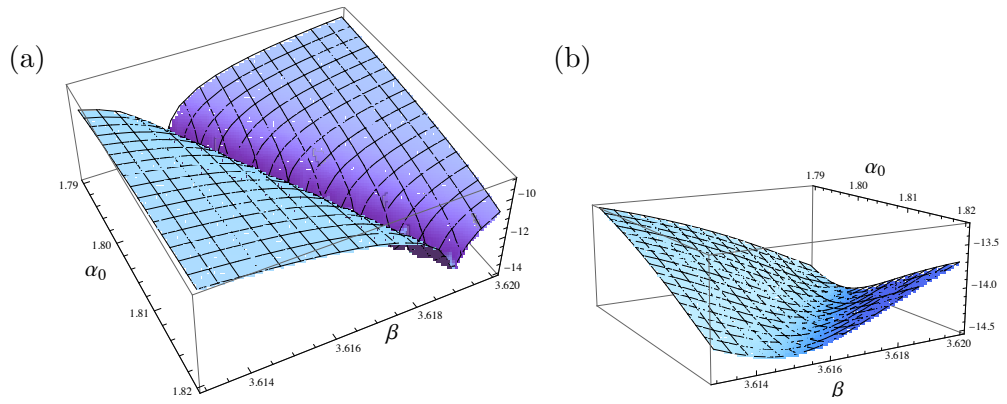

Figure 6.3: Surface plot of the logarithm of the modulus of (a) $M_{11} - M_{13}$ (odd mode) (b) $2M_{12}M_{21} - M_{11}(M_{11} + M_{13})$ (even mode) for the shifted three grating stack of rigid pins ($\xi = 0.25200$, $d = 1$), as a function of α_0 and β.

tion (6.16), -14.455) in Fig. 6.2 contains the point identified from the scattering model of the same triplet as $(\alpha_0, \beta) = (1.808735, 3.61747)$, an example of EDIT for $\theta_i = 30°$ with lateral shift $\xi = 0.25200$ of the central grating (Figs. 4.10 and 5.17). This example demonstrates the correspondence between the two methods, the scattering model and waveguide approach. The intersection of the contour plots for the waveguide's Bloch modes is used to rapidly identify a potential region for the EDIT effect in the analogous scattering problem using the Bloch parameter equation $\alpha_0 = \beta \sin\theta_i$. The fine tuning of the effect with the shift parameter ξ is then implemented to accurately evaluate the EDIT spectral parameter β for the scattering of the plane wave.

We note that we have not yet been successful in locating examples of two even modes coinciding.

6.2.3 Matrix elements near light lines

It is useful to understand the behaviour of matrix elements near light lines (see Section 2.5.5), where the matrix elements diverge. In fact, the elements contain terms which go as

$$-\frac{1}{4\beta^2}\frac{e^{i\chi_m|p-n|d}}{i\chi_m}, \text{ where } \chi_m = \sqrt{\beta^2 - \left(\alpha_0 + \frac{2\pi m}{d}\right)^2}. \tag{6.24}$$

At the light lines, the χ_m go to zero for a particular value of m, being real if β is below the light line, and imaginary if β is above the light line. This will then give either a divergent term in the real part or the imaginary part of every element of $\mathbf{M}$. Putting $X_m = e^{i\chi_m d}$, we find that the matrix $\mathbf{M}$ contains a scaling term which goes as $-1/(4\beta^2 i\chi_m)$ times the light line matrix:

$$\mathbf{M}_{LL} = \begin{pmatrix} 1 & X_m & X_m^2 \\ X_m & 1 & X_m \\ X_m^2 & X_m & 1 \end{pmatrix}. \tag{6.25}$$

This matrix has respective eigenvalues and eigenvectors

$$1 - X_m^2,\ \frac{1}{2}(2 + X_m^2 - X_m\sqrt{8 + X_m^2}),\ \frac{1}{2}(2 + X_m^2 + X_m\sqrt{8 + X_m^2}), \tag{6.26}$$

$$\begin{bmatrix} -1 \\ 0 \\ 1 \end{bmatrix},\quad \begin{bmatrix} 1 \\ \frac{1}{2}\left(-X_m - \sqrt{8 + X_m^2}\right) \\ 1 \end{bmatrix},\quad \begin{bmatrix} 1 \\ \frac{1}{2}\left(-X_m + \sqrt{8 + X_m^2}\right) \\ 1 \end{bmatrix}. \tag{6.27}$$

Approaching the light line, the eigenvalues tend to $0, 0, 3$ and the eigenvectors tend to

$$\frac{1}{\sqrt{2}}\begin{bmatrix} -1 \\ 0 \\ 1 \end{bmatrix},\ \frac{1}{\sqrt{6}}\begin{bmatrix} 1 \\ -2 \\ 1 \end{bmatrix},\ \frac{1}{\sqrt{3}}\begin{bmatrix} 1 \\ 1 \\ 1 \end{bmatrix}. \tag{6.28}$$

We note that these eigenvectors are written in the symmetrized form.

6.3 Mode symmetry in an unshifted triplet stack

We consider the modes of the triplet, with the gratings all aligned, leading to a structure with up-down and left-right symmetry. The Green's function matrix in this case is complex and symmetric:

$$\mathbf{M} = \begin{pmatrix} M_{11} & M_{12} & M_{13} \\ M_{12} & M_{11} & M_{12} \\ M_{13} & M_{12} & M_{11} \end{pmatrix}. \tag{6.29}$$

The results of Section 6.2 can be used for this special case, with $M_{12}M_{21}$ being replaced by M_{12}^2. The crossing of the odd mode trajectory with that of the even mode occurs when $M_{11} = M_{13}$, $M_{12} = M_{11}$, and for the eigenvalues 0, 0, $3M_{11}$ the eigenvectors are

$$\frac{1}{\sqrt{6}}\begin{bmatrix} 1 \\ -2 \\ 1 \end{bmatrix},\ \frac{1}{\sqrt{2}}\begin{bmatrix} -1 \\ 0 \\ 1 \end{bmatrix},\ \frac{1}{\sqrt{3}}\begin{bmatrix} 1 \\ 1 \\ 1 \end{bmatrix}. \tag{6.30}$$

For the alternative even mode, the eigenvalues are the same, and the eigenvectors are

$$\frac{1}{\sqrt{6}}\begin{bmatrix} 1 \\ 2 \\ 1 \end{bmatrix},\ \frac{1}{\sqrt{2}}\begin{bmatrix} -1 \\ 0 \\ 1 \end{bmatrix},\ \frac{1}{\sqrt{3}}\begin{bmatrix} 1 \\ -1 \\ 1 \end{bmatrix}. \tag{6.31}$$

An example for the unshifted triplet is shown in Fig. 6.4 where the level curves for the odd mode are solid and those of the even mode are dashed. The mode contours intersect near a point identified from reflection and transmission properties of the stack as being $(\alpha_0, \beta) = (1.66451, 3.596951)$. Note that the resonant even mode in this case corresponds to the first eigenvector in equation (6.31).

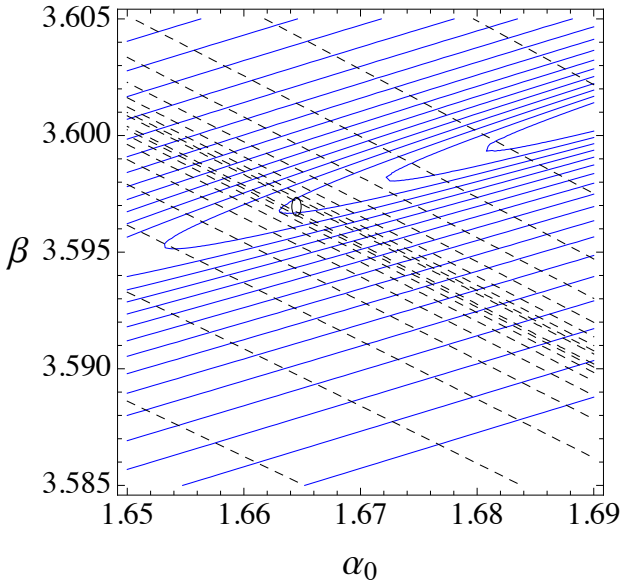

Figure 6.4: Contours for logarithm of modulus of $M_{11} - M_{13}$ (solid), and of $2M_{12}^2 = M_{11}(M_{11}+M_{13})$ (dashed) for an aligned three grating stack of rigid pins ($d = 1$, $\xi = 0$), as a function of α_0 and β. The circle corresponds to $(\alpha_0, \beta) = (1.66451, 3.596951)$.

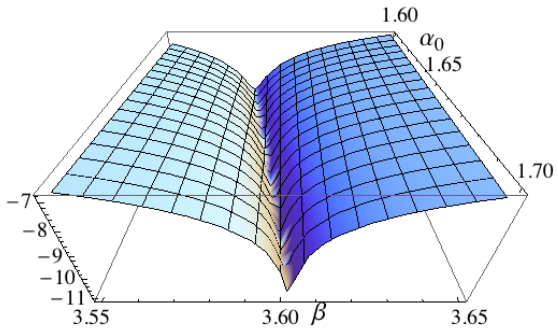

Figure 6.5: Surface plot of the logarithm of modulus of $M_{11} - M_{13}$ for an aligned three grating stack of rigid pins ($d = 1$, $\xi = 0$), as a function of α_0 and β.

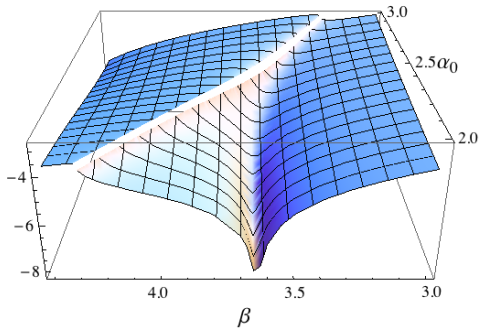

Figure 6.6: Surface plot of the logarithm of modulus of $M_{11} - M_{13}$ for an aligned three grating stack of rigid pins ($d = 1$, $\xi = 0$), as a function of α_0 and β, giving the odd mode trajectory in the vicinity of the light line.

6.3.1 Surface plots

The surface plots in Figs. 6.5 and 6.6 show the values of $\log|M_{11} - M_{13}|$ as functions of α_0 and β. Deep valleys in the surface plots can be identified with regions where there is a well defined minimum and thus a well-identified mode. Fig. 6.5 shows the region just after the crossing point of even and odd modes of Fig. 6.4, with this valley corresponding to the odd mode. In Fig. 6.6 we have moved to larger β values, and are approaching the region of intersection of the light lines associated with grating diffraction orders -1 and 0. Note that the odd mode minimum gradually gets weaker and weaker as we approach the intersection region.

6.3.2 Projection method for even modes

We discuss methods to overcome the loss in resolution of the modes, illustrated for an odd mode in Fig. 6.6. Our first attempt to overcome this problem, arising from the reduction of the single grating's reflectance, used a projection method, based on the observation that the eigenvectors of each mode vary only weakly with β and α_0. For the normalized column eigenvectors identified in equations (6.28), (6.30) and (6.31) (denoted generically by $\mathbf{v}$) we form the projection

$$p(\mathbf{v}) = \mathbf{v}^T \mathbf{M} \mathbf{v}, \tag{6.32}$$

with the superscript T denoting the transpose. This scalar just gives the estimate for the eigenvalue corresponding to $\mathbf{v}$, assuming the accuracy of the eigenvector.

We consider the case of $\alpha_0 = 2.1$ which supports two resonance modes in the corresponding scattering model, one even and one odd. The two modes are illustrated by the blue curve (the right-hand pair of peaks) in Fig. 6.7(a), and it is simple to classify the corresponding Bloch modes in the waveguide using equations (6.29)-(6.31). We consider the scattering and waveguide approaches concurrently in the remainder

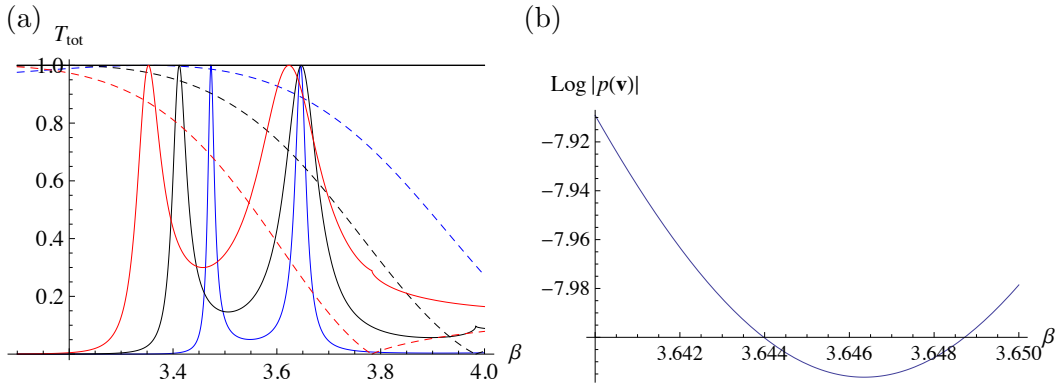

Figure 6.7: (a) Normalised transmitted energy T_{tot} versus spectral parameter β for a triplet of rigid pins ($d = 1$, $\xi = 0$) with $\alpha_0 = 2.1$ (blue curve / right-hand pair), $\alpha_0 = 2.3$ (black curve / central pair) and $\alpha_0 = 2.5$ (red curve / left-hand pair). The corresponding curves for the reflectance of a single grating of rigid pins are dashed. (b) Log$|p(\mathbf{v})|$ from equation (6.32) for $\alpha_0 = 2.1$.

of this section. We determine the value of β corresponding to the resonance on the right. We substitute this value $\beta = 3.64581$ into (6.29), obtaining the matrix $\mathbf{M}$ and its corresponding eigenvalues and eigenvectors.

Referring to equation (6.15), one of the eigenvalues corresponds to a resonant mode, and its corresponding eigenvector matches up with the odd eigenvector defined by equation (6.12). We confirm that this mode is odd by using equation (6.32) and plotting the logarithm of the modulus of $\mathbf{v}^T\mathbf{M}\mathbf{v}$, where $\mathbf{v}$ is the odd mode taken from equation (6.30) or (6.31). This is shown in Fig. 6.7(b) and the minimum occurs at around $\beta = 3.646$, the small discrepancy with the transmission resonance's value arising because of the slight difference in the eigenvectors.

The other resonance for $\alpha_0 = 2.1$ possesses a higher Q-factor, as can be observed qualitatively in Fig. 6.7(a), with $\beta = 3.473136$. We expect this mode to be of even type, with the characteristic equation (6.16). The corresponding eigenvector is one of the four types described by equations (6.30) and (6.31). We note that these even modes are of the form

$$\mathbf{v}_A = \frac{1}{\sqrt{A^2+2}} \begin{bmatrix} 1 \\ A \\ 1 \end{bmatrix},$$

with A in the range $-2 \leq A \leq 2$. We plot the surface for the logarithm of the modulus of $\mathbf{v}_A^T\mathbf{M}\mathbf{v}_A$ with $-2 \leq A \leq 2$ and β in a range including the transmission resonance's frequency $\beta = 3.473136$ in Fig. 6.8(a). The result indicates that $A = 2$ defines the correct eigenvector and this can be confirmed by filling the matrix M and determining the corresponding eigenvalues and eigenvectors.

We observe a zero eigenvalue for an eigenvector matching the first eigenvector of

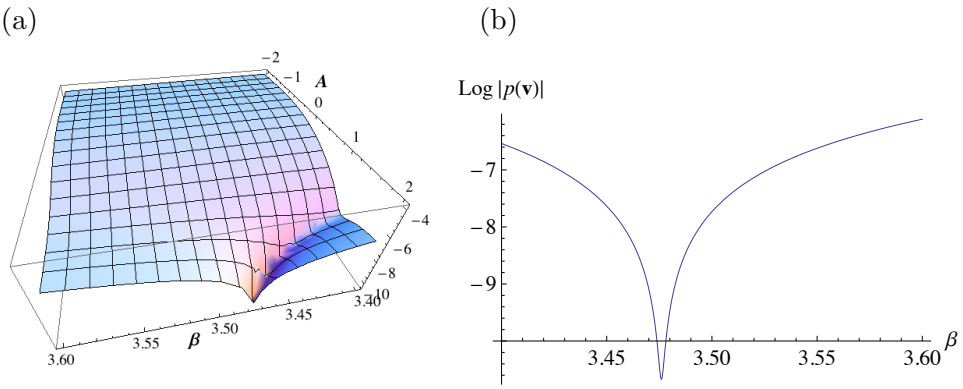

Figure 6.8: (a) Log$|p(\mathbf{v}_A)|$ with $\alpha_0 = 2.1$ ($d = 1$, $\xi = 0$), $3.4 \leq \beta \leq 3.6$ and $-2 \leq A \leq 2$. (b) Log$|p(\mathbf{v})|$ versus β for $\mathbf{v}^T = 1/\sqrt{6}(1, 2, 1)$.

equation (6.31). This indicates that the even mode arises from the equation

$$M_{12} = -\sqrt{M_{11}(M_{11} + M_{13})/2}, \tag{6.33}$$

and if we apply equation (6.32) to $\mathbf{v}^T = 1/\sqrt{6}(1, 2, 1)$, we obtain the result matching the resonance frequency in Fig. 6.8(b). We have therefore classified the two modes arising for this example of α_0 to be odd, defined by the equation $M_{11} - M_{13} = 0$, and even defined by equation (6.33).

In general, the odd and even modes arise due to these two conditions and the corresponding dispersion curves are illustrated in Fig. 6.9. This initial method is useful for classifying the nature of modes and locating the possibility of EDIT effects where the modes coincide, but is only reliable for a narrow range of parameters for $\eta = 1$ with $d = 1$. Referring to Fig. 6.9, the results for $1.2 \leq \alpha_0 \leq 2$ are well defined, but outside of this region, the valleys characterizing the Bloch modes' dispersion curves become shallower, and the resonances become broader and lose resolution. This can be seen in Fig. 6.7(a) where the transmission peaks are not aligned with the maxima for reflectance for a single grating, as well as in Figs. 6.6, 6.7(b) and 6.8(b) where the minima have relatively small magnitudes. We have developed a method that solves the two problems of mode symmetry classification and loss of high Q simultaneously, and it is described below. This superior method involves optimizing the relative grating separation η.

The evolution of mode behaviour from that characterized by narrow and deep minima to wide and ill-defined minima can be understood in terms of the reflectance of a single grating of pins. If the reflectance R_g of the single layer is very high, then a pair or triplet of gratings can support very well-confined guided waves between them. The corresponding resonant behaviour will then have a high quality factor, corresponding to a very localised region in (α_0, β) space. If we use the analogy with the classical Fabry-Pérot interferometer of Section 2.4.4 equation (2.33), the transmittance of a pair

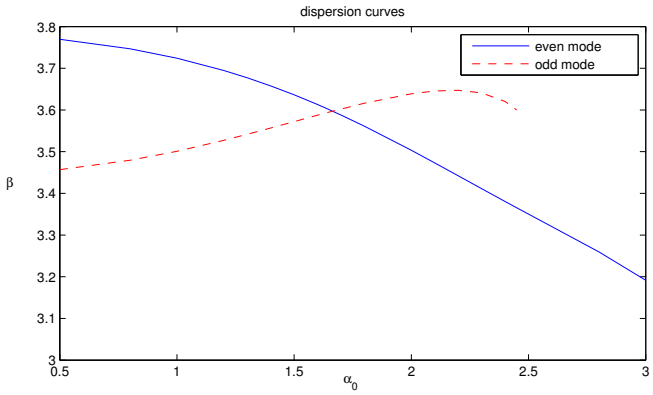

Figure 6.9: Dispersion diagram for a waveguide consisting of an unshifted triplet with the horizontal axis representing α_0 in the range $0.5 \leq \alpha_0 \leq 3$, and β on the vertical axis in the range $3 \leq \beta \leq 3.8$. The dashed curve represents the odd modes, and the blue curve, the even modes.

is given by

$$T_2 = \frac{1}{1 + F\sin^2(\delta/2)}, \quad \text{where} \quad F = \frac{4R_g}{(1-R_g)^2} \tag{6.34}$$

is related to the finesse of the interferometer, and δ corresponds to the round-trip phase accumulated between the plates (see Section 2.4.4). In terms of resonant poles of the expression (6.34), these will occur when $\delta = 2n\pi \pm i/\sqrt{F}$, so that the poles move away from the real β axis in a way which scales as $1 - R_g$. The bigger the finesse is, the narrower the resonance, and the closer it lies to the real axis. This model is useful qualitatively, but is not quantitatively accurate, since it applies to unstructured mirrors and the Helmholtz equation, and not to stacked gratings and the biharmonic plate equation.

6.4 Optimized method to steer waveguide modes

The building block for the transmission problem and the waveguide is the single grating, which, provided its reflectance is high, will then support the trapping of waves between multiple gratings with little leakage of energy. This idea allows the development of a simple procedure to construct 3-element systems that support the EDIT effect with extraordinarily high Q resonances. For a given angle of incidence θ_i, or Bloch parameter α_0 for the analogous waveguide, we start by determining the value of $\beta = \beta_{\rm g}$ for $R_{\rm g} = |R_0|^2 = 1$ for the single grating (where 0 is the only propagating order). In the examples that follow we evaluate this reflectance to at least ten decimal places.

We then take $\beta_{\rm g}$ and vary the separation parameter η to find $2\eta^*$ that determines the geometry for a pair of gratings to support an optimized trapped mode of odd up-down symmetry. This mode possesses an extremely high Q-factor and is also that of the outer pair of gratings of a triplet, for which an even mode arises for the same geometry

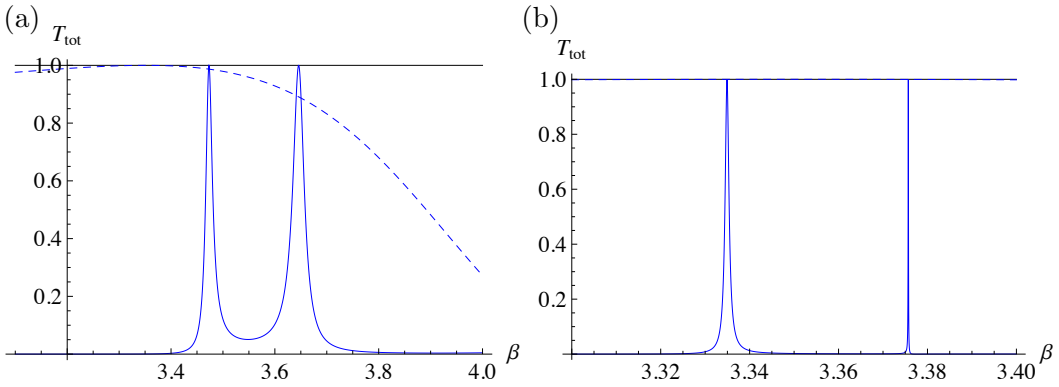

Figure 6.10: Normalised transmitted energy $T_{\rm tot}$ versus spectral parameter β for an unshifted triplet ($\xi = 0$) of rigid pins with $\alpha_0 = 2.1$ and $d = 1$ and: (a) $\eta = 1$; (b) optimized resonances for a triplet with $\eta^* = 1.185266$.

but for a different value of β. We use the additional parameter of lateral shift of the central grating ξ to align the odd and even modes to the same value of β, thereby creating the EDIT effect for the chosen angle of incidence.

An example of the second stage of this procedure for the scattering of a plane wave by a triplet of rigid pins with $d = 1$ is shown in Fig. 6.10, which is one of three examples illustrated in Fig. 6.7. The transmittance spectrum in Fig. 6.10(a) shows the vicinity of two transmission resonances, the lower one in β being of even symmetry and the upper one of odd symmetry. With the initial vertical separation of the gratings being $\eta d = 1$, the resonances have low Q-factors, since the single grating reflectance is significantly below unity. In Fig. 6.10(b), the transmittance spectrum for an optimized value of η shows the resonances after they have been moved into the high reflectance region for the single grating: both have much higher quality factors.

A useful guide for optimizing the grating separation is the model from optics of the dielectric slab waveguide studied in electromagnetic theory by, amongst others, Marcuse (1972, 1974) and Tien & Ulrich (1973). In this model, a slab of dielectric of thickness h, which is analogous to our grating separation ηd, and reflective index n_f, is situated between a cover region of index n_c and a substrate region of index n_s below it. Evanescent waves are present in the cover and substrate regions, but propagating plane waves that satisfy the Helmholtz equation arise in the dielectric region bordered by two boundaries $x = 0$ and $x = h$, on which consistency relations must be prescribed (electromagnetic boundary conditions). For non-trivial solutions, i.e. for modes to be trapped within the waveguide, a dispersion equation is derived from four equations. In our case, where the propagating waves also satisfy the Helmholtz equation, the situation is simplified by prescribing Dirichlet clamping conditions on $x = 0$ and $x = h$. We therefore obtain two equations corresponding to $x = h$ and $x = 0$:

$$Ae^{-iK_f h} + Be^{iK_f h} = 0, \; A + B = 0, \tag{6.35}$$

Table 6.1: Resonant frequencies β_{g} and the corresponding optimal grating separation $\eta^* d$ for triplets of unshifted gratings for various angles of incidence θ_i. In this table, $d = 1$. Note the good agreement between the separation equation's h^* for $m = 1$ with $\eta^* d$.

θ_i	β_{g}	α_0^{g}	h^*	$\eta^* d$
0°	4.456001	0	0.705025	0.705251
3°	4.438147	0.232275	0.708833	0.709101
6°	4.387466	0.458615	0.719982	0.720367
9°	4.311191	0.674419	0.73779	0.738331
12°	4.217801	0.87693	0.761482	0.762182
15°	4.11476	1.06498	0.790427	0.79126
18°	4.007707	1.23845	0.824228	0.825150
21°	3.900536	1.39783	0.862728	0.863689
24°	3.79580	1.54389	0.905975	0.906927
27°	3.6950925	1.67754	0.954209	0.955108
30°	3.599363	1.79968	1.00784	1.00866
33°	3.509134	1.91121	1.06748	1.06818
36°	3.424645	2.01296	1.133905	1.134490
45°	3.205694	2.26677	1.38593	1.386185
60°	2.94716	2.55232	2.131946	2.131958

where K_f is the wave number. It follows that for nontrivial solutions, $\sin(K_f h) = 0$ and therefore

$$K_f = \frac{\pi m}{h},$$

where m is an integer. The analogue of K_f in our case is $\chi_f = \beta \cos\theta_f$. Therefore for zeroth order propagating modes, $\chi_0 = \beta \cos\theta_i$ and we obtain the equation

$$h = \frac{\pi m}{\beta \cos\theta_i} = \frac{\pi m}{\sqrt{\beta^2 - \alpha_0^2}}. \tag{6.36}$$

In Table 6.1 we show computed values for optimal grating separation $\eta^* d$ and h^* obtained from equation (6.36) for $m = 1$, noting their excellent agreement.

Using Table 6.1, we can steer this mode by optimizing the separation as θ_i is altered. This is illustrated in Fig. 6.11, where we show the even modes with the blue (lower) curve, and the odd modes with the red (upper) curve. We observe that by optimizing the separation, we obtain a pair of modes that retain their relative position (i.e. higher β for the odd mode) as well as their very high Q-factors. The modes approach one another very gradually, as can be seen by their proximity for $\alpha_0 = 2.55$, which corresponds to $\theta_i = 60°$.

In the third stage of the EDIT steering procedure, the shift parameter ξ is used to bring the two modes together. As a rough guideline, for each pair of odd and even modes plotted in Fig. 6.11, a shift in the vicinity of $\xi = 0.25200$ is generally sufficient to produce EDIT effects. An example is shown in Fig. 6.12 for $\theta_i = 60°$ and $d = 1$,

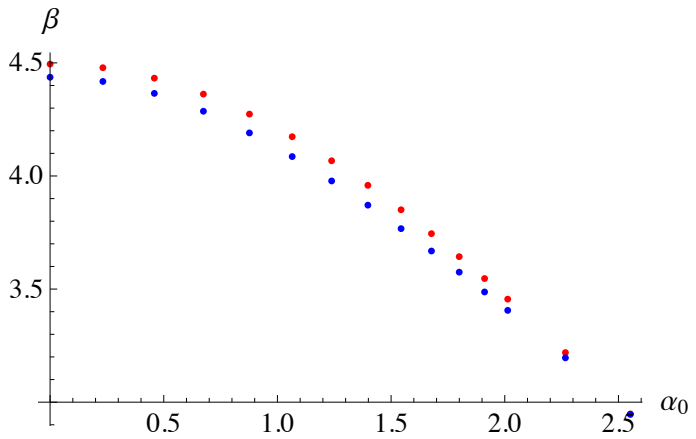

Figure 6.11: β versus α_0 for odd (red) and even (blue) modes for optimized grating separation η^* for unshifted triplets (Data from Table 6.1).

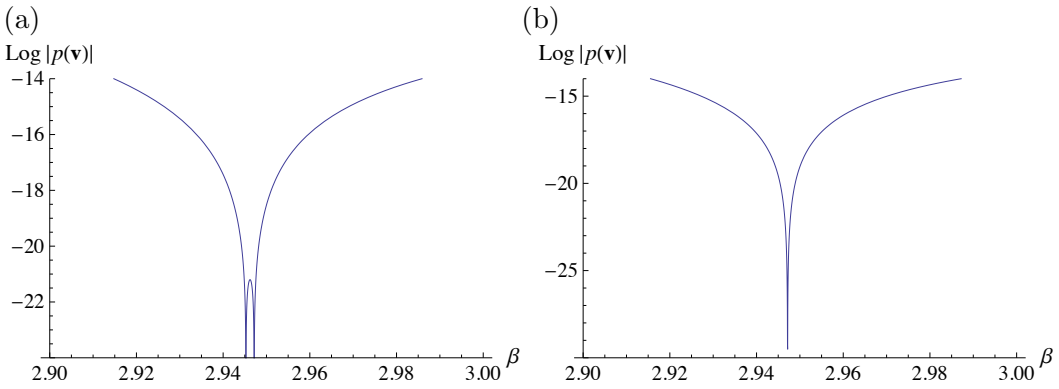

Figure 6.12: The logarithm of the modulus of the determinant of the matrix $\mathbf{M}$ as a function of β for $\theta_i = 60°, d = 1, \eta^* = 2.131958$ (a) $\xi = 0$ (b) $\xi = 0.2476$.

where the optimal shift is $\xi = 0.2476$. A fast way to find the optimal shift for high quality resonances is through determinant plots of the type shown in Fig. 6.12. The outer pair in this example has relative grating separation $2\eta^* = 4.262$.

The coincidence of the two modes shown in Fig. 6.12(b) for $\xi = 0.2476$ indicates the presence of the EDIT phenomenon for the transmission diagram, and this is given in Fig. 6.13(a), with a detailed plot of the central minimum shown in Fig. 6.13 (b). The peaks of transmittance either side of the EDIT dip reach 100%, and the Q-factor of the notch is an extraordinarily high 6.5×10^9. The Q-factor of the outer pair of gratings is around 1.50×10^5, a factor of forty thousand lower than that of the notch. This clear separation of scales in β sensitivity means that the transmittance curves seem symmetric around the EDIT point, rather than having the asymmetric Fano shape (see Fano 1961) expected of a rapidly varying term superposed on a slowly varying one.

In Figure 6.14 we show the variety of filtering curves which may arise for variations of the shift parameter ξ in the neighbourhood of the EDIT value. The very sharp rise

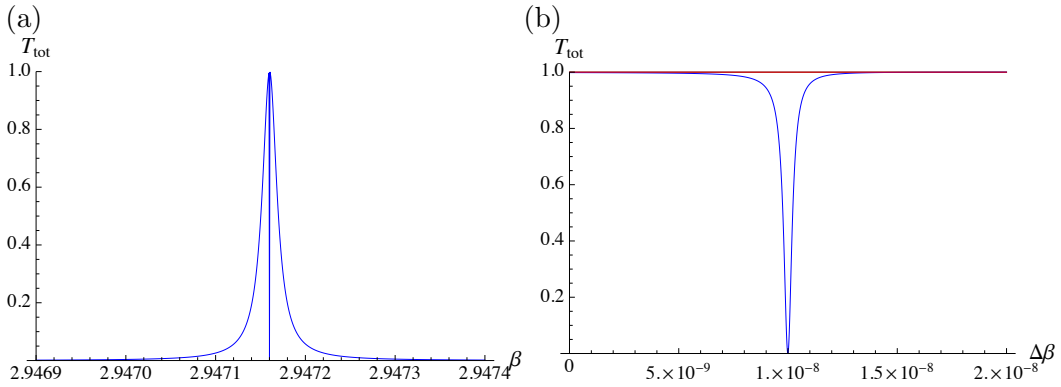

Figure 6.13: Optimized EDIT with $\theta_i = 60°$, $\eta^* = 2.13196$ and $\xi = 0.2476$ with $d = 1$. In (b), we replace β by $2.94715999 + \Delta\beta$, because the transmission minimum is so narrow.

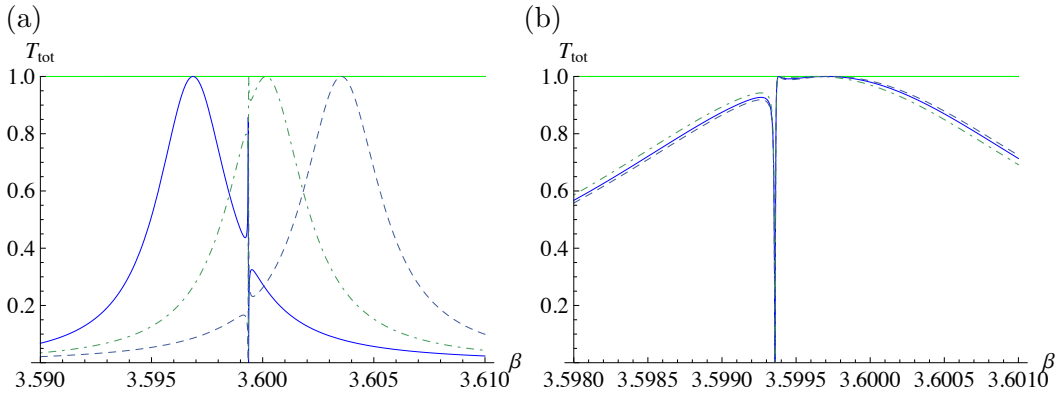

Figure 6.14: Normalised transmitted energy $T_{\rm tot}$ versus spectral parameter β for a triplet of rigid pins with $d = 1$, $\eta = 1.00866$ and $\theta_i = 30°$ for various shifts of the central grating: (a) $\xi = 0.22$ (solid curve), $\xi = 0.23$ (dot-dashed curve) and $\xi = 0.24$ (dashed curve) (b) $\xi = 0.2285$ (dot-dashed curve), $\xi = 0.2287$ (solid curve) and $\xi = 0.2288$ (dashed curve).

in transmittance from zero to unity which occurs when the shift is just below the EDIT value is the result of the even mode resonance occurring just before the odd mode resonance. This sharp rise might be useful in some filtering applications.

As the angle of incidence approaches zero, resonances due to the even modes become increasingly sharp. This makes the task of locating and optimizing the EDIT phenomenon increasingly difficult. The transmission diagram shown in Fig. 6.15 is the best we have been able to obtain for the angle of incidence $\theta_i = 1°$, and we have so far been unsuccessful in detecting the EDIT minimum for exactly normal incidence.

We conclude by stressing that the procedure we have demonstrated for steering the angle and frequency of the EDIT phenomenon makes it much more flexible than its analogue of EIT in atomic physics, for which the frequency is fixed by the occurrence of a set of appropriate energy levels. It may be that a similar procedure may be adapted to solutions of the Helmholtz equation, and other wave-bearing equations.

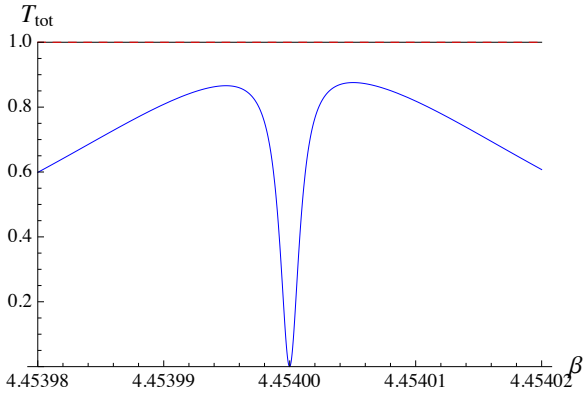

Figure 6.15: Normalised transmitted energy T_{tot} versus spectral parameter β for a triplet of rigid pins with $d = 1$ and $\theta_i = 1^\circ$ for the optimized grating separation $\eta = 0.705679367$ and the EDIT shift of the central grating $\xi = 0.165868$.

Chapter 7

Conclusions and future work

We have discussed the propagation of flexural waves in thin structured elastic plates. The periodic systems embedded in Kirchhoff-Love plates, governed by the biharmonic plate equation, are the elastic plate analogues of photonic crystals, and are known as platonic crystals. The emerging field of platonics has numerous opportunities for future research, with great strides having already been made, in particular, for two-dimensional square arrays of circular scatterers, gratings, pinned plates and wave scattering by single defects and finite clusters.

We have considered the generic case of a finite stack of periodic gratings, which is a semi-infinite platonic crystal, within an elastic plate. We provided the method of solution for the scattering of an incident plane wave by any finite number of platonic gratings comprising circular inclusions or rigid pins. The method is also applicable to arbitrarily-shaped inclusions and may be extended to point masses. The choice of circular boundaries supports an elegant method of solution using cylindrical Bessel functions, and demonstrates interesting and unusual filtering properties linked to the physical effects observed for photonic crystals in the field of optics. Photonic crystals guide and disperse light, and it has been shown that platonic crystals are able to guide and disperse flexural bending waves in plates in a similar way.

Various filtering effects have been discovered for platonic systems. In this thesis we have concentrated on the trapping and localisation of wave energy leading to resonant behaviour. Strong energy localisation in waveguides of pinned plates has potential applications in transporting wave energy over long distances. Hence there is great interest in the fabrication of more complicated platonic crystals to achieve high Q-factor wave trapping. High Q-factor structures have been widely researched in photonics (see for example Akahane *et al.* (2003) and Mohammadi *et al.* (2009)), and there is now interest in the platonic community.

Over the course of this thesis, by increasing the size and complexity of the grating systems, we have seen Q-factors rise from around 5400 for a simple unshifted pair of pinned gratings to more than 6×10^9 for a pinned triplet exhibiting the novel filtering

effect EDIT (elasto-dynamically inhibited transmission). For scatterers with nonzero radius, we have obtained Q-factors of order 10^5 but with future refinement in line with the pinned cases we considered here, Q-factors comparable with those observed for ultra-high-Q photonic cases by Song *et al.* (2005), of order 2×10^7, should be attainable. Recently lensing, shielding and cloaking properties have also been demonstrated by, amongst others, Smith *et al.* (2013), Antonakakis *et al.* (2013) and Colquitt *et al.* (2014).

It is important to understand the wave behaviour through structured plates because resonant behaviour of this magnitude is potentially destructive. It may be possible to convert this high wave energy into forms that may be guided, trapped and harnessed for more useful applications. Our early work focussed on transmission resonances directly linked to the trapping of waves and the platonic analogue of Fabry-Pérot theory, where the high reflectance of the individual elements of the system contributes to an increased quality factor of the system's transmission resonance.

A finely-tuned resonant behaviour is the EDIT effect we have observed for certain 3-grating stacks. This phenomenon is characterized by a transmission peak with a sharp central suppression region, akin to the phenomenon of electromagnetic induced transparency (EIT), a quantum-mechanical effect which arises in three-level atomic systems. As discussed in the Introduction and Section 2.4.5, there are EIT analogues in nano-optomechanical structures (NOMS) and in metamaterials, and we discovered the platonic analogue in our paper Haslinger *et al.* (2012). The EDIT effect has formed a prominent part of our published papers, and has been refined, both in its determination and quality, over the course of three papers presented here.

The most recent article by Haslinger *et al.* (2014) employed a novel method whereby the modes generated by the scattering of an incident plane wave are compared with the Bloch modes of a platonic strip waveguide. The connection of the two approaches yields a more efficient procedure to determine wave localisation and transmission resonances. It follows that more complicated examples of EDIT are attainable, where parameters such as the relative grating separation η and angle of incidence θ_i may be altered along with the relative shift control parameter ξ.

A natural way to proceed with the investigation of EDIT is to broaden its applicability to nonzero-radius gratings. Early examples were presented by Haslinger *et al.* (2013a,b) and here in this thesis in Section 5.7, but the efficient Green's function method of Section 3.3 and Chapter 6 has so far only been applied to pinned grating systems. It is envisaged that a similar method, with the Green's functions being replaced by multipole expansions, would be suitable for this step forward. It would also be interesting to research whether the EDIT phenomenon is observable for grating systems comprising point masses.

Another potential extension is to seek an analogue of electromagnetically induced

absorption (see Section 2.4.5) for platonic strips. As mentioned at the end of Section 6.2.2, we have so far been unsuccessful in locating examples of two even modes coinciding, the case for which constructive, rather than destructive, interference would arise. As mentioned by Taubert *et al.* (2012), the concept of electromagnetically induced absorption (EIA) comes from atomic physics, where coherent coupling to the dark state results in a narrow peak of enhanced absorption on top of the broader absorption feature. EDIT, EIT and EIA are all special cases of Fano resonances, and considering some of the transmission diagrams we have obtained (see Fig. 6.14 for example) one would expect to locate EIA-analogues for flexural plates.

Platonic crystals have potential applications in the manufacture of seismic metamaterials for anti-earthquake systems because of the shielding properties already demonstrated by several researchers including Farhat *et al.* (2009, 2010) and more recently by Antonakakis *et al.* (2013). The latter paper also refers to Dirac-like cones which arise in the dispersion diagram for a square array of clamped circular scatterers. In this case, they arise at triple crossings with a flat standing mode passing through the vertex.

Dirac-like cones are usually limited to graphene-like hexagonal structures (Castro Neto *et al.* 2009), but here we are talking about a square array, which is reminiscent of the Dirac-like cones for photonic crystals studied by Huang *et al.* (2011), and phononic crystals analysed by Liu *et al.* (2011). Very recent research by Smith *et al.* (2014) extends this study of Dirac cones to platonic crystals with a triangular array of pinned points in a plate. The medium is locally non-dispersive with the linear transparency linked to the Dirac cone's localised standing wave mode.

For applications of platonic studies to anti-earthquake systems, it is important to research the properties of the associated surface waves. In the Introduction, we mentioned surface acoustic waves (SAW) travelling along the surface of an elastic material, with an amplitude that typically decays exponentially with depth into the substrate. These have been investigated recently by Lawrence *et al.* (2013) for photonic crystals, with localised modes being demonstrated on the boundaries of the photonic crystal, but which decay exponentially within the crystal. The surface flexural waves present new challenges in the platonic analogues, and there are potential applications in transporting wave energy away from points of impact.

Appendix A

Grating sums and accelerated convergence

A.1 Grating sums

The matrix of the Rayleigh system of equations (3.26)-(3.27) includes grating sums, which represent periodicity of the grating and quasi-periodicity of the scattering problem. The definitions and computational formulae for these grating sums are based on the method of Twersky (1961). We also refer to previous literature for guidance in choosing appropriate truncation for both the multipole series and grating sums.

We assume that the order of truncation L for the Rayleigh system (3.26), (3.27) is chosen according to the radius of the void. As mentioned in Section 2.5.4, Poulton *et al.* (2010) provide tables for selecting the number of multipoles to achieve converged frequencies for a doubly periodic square array consisting of perforations with non-zero radii. These tables, which link the radius of the hole to the number of necessary multipoles, are applicable to the stacks of gratings that we study here. We provide a convergence table for a platonic triplet in Chapter 5. The multipole summation runs from $-L$ to L ($2L+1$ terms). The accuracy of the solution to the system depends on the precision with which we evaluate the incorporated grating sums. In the doubly periodic array, Movchan *et al.* (2007) recommended calculating the lattice sums over orders in the range $-2L$ to $2L$ ($4L+2$ terms), and we adopt the same strategy here.

The grating sums used in this thesis are denoted by $S_{l-n}^{(K,G)}$ and $S_{l-n}^{(H,G)}$, and consist of K-type modified Bessel functions and Hankel functions. The superscript G is used to denote that these are grating sums rather than those for the two-dimensional case. We defined them in Section 2.6.1, equations (2.83), (2.84) and equations (2.90), (2.91), and Movchan *et al.* (2009) expressed them in the same form. For convenience, we repeat them here. The sums over even and odd integers are expressed separately.

$$S_{2l}^{(K,G)}(\beta,\alpha_0) \;=\; 2\sum_{p=1}^{\infty} K_{2l}(\beta p)\cos(\alpha_0 p), \tag{S1}$$

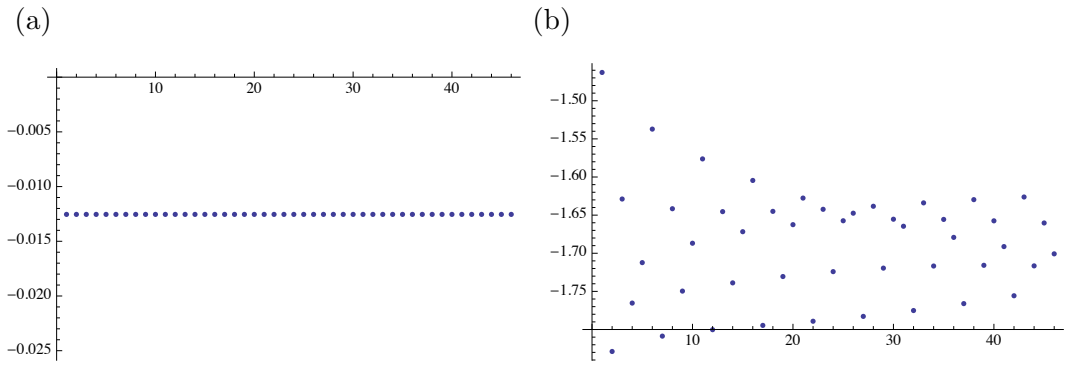

Figure A.1: (a) An example of a typical K-type grating sum which can be evaluated directly because of its exponential convergence. (b) An example of a Hankel-type grating sum which demonstrates why Twersky's alternative representation is valuable.

$$S_{2l+1}^{(K,G)}(\beta,\alpha_0) \;=\; 2i\sum_{p=1}^{\infty} K_{2l+1}(\beta p)\sin(\alpha_0 p), \tag{S2}$$

are the K-type sums. These are evaluated by direct summation, since they are exponentially convergent. Note that l can be positive or negative which is consistent with the structure of the gratings sums featured in the Rayleigh system (3.26) and (3.27). The grating sums over Hankel functions are of the form:

$$S_{2l}^{(H,G)}(\beta,\alpha_0) \;=\; 2\sum_{p=1}^{\infty} H_{2l}^{(1)}(\beta p)\cos(\alpha_0 p), \tag{S3}$$

$$S_{2l+1}^{(H,G)}(\beta,\alpha_0) \;=\; 2i\sum_{p=1}^{\infty} H_{2l+1}^{(1)}(\beta p)\sin(\alpha_0 p). \tag{S4}$$

As Movchan *et al.* (2009) mentioned, these sums are not exponentially convergent but are oscillatory, and would require an excessive number of terms to observe convergence. Figure A.1(b) shows a typical Hankel-type grating sum evaluated using direct summation. The oscillation of the sum is clearly evident and contrasts sharply with that of the exponentially convergent sum for the corresponding K-type grating sum which is shown in Fig. A.1(a).

We shall use accelerated convergence formulae based on those derived by Twersky (1961) for the Schlömich series:

$$\mathcal{H}_n \;=\; \sum_{p=1}^{\infty} H_n(p\beta)\,[\exp\{ip\,\beta\sin\theta_i\}(-1)^n \;+\; \exp\{-ip\,\beta\sin\theta_i\}], \tag{S5}$$

where $\beta\sin\theta_i = \alpha_0$ in our formulation. He states that in general, this representation converges too slowly for numerical computations and therefore demonstrates a method to derive an alternative representation using elementary functions.

In particular, it has been shown by Twersky (1961) that

$$\mathcal{H}_n \,=\, (-1)^n\,\mathcal{H}_{-n}, \tag{S6}$$

$$\mathcal{H}_{2n} \,=\, 2\sum_{p=1}^{\infty} H_{2n}(p\beta)\cos(p\beta\sin\theta_i) \,=\, 2\sum_{\mu=0}^{\infty} C_\mu\, e^{-i2n\theta_\mu} \,+\, 2\sum_{\mu=-\infty}^{-1} C_\mu\, e^{i2n\theta_\mu}$$

$$+\,\frac{i}{n\pi} \,+\, \frac{i}{\pi}\sum_{m=1}^{n} \frac{(-1)^m\,2^{2m}\,(n+m-1)!\,B_{2m}\,(\Delta\sin\theta_i)}{(2m)!\,(n-m)!\,\Delta^{2m}}, \tag{S7}$$

and

$$\mathcal{H}_{2n+1} \,=\, -2i\sum_{p=1}^{\infty} H_{2n+1}(p\beta)\sin(p\beta\sin\theta_i) \,=\, 2\sum_{\mu=0}^{\infty} C_\mu\, e^{-i(2n+1)\theta_\mu} - 2\sum_{\mu=-\infty}^{-1} C_\mu\, e^{i(2n+1)\theta_\mu}$$

$$+\,\frac{2}{\pi}\sum_{m=0}^{n} \frac{(-1)^m\,2^{2m}\,(n+m)!\,B_{2m+1}\,(\Delta\sin\theta_i)}{(2m+1)!\,(n-m)!\,\Delta^{2m+1}}, \tag{S8}$$

where $H_n = H_n^{(1)}$ is the Hankel function of the first kind, B_n is the Bernouilli polynomial as defined by Nörlund (1924) (see Twersky 1961), $\Delta = \beta/2\pi$, and C_μ and μ are defined by

$$\sin\theta_\mu \,=\, \sin\theta_i \,+\, 2\mu\pi/\beta d, \;\; \mu \,=\, 0, \pm 1, \ldots.$$

$$C_\mu \,=\, \frac{1}{\beta d\sqrt{1-\sin^2(\theta_\mu)}} \;\text{ if }\; \sin^2\theta_\mu \,<\, 1,\; C_\mu \,=\, \frac{1}{i\beta d\sqrt{\sin^2(\theta_\mu)-1}} \;\text{ if }\; \sin^2(\theta_\mu) \,>\, 1. \tag{S9}$$

The coefficient μ is equivalent to the order of diffraction p, and C_μ is equivalent to the reciprocal of the quantities χ_p or $\hat{\chi}_p$ used in this thesis, depending on $\sin^2\theta_\mu$. In expressions (S1) - (S4), we have assumed the period d to be unity (i.e. $\beta d = \beta$).

The Hankel-type grating sums (S3), (S4) are related to the Helmholtz operator and were derived in Section 2.6.1, using Graf's addition theorem, as shown by equations (2.76)-(2.84). Referring to equations (2.82) and (S5), we note that for the even Hankel sum there is no change from the Twersky formula, but for the odd sum, we multiply Twersky's representation by -1.

The K-type grating sums are linked to the modified Helmholtz operator and were derived in a similar way. We also refer to the general formula

$$S_l^{(K)}(\beta, \boldsymbol{k}_0) \,=\, \sum_{q\neq\{0,0\}} K_l\,(\beta R_q)\,e^{il\theta_q}\,e^{i\boldsymbol{k}_0\cdot\boldsymbol{R}_q}, \tag{S10}$$

used by Movchan *et al.* (2007) for the doubly periodic array. In the general case,

$$\boldsymbol{R}_q \,=\, q_1\,d\,\mathbf{e}^{(1)} \,+\, q_2\,d\,\mathbf{e}^{(2)}, \quad q \,=\, \{q_1, q_2\},\;\; q_j \,\in\, \mathbb{Z},$$

where $\mathbf{e}^{(j)}$ are basis unit vectors, or in polar coordinates,

$$\boldsymbol{R}_q \,=\, (R_q,\, \theta_q),$$

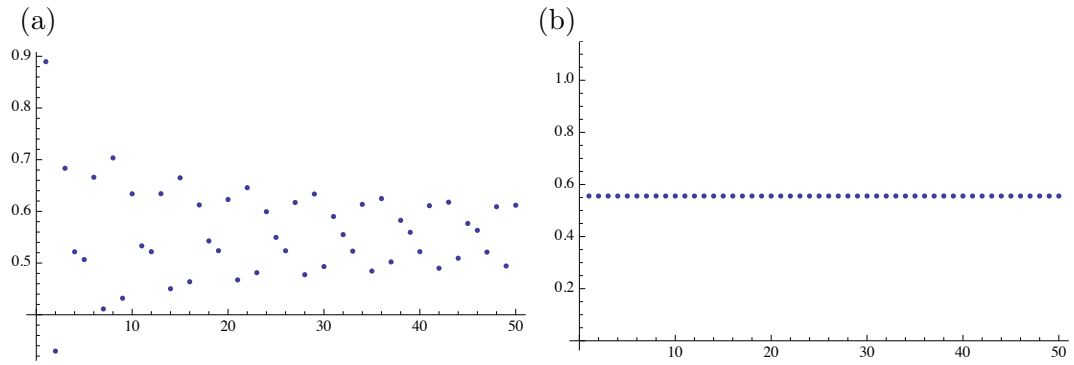

Figure A.2: (a) Real part of Hankel function grating sum evaluated by direct summation of 50 terms for $\beta = 3.6$ for normal incidence. (b) Real part of Hankel function grating sum evaluated using Twersky accelerated convergence formulae for 50 terms for $\beta = 3.6$ for normal incidence.

but we substitute parameters corresponding to the one-dimensional case of a grating: $q_2 = 0$, $q_1 \in \mathbb{Z}$ and $R_q = q_1 d$. The angular argument is satisfied by

$$\theta_q = \begin{cases} 0, & q_1 > 0 \\ \pi, & q_1 < 0, \end{cases}$$

and we replace the Bloch vector $\boldsymbol{k}_0$ by the Bloch parameter $\alpha_0 = \beta \sin\theta_i$. This yields

$$S_l^{(K,G)}(\beta, \alpha_0) = \sum_{p=1}^{\infty} K_l(\beta\, pd)\,[\exp\{i\alpha_0\, pd\} + (-1)^l \exp\{-i\alpha_0\, pd\}]. \tag{S11}$$

For l even, the imaginary parts in the sum cancel, and for l odd, the real parts cancel. Hence we obtain expressions (S1) and (S2) where we have assumed that the periodicity d of the gratings is unity. We refer to Abramowitz & Stegun (1965), equation (9.6.6) to account for negative orders of the K-type modified Bessel functions:

$$K_{-\nu}(z) = K_\nu(z),$$

where $\nu \in \mathbb{Z}$. Thus there is no change in the grating sum when the multipole order changes sign.

A.2 Accelerated convergence

We illustrate with some examples the necessity for using accelerated convergence for the Hankel grating sums. For a given value of the spectral parameter β, we compare direct summation for the Hankel function grating sums, and the corresponding Twersky formulae, for both real and imaginary parts. In Figure A.2, we show the first 50 terms of the direct sum (a) and Twersky sum (b) for the real part when $\beta = 3.6$. The equivalent sums for the imaginary part are shown in Figure A.3.

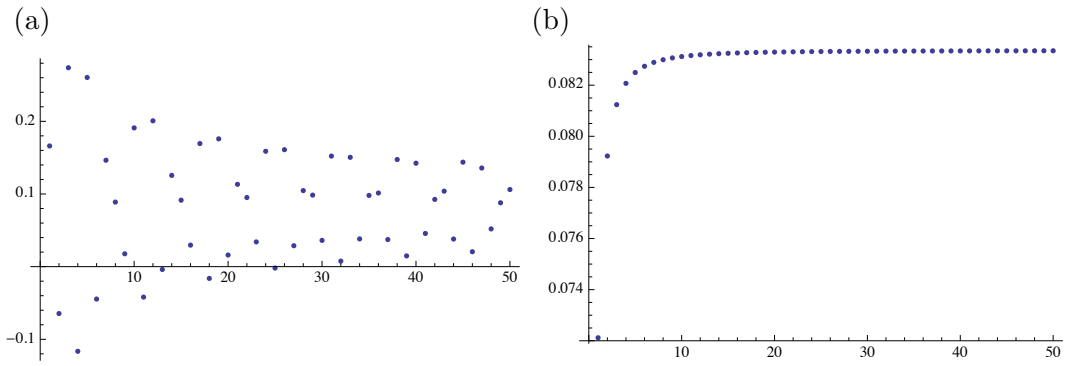

Figure A.3: (a) Imaginary part of Hankel function grating sum evaluated by direct summation of 50 terms for $\beta = 3.6$ for normal incidence. (b) Imaginary part of Hankel function grating sum evaluated using Twersky accelerated convergence formulae for 50 terms for $\beta = 3.6$ for normal incidence.

In both cases, it is clear that the direct sum results in oscillation about the converged value over a significant range. For the real part, the value varies over a range of around 0.2, approximately one third of the converged result. Several additional terms are required for satisfactory convergence, and as Twersky stated in 1961, this would considerably slow down numerical computations. In contrast for the Twersky sum, shown in parts (b) of Figs. A.2 and A.3, convergence is extremely rapid, providing accuracy to four decimal places within twenty terms for the imaginary part, and immediate convergence for the real part.

This difference is also exemplified when plotting energy versus the spectral parameter β. In Figure A.4 we plot normalised reflected energy (blue curve) and normalised transmitted energy (red) versus β for propagating orders (zero order only for this range) for a single grating of voids with radius $a = 0.1$, for normal incidence. The range for the spectral parameter is $0.1 < \beta < 2\pi$, and we plot for both direct summation and accelerated convergence.

For direct summation (Fig. A.4 (a)), we observe oscillation about the genuine values of 1 for the reflected energy and 0 for the transmitted energy. In contrast, this oscillatory effect is effectively eliminated when using the Twersky accelerated convergence formulae (Fig. A.4 (b)). We note that the conservation of energy for the grating is clearly illustrated in Fig. A.4(b), but appears to be unsatisfied for the evaluation of the Hankel sums using direct summation in part (a).

For a grating of rigid pins, the plot that we obtain for reflectance of a single grating does not depend on the choice of summation technique. This is because this is the monopole case, where the sums are reduced to one term only.

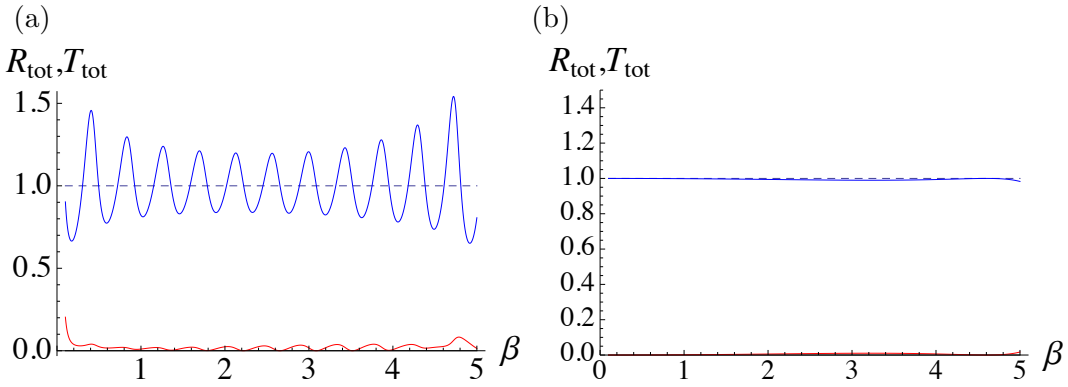

Figure A.4: Normalised reflected energy R_{tot} (blue curve) and transmitted energy T_{tot} (red) versus spectral parameter β for normal incidence for a single grating with $a = 0.1$ in the range $0.1 < \beta < 2\pi$ for propagating orders (zeroth order only in this range). (a) grating sums evaluated by direct summation and (b) Twersky accelerated convergence formulae.

Bibliography

[1] Abramowitz, M. & Stegun, I. A. (1965) *Handbook of Mathematical Functions with Formulas, Graphs, and Mathematical Tables*. Dover Reprint.

[2] Akahane, Y., Asano, T., Song, B. S. & Noda, S. (2003) High-Q photonic nanocavity in a two-dimensional photonic crystal. *Nature*, **425**(6961):944-947.

[3] Antonakakis, T. & Craster, R. V. (2012) High-frequency asymptotics for microstructured thin elastic plates and platonics. *Proc. R. Soc. A* **468**(2141):1408-1427.

[4] Antonakakis, T., Craster, R. V. & Guenneau, S. (2013) Moulding and shielding flexural waves in elastic plates *arXiv*: 1304.5782.

[5] Bertoldi, K., Bigoni, D. & Drugan, J. W. (2007a) Structural interfaces in linear elasticity. Part I: Nonlocality and gradient approximations *J. Mech. Phys. Solids*, **55**, 1-34.

[6] Bertoldi, K., Bigoni, D. & Drugan, J. W. (2007b) Structural interfaces in linear elasticity. Part II: Effective properties and neutrality *J. Mech. Phys. Solids*, **55**, 35-63.

[7] Bertoldi, K., Bigoni, D. & Drugan, J. W. (2007c) A discrete-fibers model for bridged cracks and reinforced elliptical voids. *J. Mech. Phys. Solids*, **55**, 1016-1035.

[8] Bigoni, D., Gei, M. & Movchan, A. B. (2008) Dynamics of a prestressed stiff layer on an elastic half space: filtering and band gap characteristics of periodic structural models derived from longwave asymptotics. *J. Mech. Phys. Solids*, **56**, 2494-2520.

[9] Bigoni, D. & Movchan, A. B. (2002) Statics and dynamics of structural interfaces in elasticity. *Int. J. Solids Struct.*, **39**, 4843-4865.

[10] Born, M. & Wolf, E. (1959) *Principles of Optics*, Pergamon Press, London.

[11] Borwein, J., Glasser, L., McPhedran, R. C., Wan, J. & Zucker J. (2013) *Lattice Sums Then and Now*, Cambridge University Press.

[12] Botten, L. C., McPhedran, R. C. & Lamarre, J. M. (1985) Inductive grids in the resonant region: theory and experiment. *Int. J. of Infrared and Millimeter Waves*, **6**, 511-575.

[13] Botten, L. C., Nicorovici, N. A., McPhedran, R. C., de Sterke, C. M. & Asatryan, A. A. (2001) Photonic band structure calculations using scattering matrices. *Phys. Rev. E*, **64**, 046603. (doi: 10.1103/PhysRevE.64.046603)

[14] Botten, L. C., McPhedran, R. C., Nicorovici, N. A., Asatryan, A. A., M. de Sterke, C., Robinson, P. A., Busch, K., Smith, G. H. & Langtry, T. N. (2003) Rayleigh Multipole Methods for Photonic Crystal Calculations, Progress In Electromagnetics Research, PIER 41, 2160.

[15] Brillouin, L. (1953) *Wave Propagation in Periodic Structures*, Dover Publications, Inc. New York

[16] Brun, M., Guenneau, S., Movchan, A. B. & Bigoni, D. (2010) Dynamics of structural interfaces: Filtering and focussing effects of elastic waves. *J. Mech. Phys. Solids*, **58**, 9, 1212-1224.

[17] Castro Neto, A. H., Guinea, F., Peres, N. M. R., Novoselov, K. S. & Geim, A. K. (2009) The electronic properties of graphene. *Rev. Mod. Phys.*, **81**, 1, 109-162.

[18] Chang, C.-S. & Chang, H.-C. (1994) Theory of the circular harmonics expansion method for multiple-optical-fiber system. *J. Lightwave Technol.* **12**, 415417. (doi:10.1109/50.285344)

[19] Chin, S. K., Nicorovici, N. A. & McPhedran, R. C. (1994) Green's function and lattice sums for electromagnetic scattering by a square array of cylinders. *Phys. Rev. E* **49**, 45904602. (doi:10. 1103/PhysRevE.49.4590)

[20] Colquitt, D. J., Brun, M., Gei, M., Movchan, A. B., Movchan, N. V. & Jones, I. S. (2014) Transformation elastodynamics and cloaking for flexural waves. *arXiv*: 1401.7579.

[21] Deymier, P. (2013) *Acoustic Metamaterials and Phononic Crystals*, Springer.

[22] Dossou, K., Byrne, M. A. & Botten, L. C. (2006) Finite element computation of grating scattering matrices and application to photonic crystal band calculations. *Journal of Computational Physics*, **219**(1):120143.

[23] Dubois M., Farhat M., Bossy E., Enoch S., Guenneau S. & Sebbah P. (2013) Flat lens for time-domain focusing of elastic waves in thin plates; *arXiv*: 1303.3022.

[24] Eichenfield, M., Chan, J., Camacho, R. M., Vahala, K. J. & Painter, O. (2009) Optomechanical crystals, *Nature Letters*, **462**, 78-82. (doi: 10.1038/nature08524)

[25] Evans, D. V. & Meylan, M. H. (2005) Scattering of flexural waves by a pinned thin elastic sheet floating on water. 20th international workshop on water waves and floating bodies, Longyearbyen, Svalbard.

[26] Evans, D. V. & Porter, R. (2006) Wave diffraction by a periodically constrained elastic plate floating on water. Proceedings of the 21st International Workshop on Water Waves and Floating Bodies, Loughborough, UK.

[27] Evans, D. V. & Porter, R. (2007) Penetration of flexural waves through a periodically constrained thin elastic plate in *vacuo* and floating on water. *J. Eng. Maths.* **58**, 317-337. (doi: 10.1007/s10665-006-9128-0)

[28] Evans, D. V. & Porter, R. (2008) Flexural waves on a pinned semi-infinite thin elastic plate. *Wave Motion*, **45**(6):745757.

[29] Fano, U. (1961) Effects of configuration interaction on intensities and phase shifts, *Phys. Rev.*, **124**, No. 6, 1866-1878.

[30] Fano, U. (1941) The theory of anomalous diffraction gratings and of quasi-stationary waves on metallic surfaces (Sommerfeld's waves), *J. Opt. Soc. Am.* **31**, 213-222.

[31] Farhat, M., Guenneau, S., Enoch, S. & Movchan, A. B. (2009) Cloaking bending waves propagating in thin elastic plates. *Phys. Rev. B* **79**, 033102.

[32] Farhat, M., Guenneau, S., Enoch, S., Movchan, A. B. & Petursson, G. G. (2010a) Focussing bending waves via negative refraction in perforated thin plates. *Applied Physics Letters*, **96**(8):081909.

[33] Farhat, M., Guenneau, S. & Enoch, S. (2010b) High directivity and confinement of flexural waves through ultra-refraction in thin perforated plates. *Euro. Phys. Lett.* **91**, 54003.

[34] Fleischhauer, M., Imamoglu, A. & Marangos, J. P. (2005) Electromagnetically induced transparency: optics in coherent media. *Reviews of Modern Physics*, **77**, 633-673.

[35] Gei. M., Movchan, A. B. & Bigoni, D. (2009) Band-gap shift and defect-induced annihilation in prestressed elastic structures *J. Appl. Phys.*, **105**, 063507.

[36] Graff, K. F. (1975) *Wave motion in elastic solids*, Oxford, UK: Clarendon Press.

[37] Guida, G., Maystre, D., Tayeb, G. & Vincent, P. (1998) Mean field theory of photonic crystals, *J. Opt. Soc. Am. B*, **15**, 23082315.

[38] Ha, S., Sukhorukov, A. A., Lavrinenko, A. V., Shadrivov, I. V., Powell, D. A. & Kivshar, Y. S. (2011) Observation of tunneling of slow and fast electromagnetic modes in coupled periodic waveguides. *Applied Physics Letters*, **98**, 061909.

[39] Halkjær, S., Sigmund, O. & Jensen, J. S. (2006) Maximizing band gaps in plate structures. *Struct. Multidisc. Optim.* **32**, 263275. (doi:10.1007/s00158-006-0037-7)

[40] Harris, S. E. (1989) Lasers without inversion: Interference of lifetime-broadened resonances *Phys. Rev. Lett.* **62**, 1033-1036.

[41] Haslinger, S. G., Movchan, N. V., Movchan, A. B. & McPhedran, R. C. (2012) Transmission, trapping and filtering of waves in periodically constrained elastic plates. *Proc. R. Soc. A* **468**, 76-93.

[42] Haslinger S. G., McPhedran R. C., Movchan N. V. & Movchan A. B. (2013a) Localisation near defects and filtering of flexural waves in structured plates. *Int. J. Fract.*. DOI 10.1007/s10704-013-9812-9

[43] Haslinger S. G., McPhedran R. C., Movchan N. V. & Movchan A. B. (2013b) Structured interfaces for flexural waves - trapped modes and transmission resonances. *Journal of Physics: Conference Series* **451** 012024.

[44] Haslinger S. G., Movchan A. B., Movchan N. V. & McPhedran R. C. (2014) Symmetry and resonant modes in platonic grating stacks. In press in *Waves in Random and Complex Media*

[45] Hau, L. V., Harris, S. E., Dutton, Z. & Behroozi, C. H. (1999) Light speed reduction to 17 metres per second in an ultracold atomic gas. *Nature*, **397**, 594-598.

[46] Hessel, A. & Oliner, A. A. (1965) A new theory of Wood's anomalies on optical gratings. *Appl. Opt.* **4**, 1275-1297.

[47] Huang X, Lai Y, Hang Z H, Zheng H & Chan C. T. (2011) Dirac cones induced by accidental degeneracy in photonic crystals and zero-refractive-index materials. *Nat. Mater.* 2011;**10**: 582-586.

[48] Hutley, M. C. (1970) *Diffraction Gratings*, Academic Press (New York).

[49] Jenkins, F. A. & White, H. E. (1981) *Fundamentals of Optics*, McGraw-Hill (Singapore).

[50] Joannopoulos, J., Johnson, S. G., Winn, J. N. & Meade, R. D. (2008) *Photonic Crystals: Molding the Flow of Light*, Princeton University Press.

[51] Kittel, C. (1971) *Introduction to solid state physics*. Wiley, New York.

[52] Konenkov, Y. K. (1960) A Rayleigh-type flexural wave *Soviet Physics Acoustics*, **6**:122123.

[53] Konenkov, Y. K. (1964) Diffraction of a flexural wave by a circular obstacle in a plate. *Soviet Physics Acoustics*, **10**(2):153156.

[54] Lawrence, F. J., Botten, L. C., Dossou, K. B., McPhedran, R. C. & Martijn de Sterke, C. (2010) Photonic-crystal surface modes found from impedances *Phys. Rev. A* **82**, 053840.

[55] Lawrence, F. J., Martijn de Sterke, C., Botten, L. C., McPhedran, R. C. & Dossou, K. B. (2013) Modelling photonic crystal interfaces and stacks: impedance-based approaches *Advances in Optics and Photonics* **5**, 385-455.

[56] Leissa, A. W. (1969) *Vibration of plates*, NASA SP-160, Washington D. C.

[57] Lin, Q., Rosenberg, J., Chang, D., Camacho, R., Eichenfield, M., Vahala, K. J. & Painter, O. (2009) Coherent mixing of mechanical excitations in nano-optomechanical structures *arXiv*: 0908.1128.

[58] Linton, C. M. & McIver, P. (2001) *Handbook of Mathematical Techniques for Wave/Structure Interactions*. Chapman & Hall, Boca Raton.

[59] Liu, N., Langguth, L., Weiss, T., Kästel, J., Fleischhauer, M., Tilman, P. & Giessen, H. (2009) Plasmonic analogue of electromagnetically induced transparency at the Drude damping limit *Nat. Mater.* **8** 758-762

[60] Liu, N., Weiss, T., Mesch, M., Langguth, L., Eigenthaler, U., Hirscher, M., Sönnichsen, C. & Giessen, H. (2010) Planar metamaterial analogue of electromagnetically induced transparency for plasmonic sensing *Nano Lett.* **10** 1103-1107.

[61] Liu R., Lai Y., Huang X. & Chan C. T. (2011) Dirac cones at $\mathbf{k} = 0$ in phononic crystals. *Phys. Rev. B* **84**:224113.

[62] Lo, K. M., McPhedran, R. C., Bassett, I. M. & Milton, G. W. (1994) An electromagnetic theory of dielectric waveguides with multiple embedded cylinders. *J. Lightwave Technol.* **12**, 396410. (doi:10.1109/50.285321)

[63] Loewen, E. G. (1970) *Diffraction Grating Handbook* (Online).

[64] Loewen, E. G. & Popov, E. (1997) *Diffraction Gratings and Applications*. Marcel Dekker, New York.

[65] Lu, T. H. (1966) *Diffraction of flexural waves by circular rigid inclusion in an elastic plate and dynamic stress concentration*. Masters thesis, National Taiwan University, Taiwan.

[66] Mahmoodian, S., Sukhorukov, A. A., Ha, S., Lavrinenko, A. V., Poulton, C. G., Dossou, K. B., Botten, L. C., McPhedran, R. C. & de Sterke, C. M. (2010) Paired modes of heterostructure cavities in photonic crystal waveguides with split band edges, *Optics Express*, **18**, (25): 25693 - 25701.

[67] Marcuse, D. (1972) *Light Transmission Optics*. Van Nostrand Reinhold Co., New York.

[68] Marcuse, D. (1974) *Theory of Dielectric Optical Waveguides*. Academic Press, New York.

[69] McPhedran, R. C. & Waterworth, M. D. (1972) A theoretical demonstration of properties of grating anomalies (S-polarization) 1972 *Optica Acta*, **19**, (11) 877-892.

[70] McPhedran, R. C. & Waterworth, M. D. (1973) Properties of diffraction grating anomalies 1973 *Optica Acta*, **20**, (7) 533-547.

[71] McPhedran, R. C. & Maystre, D. (1977) On the theory and solar application of inductive grids. *Appl. Phys.*, **14**, 1-20.

[72] McPhedran, R. C., Nicorovici, N. A., Botten, L. C. & Grubits, K. A. (2000) Lattice sums for gratings and arrays. *Journal of Mathematical Physics*, **41**(11):78087816.

[73] McPhedran, R. C., Movchan, A. B. & Movchan, N. V. (2009) Platonic crystals: Bloch bands, neutrality and defects, *Mechanics of Materials* **41**, 356-363. (doi: 10.1016/ j.mechmat.2009.01.005)

[74] Meylan M.H. & McPhedran R. C. (2011) Fast and slow interaction of elastic waves with platonic clusters. *Proc. R. Soc. A*; **467**: 3509-3529.

[75] Mohammadi, S., Eftekhar, A. A., Hunt, W. D. & Ali Adibi, A. (2009) High-Q micromechanical resonators in a two-dimensional phononic crystal slab, *Applied Physics Letters*, **94**, 051906. (doi: 10.1063/1.3078284)

[76] Moroz, A. (2006) Quasi-periodic Greens functions of the Helmholtz and Laplace equations. *J. Phys. A* **36**, 11 24711 282. (doi:10.1088/0305-4470/39/36/009)

[77] Morse, P. M. & Feshbach, H. (1953) *Methods of Theoretical Physics*. McGraw-Hill Book Company Inc.

[78] Movchan, A. B. & Movchan, N. V. (1995) *Mathematical modelling of solids with non-regular boundaries*. CRC Press, Inc.

[79] Movchan, A. B., Movchan, N. V. & Poulton, C. G. (2002) *Asymptotic Models of Fields in Dilute and Densely Packed Composites*, Imperial College Press, London.

[80] Movchan, A. B., Movchan, N. V. & McPhedran, R. C. (2007) Bloch-Floquet bending waves in perforated thin plates. *Proc. R. Soc. A* **463**, 2505-2518.

[81] Movchan, N. V., McPhedran, R. C., Movchan, A. B. & Poulton, C. G. (2009) Wave scattering by platonic grating stacks. *Proc. R. Soc. A* **465**, 3383 - 3400. (doi: 10.1098/rspa.2009.0301)

[82] Movchan, N. V., McPhedran, R. C. & Movchan, A. B. (2011) Flexural waves in structured elastic plates: Mindlin versus bi-harmonic models. *Proc. R. Soc. A* **467**, 869-880.

[83] Nicorovici, N. A., McPhedran, R. C. & Petit, R. (1994a) Efficient calculation of the Green's function for electromagnetic scattering by gratings. *Phys. Rev. E* **49** 4563-4577.

[84] Nicorovici, N. A. & McPhedran, R. C. (1994b) Lattice sums for off-axis electromagnetic scattering by gratings. *Phys. Rev. E* **50** 3143-3160.

[85] Nicorovici, N. A., McPhedran, R. C. & Botten, L. C. (1995a) Photonic band gaps: non-commuting limits and the acoustic band. *Phys. Rev. Lett.* **75**, 15071510. (doi:10.1103/PhysRevLett.75. 1507)

[86] Nicorovici, N. A., McPhedran, R. C. & Botten, L. C. (1995b) Photonic band gaps for arrays of perfectly conducting cylinders. *Phys. Rev. E* **52**, 11351145. (doi:10.1103/PhysRevE.52.1135)

[87] Norris, A. N. & Vemula, C. (1995) Scattering of flexural wave on thin plates. *J. Sound Vib.* **181**, 115125. (doi:10.1006/jsvi.1995.0129)

[88] Pao, Y. H. & Chao, C. C. (1964) Diffraction of flexural waves by a cavity in an elastic plate. *J. AIAA* **2**, 20042010. (doi:10.2514/3.2716)

[89] Papasimakis, N., Fedotov, V. A., Zheludev, N. I. & Prosvirnin, S. L. (2008) Metamaterial analog of electromagnetically induced transparency *Phys. Rev. Lett.* **101** 253903.

[90] Pelton, E.L. & Munk, B.A. (1979) Scattering from periodic arrays of crossed dipoles *IEEE Trans* **AP-27**, 323-330.

[91] Pendry, J. B., Holden, A. J., Stewart, W. J. & Youngs, I. (1996) Extremely low frequency plasmons in metallic mesostructures. *Phys. Rev. Lett.* **76**, 47734776. (doi:10.1103/PhysRevLett.76.4773)

[92] Petit, R. (1980) *Electromagnetic Theory of Gratings*, Springer-Verlag, New York.

[93] Platts, S. B., Movchan, N. V., McPhedran, R. C. & Movchan, A. B. (2002) Two-dimensional phononic crystals and scattering of elastic waves by an array of voids *Proc. R. Soc. Lond. A* **458**, 2327-2347. (doi: 10.1098/rspa.2002.0960)

[94] Platts, S. B., Movchan, N. V., McPhedran, R. C. & Movchan, A. B. (2003) Band gaps and elastic waves in disordered stacks: normal incidence *Proc. R. Soc. Lond. A* **459**, 221-240. (doi: 10.1098/rspa.2002.1041)

[95] Popov, E., Mashev, L. & Maystre, D. (1986) Theoretical study of the anomalies of coated dielectric gratings, *Optica Acta* (currently *Journal of Modern Optics*), **33**, 607-619. (doi: 10.1080/713821994)

[96] Poulton, C. G. (1999) Asymptotics and Wave Propagation in Cylindrical Geometries: PhD thesis, University of Sydney.

[97] Poulton, C. G., Botten, L. C., McPhedran, R. C., Nicorovici, N. A. & Movchan, A. B. (2001) Noncommuting limits in electromagnetic scattering: asymptotic analysis for an array of highly conducting inclusions. *SIAM J. Appl. Math.* **61**, 1706-1730.

[98] Poulton, C. G., McPhedran, R. C., Movchan, N. V. & Movchan, A. B. (2010) Convergence properties and flat bands in platonic crystal band structures using the multipole formulation. *Waves in Random and Complex Media* **20**, 702-716.

[99] Poulton, C. G., Movchan, A. B., Movchan, N. V. & McPhedran, R. C. (2012) Analytic theory of defects in periodically structured elastic plates. *Proceedings of the Royal Society A* **468** (2140):11961216.

[100] Sakoda, K. (2005) *Optical Properties of Photonic Crystals*, Springer.

[101] Smith, M. J. A., Meylan, M. H. & McPhedran, R. C. (2011) Scattering by cavities of arbitrary shape in an infinite plate and associated vibration problems. *Journal of Sound and Vibration*, **330**(16):40294046.

[102] Smith M. J. A., McPhedran R. C., Poulton C. G. & Meylan M. H. (2012a) Negative refraction and dispersion phenomena in platonic clusters. *Waves in Random and Complex Media*. **22**: 4: 435-458.

[103] Smith M. J. A, Porter R. & Williams T. D. (2012b) The effect on bending waves by defects in pinned elastic plates. *Journal of Sound and Vibration*. **331**: 23: 5087-5106.

[104] Smith, M. J. A., Meylan, M. H. & McPhedran, R. C. (2013) Flexural wave filtering and platonic polarizers in thin elastic plates. *The Quarterly Journal of Mechanics and Applied Mathematics* **66**(4): 437-463.

[105] Smith M. J. A. (2013) PhD Thesis: Wave propagation through periodic structures in thin plates, University of Auckland, New Zealand.

[106] Smith M. J. A., McPhedran, R. C. & Meylan, M. H. (2013) Double Dirac cones at $\kappa = 0$ in pinned platonic crystals. (In press in Waves in Random and Complex Media).

[107] Stenger, N., Wilhelm, M. & Wegener, M. (2012) Experiments on elastic cloaking in thin plates. *Phys. Rev. Lett.* **108**, 014301.

[108] Tassin, P., Zhang, L., Koschny, T., Economou, E. N. & Soukoulis, C. M. (2009) Planar designs for electromagnetically induced transparency in metamaterials *Phys. Rev. Lett.* **102** 053901.

[109] Tassin, P., Zhang, L., Koschny, T., Economou, E. N. & Soukoulis, C. M. (2012) Electromagnetically induced transparency and absorption in metamaterials: the radiating two-oscillator model and its experimental confirmation *Phys. Rev. Lett.* **109** 187401.

[110] Taubert, R., Hentschel, M., Kästel, J. & Giessen, H. (2012) Classical Analogue of Electromagnetically Induced Absorption in Plasmonics *Nano Lett.* **12** 1367-1371.

[111] Taubert, R., Hentschel, M. & Giessen, H. (2013) Plasmonic analogue of electromagnetically induced absorption: simulations, experiments and coupled oscillator analysis *J. Opt. Soc. Am. B* **30** 3123-3134.

[112] Twersky, V. (1961) Elementary function representations of Schlömilch series. *Arch. Ration. Mech. Anal.* **8**, 323-332.

[113] Ulrich, R. & Tacke, M. (1973) Submillimeter wave-guiding on periodic metal structure. *Appl. Phys. Lett.* **22**, 251-253.

[114] Vemula, C. & Norris, A. N. (1997) Flexural wave propagation and scattering on thin plates using Mindlin theory. *Wave Motion* **26**, 112. (doi:10.1016/S0165-2125(97)00016-4)

[115] Wang, J., Baohe, Y., Fan, C., He, J., Ding, P., Xue, Q. & Liang, E. (2013) A novel planar metamaterial design for electromagnetically induced transparency and slow light. *Optics Express* Optical Society of America.

[116] Wood, R. W. (1902) On the remarkable case of uneven distribution of light in a diffraction grating spectrum, *Philos. Mag.* **4**, 396-402.

[117] Zhang, S., Genov, D. A., Wang, Y., Liu, M. & Zhang, X. (2008) *Phys. Rev. Lett.* **101** 047401.